Max-Planck-Institut
für Meteorologie

REPORT No. 102

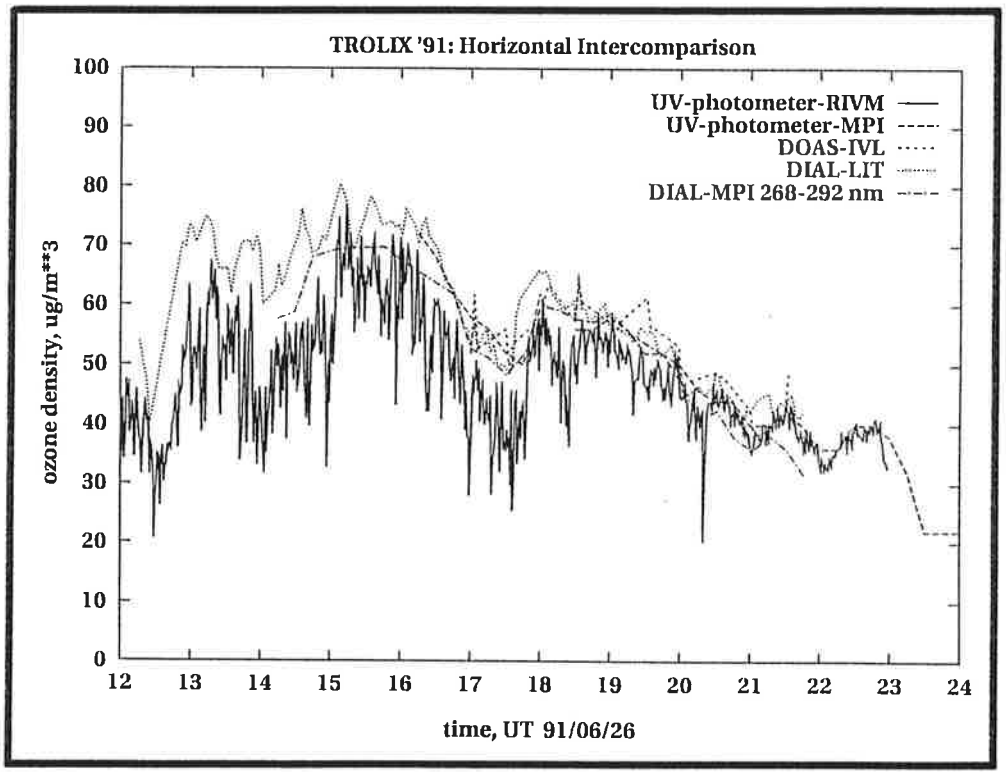

TROPOSPHERIC OZONE LIDAR INTERCOMPARISON EXPERIMENT, TROLIX '91 FIELD PHASE REPORT

by

JENS BÖSENBERG • GERARD ANCELLET • ARNOUD APITULEY • HANS BERGWERFF
GÖTZ v. COSSART • HANS EDNER • JENS FIEDLER • BO GALLE • CORA de JONGE
JOHAN MELLQVIST • VALENTIN MITEV • THORSTEN SCHABERL • GERD SONNEMANN
JAN SPAKMAN • DAAN SWART • EVA WALLINDER

HAMBURG, APRIL 1993

Tropospheric Ozone Lidar Intercomparison Experiment, TROLIX '91, Field Phase Report

Jens Bösenberg[1], Gerard Ancellet[2], Arnoud Apituley[3], Hans Bergwerff[3], Götz v. Cossart[4], Hans Edner[5], Jens Fiedler[4], Bo Galle[6], Cora de Jonge[3], Johan Mellqvist[6], Valentin Mitev[2], Thorsten Schaberl[1], Gerd Sonnemann[4], Jan Spakman[3], Daan Swart[3], Eva Wallinder[5]

March 31, 1993

(1) Max-Planck-Institut für Meteorologie (MPI), Hamburg, Germany
(2) CNRS/Service d'Aeronomie (CNRS/SA), Paris, France
(3) Rijksinstitut voor Volksgezondheid en Milieuhygiene (RIVM), Bilthoven, The Netherlands
(4) Observatorium für Atmosphärenforschung (OAF), Kühlungsborn, Germany
(5) Lund Tekniska Högskola (LIT), Lund, Sweden
(6) Institutionen för Vatten- och Luftvardsforskning (IVL), Göteborg, Sweden

ISSN 0937–1060

Abstract

The Tropospheric Ozone Lidar Intercomparison Experiment TROLIX '91 has been initiated as part of the TESLAS subproject of the cooperative programme EUROTRAC. It has been performed in June 1991 at the Rijksinstitut voor Volksgezondheid en Milieuhygiene (RIVM) in Bilthoven, The Netherlands. The experiment was based on the simultaneous operation of different types of differential absorption lidars (DIAL), a special version of a Differential Optical Absorption Spectroscopy Instrument (DOAS), helicopter borne in situ instruments, and many other supporting measurements. After a short introduction to the general methodology the instruments are described, the experimental operations are explained, and a selection of data are presented. Some examples are given for the results of the intercomparison, as far as they have been available at the present stage of evaluation. The main purpose of this report, however, is to provide an overview over the material collected during the experiment, in order to facilitate further detailed studies in cooperation between the different groups which have participated.

Contents

Chapter 1

Introduction

TESLAS as a subproject of EUROTRAC has taken an initiative to develop differential absorption lidar systems for ozone measurements with the intention of routine use for tropospheric profiling. Most of them have been designed to operate in the UV wavelength region, roughly between 248 and 313 nm. The laser sources used for these instruments include NdYag with frequency quadrupling and subsequent first order stimulated Raman scattering (SRS) in hydrogen and deuterium, KrF excimer lasers with subsequent SRS in hydrogen and deuterium up to second order, and NdYag pumped dye lasers with subsequent frequency doubling.

In the troposphere ozone concentrations usually are much smaller than in the stratosphere, aerosol load is generally higher, with rather large gradients in particular at air mass boundaries. These effects make DIAL measurements in the troposphere much more difficult than the rather well established stratospheric measurements, see e.g. [Uch 83] [Wern 83] [Pelo 86] [Godi 89] [McDe 90] [Neub 91]. In addition, interference with oxygen, water vapor, sulfur dioxide, and possibly other pollutants can cause problems.

At low ozone concentration the requested high vertical resolution can only be achieved when wavelengths in the strong part of the Hartley band are used. In the whole band the wavelength dependence of the absorption cross section is weak, making a large separation necessary between online and offline wavelengths. Therefore, differential extinction and backscatter effects of the aerosol can no longer be neglected. These problems are most serious in the boundary layer, where both the concentration of pollutants and the aerosol loading can be high. The actual influence is strongly dependent on the individual choice of wavelengths, e.g. structures in the SO_2 spectrum are narrower than 1 nm [Thom 90], thus it can be quite different for the different systems.

It has often been claimed that the DIAL method is self calibrated. In principle this is true, if all the abovementioned effects are properly accounted for. Under realistic conditions, however, due to the the large number of error sources, and the lack of knowledge on actual aerosol properties, the accuracy of the retrieval has to be assessed, by intercomparison of different lidar methods as well as by cross comparison to conventional in situ measurements. Therefore it was decided to have a first TESLAS intercomparison campaign, which was focussed on measurements in the lower troposphere.

The opportunity of having an extended field experiment with several instruments was also used to perform an intensive study of the ozone distribution in the lower troposphere.

The major objectives of the experiment were:

- to determine, which and how many wavelengths are required for a sufficiently accurate ozone retrieval in the lower troposphere, in the presence of aerosol, water vapor, oxygen, sulfur dioxide, and possibly other pollutants
- to assess the accuracy which can be achieved under realistic conditions
- to compare the performance of different types of systems already developed
- to compare Lidar to in situ measurements
- to study ozone vertical distribution with high temporal resolution and coverage (including diurnal cycle)
- to study the relation between ground level ozone concentrations and vertical distribution for several meteorological conditions.

Not all lidar systems developed so far in the TESLAS subproject could participate in the intercomparison, because most systems are not mobile at the present time. But, fortunately, we had at least one of the different types of UV-DIAL present. In addition to the intercomparison of different instrument types, this led to the acquisition of a unique data set comprised of simultaneous measurements at up to eight UV wavelengths between 248 and 313 nm, plus one measurement at 1064 nm. This data set will be especially useful in the assessment of aerosol influence on the DIAL evaluation. In particular a distinction between aerosol properties and interference by absorption of pollutants should be possible, as well as a characterization of different aerosol types for behavior in the UV.

Chapter 2

General methodology

The principles of the differential absorption lidar technique (DIAL) have been described previously by several authors, both in general [Scho 74] [Meas 84], and for the specific case of ozone measurements in the UV [Megi 77] [Pelo 82] [Brow 85]. They will only briefly be summarized in the following.

When a short laser pulse is transmitted into the atmosphere, the signal obtained from a detector connected to a receiving telescope collecting the backscattered light is described by the lidar equation

$$P_i(R) \cdot R^2 = P_{i,0} \cdot E \cdot F \cdot \beta_i(R) exp\left\{-2 \int_0^R (\alpha_{i,O_3}(r) + \gamma_i(r))\, dr\right\} \tag{2.1}$$

where $P_i(R)$ is the received power at wavelength λ_i, R is the distance to the scattering volume, $P_{i,0}$ is the transmitted power, E is the total system efficiency, F is the receiver area, $\beta_i(R)$ is the total backscatter coefficient at range R, $\alpha_{i,O_3}(r)$ is the ozone absorption coefficient at wavelength λ_i and range r, and $\gamma_i(r)$ is the remaining extinction coefficient, where extinction by Rayleigh scattering, aerosol extinction, and absorption by other gases are lumped together. In the usual two-wavelengths DIAL technique, two measurements at wavelengths with a suitable difference in absorption cross section of the gas under study are made. Let λ_2 be the off-line wavelength, and λ_1 the on-line. Then taking the ratio of the two lidar equations, and logarithmically differentiating, yields

$$\frac{d}{dR} ln \frac{P_2(R)}{P_1(R)} = 2 \cdot \left\{\Delta\alpha(R) + \Delta\gamma(R) + \frac{d}{dR} ln \frac{\beta_2(R)}{\beta_1(R)}\right\} \tag{2.2}$$

where $\Delta\alpha(R) = \alpha_1(R) - \alpha_2(R)$ is the desired differential ozone absorption, $\Delta\gamma(R) = \gamma_1(R) - \gamma_2(R)$ is the error term caused by the differential extinction except for ozone, and the last term is the error due to a gradient in differential backscattering.

In typical DIAL applications using narrow absorption lines and correspondingly small differences between on- and off-line wavelengths, only the first term on the righthandside of equation (2) has to be considered, the two other terms are generally neglected. But in the poorly structured Hartley-Huggins absorption band of ozone, the wavelength difference between the on- and off-line measurements has to be rather large (at least several nm) in order to reach a suitable differential absorption. Under these conditions the error terms

generally are considerable, and the ozone number density n_{O_3} is obtained as

$$\begin{aligned} n_{O_3}(R) &= \frac{\Delta\alpha(R)}{\Delta\sigma(R)} \\ &= \frac{1}{\Delta\sigma}\left\{\frac{1}{2}\frac{d}{dR}ln\frac{P_2(R)}{P_1(R)} - \Delta\gamma - \frac{1}{2}\frac{d}{dR}ln\frac{\beta_2(R)}{\beta_1(R)}\right\} \qquad (2.3) \\ & \qquad (2.4) \end{aligned}$$

where $\Delta\sigma$ is the differential absorption cross section of ozone.

For a more detailed analysis, we can write

$$\Delta\gamma = \Delta\alpha_R + \Delta\alpha_{SO_2} + \Delta\alpha_P + \Delta\alpha_a \qquad (2.5)$$

where $\Delta\alpha_R$ stands for the difference in Rayleigh extinction, $\Delta\alpha_a$ is the difference in aerosol extinction, $\Delta\alpha_{SO_2}$ is the differential absorption for sulfur dioxide, and $\Delta\alpha_P$ includes all differential absorption terms which may arise from the presence of other gases, e.g. oxygen, water vapor, nitrogen dioxide, and possibly other pollutants.

The Rayleigh differential extinction, $\Delta\alpha_R$, can be calculated with sufficient accuracy using the approximate density obtained from the standard aerological observations of the weather service, and the known wavelength dependence of Rayleigh scattering.

The interference with SO_2 is a problem which cannot be handled generally for all different systems, since SO_2 has a highly structured absorption spectrum with narrow features [Thom 90]. Thus the cross sensitivity strongly depends on the actual wavelengths of the DIAL system. To give an example, for the 277-313 nm line pair of the hydrogen shifted KrF laser, the cross sensitivity is 12%, i.e. 12 % of of the SO_2 density would be interpreted as ozone. This is a problem only for a measurement in a polluted boundary layer, and it should be noted that this is still much better than the in situ measurement by the ECC-sondes, where the cross sensitivity has been determined as 67%, see section 4.8.

In the combined term $\Delta\alpha_P$ the oxygen absorption part can easily be accounted for, by using the known air density, the known mixing ratio of oxygen, and the absorption cross section for the actual wavelength.

For water vapor absorption, the situation is somewhat confusing in the wavelength region under consideration. Recently, laboratory results have been published [Karm 90], claiming the existence of a strong absorption band of water vapor below ≈ 290 nm. This has not yet been confirmed by other measurements. The question whether or not the existence of this strong absorption band is compatible with atmospheric Lidar measurements will be specifically addressed in the evaluation of TROLIX results.

Other pollutants are very unlikely to reach concentration levels high enough to cause serious errors, except for extremely polluted areas. For the case of TROLIX measurements, they can be neglected.

The correction for differential aerosol extinction, $\Delta\alpha_a$, is not known a priori. A correction method has been described by [Brow 85], relying on the standard procedure of obtaining the aerosol extinction coefficient from a single wavelength lidar measurement, as described by many authors in different variations, e.g. [Klet 81] [Fern 84] [Ferg 83]

[Sasa 85]. Common to all these proposed algorithms is the necessity to make an assumption on α_a at a calibration range, and a power law relation

$$\alpha_a = S \cdot \beta_a^q \tag{2.6}$$

where the constants S, the so called lidar ratio, and q have to be known (or guessed) for the particular aerosol type(s) present in the atmosphere under study. Both the aerosol extinction profile $\beta_a(R)$ and the aerosol extinction profile $\alpha_a(R)$ can than be calculated using one of the proposed algorithms [Klet 81] [Fern 84] [Ferg 83] [Sasa 85]. For details of the best choice of the algorithm and the numerical stability problems, the reader is referred to the literature. Finally, when an extinction profile is calculated at one wavelength, the wavelength dependence of the aerosol extinction has to be known. Generally, an Ångström law is assumed,

$$\alpha_{a,\lambda_2} = \alpha_{a,\lambda_1} \cdot \left(\frac{\lambda_1}{\lambda_2}\right)^{k_\alpha} \tag{2.7}$$

where the exponent k has to be guessed for the particular aerosol.

This attempt can also be used to calculate the third term of equation (3), the gradient of differential backscatter, since $\beta_a(R)$ is provided by this method as well. For the wavelength dependence of $\beta_a(R)$ again an Ångström law is assumed, with a possibly different exponent k_β.

It is obvious from this description, that a couple of assumptions have to be made regarding the aerosol properties in order to calculate a correction in particular for the differential backscatter gradient term. The question is, to what extent the resulting correction is dependent on the accuracy of these parameters, and how good they can be estimated under realistic conditions. Sensitivity studies on this subject are sparse [Papa 89], and are hardly covering all possible cases. In the description of results in chapter 5, some examples will be given for the dependence of the ozone retrieval on the aerosol parameters.

It should be emphasized here, that the ambiguity of aerosol retrieval is a principal problem of a single wavelength backscatter measurement, and hence of a two wavelengths DIAL experiment; there is no more information on the required aerosol properties contained in the signal. To improve the aerosol correction, additional measurements have to be incorporated in the scheme. A proposal has been made [Sasa 89] to use a three wavelength measurement, but applications to real measurements are still missing.

Chapter 3

Experimental strategy

The intercomparison of profiling instrumentation in the atmosphere quite generally poses some problems, mainly caused by the different sampling properties of different types of instruments. For the experiment described here, logistic problems and the problem of obtaining permissions to operate either free flying balloon borne ozone sondes or a tethered balloon system made the task even more difficult. So we finally ended up with the following strategy:

- compare different lidar systems, colocated, operated simultaneously, pointing vertically (with the exception of the CNRS/SA-lidar, operating at 30^0 off zenith)
- compare these lidars to in situ instruments carried by a helicopter circling around the lidars in discrete height steps
- compare horizontally pointing lidars to DOAS using a nearby path, and to ground based in situ instruments
- provide additional information on meteorology and chemistry as available (mostly ground based)

To reach these goals the following instruments were incorporated in the experiment:

1. NdYag based Lidar (two systems)
2. KrF based Lidar
3. Dye laser based Lidar
4. Ozone monitor on helicopter
5. NO_2 monitor on helicopter
6. ECC-ozonesondes on helicopter
7. Ground level ozone monitor
8. NO_2-Lidar

9. Meteorological radiosondes

10. Ground level standard meteorology

11. Ground level standard chemistry

These instruments will be described in detail in chapter 4.

The location of the experimental site, at the Rijksinstitut voor Volksgezondheid en Milieuhygiene in Bilthoven, The Netherlands, was chosen because

- there was excellent support for the operation of the lidars
- all necessary amending measurements could be provided
- the surrounding terrain was quite flat and homogeneous, minimizing the problems when the instruments were not exactly colocated
- extended support was kindly provided for the helicopter measurements by the Royal Dutch Air Force from a nearby airport

The location proved to be excellent during the experiment, only weather conditions were extraordinarily bad, with lots of rain and low clouds. In spite of these unfavorable weather conditions a rather large data set has been collected.

Chapter 4

Measurement systems

4.1 The RIVM ozone DIAL

In figure 4.1 a schematic overview of the RIVM Tropospheric Ozone LIDAR is shown. The system is set up in a laboratory in the attic (about 5 m above sea level), such that access to the vertical direction can be obtained through a window in the roof. The telescope is positioned underneath a quartz window, while the laser beams sounding the atmosphere are directed upward through small holes in the roof, just beside the window. The holes can be closed to protect the system against temperature changes and precipitation. The most important characteristics of the system are summarized in table 4.1. An elaborate system description can be found in [Sune 91].

Overall system control is provided by a mini-computer executing a real-time equivalent operating system. Software has been developed for data acquisition and processing. In a measurement session, the operator initiates a series of measurements, after which control is passed to the computer. The LIDAR data obtained from the setup is stored on disk and processed subsequently. A typical evaluation consists of three phases. These phases are illustrated in figure 4.2. First, the background signal level is determined from each of the signals and subtracted. The signal is displayed on a elog-scale, corrected for geometrical attenuation. Then, the ratio of two signal pairs is calculated: the 266 nm signal to the 289 nm signal and the 289 nm signal to the 299 nm signal. In this stage the correction for differential Rayleigh scattering is applied. In the final phase, the ozone concentrations are calculated by stepwise linearization of the ratioed curves (i.e. DIAL-curves) obtained in the previous stage. This linearization is carried out by least squares regression, such that an estimate of the uncertainty of the measurement can be obtained at the same time. For further details, see [Sune 91].

	EMITTER		
Lasers	Spectra Physics DCR3D 10 Hz rep.rate $\approx$ 700 mJ/pulse @ 1064 nm	Nd:YAG 10-15 ns pulse length $\approx 80 - 90$ mJ/puls @ 266 nm	
Raman cells	Custom made 1100 mm focussing lens Suprasil windows (uncoated)	length 2m 1100 mm collimating lens	
	10 bar D_2 with 25 bar Ar for first Stokes D_2 (289 nm) 5 bar D_2 with 23 bar Ar for first Stokes H_2 (299 nm)		
Emitted energy	266 nm, $\approx$ 30 mJ/pulse 289 nm, $\approx$ 25 mJ/pulse 299 nm, $\approx$ 40 mJ/pulse	$<$ 1 mrad divergence $<$ 1 mrad divergence $<$ 1 mrad divergence	
	RECEIVER		
Telescope	Optical Surfaces $\oslash$600 mm	Dall-Kirkham type 2 mrad max. full angle	f/12
Monochromator	Bentham M300HR 1800 lines/mm grating	Czerny-Turner type 300 mm focal length	f/4.2
	instrument adapted for simultaneous detection of three wavelengths		
Photodetectors	Thorn-EMI 9817QA S20 cat. (15-20 % QE)	Linear focussed type 12 dynodes (BeCu)	3.10^6 gain
Digitizers	LeCroy TR6810 5 MHz sampling rate	409.6 mV max.sens. (full scale) 12 bit resolution	
Computer	HP 1000/A600+ mini computer		

Table 4.1: Characteristics of the tropospheric ozone LIDAR

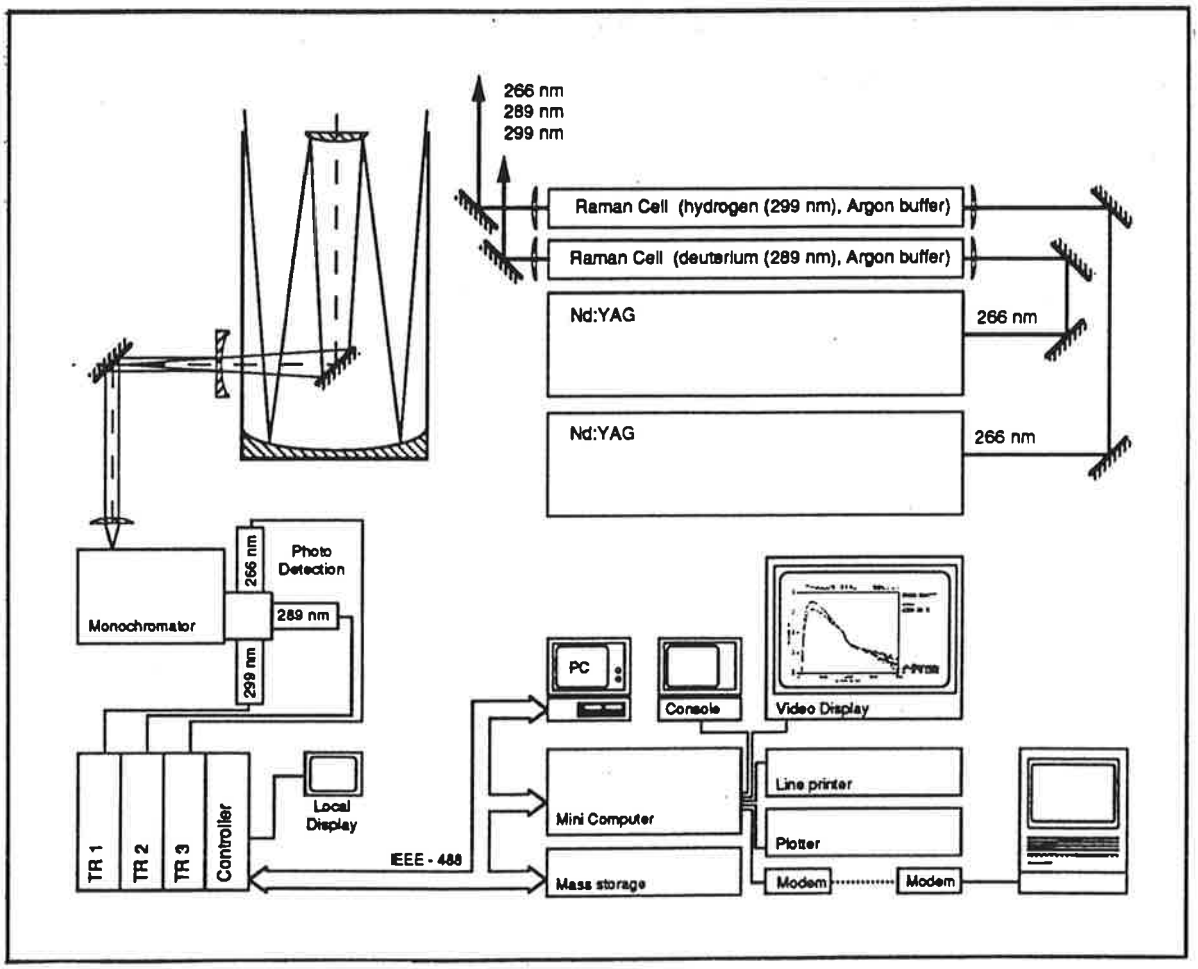

Figure 4.1: Schematic overview of the system.

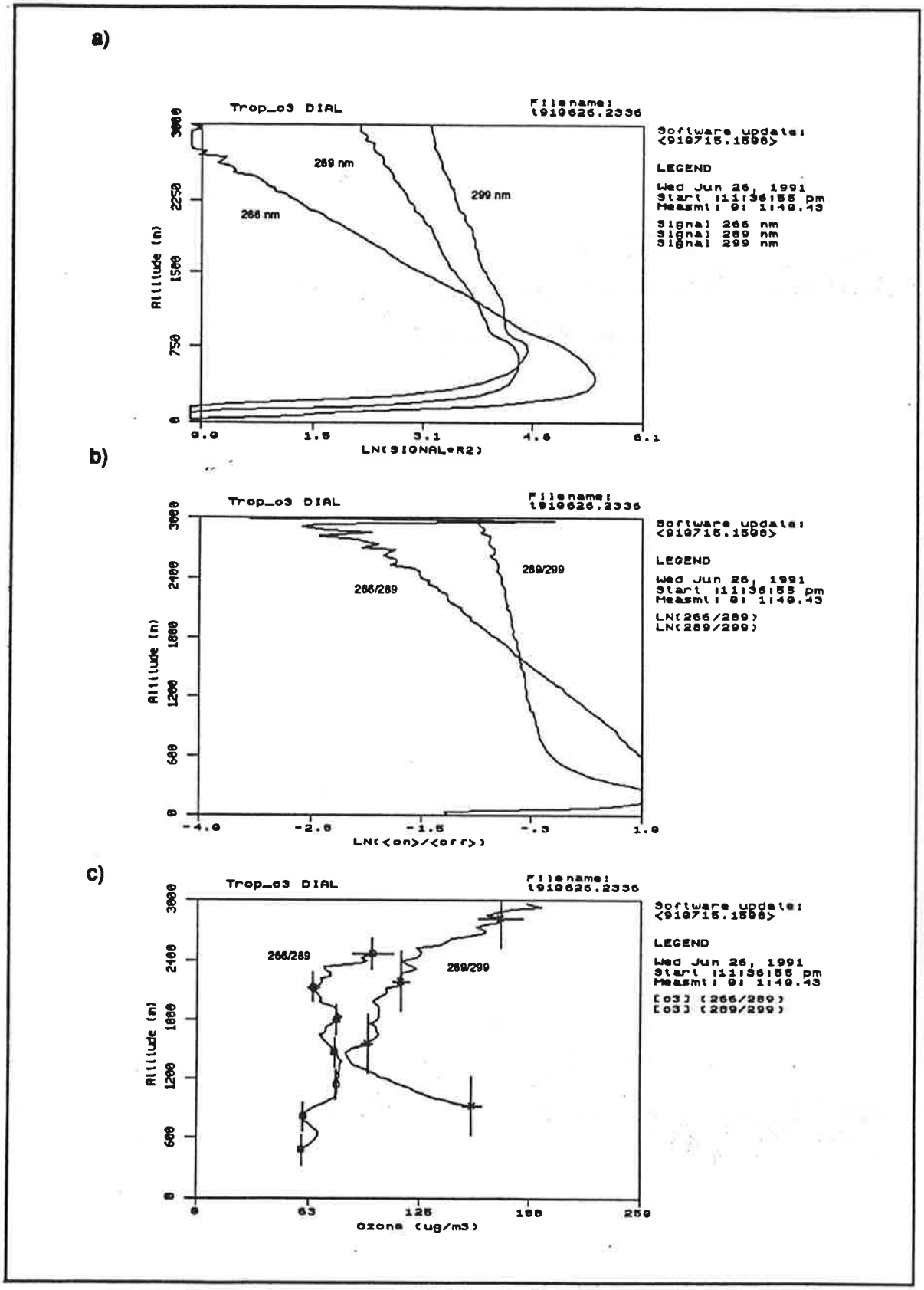

Figure 4.2: Illustration of LIDAR data evaluation. a) $P \cdot R^2$ representation of LIDAR data on ln-scale, b) DIAL-curves, c) derived ozone concentrations.

4.2 The CNRS/SA ozone DIAL

The transmitter of the lidar system which was developed by the CNRS/SA for ozone monitoring in the lower troposphere, is based on the use of a Nd:YAG laser (Spectra Physics GCR 11) since it is a very reliable laser source for field measurements. To obtain an emission at the near UV wavelengths necessary for ozone absorption measurements, the near IR fixed frequency of the Nd:YAG (1064 nm) is converted down to its fourth harmonic (266 nm) by non linear mixing in KDP crystals. The energy stability of the laser output at 266 nm is obtained through the use of an active feedback loop controlling the KDP crystal tuning angle according to the measured residual laser radiation at 532 nm. The 4^{th} harmonics of two small Nd:YAG lasers are focussed into two 1 m closed cells filled respectively with hydrogen and deuterium for generation of the 289 and 299 nm wavelengths by Stimulated Raman Scattering (SRS). A mix of the Raman gas with helium as a buffer gas was chosen to increase the efficiency of the conversion into the first Stokes line while the generation of stimulated rotational Raman scattering was minimized [Milt 90]. The residual 266 nm after the hydrogen cell is also used for measurements in the lowest range while a fourth wavelength in the visible is obtained from the third harmonic of the Nd-YAG laser for aerosol measurements in the spectral range free of ozone absorption. Laser output energies are summarized in the table 4.2.

The optical receiver collector is a 30 cm Cassegrain telescope which inputs a four channel grating spectrometer for wavelength separation and background light filtering. Multialkali photomultiplier tubes (PMT) are used for signal detection behind each slit of the spectrometer. The transmitted beams are not coaxial with the telescope axis to reduce the nearby laser scattered light which overloads the PMT photocathodes. The separation between the transmit and receive axis is less than 20 cm to reduce the effect of the relative misalignment of the various beams on the calculated ozone concentrations. The resulting error on the ozone concentration is then expected to be negligible for ranges larger than 500 m. The data acquisition system includes four 12 bits, 10 MHz waveform recorders for near range detection (0.3 - 2 km) and two 1 MHz photocounting channels to record the weaker part of the signal corresponding to larger ranges (2 - 5 km). The various recorders can be run simultaneously and the recorded wavelengths are indicated in table 4.2.

Data are averaged on dedicated electronic boards and then stored on a 386 PC com-

wavelength	266 nm	289 nm	299 nm	355 nm
energy	15 mJ	10 mJ	7 mJ	10 mJ
Analog detection	x	x	x	x
Photocounting		x	x	

Table 4.2: lidar wavelength

puter which also provides a real time display of the raw signals and a color coded display of the ozone vertical distribution as a function of time. The number of averaged laser shots can be selected by the operator and is generally chosen between 600 and 1000 shots corresponding to a 1-2 min integration time. The main characteristics of the lidar system are summarized in table 4.3 and the instrument block diagram is represented in figure 4.3.

Calculation of the ozone concentration is obtained using the standard DIAL equation presented in the first part of the document. The numerical scheme which was chosen to compute the slope of the signal dln(S)/dR is a numerical filtering of ln(S) with a polynomial derivative filter which corresponds to a least square fit of a 2nd order polynomial to successive windows of N data points [Ance 89]. The estimated slope of the signal is then given by the derivative of the polynomial function calculated for each window. The size of this window increases with altitude to reduce the ozone concentration statistical error as the signal-to-noise ratio decreases. The spatial resolution of the ozone profile depends on the size of the window chosen for the slope calculation. For example, analog signals are sampled every 15 m and the spatial resolution decreases from 120 m at 0.3 km to 220 m at 2 km.

Corrections of expected systematic errors are also included in the data processing algorithm:

- the temperature variation of the ozone absorption cross-section is included through the use of a standard atmospheric temperature and pressure model which varies with the season and the latitude (polar region, middle-latitudes, tropics) [Ched 85],

- the Rayleigh differential absorption is corrected using the previous model to calculate the atmospheric density.

- the saturation of the photocounting signal when the number of photons becomes larger than one tenth of the counter resolution (250 MHz), is corrected assuming that the PMT detection statistics follows a Poisson distribution. This correction is mandatory to obtain an overlap between the analog and the photocounting mode.

- the overload of the PMT and of the preamplifiers, during the first μs after the laser firing, generates a weak signal with a rather slow decreasing time constant (several tens of μs). This weak signal induced noise represents a strong perturbation for the ranges where the signal becomes comparable to the noise value. Its signature is different in the analog mode where it becomes important at ranges of the order of 1.5 km and in the photocounting mode where it perturbes the signal above 3.5 km. It is related to the fact that the latter generally includes only the PMT overload and is not very sensitive to the preamplifier response to the initial perturbation. This effect is partially removed by subtracting a time decreasing background from the signal. This time varying background is estimated by fitting a high order polynomial function (4th order) to the signal in the region where the atmospheric return is no longer expected. When using the extrapolation of this estimated function into the region where the signal is processed, one obtains larger values of the atmospheric returns slopes since S(R) is smaller and therefore dln(S)/dr larger.

No correction of the differential absorption by SO_2, aerosol, O_2 (for the 266/289 nm pair), and NO_2 are included in the standard processing algorithm. Aerosol and SO_2 interferences can be corrected afterwards when required by atmospheric conditions. Oxygen

differential absorption for the 266/289 nm wavelength pair corresponds approximately to a $5\mu g \cdot m^{-3}$ overestimate of the ozone concentration at the lower altitudes and will be neglected to a first approximation. It will be added latter using the atmospheric density profile already included in the data processing algorithm. NO_2 interferences are neglected since it becomes noticeable only in very polluted environment ($NO_2 > 100\mu g \cdot m^{-3}$).

The lidar system was transported dismounted in a small van to Bilthoven where it was reassembled in a room of the RIVM institute. The lidar was easily reassembled in two days since the ruggedized design of the Nd:YAG laser did not require any realignment of the laser cavity and since all the holders of the optical elements (Raman cells, lenses, mirrors) were kept in place during the trip. Only the alignment of the telescope and of the grating spectrometer were checked after being installed. A steering mirror offers the advantage of measurements along a slant angle between 0 and 30 degrees from the vertical axis. A slant angle was not necessary for the operation in the RIVM building which has a 1 x 1 m opening in the roof. However we used the 30 degrees slant angle to improve the vertical resolution in the boundary layer and to avoid having the steering mirror under the opening in case of rain.

Transmitter:	Two Nd: YAG lasers (GCR-11 Spectra Physics) 4^{th} harmonic + Stimulated Raman Scattering in Hydrogen and Deuterium (see table 4.2)
Receiver:	Cassegrain Telescope: area = 30 cm Cerzy Turner Spectrometer with a 3600 gr/mm holographic grating: bandwidth = 1.2 nm efficiency = 40 % Multialkali photomultipliers: Hamamatsu R1464 size = 14 mm risetime = 2.2 ns gain = 10^6
Data acquisition:	Analog detection (4 units): resolution = 12 bits sampling = 10 MHz Photocounting detection (2 units): time gate = $1\mu s$ counter frequency = 250 MHz Hardware averaging Data storage and processing on a 386 PC computer (Compaq)

Table 4.3: lidar characteristics

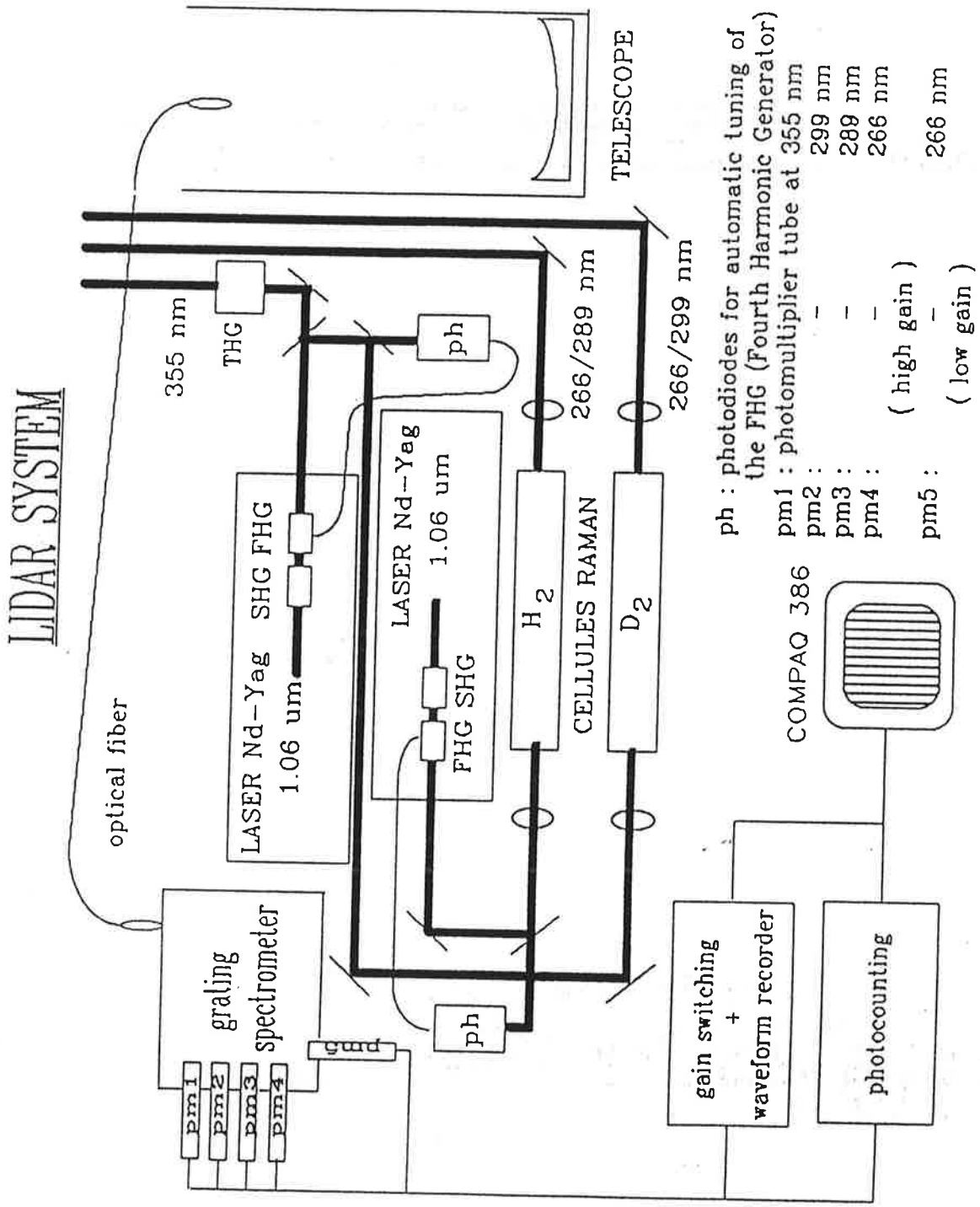

Figure 4.3: Block diagram of the CNRS lidar system

4.3 The LIT ozone DIAL

The LIT mobile DIAL is a flexible system which is constructed for measurements of various species [Edne 87] [Edne 89]. An overview of the system is given in fig.4.4. The laser, telescope and all electronics are contained in a Volvo F610 truck with a specially designed cargo compartment of size 6.0 x 2.3 x 2.1 m. The truck is equipped with four sturdy supporting legs that can be hydraulically lowered to achieve high stability during measurements requiring high directional accuracy in the optical system.

The important characteristics of the DIAL system are summarized in table 4.4. The laser transmitter is a Nd:YAG pumped dye laser with frequency doubling and/or mixing to the UV and IR regions. The dye laser is equipped with a dual wavelength option, enabling the laser to alternately be fired at two different preset wavelengths. The dye laser wavelength scale is calibrated against known Ne lines, observed with the optogalvanic signal from a Ne-filled hollow cathode lamp, illuminated with a small part of the laser beam. The wavelengths used for ozone monitoring during the campaign were 278.7 nm and 286.3 nm, which were chosen to minimize the interference due to SO_2 absorption.

The outgoing laser beam is directed coaxially with a vertically mounted telescope and transmitted into the atmosphere via a large flat mirror in a retractable transmitting/receiving dome on the roof. A quartz window seals off the dome. Stepping motors are used to turn the dome and to tilt the mirror. Thus it is possible to steer the measurement direction 360 degrees horizontally and within an angle of 45 degrees vertically. An extra folding mirror was installed on the roof to facilitate vertical measurements. In order to protect the mirror coating, the exiting laser beam is expanded with a 6x beam expander. Servo motors and micrometer screws offer remote control of the final turning prism, through which the overlap between the laser transmission lobe and the telescope field of view is controlled. Two video cameras are used to control and supervise the measurement direction. A mechanical chopper can block the beam if desired. The computer-controlled chopper is automatically used during a lidar measurement to obtain the signal due to background light and preamplifier offset.

An adjustable field stop is placed in the focus of the receiving Newtonian telescope, by means of which the field of view can be varied from 2 to 5 mrad. After passing through an interference filter the light is detected by a photomultiplier tube. Due to the fact that the beam is emitted coaxially with the telescope, the near field backscattered light is very strong. To prevent detector overload and to reduce the dynamic range of the signal, the gain of the PMT is modulated. This is performed by changing the voltage difference in the dynode chain. The gain is very low in the beginning and does not reach its full value until after 2-10 μs (the rise time is variable). The signal from the PMT is preamplified and captured with a 8-bit 100-MHz transient digitizer. Normally 2000 channels, each 10 ns wide, are recorded, corresponding to a lidar measuring range of 3 km. After the recording, the data are transferred via a GPIB interface to the computer where they are added into a 32-bit data array at a repetition rate of 20 Hz. A DIAL measurement cycle consists of 8 shots on each wavelength, fired alternately, and finally two shots with the chopper closed. Several cycles are then averaged and stored on disk after background subtraction. During the TROLIX campaign normally 100 or 200 cycles were averaged, corresponding to a measurement time of 1.5 and 3 min., respectively. When vertical

scanning were performed the measurement time for each direction was divided in several repetitions. While system control and on-line data handling are controlled by the system computer, data processing and evaluation can be performed on a separate computer. A typical evaluation consists of three phases. First a Gaussian smoothing function of a few channels width is applied on the raw lidar signals. Then the ratio of the lidar signal at the different wavelengths is calculated. A running average function of adjustable width is finally used to evaluate the concentration as a function of distance. The concentrations are then also corrected for differential extinction due to Rayleigh scattering. Several concentration profiles can be averaged over a chosen time period. Data from horizontal or vertical scans are presented as a 2D-plot with the concentration value indicated with a grey scale. The data from a vertical scan can also be transferred to a single vertical profile with a vertical projection.

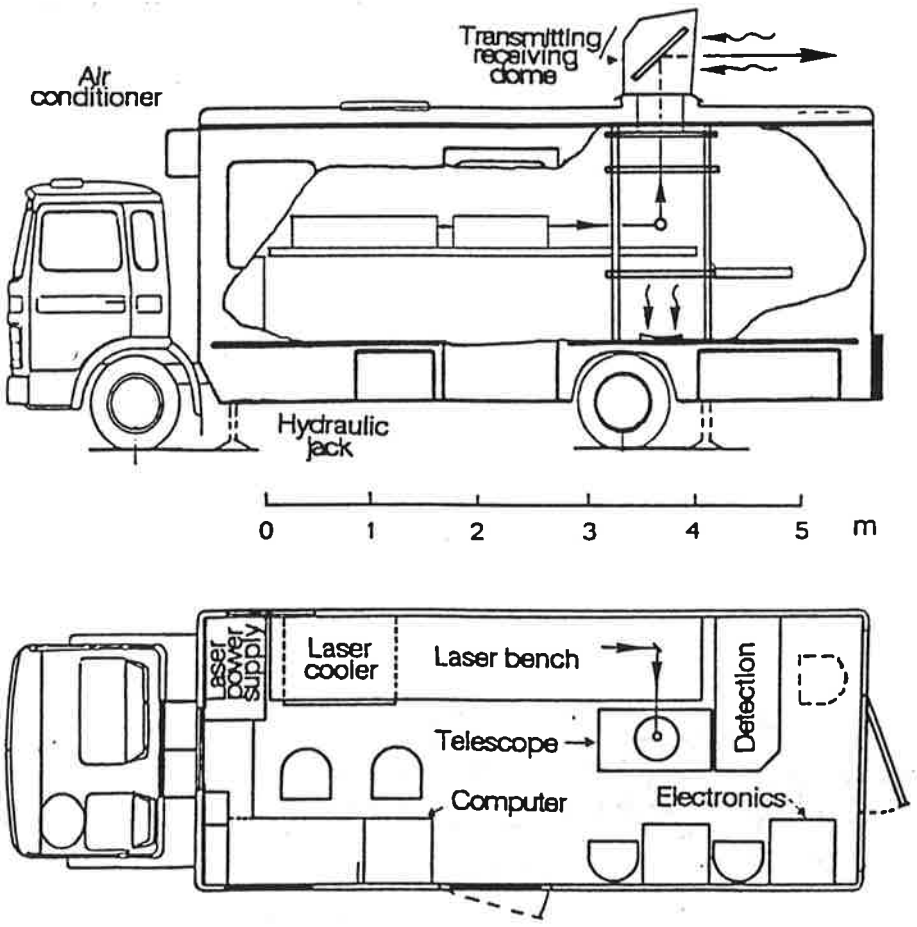

Figure 4.4: Overview of the mobile DIAL system

Emitter	
Laser	Continuum, YG682-20, Nd:YAG
	rep. rate 20 Hz, 6-9 ns pulse length
	1200 mJ 1064
Dye laser	Continuum, TDL60
	Dye: R6G
	dual wavelength, alternate switching
Wavelengths Used	278.7 nm: 5 mJ 0.5 mrad
for Ozone	286.25 nm: 5 mJ 0.5 mrad
Monitoring	
Receiver	
Telescope	Newtonian telescope, 40 cm diameter, f/2.5
	computer controlled steering mirror
Photo detector	Thorn-EMI 9816QA, S20 cathode
	gain 10^7, ramped 2-10μs
Digitizer	Le Croy units 6102 2 x TR 8818
	2 x NM8103A, 8013. 8-bit, 100-MHz
Computers	2 x IBM compatible PC, 386

Table 4.4: Characteristics of the DIAL system

4.4 The MPI ozone DIAL

An overview over the ozone DIAL system of the MPI für Meteorologie is given in fig. 4.5, it's main parameters are listed in table 4.5. The system is based on the use of a KrF excimer laser in an oscillator-amplifier configuration to provide narrowband, linearly polarized, low divergence UV-radiation at $\approx 248nm$ which is tunable over the laser linewidth of about 0.8 nm.

Excimer Laser:

Type	:	Lambda Physik, EMG 150 MSC-T
Wavelength	:	248 nm
Output Energy	:	250 mJ
Bandwidth (FWHM)	:	0.001 nm
Tuning Range	:	0.8 nm
Repetition Rate	:	max. 80 Hz
Divergence (full angle)	:	< 0.2 mrad
Locking Efficiency	:	90 %
Pulse Width (FWHM)	:	22 ns
Beam Shape (v x h)	:	21 x 5 mm^2
Polarization	:	horizontally, 90:10

Raman Cells:

Gases	:	H_2 and/or D_2
Pressure	:	max. 40 bar
Length	:	1 m
Windows	:	Suprasil 1, Brewster angle, uncoated
Focusing Lenses	:	Plano-convex, f = 1 m
Typical Mixtures	:	20 bar H_2 and 20 bar He; 40 bar D_2
Output Energy	:	> 27 mJ for 277 nm/313 nm (H_2)
		> 33 mJ for 268 nm/291 nm (D_2)
Divergence (full angle)	:	< 0.6 mrad

Telescope:

Mirror	:	parabolic, f = 1200 mm, ϕ = 400 mm,
Exit	:	quartz fiber, ϕ_{core} = 1 mm, N.A. = 0.2
Field of view (full angle)	:	0.8 mrad
Window	:	Suprasil, broadband anti-reflection coated

Spectrometer:

Type	:	modified Czerny-Turner
Grating	:	ruled, plane reflectance grating, blazed for 250 nm, 1200 grooves/mm,120 x 140 mm^2
Collimating Mirror	:	parabolic, f = 280 mm, ϕ = 130 mm, dielectric broadband HR coating
Camera Mirror	:	spherical, f = 280 mm, ϕ = 150 mm, dielectric broadband HR coating
Entrance	:	1 mm quartz fiber
Exit	:	6 wavelengths, 1.5 mm quartz fibers, solar blind filters

Data Acquisition:

Photomultiplier Tube EMI 9813QB, 14 dynodes BeCu
Preamplifier Analog Modules, 310-3, 10 Hz - 10 MHz
Three chanel transient digitizer (dsp 2012S), 12 bit, 20 MHz
Data storage on a personal computer

Table 4.5: MPI ozone DIAL characteristics

The necessary additional wavelengths are produced by stimulated Raman scattering in hydrogen or deuterium. The Raman cells are provided with Brewster windows to avoid reflection losses, and can be operated at a pressure up to 40 bar. Detailed studies have been performed to optimize operating conditions (hydrogen/deuterium pressure, buffer gas pressure) [Schaberl 1990]. During the experiment the wavelengths set of either 248, 277, 313 nm produced in hydrogen or 248, 268, 292 nm produced in deuterium has been used. One set of wavelengths is transmitted simultaneously into the atmosphere via a remotely controlled turning prism.

The system has been set up bistatic with ≈40 cm separation between transmitter and receiver axes in order to suppress the close range returns. This reduces the dynamic range of the signals and helps to avoid detector overload and associated memory effects of the photomultipliers.

The backscattered radiation is collected by a telescope consisting of a 40 cm diameter parabolic mirror directly coupled to a 1 mm core diameter quartz fiber fixed in the focal plane. The aluminum coated primary mirror is protected by a quartz window with hard dielectric antireflection coatings.

The output of the telecope is transmitted by the quartz fiber to the spectrograph, which separates the different wavelengths. It is a modified Czerny Turner design, with the fiber optic input directly on the axis of a parabolic collimating mirror. A plane ruled grating blazed at 250 nm provides a linear dispersion of 0.36 mm/nm at the output. Six quartz fibers with a core diameter of 1.5 mm are mounted in the exit plane to collect the different transmitted wavelengths and divert them to the photomultipliers which are used as detectors.

The signals for the three wavelengths are amplified and digitized simultaneously by 12 bit 20 MHz transient recorders. Averages over typically 100 shots (software selectable) are computed by hardware averagers, transferred to a computer, stored on hard disk for off-line evaluation, and displayed in almost real time. In particular the signals and the logarithm of the ratio of two signals after offset subtraction can be displayed, and zoom functions are available on all axes for full experiment control.

The system is mounted in a standard 20' container to make it easily transportable to different experimental sites. Only the telescope, the cooling system, and the gas cabinet are attached at the outside walls of the container and have to be removed during transport. All optical elements are set up on two optical tables, which are are mounted shock-proof during transport and fixed to the supporting structure of the container during operation.

Figure 4.5: Schematic overview over the tropospheric ozone DIAL system of the MPI für Meteorologie, Hamburg

4.5 The RIVM NO_2 DIAL

This chapter will briefly describe the RIVM NO_2 DIAL system equipment. For a general explanation of the DIAL technique, the reader is referred to the references [Hink 76], [Meas 84]. The NO_2 DIAL is a mobile and completely self-supporting scanning system mounted in a van. The system is mainly applied to the boundary layer. The main technical data are summarized in table 4.7; a comprehensive system description is found in [Jong 91a]. The experimental setup of the system is shown in figure 4.6. Table 4.6 presents the most important system specifications.

The system emits alternately 'on' and 'off' laser pulses (448.1 and 449.9 nm respectively), with a 10-Hz repetition rate. Inside the van the laser beam is directed vertically to the open roof of the van. The beam passes two 90° prisms, mounted on a vertical and horizontal rotation table respectively, before leaving the system. In this way the beam direction can range over approximately half a sphere. The system is equipped with two HP1000 computers, one for real-time system control and the other for storing data and on-line data processing.

For daytime measurements the elevation angle must be small, in order to keep the DC level of the detected signal sufficiently low. The maximum elevation angle for daytime measurements is 10-20°, depending on the weather, season and time of the day. At high elevation angles, the contribution of background light, the DC level, in the signal is too dominant to calculate valid NO_2 concentration profiles.

Usually, a NO_2 concentration profile is calculated from an average of 1000 Lidar echoes at each wavelength, so one measurement lasts approximately 5 min. In the detection, echoes up to 6 km are stored. The zero level of each shot is sampled in 256 pre-shot channels. If background concentrations have to be measured, NO_2 concentrations are usually calculated over 500 or 1000-m range segments, unless there is an obvious vertical gradient.

The differential cross section used is equal to 0.437 +/- 0.047 m^2 g^{-1} at atmospheric pressure and 293 K [Wood 78].

Detection limit	$4\mu g \cdot m^{-3}$ NO_2 (500 - 1000 meter range segment)
Distance range lower limit upper limit	 0.3 - 0.5 km 1.0 - 6.0 km
Range resolution	7.5 meter (Lidar signal) 100 -2000 meter (NO_2 profile)
Time resolution	4.5 minutes per NO_2 profile (1000 on/off pairs average)

Table 4.6: RIVM NO_2 DIAL system specifications

Emitter	
Pump laser	Nd:YAG laser, Quanta Ray model DCR1A
wavelength	1064 nm
pulse duration	8-9 ns
repetition rate	10 Hz
energy	700 mJ (stability < 5 %)
Harmonic generator	Quanta Ray model HG2 (temp. stabilized)
crystal	2 KD*P crystals
wavelengths	532 nm and 355 nm
energy	125 mJ (355 nm)
Wavelength separation	dichroic mirrors, Quanta Ray model 002-0201 and0100-9690-2
output wavelength	355 nm
Dye laser	Quanta Ray model PDL2
medium	Coumarine 120 in methanol
beam divergence	< 1 mrad (full angle)
energy	8 mJ (at 448.1 and 449.9 nm)
pulse duration	10 ns

Receiver	
Telescope	Schmidt-Cassegrain, Celestron 11
diameter primary mirror	27,5 cm
total viewing angle	2 mrad
Interference filter	Melles Griot, model 03FIVO78
peak wavelength	450 nm
bandwidth	10 nm (fwhm)
peak transmission	50 %
Light detector	photomultiplier, Thorn EMI model LF 9818QA
gain	$0.3 \cdot 10^6$ (at 1700 Volt)
quantum efficiency	19 % (at 450 nm)
transit time spread	2.7 ns
Pre-amplifier	DSP model 1020
selectable filter	bandwidth 5 MHz
choosier recorder	DSP model 2012S (12 bit, 20 MHz)
Average module	DSP model 4101

Table 4.7: Technical data of the RIVM NO_2 Dial system

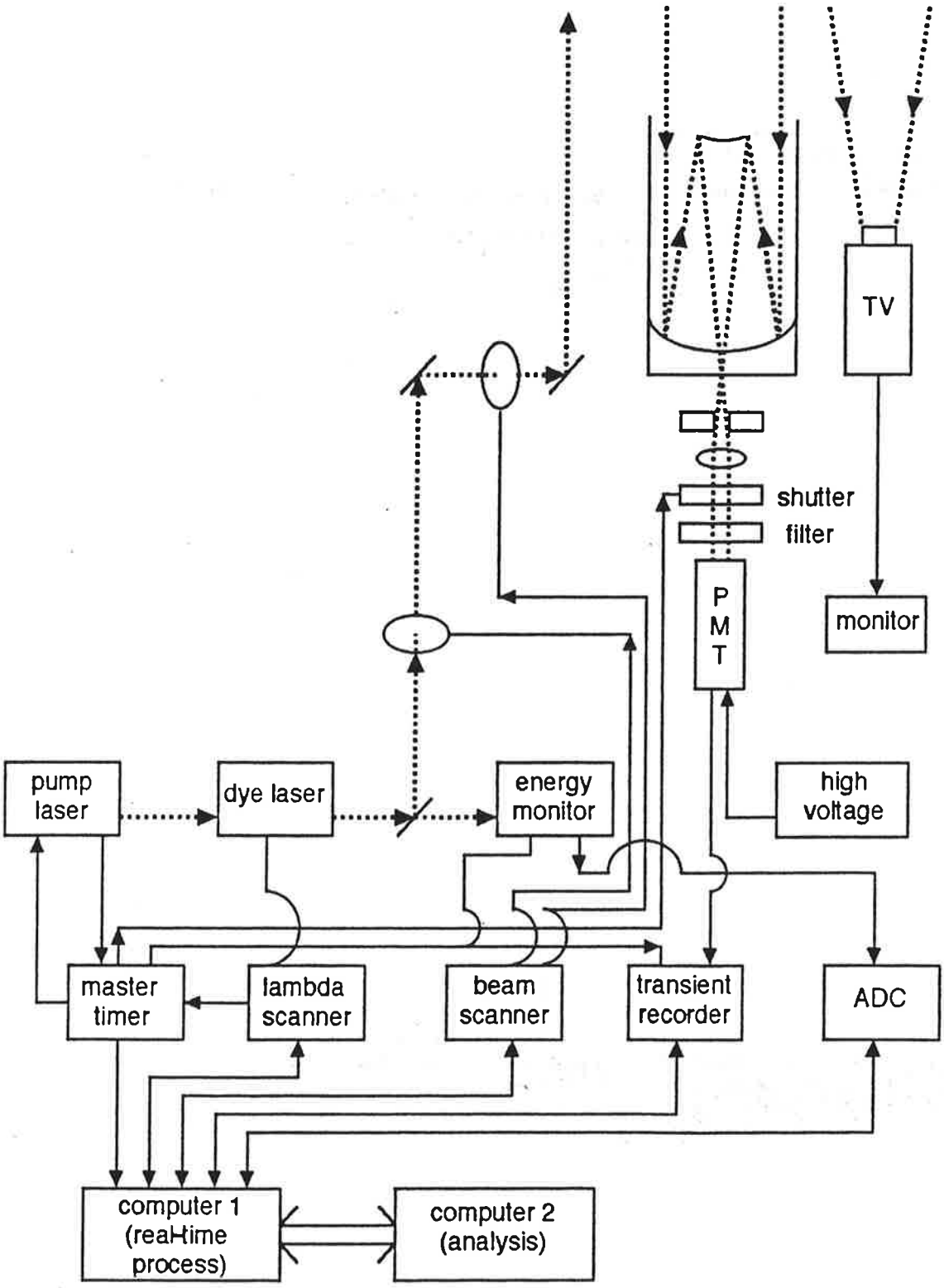

Figure 4.6: Experimental setup of the RIVM (bi-axial) NO_2 Dial system

4.6 The RIVM MIE lidar

This chapter is a brief description of the RIVM PBL Lidar system equipment. For general explanation of the Lidar technique, the reader is referred to literature [Hink 76], [Meas 84]. The experimental setup of the system is shown in figure 4.7, the main technical data are summarized in table 4.8. For details the reader is referred to [Swar 85], [Sale 85].

The PBL Lidar system operates routinely and continuously. The laser beam (1064 nm) is directed vertically, through a laboratory roof window. The system emits bursts of 127 laser shots (duration 13 seconds). The time gap between two successive bursts is usually 210 seconds.

After detection, each shot is accumulated in a HP1000/A600 computer. The burst average, corrected for geometric attenuation, is stored on a datafile, after reducing the range resolution to 40 meters (by linear averaging). The detection stores echoes up to 6 km distance (height) i.e. 2000 channels with 4.5 meter range resolution. Each burst average provides a backscatter profile (time resolution 13 seconds). With a time gap of 210 seconds between bursts this means a time resolution of about 4 minutes for boundary layer height values.

The boundary layer height is calculated, visually checked, as the altitude half-way the first obvious negative gradient in the averaged backscatter signal.

Emitter	
Laser	Nd:YAG laser, Quanta Ray model DCR11
wavelength	1064 nm
pulse duration	10 ns
repetition rate	10 Hz
energy	70 - 300 mJ
Receiver	
Telescope	Fresnel lens
dimension	100 mm
focal length	101.6 mm
Interference filter	Corion model SD-10-1064-F
peak transmission	65 % (at 1064 nm)
fwhm	10 nm
Light detector	Avalanche photo diode, RCA model C30955
Pre-amplifier (ten times)	Analog Modules Inc., model LNVA (20db,DC-30MHz)
Transient recorder	LeCroy model TR 8837F
sample frequency	32 MHz (8000 channels memory)
AD-conversion	8 bit (256 levels)

Table 4.8: Main technical data of RIVM Boundary Layer Height Lidar system

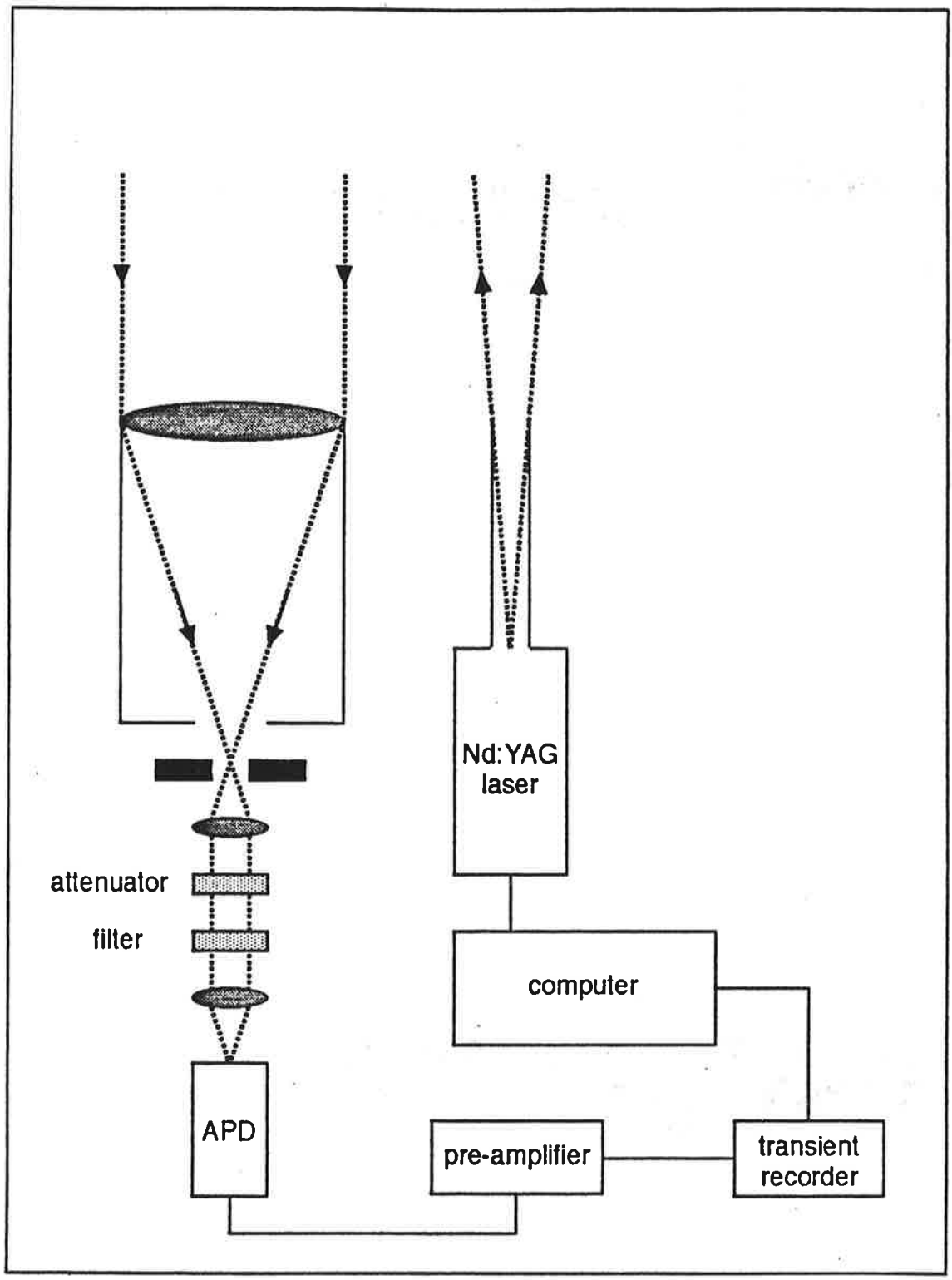

Figure 4.7: Experimental setup of the RIVM PBL Lidar system

4.7 The RIVM helicopter instrumentation

Air samples are taken with a 15 m long FEP tube (transmission time $\approx$ 2 s) or through a filter containing activated coal, and led to a UV photometric ambient O_3 analyzer [Ther 49] and a chemiluminescence NO_x monitor [Ther 42].The FEP tube was firmly attached to a 10 m long sling, stabilized with two sandbags, and hanging under the helicopter (see figure 4.8). In the trade-off made between flight safety and distance between the engine exhaust and the sampling point, 10 m was found to be the optimum sling length. All instruments were powered by a 220V AC battery power supply. The pressure was measured in the cockpit by a digital pressure indicator. The analog output signals were sampled every 10 s by a portable computer using a 12-bit analog/digital converter and a signal transmitter. The transmitter both buffers and prepares the data parcels for storage on disc in the computer.

The analog NO_x monitor output listed is in absolute units $\mu g \cdot m^{-3}$.The analog O_3 monitor output is in relative units (ppb). In the tables given later in this report ozone concentrations are given in absolute units, the transformation is performed using the local pressure measurements previously mentioned and an average temperature of 283 K.

4.7.1 Calibration

Ozone monitor The UV photometer determines ozone concentrations by measuring the attenuation of light due to ozone in an absorption cell at a wavelength of 254 nm.The concentration of ozone is directly related to the magnitude of attenuation.To make sure that the measurement setup was functioning well during the campaign four investigations were carried out to establish:

- A - Monitor comparison;
- B - Influence of the 15 m long FEP tube;
- C - Degradation of the total measurement setup;
- D - Interference due to NO_2 and SO_2.

Monitor comparison: On 27 June a comparison was carried out between the monitor used in the measurement setup and a reference monitor used with the RIVM Laboratory of Air Research (LLO) facilities after the airborne measurements. The results are shown in figure 4.9.

UV Photometric ambient O_3 monitor [1]
(Thermo Environmental Instruments Inc. Model 49)

Full-scale range	:	1000 ppb
Precision	:	2 ppb
Response time (0-95%)	:	20 s
Flow rate	:	2 l min-1
Analog output range	:	0-10 V

Chemiluminesence NO_x monitor [2]
(Thermo Environmental Instruments Inc. Model 42)

Full-scale range	:	2054 $\mu g \cdot m^{-3}$
Precision	:	1 $\mu g \cdot m^{-3}$
Response time (0-95Flow rate	:	0.7 lmin-1
Analog output range	:	0-10 V

Pressure indicator [3]
(Druck Limited Model DPI 260)

Full-scale range	:	600- 1100 mbar
Precision	:	0.6 mbar
Response time	:	0.5 s
Analog output range	:	0-10 V

FEP tube

Length	:	15 m
Inner diameter	:	4.35 mm

Power supply
(Topaz)

Output voltage	:	220 VAC
Capacity	:	1000 VA
Typical backup time		
Full load	:	9 min
Half load	:	30 min

ADC and transmitter
bf (Imko Gmbh model GM7K16 and GM23U)

Reaction time (five ch.)	:	200 ms
Sensitivity	:	2.5 mV bit^{-1}
Input range	:	0-10 V

Portable computer
(Zenith 386 SX)

I/O connection	:	RS232 (2400 Baud)
Data storage	:	120 Mb Hard disc
		730 Kb Floppy disc

Table 4.9: Specifications for helicopter instrumentation

Influence of the 15 m-long FEP tube: Measurements on 11 June and 28 June show the influence of the 15-m long tube (see figure 4.10). This influence is given by the equation :

$$O_3 = 1.13\ O_3' + 3.5\ \mu g \cdot m^{-3} \tag{4.1}$$

where O_3' : Ozone monitor reading $\mu g \cdot m^{-3}$ O_3 : Measured ozone concentration corrected for tube losses.

Degradation of the total measurement setup: Two comparisons were carried out, one before the airborne measurements (91/06/11) and one afterwards (91/06/28). In both measurements the complete setup was used. There was no difference found between the two measurements.(Figure 4.10) Therefore it can be concluded that the instrument has not degraded during the flights.

Interference due to NO_2 and SO_2: A search for interference due to the presence of NO_2 (range 0-300 $\mu g \cdot m^{-3}$) and SO_2 (range 0-40 $\mu g \cdot m^{-3}$) was carried out. No influence was found.

NO_x monitor The monitor was calibrated using the RIVM LLO calibration facility.The method is based on permeation tubes filled with nitrogen dioxide and rarefied with zero gas. The method is described by H.J. van de Wiel [Toel 79].

Pressure indicator The pressure indicator was calibrated by the manufacturer before the campaign [Druc 91].

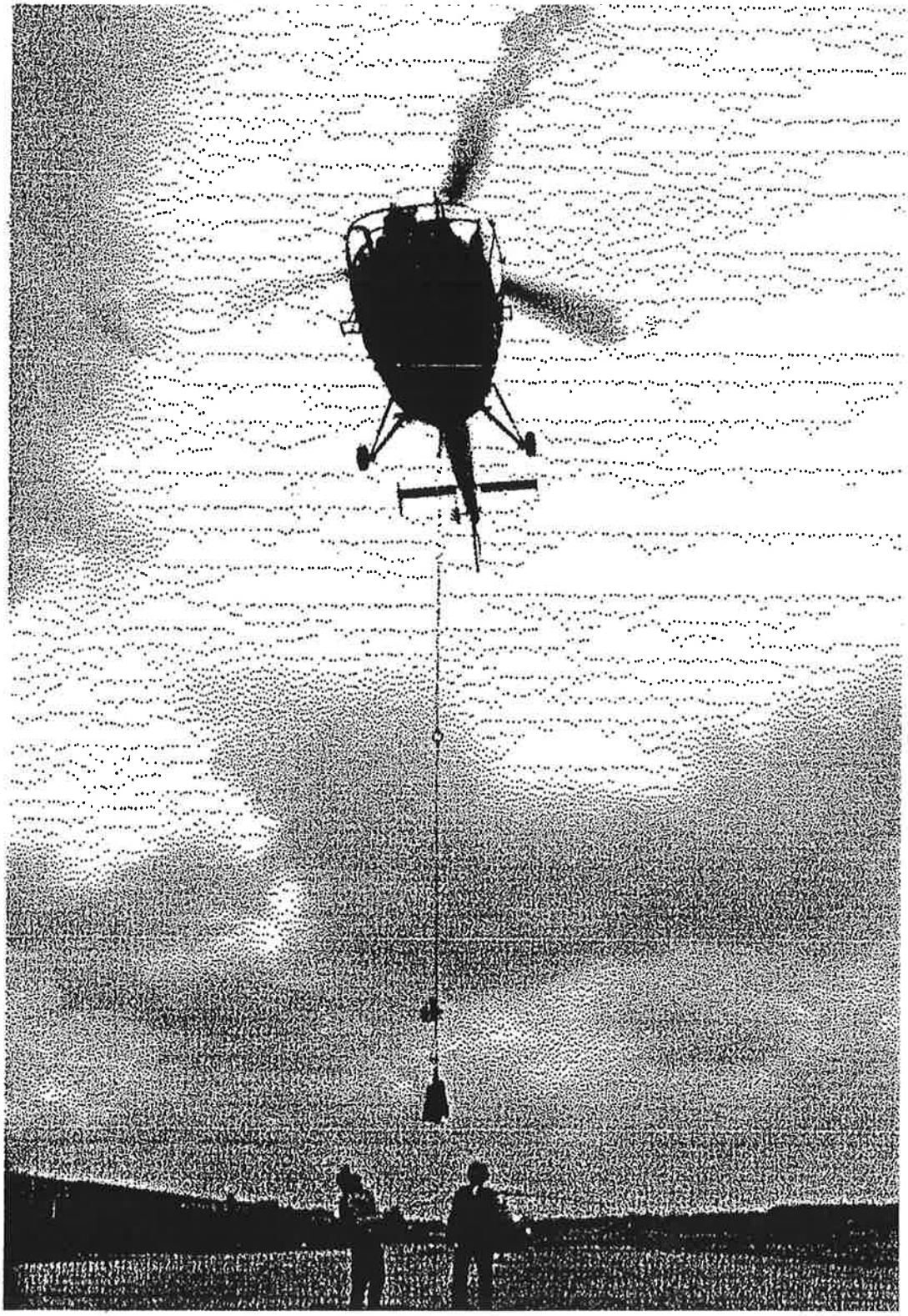

Figure 4.8: Helicopter with sonde at take off

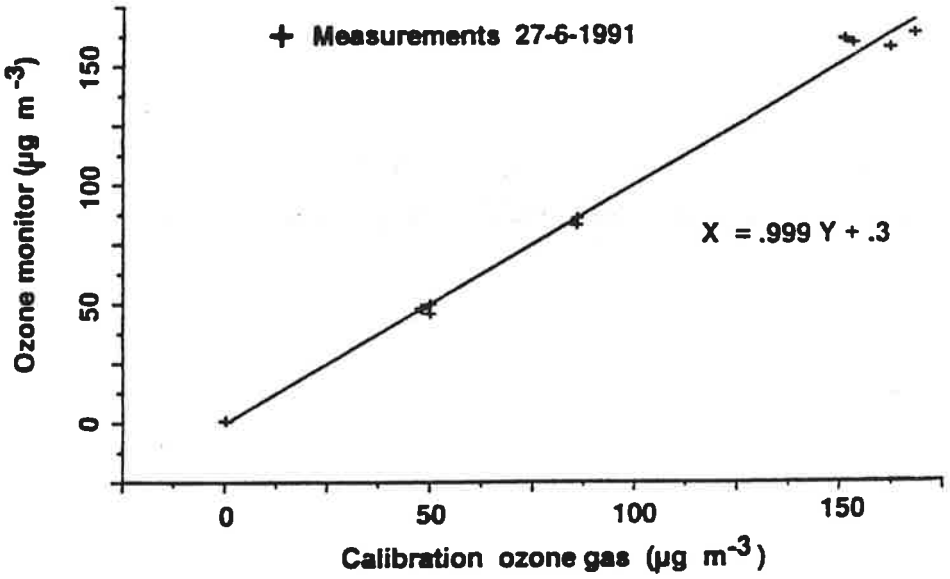

Figure 4.9: Comparison with 3 m Tube

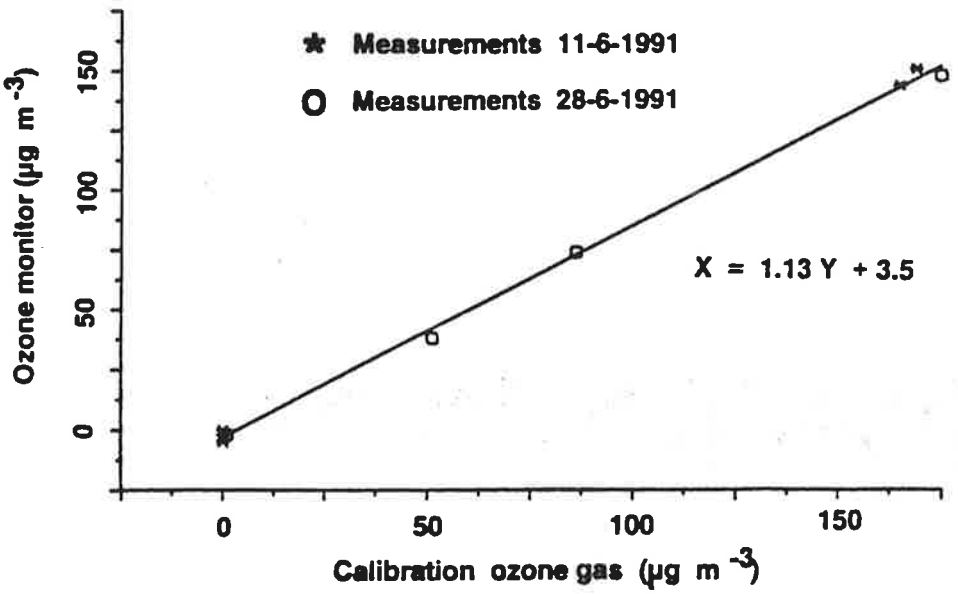

Figure 4.10: Comparison with 15 m Tube

4.8 The OAF ECC ozonesonde

Measurements by means of the ECC-sonde (electrochemical concentration cell) were to provide data, essentially within the boundary layer, simultaneously to data of the O_3-lidar experiment. Radiosonde measurements of temperature, humidity and pressure are accompanying meteorological data, which permit to interpret the ozone measurements in terms of meteorological elements. By means of the hydrostatic equation the height of flight of the helicopter carrying the sondes has been computed from the measurements of pressure and temperature. Unfavourable weather conditions allowed only three flights during the whole campaign. The last flight does not yield any usable ECC-sonde-data because of a technical failure. At the same time a measuring device of the Dutch colleagues from Rijksinstitut voor Volksgezondheid en Milieuhygiene, Laboratory for Air Research operates on board of the helicopter in order to measure O_3 and NO_x. The successful flights took place on June 20^{th} and 24^{th} 1991. Before the flight the sondes have been prepared and tested in laboratory according to a checklist provided by the 2. Institut für Chemie of the KFA Jülich. The ECC-sonde, also called Komhyr-sonde [Komh 67] [Komh 69], is based on the iodometric measuring principle, for which several chemical processes are not clarified [McEl 85]. The data conversion of the measured electrical current into ozone concentration is based on the law of Faraday [Komh 86].

Computation of the flight altitude

Starting with ground pressure as the initial value, the height of flight has been determined from the change of pressure. The height is given by

$$h = -\frac{k}{\bar{m}g}\int_{P_o}^{P(h)} \frac{T(h')}{p^*(h')} dp^*(h') \tag{4.2}$$

with k:Boltzmann constant , $\bar{m}$: mean molecular weight of air, g: acceleration of gravity, p: pressure and T: temperature. The dependence of g on the height can be neglected. As a numerical approach

$$h = -2,93 \cdot 10^{-2} \sum_{i=1}^{N} \frac{T_i}{p_i} (p_{i-1} - p_i) \tag{4.3}$$

can be used, and as a still suitable analytical formula, it is convenient to take

$$h = -\bar{H} \cdot ln \frac{p(h)}{p_o} \tag{4.4}$$

if we use a mean scale height $\bar{H} \approx 8,29km$ for $T = 283$ K. The maximum altitude of the flights is 1584 and 1656 m, respectively. The height error on this occasion is not critical. Figures 4.11 and 4.12 depict the flight height via the flight time computed after (4.3). They show the flight regime of a stepwise relatively slow ascent and a following relatively fast descent.

The relaxation law and ascent behaviour of the ECC sonde

Between the changing O_3-signal and respective registration by the sonde a time delay exists described by the so called response time. The response time of the quantity I (here the sonde current) is defined as the time scale according to

$$\frac{1}{\tau} = \left| \frac{1}{I} \frac{dI}{dt} \right| \tag{4.5}$$

The analysis of the time behaviour due to relaxation of the sonde from a constant ozone flux to a zero flux yielded a hyperbolic decrease of the sonde current. The increase of the sonde current from zero to a constant value, respectively to a constant ozone flux, can be described as a hyperbola, too. The slow response of the sonde to the changing O_3-concentration smoothes real structures. Without consideration of further details in this discussion, the measured current (ozone) values have to be corrected approximately after a procedure derived from the differential time scale, the relaxation and the ascent law of the sonde. The response time correction is generally small (Fig. 4.13 and 4.14) except for regions of continuous strong change in ozone.

Interference of the ECC-sonde with other minor constituents

Questions about the interference of a monitor with other influences are always the basic methodical problem. For that reason the ECC-sonde has been checked in the gauging lab of the Rijksinstitut voor Volksgezondheid regarding the influence of humidity, NO_2, and SO_2 for a single case only. The conclusion from this rough test can be summarized as follows: there is no distinct interference with H_2O-vapour. On the average there is an error of about 15% with respect to $NO_2, \Delta\,[O_3] \approx 0,15\,[NO_2]$. A extremely large influence results from $SO_2, \Delta\,[O_3] \approx -0,674\,[SO_2]$. The brackets mark concentration values in ppbv.

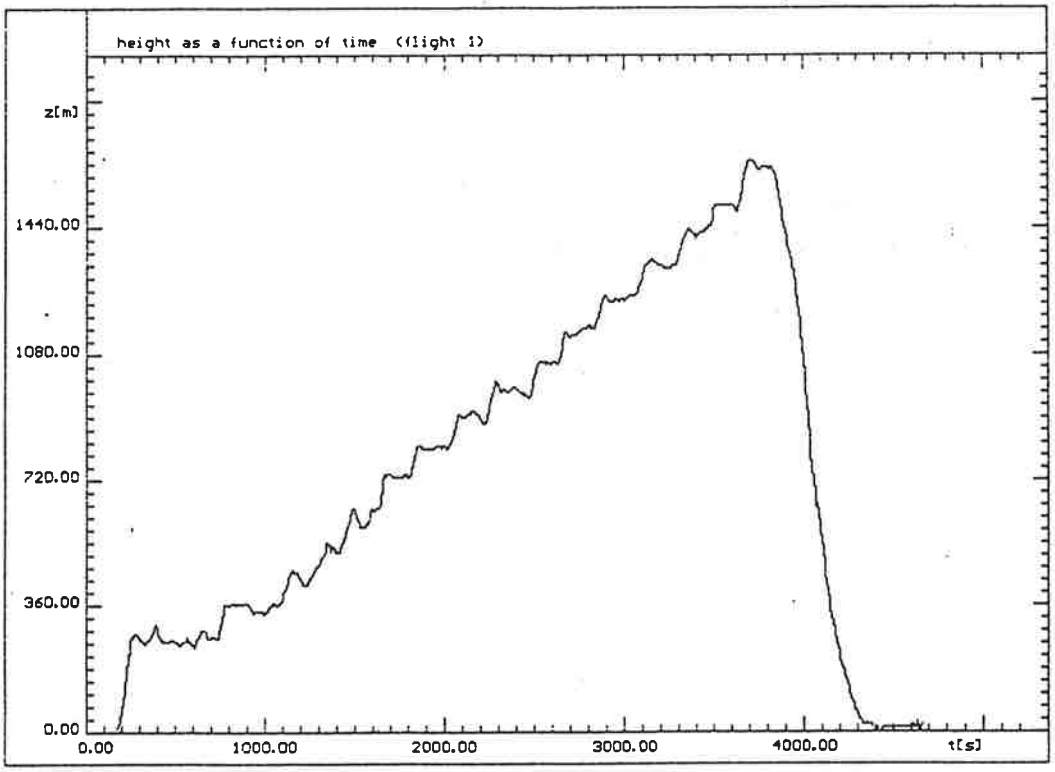

Figure 4.11: height as a function of time (flight 1)

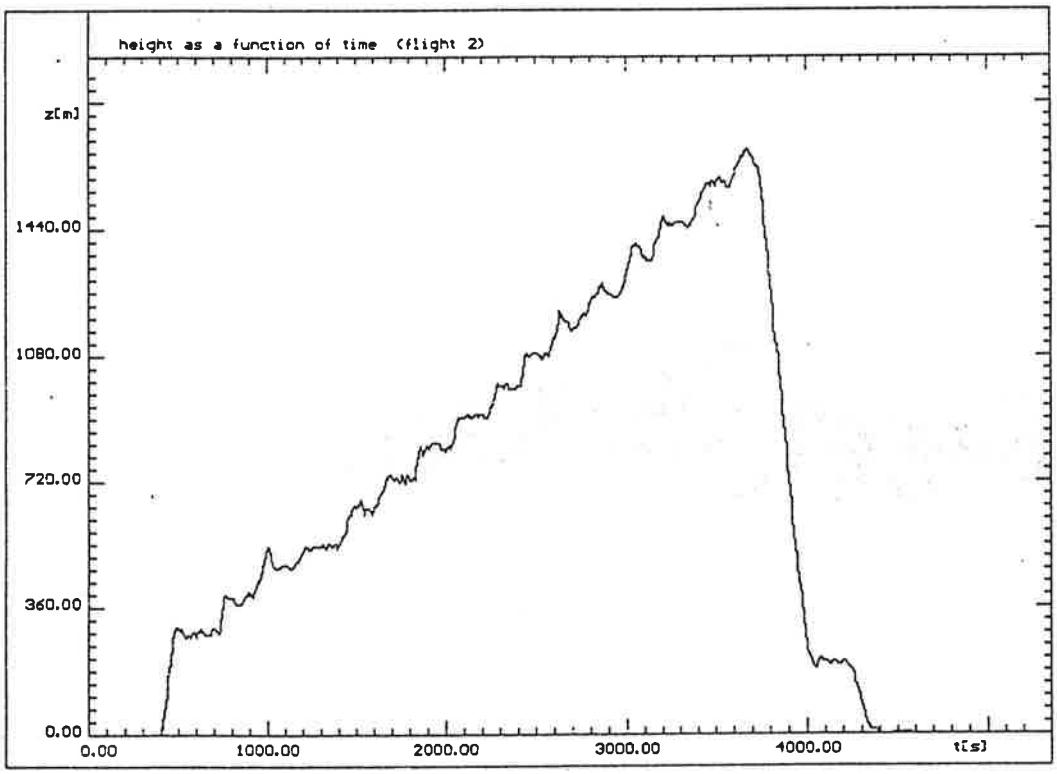

Figure 4.12: height as a function of time (flight 2)

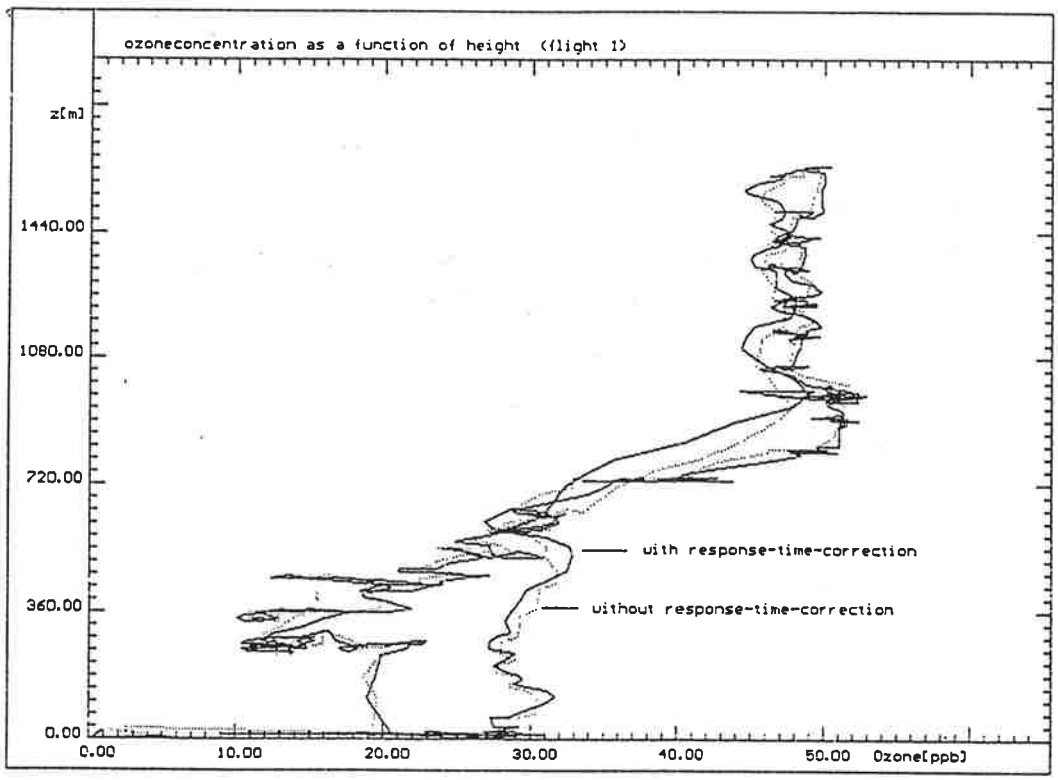

Figure 4.13: ozone concentration as a function of height (flight 1)

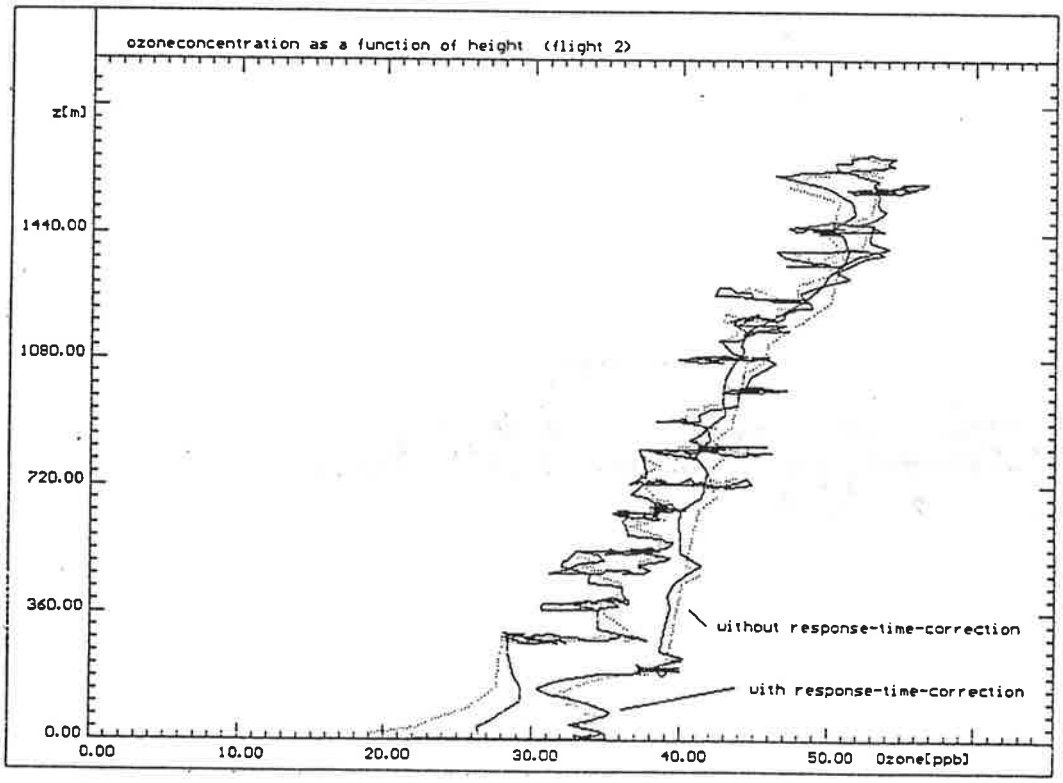

Figure 4.14: ozone concentration as a function of height (flight 2)

4.9 The IVL DOAS

The IVL DOAS system described here was run in a dual path mode making possible path averaged measurements of SO_2, O_3 and aerosol extinction.

The long path UV-system

The basic instrument is built similar to the DOAS system described by Platt and Perner [Plat 79]. The major difference being in the transmitting and receiving system, were a retroreflector system is being used [Gall 91a] and thus facilitating the use of different optical paths. A schematic view of the system is given in figure 4.15.

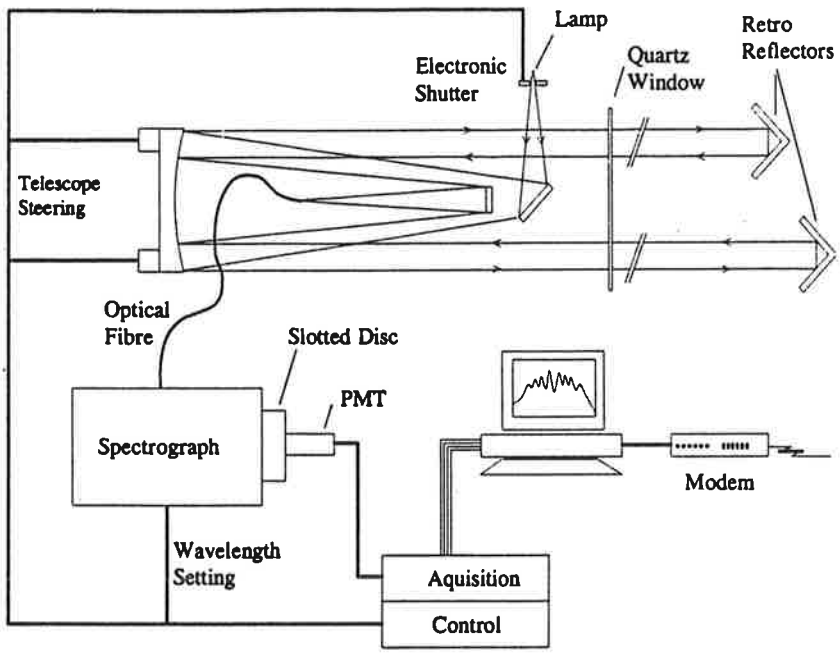

Figure 4.15: Schematic view of the UV-absorption instrument.

Broad band UV light from a 150 W xenon arc lamp (Hamamatsu 2304) is by means of a telescope transmitted over the measurement path towards a retro-reflector and back again. The special design of the telescope system makes possible the use of a single parabolic mirror for both transmission and receiving of the light, and also makes it possible to change optical path only by reaiming this mirror [Gall 91a]. Thus changing optical path can be done by the two computer controlled stepper-motors. The returning light is transmitted through an optical fibre into a 0.5 m spectrograph (spex 1850B). By means of a scanning slotted disc system on the exit port of the spectrograph [Plat 79] a 40 nm wide spectrum, centered according to the computer controlled grating setting of the spectrograph, is recorded with a resolution of 0.4 nm. Spectra are recorded at a repetition rate of 100 Hz, digitized and stored in 1024 channels with a customized MCA-card. Thus 12000 spectra are recorded and summed within two minutes. Due to the fast scanning rate and

averaging the influence of atmospheric turbulence is strongly suppressed and statistical noise is reduced. In this study the wavelength region 275 - 300 nm was selected. This region is relevant for LIDAR measurements of ozone and also covers absorption features making possible the determination of O_3 and SO_2 using differential optical absorption spectroscopy (DOAS) [Axel 90]. The system was used in a dual path mode. In this configuration the system is sequencially switched between two nearly collinear paths of different pathlength, recording one spectrum on each path. The paths used here was 884 and 2000 meters respectively.

Gas measurements

To obtain the mean gas concentration over the actual path a standard DOAS algorithm was used [Plat 79]. By the use of unique differential absorption features and polynom short pass filtering the influence of instrument factors, aerosols and slowly varying gaseous absorption are suppressed, and by multiple regression fitting of reference spectra the concentration of the studied gases are obtained. Reference spectra were obtained using a 2m gas cell and cross-sections were derived using certified standard gas (SO_2) and tabulated data (O_3) [Moli 86]. Thus the mean concentrations over 0-884m and by ratioing 884-2000m, were obtained providing information on spatial variation of the studied gases.

Aerosol extinction measurements

Aerosol extinction was measured using a dual path method [Gall 92]. The spectrum obtained when light from a broadband lamp is transmitted over an optical long path in the atmosphere is caused by a superposition of different mechanisms. Instrument factors, absorption in gaseous molecules and particles, and attenuation due to scattering in particles and molecules (Mie-and Rayleigh scattering). In order to obtain an aerosol extinction spectrum the other mechanisms contributing to the recorded spectrum have to be eliminated. By ratioing the spectra from the two paths, instrument factors are eliminated and a spectrum from the distance 884-2000m is obtained. Using DOAS algorithms the concentration of relevant gases (O_3, SO_2) in the ratioed spectrum may be determined. By means of recorded absolute crossections of these gases and by applying Beer-Lamberts law, the contribution to the ratioed spectrum from gaseous absorption can be eliminated. Finally Rayleigh scattering has a known wavelength dependence only determined by air density and thus is easily eliminated from the spectrum, providing an aerosol extinction spectrum over the range 884-2000m [Penn 57].

4.10 The RIVM ground level chemistry

The local installation of the RIVM-LLO were used to provide data as chemical composition of the air at ground level.

4.10.1 Instrumentation

The experimental setup for O_3 measurements is shown in figure 4.16; technical data are summarized in table 4.10. For a full description see [Lab 89].

The O_3 analyzer analog output represents pressure-corrected mixing ratios (ppb). The analogue signal is sampled every 10 s by an AD converter with a 12-bit resolution. A signal transmitter prepares the digital signal for accumulation in a computer. The computer calculates average minute values with standard error of distribution, whereby the monitor response time is taken into account. Finally, concentration values are stored on disc.

From table 4.10, it can be concluded that the digitizer precision amounts to 0.25 ppb (1 count). However, monitor precision amounts to 2 ppb, so total precision of O_3 measurements amounts to about 2 ppb.

UV photometric ambient O_3 analyzer; Thermo Environmental Instruments, model 49	
Full-scale range	1000 ppb
Precision	2 ppb
Response time (0-95%)	20 s
Flow rate	2 l min^{-1}
Analog output range	0 - 10 volt
Fluorinated ethylene propylene (FEP) tube	length 3 m; inner diameter 4.35 mm
ADC and transmitter; Imko Gmbh, model GM7K16 and GM23U	
Reaction time	80 ms
Sensitivity	2.5 mV/bit
Input range	0 - 10 volt
Personal computer; Compaq, model 386-20E	
I/O connection	RS232
Hard disc	40 Mbyte
Data storage	Floppy disc, 730 kbyte

Table 4.10: Technical specifications of O_3 measuring equipment

SO_2, NO, NO_2 and CO measurements

One of the macro-stations of the RIVM LML is situated in Bilthoven. A detailed technical description may be found in [Lab 89]. Almost all compounds in the LML are measured once per minute. Analogue monitor output signals are digitized by the station processor and organized for transmission to the central acquisition system. The multichannel AD converter of the station processor has a 12-bit resolution, the full-scale range corresponds to the full-scale analogue output of the monitor concerned. The central data acquisition system in Bilthoven collects all data from all station processors. Average hourly values, including standard error of distribution, for each compound at each station are calculated and stored in a database.

For Trolix '91 all one minute concentration values (for SO_2, NO, NO_2 and CO) from station 627 (Bilthoven) in the period of 10-28 June 1991 were stored on floppy discs.

Technical specifications of the SO_2, NO_x and CO analyzer are shown in table 4.11.

NO_2 concentration is determined as the difference measured between NO_x and NO concentration. If monitor precision as well as digitizer precision are taken into account, accuracy of NO_2 concentration values is about 2 ppb.

For SO_2 and CO measurements monitor precision is dominant over digitizer precision. Therefore the accuracy of SO_2 concentration is 3 $\mu g \cdot m^{-3}$ and of CO, 0.1 $\mu g \cdot m^{-3}$.

Concentrations in the LML are measured in ppb and are related to local pressure. All values are converted to $\mu g \cdot m^{-3}$ units by multiplying with a constant (atmospheric pressure and 293 K) before storing in a database.

4.10.2 Calibration

O_3 analyzer calibration

The UV photometer of the O_3 analyzer determines ozone concentrations by measuring the light attenuation due to presence of ozone in an absorption cell at a wavelength of 254 nm. The ozone concentration is directly related to the magnitude of attenuation.

Calibration measurements were carried out before and after the campaign through the RIVM's Laboratory for Air Research (LLO) calibration facility. This method is described by H.J. van der Wiel [Toel 79]. In both cases, zero gas and 75 ppb O_3 were sampled, zero gas by means of an impregnated and activated carbon filter. The monitor output did show a slight overestimation of the concentration value in both cases. Figure 4.17 shows the fit of the calibration measurements. All concentrations are re-calculated according to this line.

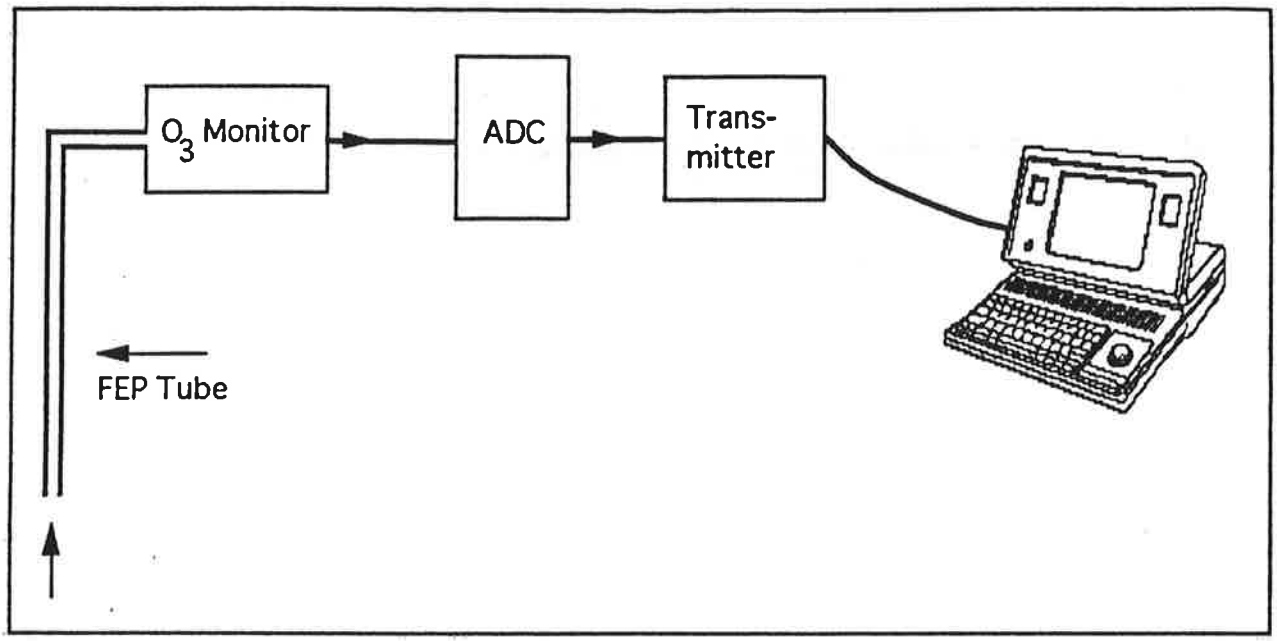

Figure 4.16: Experimental setup for ground-level O_3 measurements.

SO_2, NO_x and CO analyzer calibration

Each LML station is equipped with a calibration unit. Analyzer zero is calibrated every night (24.00) by removing the pollutant from the sampling flow by means of impregnated and activated carbon. Every week the monitor is calibrated by sampling with a pressure bottle containing the pollutant concerned in a known concentration. The calibration details are described in [Toel 79], [Lab 89].

4.10.3 Additional ozone monitor (MPI)

In addition to the instruments described above, a photometric monitor (environnement OM 431) was occasionally operated by the MPI. This was mainly used for the calibration of the ECC-ozonesondes. During the horizontal intercomparisons it was installed in the DOAS-laboratory, with the air sampled throug a three m long PTFA-tube which was fixed on a rod sticking out of the laboratory window.

The system had been calibrated by the manufacturer on delivery immediately before the experiment. This calibration was checked against the RIVM-LLO standard. No significant deviation was observed (larger than the reading accuracy of ± 1 ppbV).

SO_2 analyzer; Thermo Environmental Instruments Inc., model 43W, version 2	
Principle of operation	Gas-phase fluorescence
Full-scale range	750 ppb (2000 $\mu g \cdot m^{-3}$)
Precision	1% (80% full-scale), minimum 1 ppb
Response time (0-99%)	3 min
Flow rate	< 0.5 l min^{-1}
NO_2 analyzer; Philips, model PW 9762/00	
Principle of operation	Chemiluminescence
Full-scale range	4000 ppb (5000 $\mu g \cdot m^{-3}$) for NO
	5000 ppb for NO_x
Precision	$< 1\%$ (80% full-scale), minimum 1 ppb
Response time (0-99%)	3 min
Flow rate	0.9 l min^{-1}
CO analyzer; Thermo Environmental Instruments Inc., model 48	
Principle of operation	Gas-filter correlation spectrometry
Full-scale range	50 ppm (58 000 $\mu g \cdot m^{-3}$)
Precision	$< 1\%$ (80% full-scale), minimum 0.1 ppm
Response time (0-99%)	< 5 min (99% full-scale)
Flow rate	0.5 l min^{-1}

Table 4.11: Technical specifications of the SO_2, NO_x and CO analyzers [Lab 89]

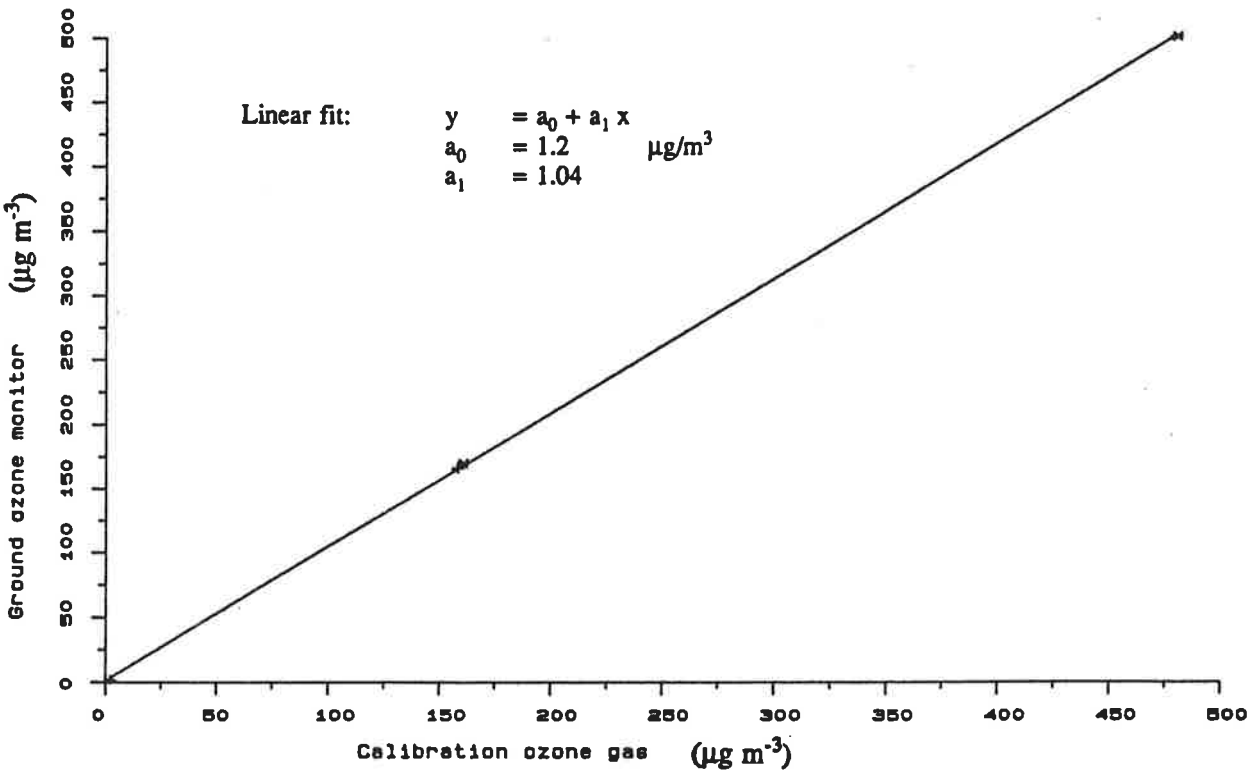

Figure 4.17: Calibration results

4.11 The KNMI meteorological measurements

No special meteorological measurements were performed for this experiment, since all necessary measurements were provided by the Royal Dutch Meteorological Institute (KNMI), which is only 2 km apart from there experiment location. Measurements of pressure, temperature, humidity, wind speed and direction, precipitation, and cloud cover were performed according to the standards of the weather service, and were supplied to the TROLIX group as data files. This support from the KNMI is gratefully acknowledged.

Chapter 5

Data

5.1 Weather situation

The following items are presented for each day of the experiment:

- a surface analysis
- mean and extreme values of surface observations
- hourly averages of surface observations
- a satellite image, meteosat ch. 4 (IR), including brief description

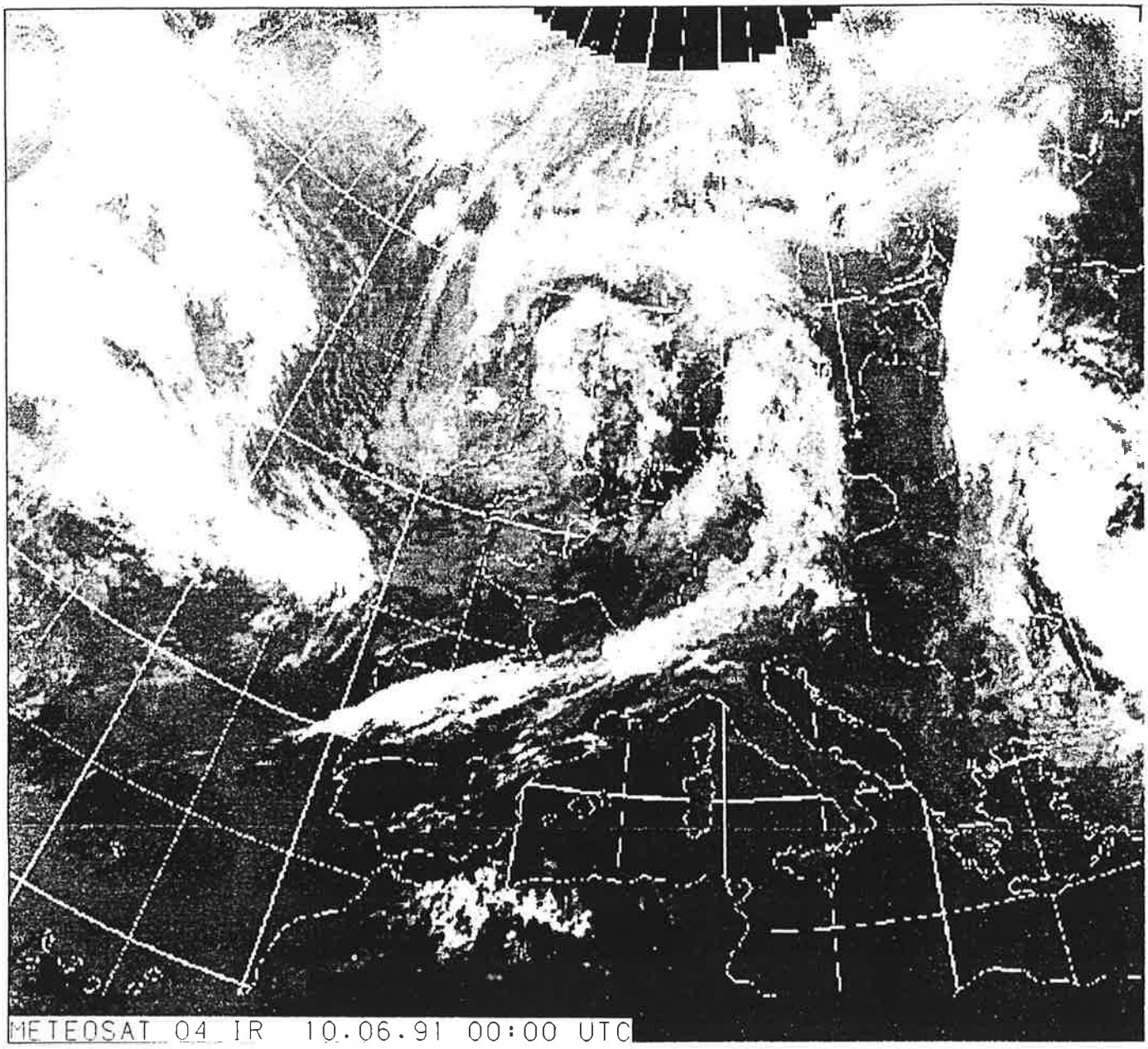

Weather Situation

The frontal system of an east-atlantic low pressure area moved easterly over Germany during the day, causing heavy rainfalls and increasing clouds. An advection of warm air, which preceeded the frontal system, caused increasing clouds already during sunday night. Measurements of precipitation in the morning were low. Partly heavy rainfalls occurred in the north of Germany in the morning.

The satellite picture shows the frontal cloud line over the eastern and southern part of Germany. The western part of Germany had overcast skies and relatively low temperature for the season (14 - 18 °C). The frontal system was accompanied by partly heavy rainfalls. In some regions, more than 10 l/m² of precipitation were measured.

MAANDAG 10 JUNI 1991 1200 UTC.

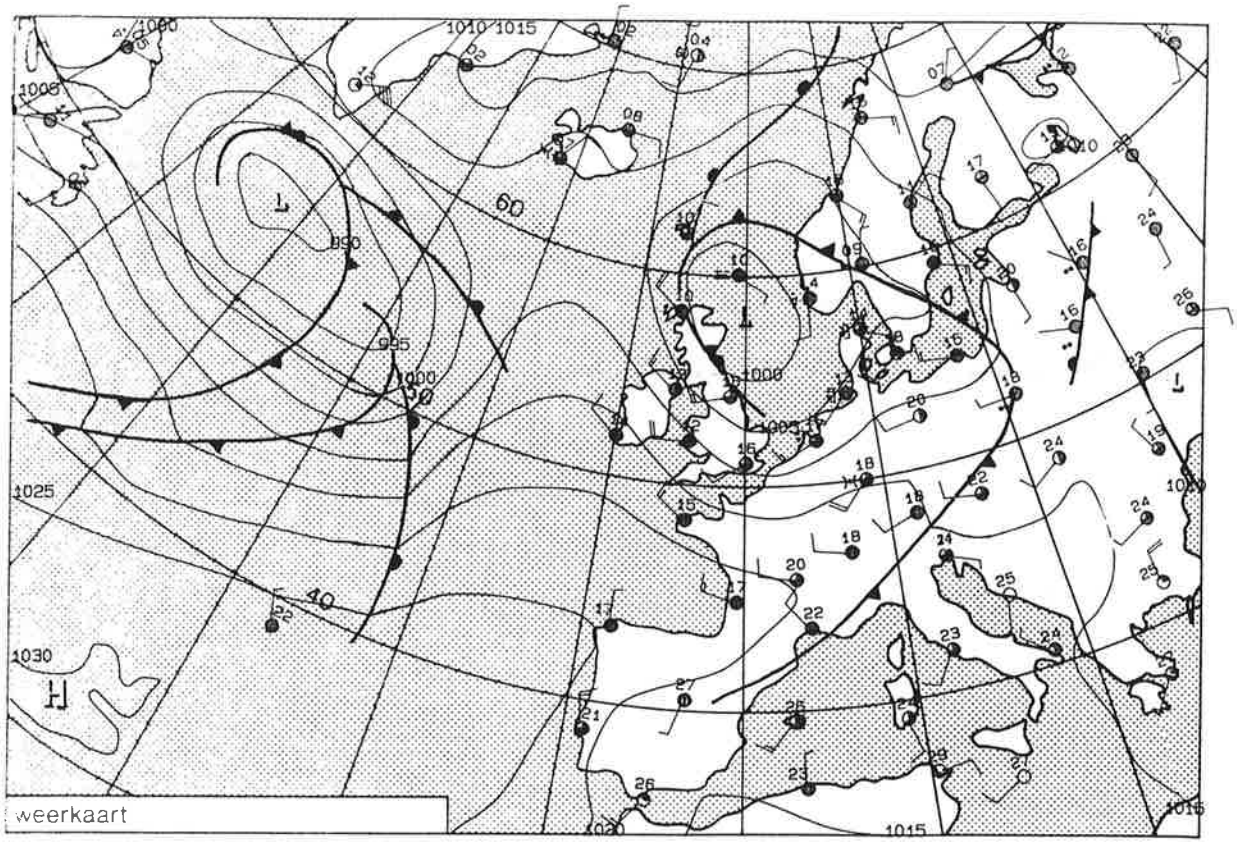

DOW 5 GEMIDDELDEN, SOMMEN EN EXTREMEN (ETMAAL 0 - 24 UUR)

10 JUNI 1991

	WINDSNELHEID UUR GEM HALVE	WINDSNELHEID MAX VLAAG M/SEC.	TEMPERATUUR 10 CM GRADEN	TEMPERATUUR 150 CM CELSIUS	VOCHTIGHEID * DAMP DRUK MBAR	VOCHTIGHEID * RELA TIEF PROC	NEERSLAG HOEVEELHEID MM	NEERSLAG DUUR UREN	LUCHTDRUK * ZEENIVEAU MBAR	BE * WOL KING 1/8
260 DE BILT										
GEM.	11	-	-	13,9	12,2	77	-	-	1008,7	7
SOM	-	-	-	-	-	-	1,7	2,5	-	-
MAX.	15	32	-	17,2	13,3	92	0,6	-	1014,0	8
MIN.	5	-	10,7	11,6	10,2	64	-	-	1005,6	1

yymmddhh	temp	rh	press	wd	wv
91061001	11.9	73	1005.7	22	9
91061002	11.6	76	1006.1	22	8
91061003	12.3	77	1006.2	22	8
91061004	12.6	78	1006.3	22	11
91061005	12.6	79	1006.3	20	10
91061006	12.8	81	1006.6	20	10
91061007	13.4	81	1006.9	22	12
91061008	13.7	77	1007.0	22	12
91061009	13.5	81	1007.4	21	11
91061010	13.3	85	1007.6	21	12
91061011	13.9	84	1007.9	23	13
91061012	16.5	69	1008.2	24	12

yymmddhh	temp	rh	press	wd	wv
91061013	16.6	64	1008.2	26	13
91061014	16.8	64	1008.7	25	15
91061015	16.3	66	1009.0	25	15
91061016	16.0	66	1009.2	24	14
91061017	16.0	70	1009.5	26	12
91061018	14.6	71	1010.1	26	10
91061019	14.8	75	1010.6	26	10
91061020	13.4	83	1011.2	25	9
91061021	13.3	83	1012.1	26	8
91061022	12.8	86	1013.0	26	8
91061023	12.2	90	1013.7	27	8
91061024	11.7	92	1014.1	25	5

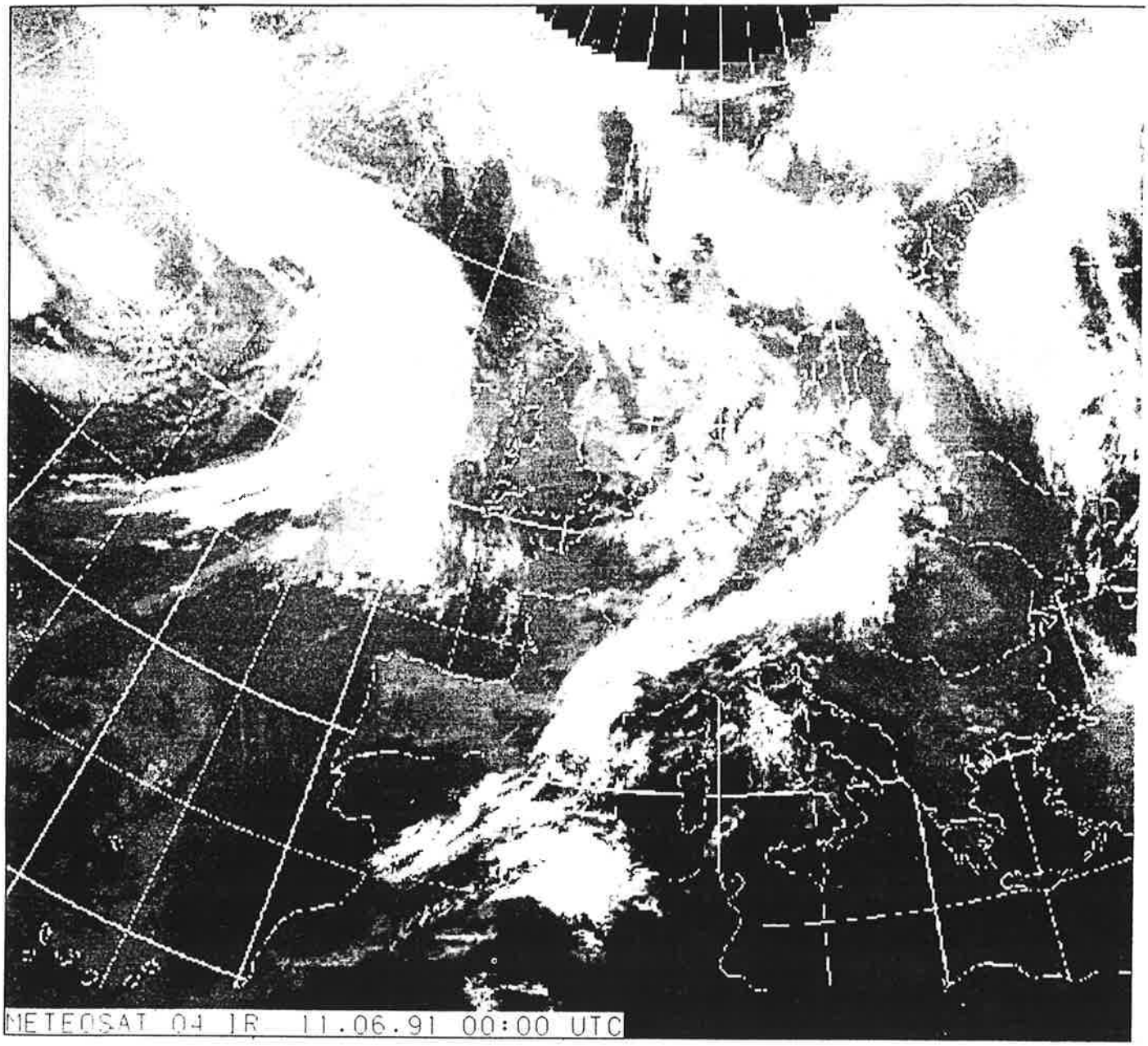

Weather Situation

A cold front which crossed Germany almost entirely during the late morning and the afternoon was followed by heavy rainfalls and, in some regions, thunderstorms.

The satellite picture shows a cloud vortex south of Iceland and a cloud line which has its origins in the cloud vortex. It belongs to the frontal system of an atlantic low pessure area the warm front of which had already moved to Ireland.

DINSDAG 11 JUNI 1991 1200 UTC.

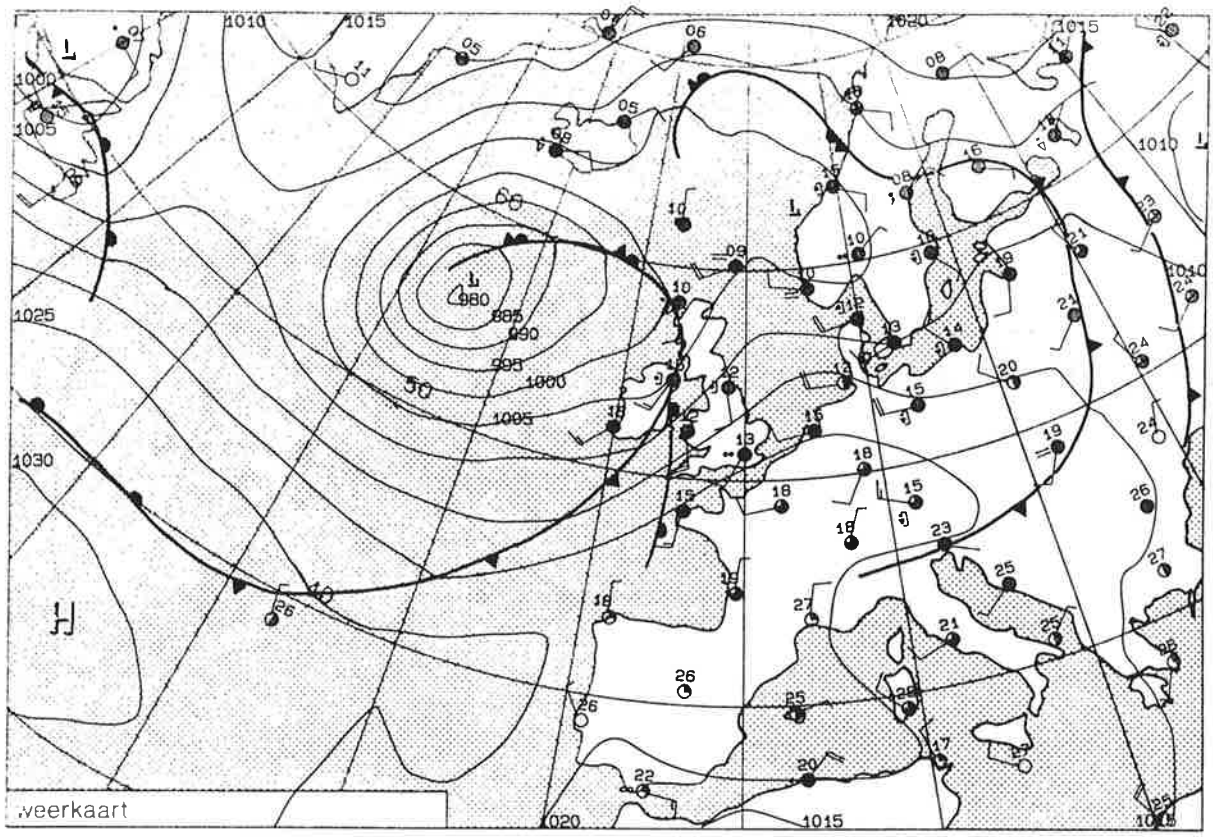

DOW 5 GEMIDDELDEN, SOMMEN EN EXTREMEN (ETMAAL 0 - 24 UUR)

11 JUNI 1991

	WINDSNELHEID UUR GEM HALVE	MAX VLAAG M/SEC.	TEMPERATUUR 10 CM GRADEN	150 CM CELSIUS	* VOCHTIGHEID DAMP DRUK MBAR	* RELA TIEF PROC	NEERSLAG HOEVEELHEID MM	DUUR UREN	* LUCHTDRUK ZEENIVEAU MBAR	* BE WOL KING 1/8
260 DE BILT										
GEM.	8	-	-	13,7	10,4	67	-	-	1017,9	7
SOM	-	-	-	-	-	-	0,0	.	-	-
MAX.	12	27	-	17,0	11,7	85	0,0	-	1020,2	8
MIN.	4	-	10,7	11,2	8,3	48	-	-	1014,6	6

yymmddhh	temp	rh	press	wd	wv
91061101	11.7	85	1014.7	27	6
91061102	11.6	82	1015.1	27	6
91061103	12.0	78	1015.6	27	7
91061104	11.7	77	1016.1	27	7
91061105	11.3	78	1016.7	26	8
91061106	11.5	79	1017.2	26	7
91061107	12.1	76	1018.1	27	7
91061108	12.8	75	1018.6	26	8
91061109	13.7	69	1019.1	28	7
91061110	14.1	57	1019.3	27	9
91061111	15.2	52	1019.6	27	12
91061112	15.2	48	1020.0	26	11
91061113	15.3	52	1020.3	27	10
91061114	16.3	53	1019.9	26	9
91061115	15.5	48	1019.7	26	10
91061116	16.0	61	1019.2	24	8
91061117	14.8	65	1019.0	27	9
91061118	14.7	60	1018.4	23	7
91061119	14.5	67	1018.3	23	7
91061120	14.3	60	1018.5	23	8
91061121	14.1	65	1018.2	23	8
91061122	13.8	69	1017.5	20	6
91061123	12.9	75	1016.6	17	4
91061124	14.0	72	1015.9	19	5

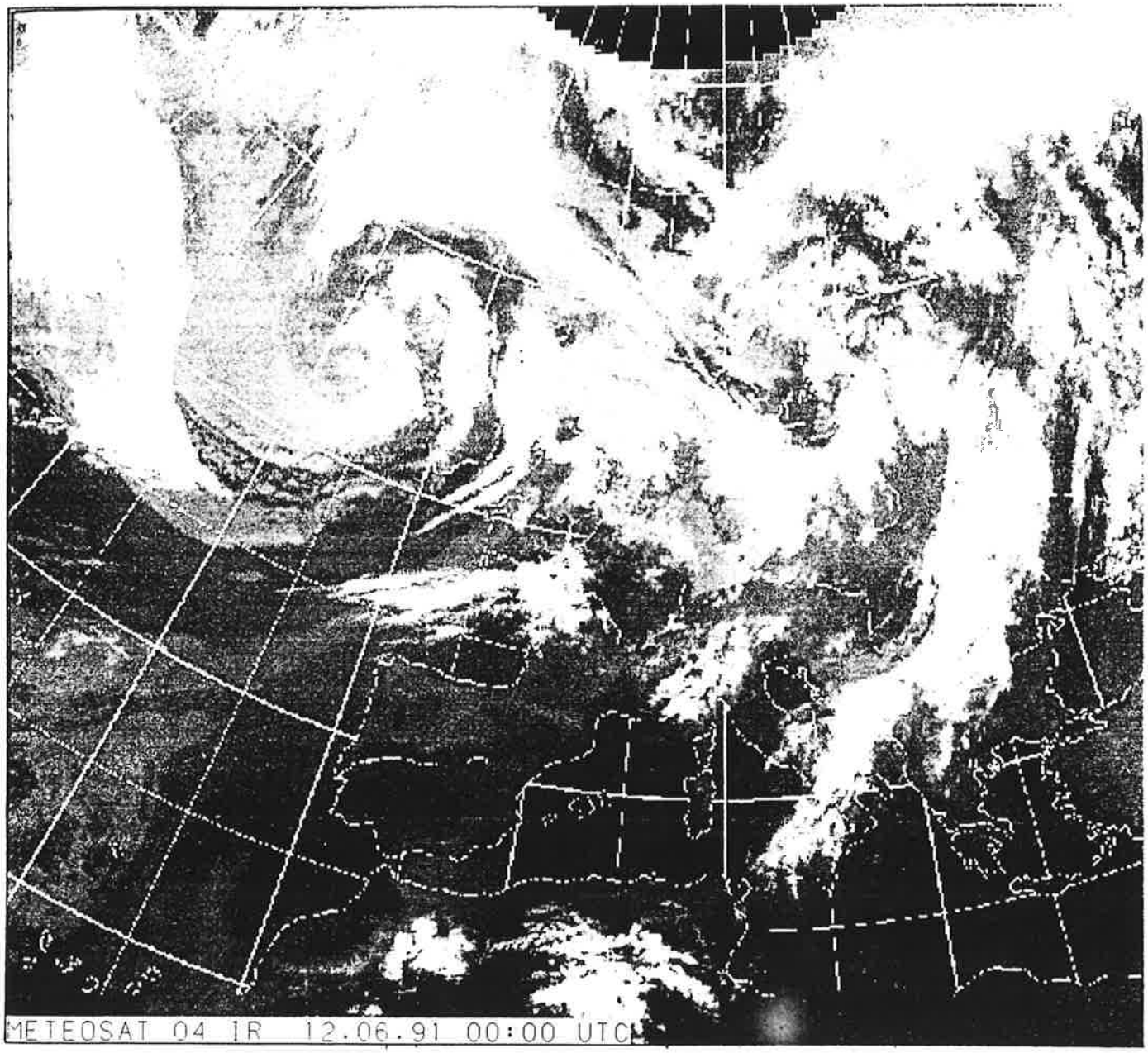

Weather Situation

On Tuesday, the frontal system west of Ireland moved to the British Isles during the day, causing rainfalls. The accompanying warm front crossed Great Britain nearly entirely whereas the following cold front moved first to Ireland and Scotland causing partly heavy rainfalls. Rainfalls in the western part of Germany diminished. Increasing clouds in the west are the first sign for the following warm front moving in from the atlantic ocean.

The satellite picture shows a cloud vortex which indicates the position of the atlantic low pressure area .

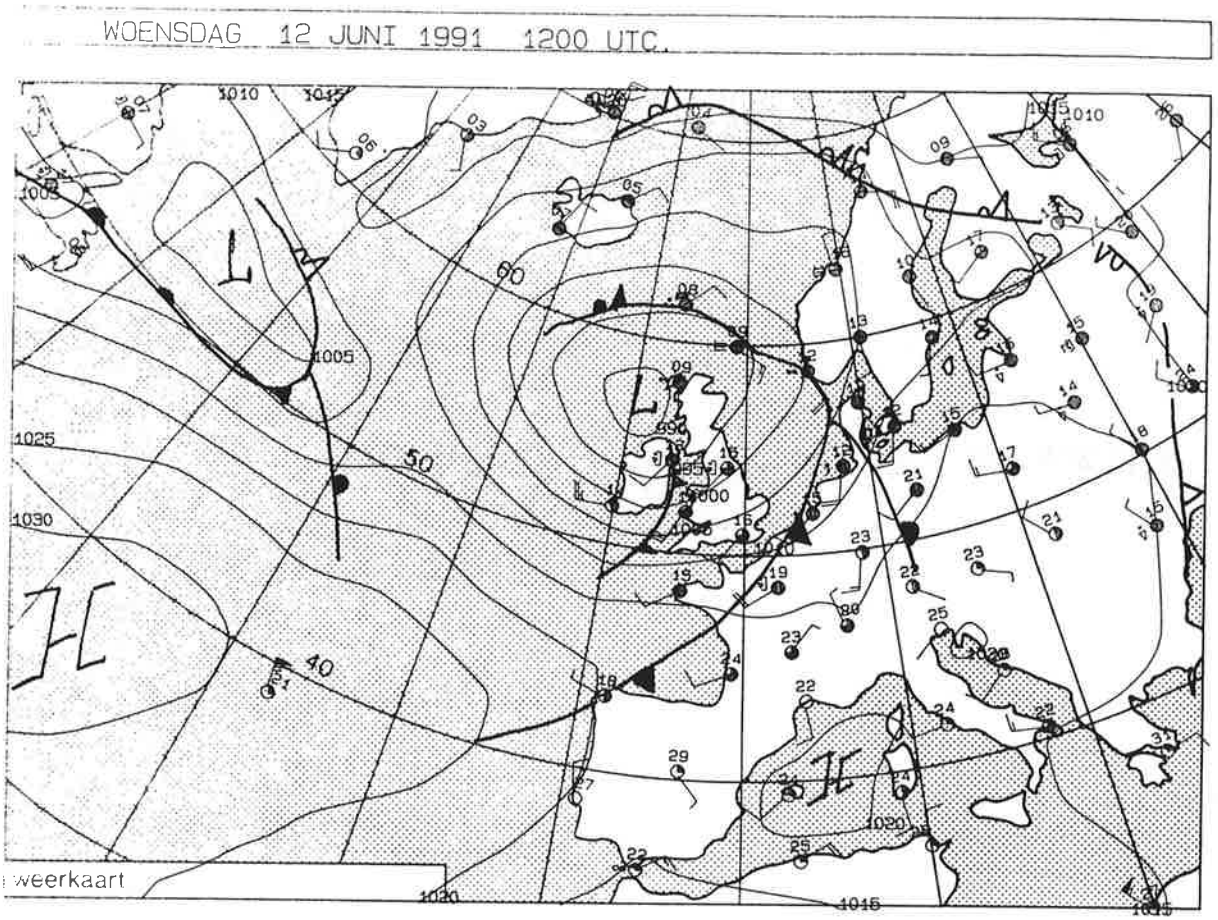

DOW 5 GEMIDDELDEN, SOMMEN EN EXTREMEN (ETMAAL 0 - 24 UUR)

12 JUNI 1991

	WINDSNELHEID UUR GEM HALVE	WINDSNELHEID MAX VLAAG M/SEC.	TEMPERATUUR 10 CM GRADEN	TEMPERATUUR 150 CM CELSIUS	* VOCHTIGHEID DAMP DRUK MBAR	* VOCHTIGHEID RELA TIEF PROC	NEERSLAG HOEVEELHEID MM	NEERSLAG DUUR UREN	* LUCHTDRUK ZEENIVEAU MBAR	* BE WOL KING 1/8
260 DE BILT										
GEM.	9	-	-	13,9	13,6	85	-	-	1010,0	7
SOM	-	-	-	-	-	-	9,0	5,5	-	-
MAX.	12	25	-	15,4	15,2	94	2,0	-	1014,8	8
MIN.	6	-	11,0	11,9	10,5	69	-	-	1006,6	2

yymmddhh	temp	rh	press	wd	wv
91061201	14.3	71	1014.9	20	7
91061202	14.5	69	1014.1	20	8
91061203	14.6	69	1013.5	20	8
91061204	12.7	90	1013.2	20	9
91061205	12.7	91	1012.8	19	6
91061206	13.1	89	1012.0	18	7
91061207	13.4	88	1011.8	20	8
91061208	13.0	91	1011.5	22	8
91061209	14.1	88	1010.9	20	9
91061210	14.9	81	1010.7	21	11
91061211	15.2	78	1010.1	22	10
91061212	14.6	86	1009.8	22	11

yymmddhh	temp	rh	press	wd	wv
91061213	13.8	94	1009.7	22	9
91061214	13.9	94	1009.6	21	9
91061215	14.2	92	1009.3	21	8
91061216	14.2	94	1008.6	20	9
91061217	14.5	92	1008.3	21	9
91061218	15.1	87	1007.9	21	9
91061219	15.3	86	1007.6	21	9
91061220	14.5	90	1007.6	21	7
91061221	13.6	91	1007.4	20	6
91061222	13.0	90	1007.0	21	6
91061223	12.8	74	1006.8	23	12
91061224	12.0	75	1006.7	23	11

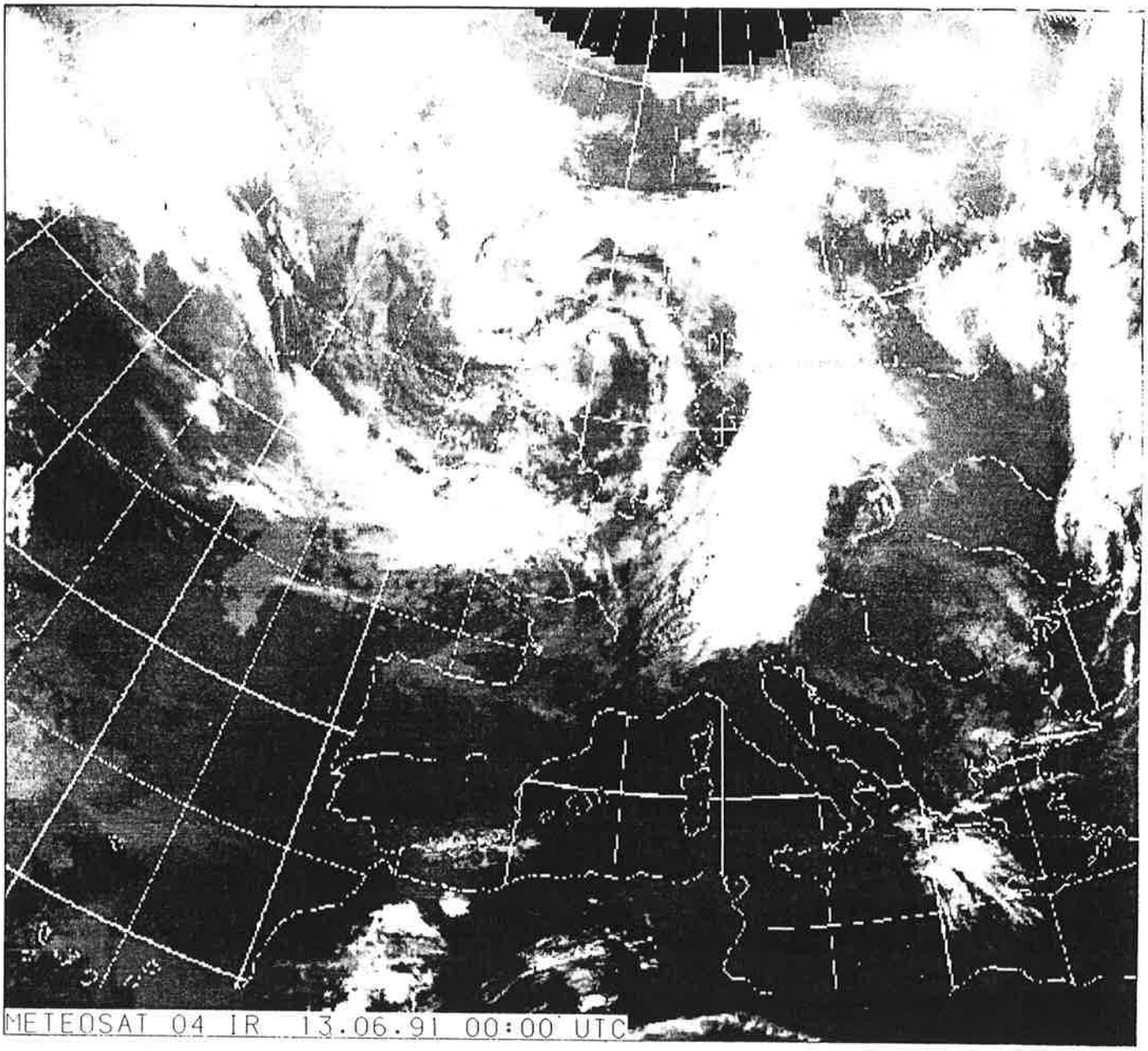

Weather Situation

An atlantic low pressure area moved from the sea area between Iceland and Ireland to Scotland. The frontal system belonging to the low pressure area moved over Germany during the day; the warm front spread over the whole of Germany, the cold front only over the northern and the western part. The warm front caused rainfalls in northern Germany. In some parts, more than 10 l/m² of precipitation were measured. In front of the cold front and in its area, rainfalls occurred. The warm air coming from the south-west entailed temperatures up to 20° C.

DONDERDAG 13 JUNI 1991 1200 UTC.

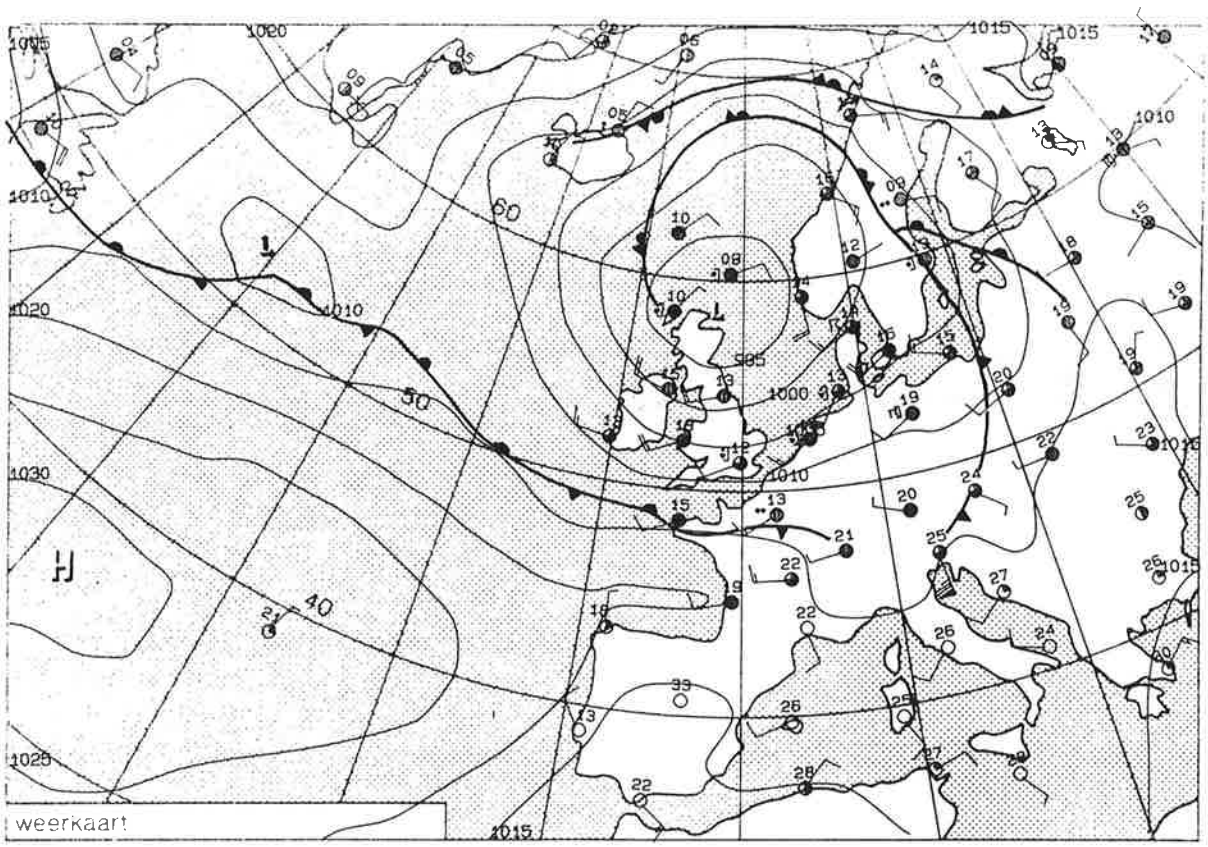

DOW 5 GEMIDDELDEN, SOMMEN EN EXTREMEN (ETMAAL 0 - 24 UUR)

13 JUNI 1991

	WINDSNELHEID UUR GEM HALVE	WINDSNELHEID MAX VLAAG M/SEC.	TEMPERATUUR 10 CM GRADEN	TEMPERATUUR 150 CM CELSIUS	* VOCHTIGHEID DAMP DRUK MBAR	* VOCHTIGHEID RELA TIEF PROC	NEERSLAG HOEVEELHEID MM	NEERSLAG DUUR UREN	* LUCHTDRUK ZEENIVEAU MBAR	* BE WOL KING 1/8
260 DE BILT										
GEM.	13	-	-	13,1	11,1	74	-	-	1007,0	6
SOM	-	-	-	-	-	-	5,6	2,8	-	-
MAX.	18	34	-	17,0	12,7	89	2,2	-	1007,9	8
MIN.	10	-	10,6	11,0	8,9	49	-	-	1006,5	3

yymmddhh	temp	rh	press	wd	wv
91061301	11.6	80	1006.6	23	10
91061302	11.7	82	1006.7	22	12
91061303	11.5	85	1006.6	23	11
91061304	11.8	85	1006.6	23	11
91061305	12.0	85	1006.6	22	11
91061306	12.1	86	1006.9	22	11
91061307	12.2	86	1006.9	23	11
91061308	13.4	77	1006.9	23	13
91061309	13.5	77	1007.2	23	14
91061310	11.0	89	1007.4	24	13
91061311	12.5	85	1007.2	24	12
91061312	14.5	77	1007.2	23	13

yymmddhh	temp	rh	press	wd	wv
91061313	15.1	70	1006.8	24	13
91061314	16.4	56	1006.8	24	18
91061315	16.3	50	1006.9	25	17
91061316	15.9	49	1007.2	25	18
91061317	15.2	55	1007.1	25	16
91061318	14.6	57	1007.2	24	16
91061319	13.5	65	1007.3	24	12
91061320	13.1	69	1007.6	24	11
91061321	12.4	76	1007.8	23	10
91061322	12.1	77	1007.9	23	10
91061323	11.5	81	1007.9	22	10
91061324	11.5	83	1008.0	23	10

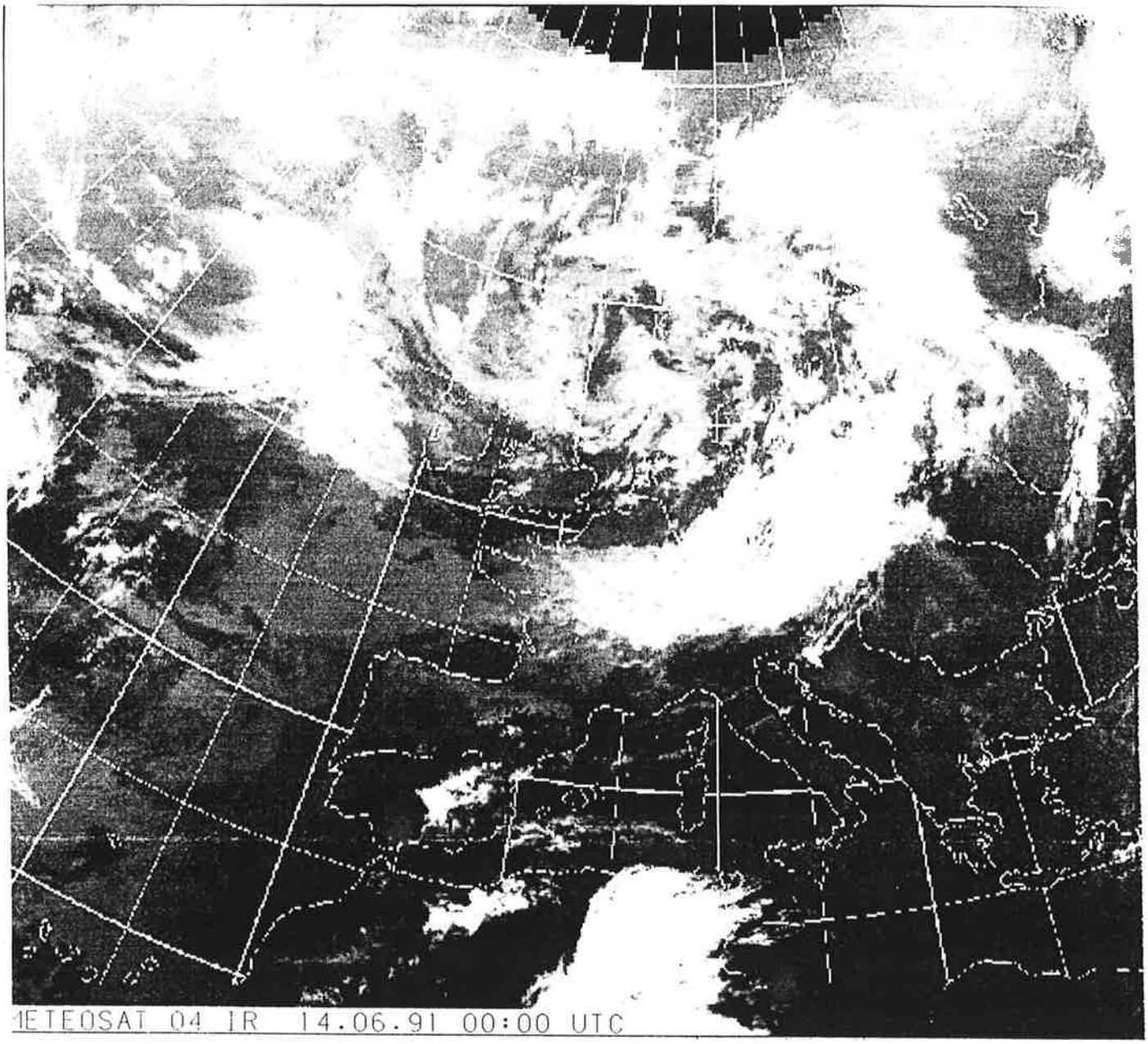

Weather Situation

The weather situation was characterised by a frontal zone directed form North America over the nothern part of the atlantic ocean to Central Europe and a low pressure area over the noth-western part of Europe. In Germany it was windy. Cold air moving in from the atlantic ocean caused increasing clouds and - especially in the nothern and southern parts of Germany - thunderstorms. The satellite picture shows overcast but partly cloudless skies all over Germany. Cloudiness in the frontal area of the cold front mentioned above shows to be compact over Poland.

VRIJDAG 14 JUNI 1991 1200 UTC.

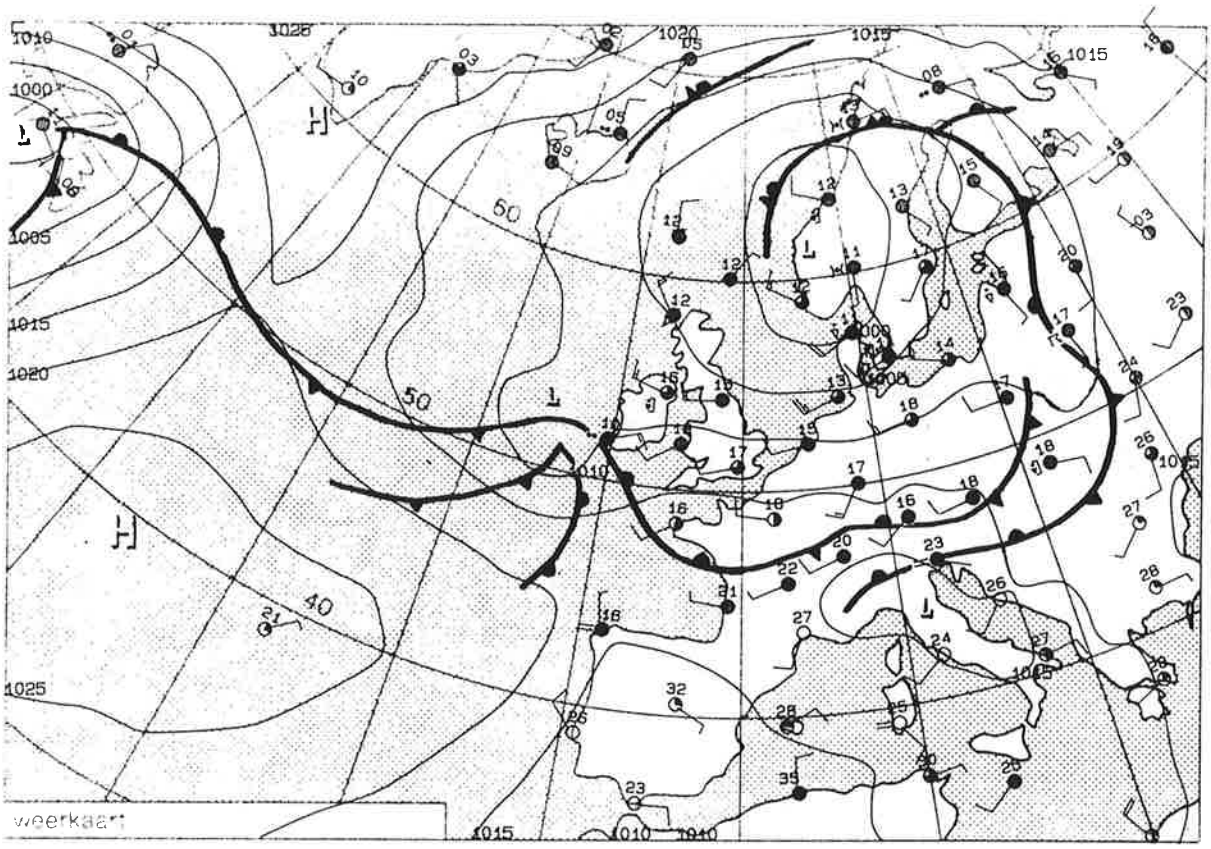

DOW 5 GEMIDDELDEN, SOMMEN EN EXTREMEN (ETMAAL 0 - 24 UUR)

14 JUNI 1991

	WINDSNELHEID UUR GEM HALVE	MAX VLAAG M/SEC.	TEMPERATUUR 10 CM GRADEN	150 CM CELSIUS	* VOCHTIGHEID DAMP DRUK MBAR	* RELA TIEF PROC	NEERSLAG HOEVEELHEID MM	DUUR UREN	* LUCHTDRUK ZEENIVEAU MBAR	* BE WOL KING 1/8
260 DE BILT										
GEM.	10	-	-	13,7	11,0	71	-	-	1010,4	6
SOM	-	-	-	-	-	-	0,0	.	-	-
MAX.	13	27	-	17,6	12,4	91	0,0	-	1012,1	8
MIN.	8	-	10,2	10,8	9,3	50	-	-	1008,0	3

yymmddhh	temp	rh	press	wd	wv
91061401	11.1	87	1008.1	23	8
91061402	11.1	90	1008.2	23	8
91061403	11.5	89	1008.4	23	8
91061404	11.3	91	1008.6	23	8
91061405	11.3	91	1008.9	23	8
91061406	11.9	89	1009.4	22	9
91061407	12.3	86	1009.7	22	10
91061408	13.1	82	1009.9	23	10
91061409	13.8	75	1010.0	24	12
91061410	14.0	70	1010.3	25	11
91061411	14.5	71	1010.6	25	13
91061412	15.1	66	1010.8	26	12

yymmddhh	temp	rh	press	wd	wv
91061413	15.3	64	1011.1	26	12
91061414	16.3	57	1011.2	26	11
91061415	16.0	51	1011.4	27	13
91061416	16.4	50	1011.4	27	13
91061417	16.6	51	1011.6	26	13
91061418	15.6	53	1011.5	26	11
91061419	14.9	62	1011.8	24	9
91061420	14.0	68	1012.1	24	9
91061421	13.4	65	1012.1	24	10
91061422	13.4	65	1012.2	24	9
91061423	13.0	71	1012.0	22	8
91061424	12.5	71	1011.7	23	8

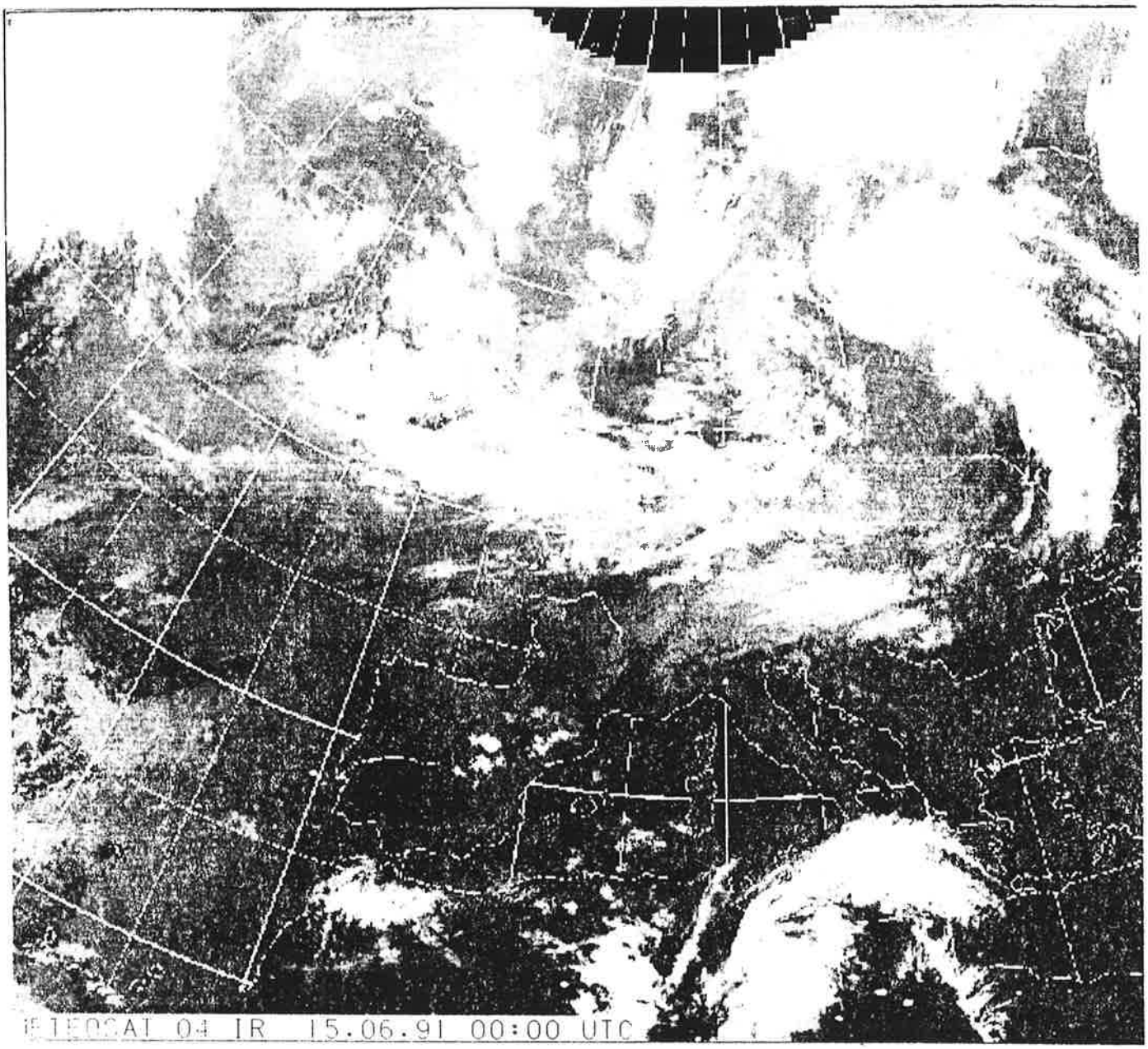

Weather Situation

On Saturday, a low pressure area covered the nothern part of Europe. The frontal zone at its southern side ranged from the atlantic ocean to Bjelorussia. In most of France and in the southern and middle part of Germany temperatures rised at about 3 to 5 K. In Belgium and the south-eastern part of England the approaching of an upper level ridge caused rising of the temperatures (+ 8 k in De Bilt, Netherlands). In the north-western part of Germany, rain fell during the morning hours caused by a warm front . The satellite picture shows the cloud area of the warm front over the southern part of the British Isles.

ZATERDAG 15 JUNI 1991 1200 UTC.

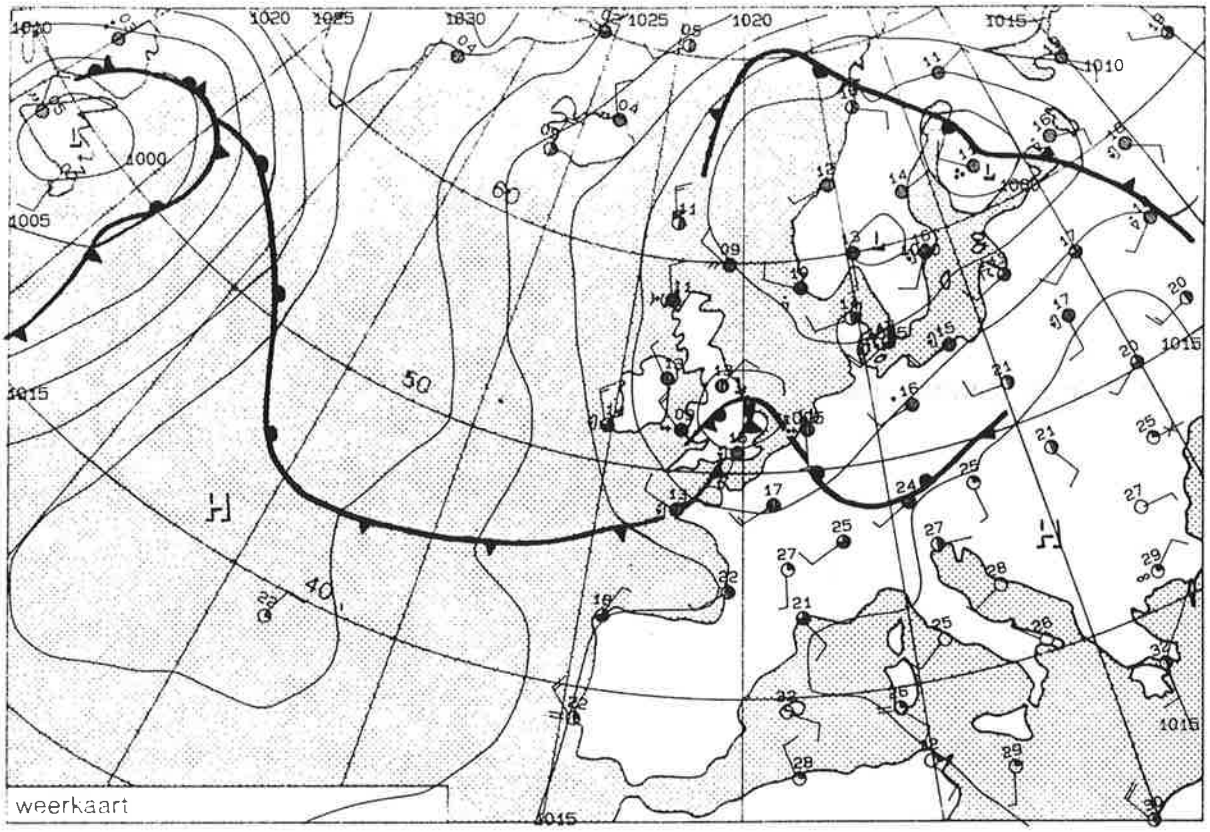

DOW 5 GEMIDDELDEN, SOMMEN EN EXTREMEN (ETMAAL 0 - 24 UUR)

15 JUNI 1991

	WINDSNELHEID UUR GEM HALVE	MAX VLAAG M/SEC.	TEMPERATUUR 10 CM GRADEN	150 CM CELSIUS	* VOCHTIGHEID DAMP DRUK MBAR	* RELA TIEF PROC	NEERSLAG HOEVEELHEID MM	DUUR UREN	* LUCHTDRUK ZEENIVEAU MBAR	* BE WOL KING 1/8
260 DE BILT										
GEM.	9	-	-	11,9	12,5	90	-	-	1006,1	8
SOM	-	-	-	-	-	-	17,3	11,8	-	-
MAX.	16	33	-	14,4	14,8	97	3,9	-	1011,2	8
MIN.	5	-	9,8	9,7	10,2	74	-	-	1000,6	5

yymmddhh	temp	rh	press	wd	wv
91061501	12.0	74	1011.3	23	7
91061502	11.4	76	1010.9	22	7
91061503	11.0	81	1010.6	22	6
91061504	10.9	85	1010.6	23	7
91061505	10.4	92	1010.2	22	6
91061506	10.2	90	1010.2	23	5
91061507	9.8	94	1009.9	20	6
91061508	9.8	95	1009.5	18	6
91061509	9.9	95	1008.1	16	7
91061510	10.2	97	1007.6	16	8
91061511	10.8	97	1007.3	17	7
91061512	11.4	95	1006.8	18	6

yymmddhh	temp	rh	press	wd	wv
91061513	12.2	95	1006.2	19	6
91061514	13.3	94	1005.7	20	8
91061515	13.7	94	1005.2	21	9
91061516	14.0	91	1004.5	20	9
91061517	14.3	91	1003.8	20	9
91061518	14.4	90	1002.8	19	8
91061519	14.0	92	1002.0	20	8
91061520	13.6	92	1001.3	21	10
91061521	13.1	84	1000.9	23	14
91061522	12.6	82	1000.7	23	16
91061523	11.7	85	1000.9	26	14
91061524	10.9	89	1001.6	26	15

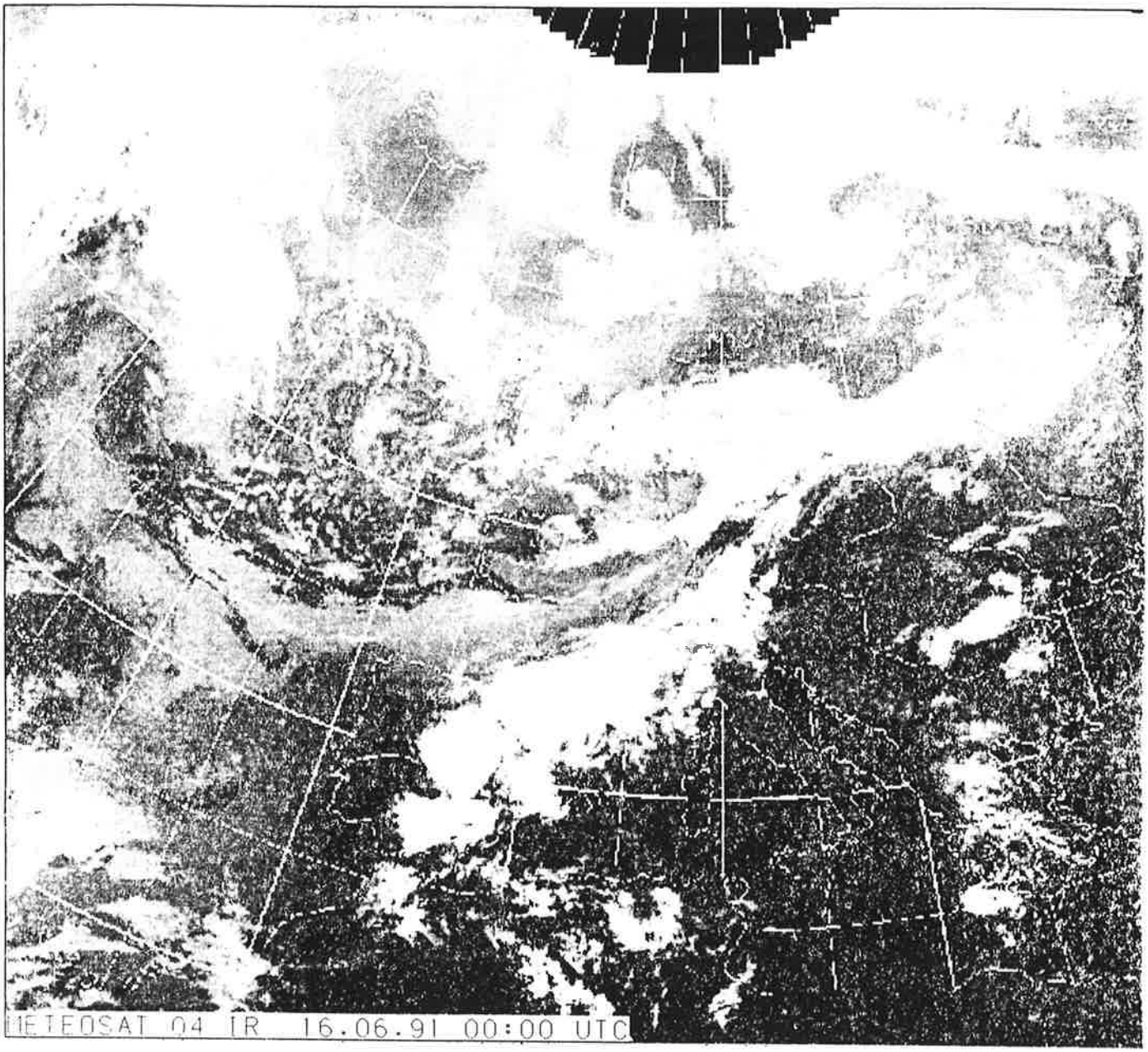

Weather Situation

The low pressure area which was over Wales on Sunday moved to the German Bight. At the same time, a trough coming from Ireland approached Belgium. It itensified and formed a proper low pressure area over the southern part of the North Sea. The warm front of the low pressure system crossed most of Germany. Rising warm air in front of the front caused heavy rainfalls with 15 to 20 l/m² of precipitation. The temperatures were at 15 °C. The cold front crossed the western and northern part of Germany with only marginal changes of weather conditions.

ZONDAG 16 JUNI 1991 1200 UTC.

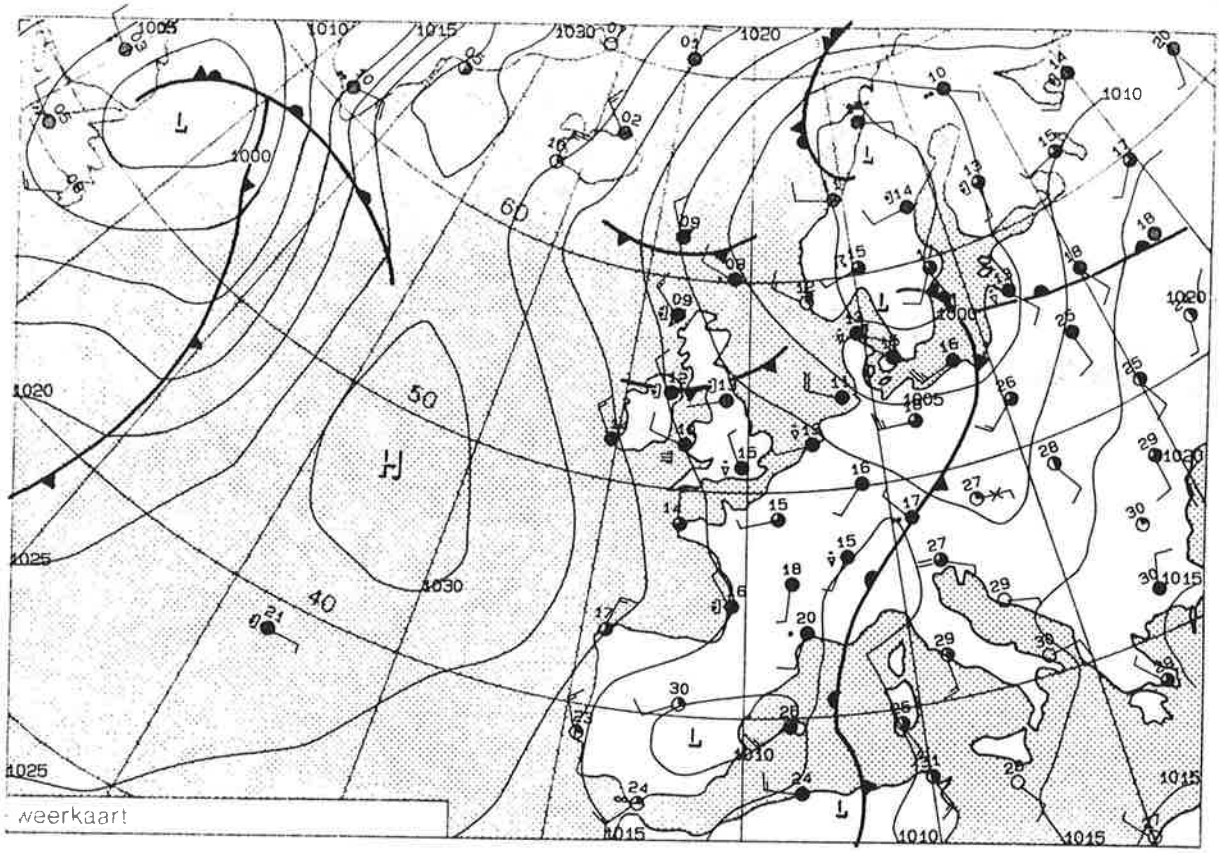

DOW 5

GEMIDDELDEN, SOMMEN EN EXTREMEN (ETMAAL 0 - 24 UUR)

16 JUNI 1991

	WINDSNELHEID UUR GEM HALVE	MAX VLAAG M/SEC.	TEMPERATUUR 10 CM GRADEN	150 CM CELSIUS	* VOCHTIGHEID DAMP DRUK MBAR	* RELA TIEF PROC	NEERSLAG HOEVEELHEID MM	DUUR UREN	* LUCHTDRUK ZEENIVEAU MBAR	* BE WOL KING 1/8
260 DE BILT										
GEM.	6	-	-	11,2	10,8	81	-	-	1009,9	6
SOM	-	-	-	-	-	-	7,2	2,4	-	-
MAX.	15	37	-	14,8	12,2	96	2,5	-	1013,7	8
MIN.	1	-	1,6	5,5	8,7	70	-	-	1003,1	0

yymmddhh	temp	rh	press	wd	wv
91061601	11.2	84	1003.2	27	15
91061602	11.1	83	1004.1	28	11
91061603	11.1	82	1005.1	27	11
91061604	10.9	85	1006.0	27	10
91061605	10.4	93	1006.8	30	6
91061606	10.9	90	1007.7	28	7
91061607	11.3	85	1008.5	28	7
91061608	12.5	78	1009.0	29	7
91061609	12.4	76	1009.6	28	7
91061610	12.2	71	1010.1	28	7
91061611	13.7	71	1010.4	27	7
91061612	12.5	84	1010.7	26	7

yymmddhh	temp	rh	press	wd	wv
91061613	11.4	86	1011.3	31	6
91061614	13.0	77	1011.3	31	3
91061615	13.3	75	1011.6	27	4
91061616	13.2	72	1011.8	30	3
91061617	13.3	71	1011.8	32	5
91061618	12.7	70	1012.1	32	5
91061619	12.4	72	1012.4	32	6
91061620	10.4	76	1013.0	32	4
91061621	9.0	85	1013.2	33	2
91061622	7.6	93	1013.5	30	2
91061623	7.4	95	1013.6	28	2
91061624	5.6	96	1013.8	0	1

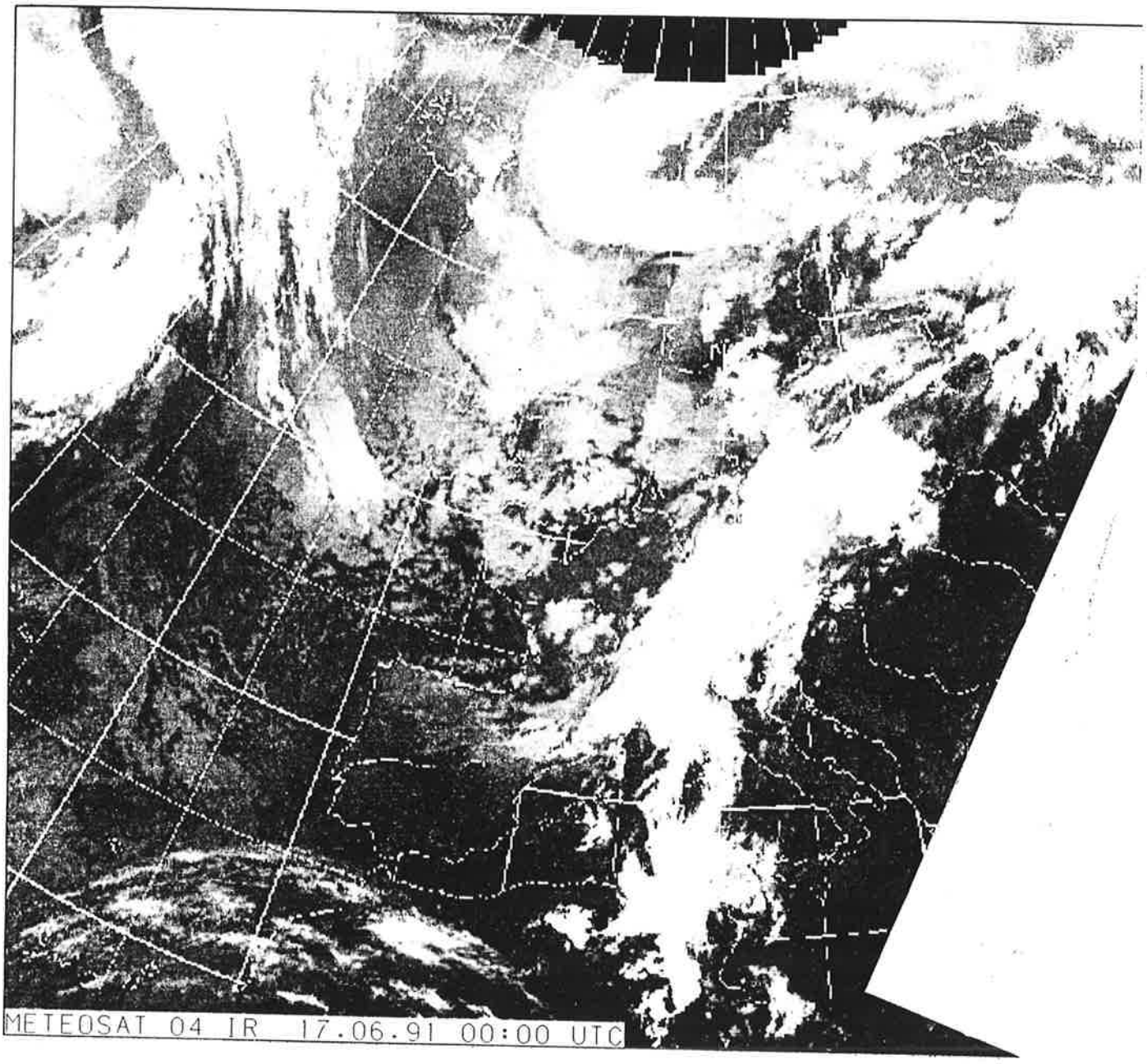

Weather Situation

The trough at upper levels which was over the atlantic ocean on Sunday morning moved easterly and strengthened the trough over the Bene-Lux-Contries which caused the formation of a strong trough ranging from the southern part of the North Sea to the south of France. The satellite picture shows the cloudband which was formed in front of this trough.

MAANDAG 17 JUNI 1991 1200 UTC.

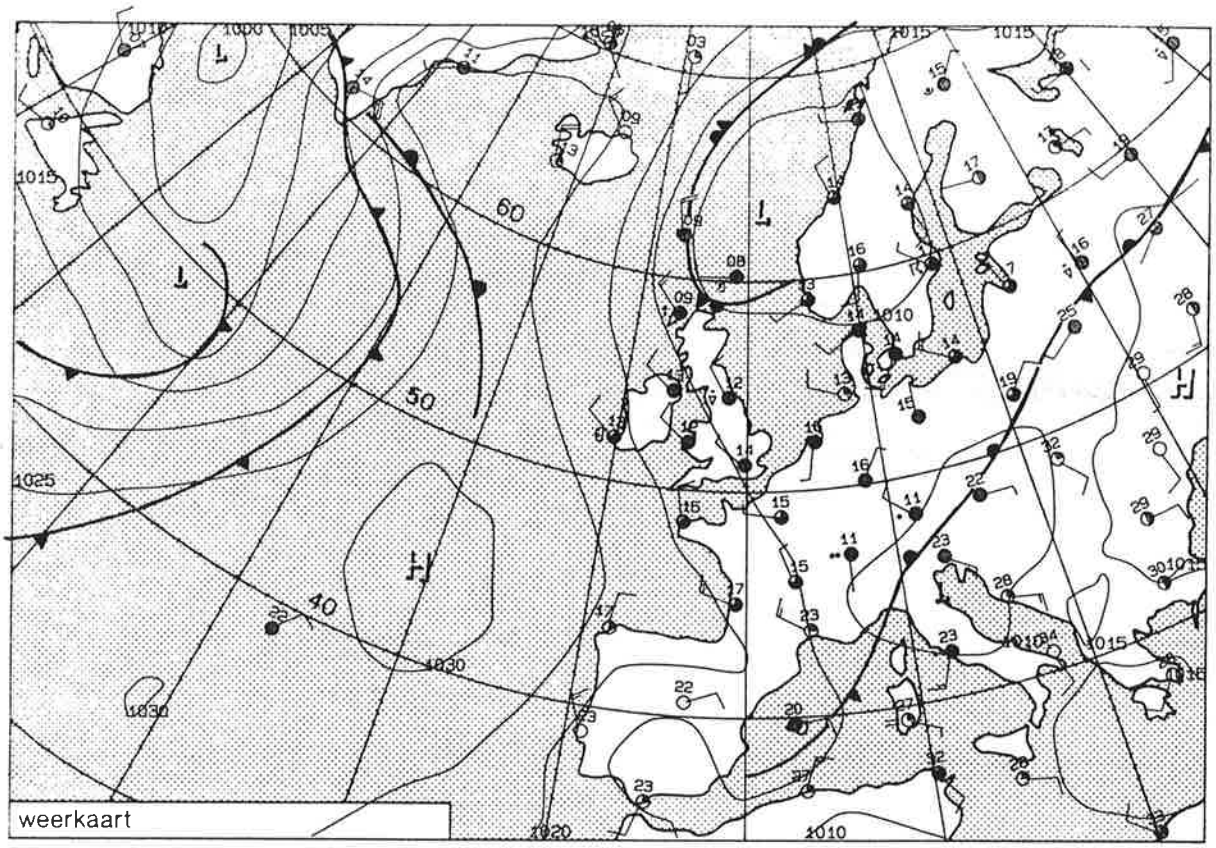

DOW 5

GEMIDDELDEN, SOMMEN EN EXTREMEN (ETMAAL 0 - 24 UUR)

17 JUNI 1991

	WINDSNELHEID UUR GEM HALVE	WINDSNELHEID MAX VLAAG M/SEC.	TEMPERATUUR 10 CM GRADEN	TEMPERATUUR 150 CM CELSIUS	VOCHTIGHEID * DAMP DRUK MBAR	VOCHTIGHEID * RELA TIEF PROC	NEERSLAG HOEVEELHEID MM	NEERSLAG DUUR UREN	LUCHTDRUK * ZEENIVEAU MBAR	BE * WOL KING 1/8
260 DE BILT										
GEM.	2	-	-	11,3	10,4	79	-	-	1014,3	5
SOM	-	-	-	-	-	-	6,2	0,8	-	-
MAX.	5	16	-	16,7	13,0	100	6,2	-	1015,0	7
MIN.	0	-	0,6	3,5	8,2	54	-	-	1013,5	1

yymmddhh	temp	rh	press	wd	wv
91061701	4.9	100	1014.0	99	1
91061702	4.3	99	1014.2	11	1
91061703	4.3	99	1014.4	0	1
91061704	4.2	100	1014.5	16	0
91061705	6.0	100	1014.7	16	1
91061706	10.1	92	1014.8	18	1
91061707	12.0	70	1014.7	24	3
91061708	12.9	65	1014.7	23	4
91061709	13.4	64	1015.0	20	4
91061710	14.2	61	1015.1	22	4
91061711	15.6	56	1015.0	17	4
91061712	15.9	57	1014.7	19	5

yymmddhh	temp	rh	press	wd	wv
91061713	16.0	54	1014.6	20	3
91061714	15.9	54	1014.3	29	3
91061715	13.4	80	1014.2	29	4
91061716	15.0	76	1014.0	36	2
91061717	14.7	73	1014.2	32	2
91061718	15.2	66	1014.4	3	2
91061719	14.1	70	1014.2	8	3
91061720	11.6	86	1014.5	0	1
91061721	10.4	92	1014.3	0	1
91061722	9.1	97	1014.4	0	1
91061723	8.5	96	1014.1	0	0
91061724	9.0	96	1013.6	0	0

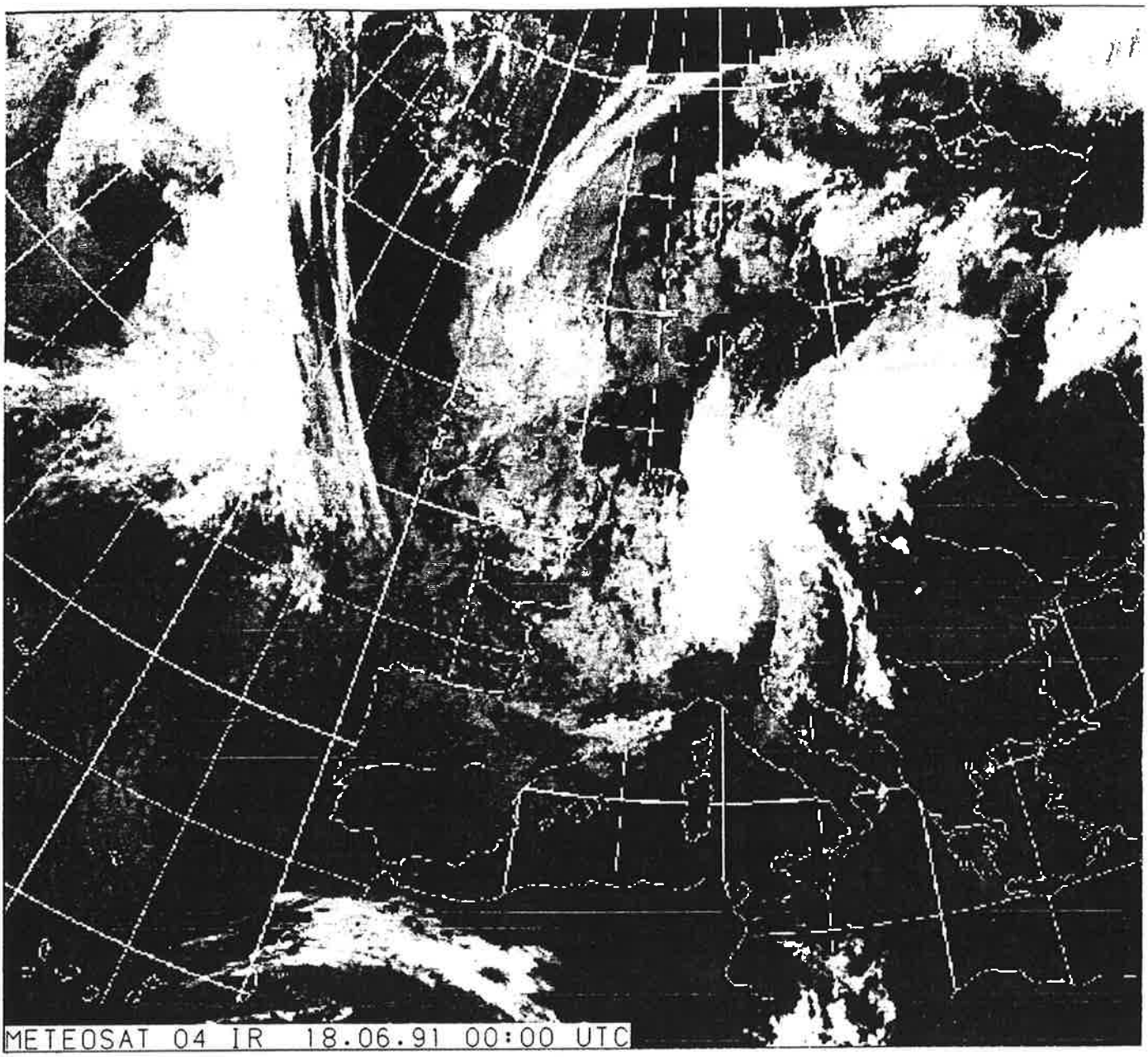

Weather Situation

Monday was characterised by a decrease of temperature from southern to northern Europe caused by a long wave trough over the western part of Europe. On its back, cold air from the pole moved in causing temperatures of 14 to 17 °C in the area from Great Britain to the southern part of France. During the evening hours, showers and thunderstorms occurred in the western part of Germany.

DINSDAG 18 JUNI 1991 1200 UTC.

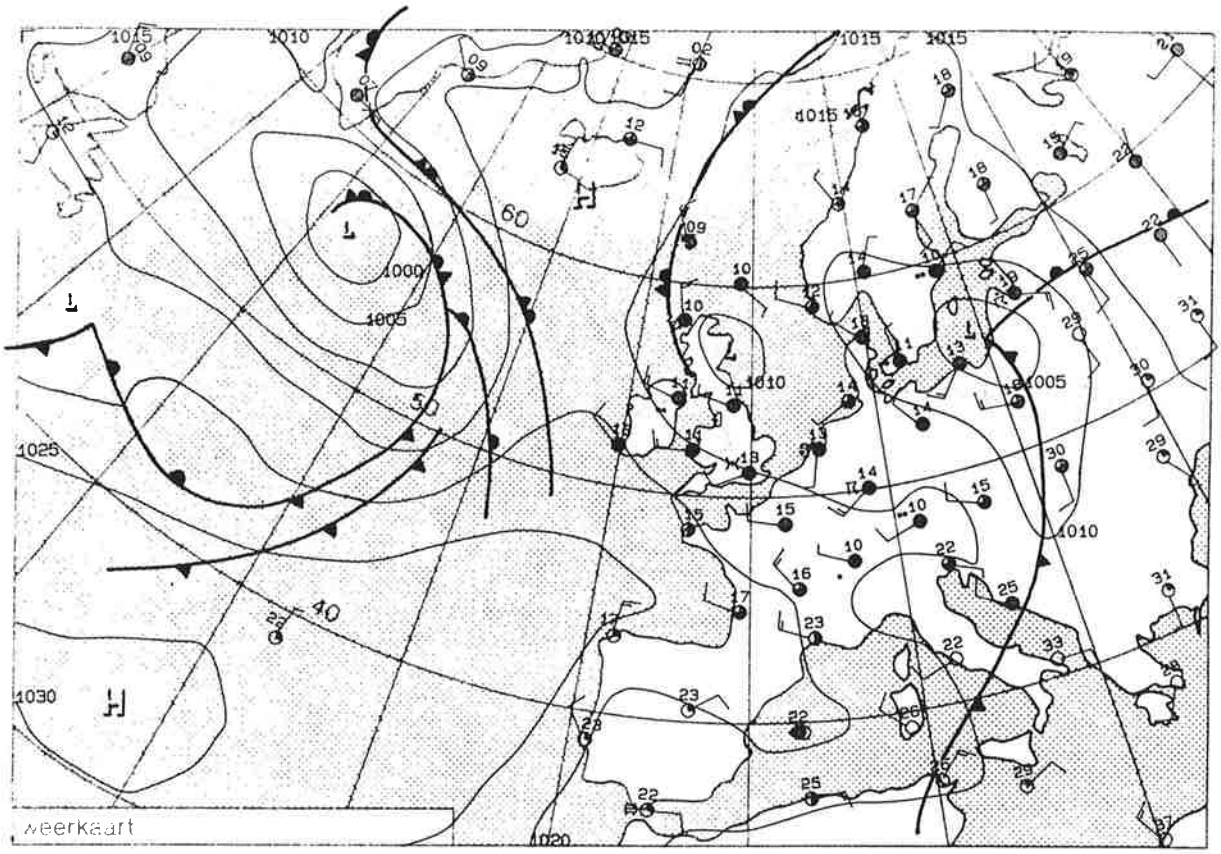

DOW 5 GEMIDDELDEN, SOMMEN EN EXTREMEN (ETMAAL 0 - 24 UUR)

18 JUNI 1991

	WINDSNELHEID UUR GEM HALVE	MAX VLAAG M/SEC.	TEMPERATUUR 10 CM GRADEN	150 CM CELSIUS	* VOCHTIGHEID DAMP DRUK MBAR	* RELA TIEF PROC	NEERSLAG HOEVEELHEID MM	DUUR UREN	* LUCHTDRUK ZEENIVEAU MBAR	* BE WOL KING 1/8
260 DE BILT										
GEM.	4	-	-	11,8	11,2	82	-	-	1013,1	7
SOM	-	-	-	-	-	-	6,3	3,3	-	-
MAX.	8	18	-	15,4	13,3	99	2,3	-	1013,6	8
MIN.	0	-	8,1	8,9	9,3	59	-	-	1012,0	3

yymmddhh	temp	rh	press	wd	wv
91061801	9.1	99	1013.5	0	0
91061802	9.8	96	1013.3	27	1
91061803	10.3	94	1013.3	30	2
91061804	10.3	95	1013.1	99	2
91061805	10.5	92	1013.4	26	2
91061806	10.3	94	1013.3	9	1
91061807	10.9	92	1013.5	17	4
91061808	10.0	89	1013.7	24	4
91061809	11.9	88	1013.2	19	3
91061810	13.0	82	1013.3	22	5
91061811	10.5	88	1013.4	21	6
91061812	13.2	74	1013.2	19	4

yymmddhh	temp	rh	press	wd	wv
91061813	13.1	88	1013.2	22	6
91061814	13.8	77	1013.1	26	4
91061815	15.1	69	1013.1	29	7
91061816	14.2	62	1013.1	26	8
91061817	14.0	59	1012.9	27	8
91061818	13.2	66	1013.1	26	8
91061819	12.8	63	1013.2	26	6
91061820	12.1	73	1013.1	23	4
91061821	11.9	76	1013.2	24	4
91061822	11.6	76	1012.9	23	6
91061823	11.1	81	1012.6	21	6
91061824	10.2	88	1012.1	22	6

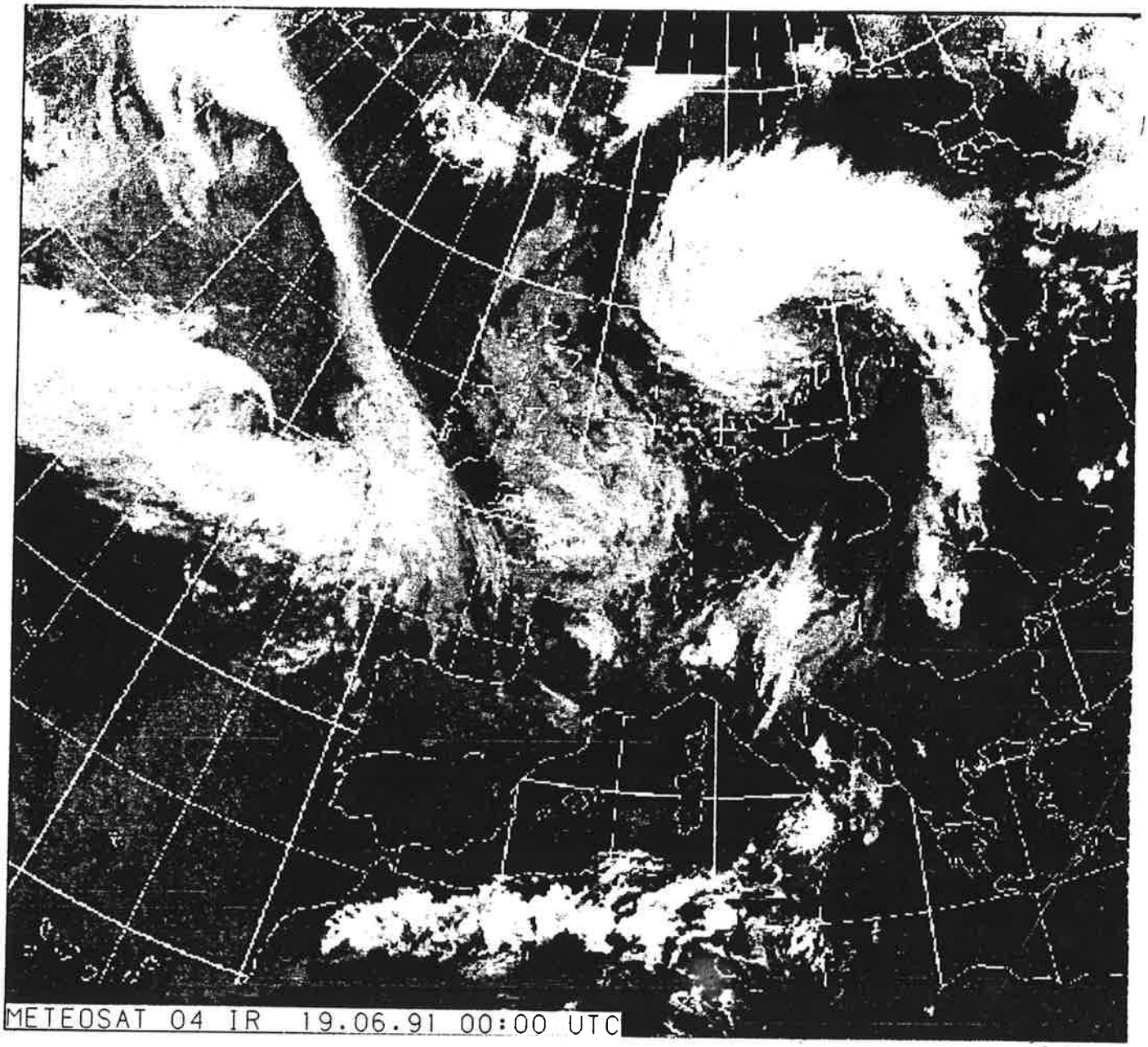

Weather Situation

The low pressure area which was over the southern part of Poland on Tuesday moved northerly and up to Stockholm during the day. During the afternoon hours, clouds increased especially over the western part of Germany causing showers and thunderstorms. The satellite picture shows a cloudless sky over most of Germany and Poland with a new cloud area approaching from the west.

WOENSDAG 19 JUNI 1991 1200 UTC.

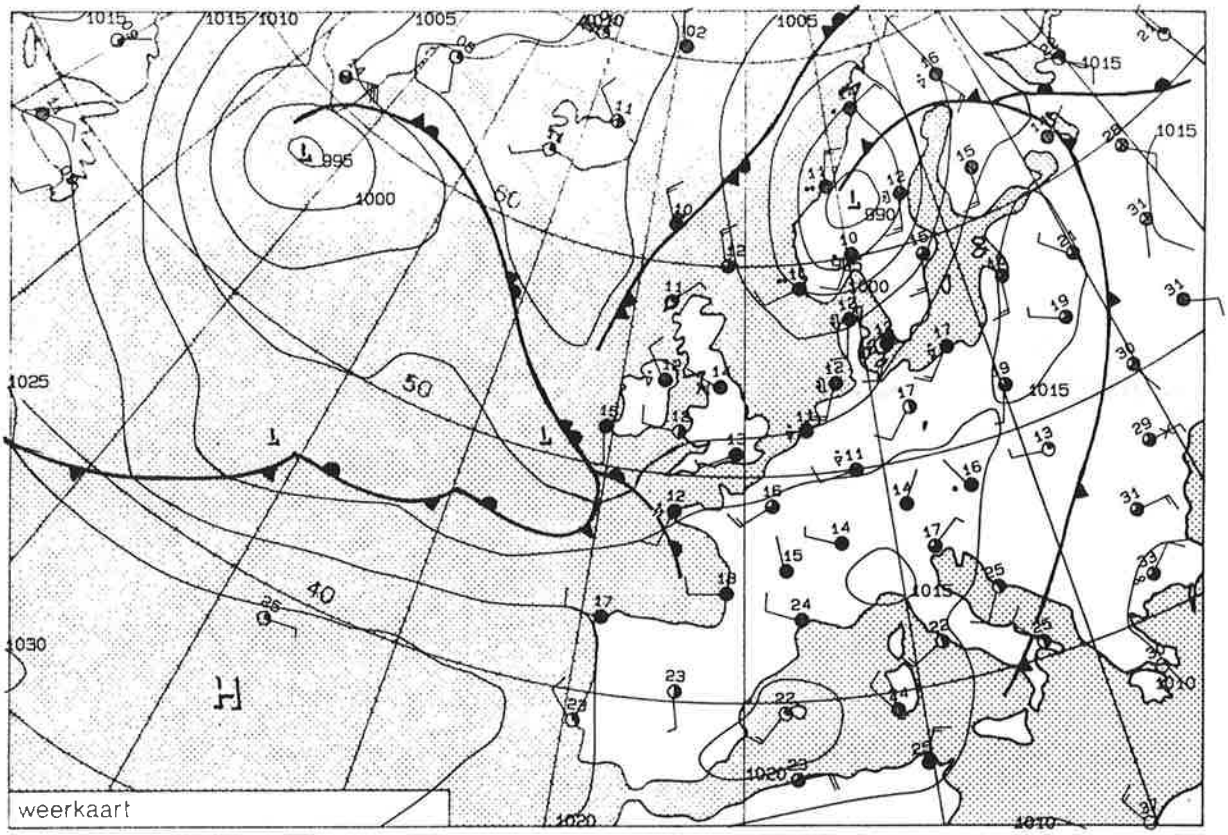

DOW 5 GEMIDDELDEN, SOMMEN EN EXTREMEN (ETMAAL 0 - 24 UUR)

19 JUNI 1991

	WINDSNELHEID UUR GEM HALVE	WINDSNELHEID MAX VLAAG M/SEC.	TEMPERATUUR 10 CM GRADEN	TEMPERATUUR 150 CM CELSIUS	VOCHTIGHEID * DAMP DRUK MBAR	VOCHTIGHEID * RELA TIEF PROC	NEERSLAG HOEVEELHEID MM	NEERSLAG DUUR UREN	LUCHTDRUK * ZEENIVEAU MBAR	BE WOL KING 1/8
260 DE BILT										
GEM.	7	-	-	11,0	11,6	88	-	-	1010,2	8
SOM	-	-	-	-	-	-	7,9	9,0	-	-
MAX.	11	26	-	13,0	13,0	93	4,5	-	1011,5	8
MIN.	4	-	9,8	9,8	10,8	81	-	-	1009,6	6

yymmddhh	temp	rh	press	wd	wv
91061901	10.0	90	1011.6	21	6
91061902	10.3	92	1011.3	22	6
91061903	10.2	92	1010.7	21	5
91061904	9.9	93	1010.4	21	7
91061905	9.9	92	1010.2	21	8
91061906	9.8	90	1010.1	21	8
91061907	10.3	89	1010.1	22	8
91061908	10.3	89	1010.2	22	9
91061909	10.1	90	1010.1	22	9
91061910	11.3	85	1010.1	23	9
91061911	11.7	84	1010.2	22	11
91061912	11.4	87	1010.3	22	9

yymmddhh	temp	rh	press	wd	wv
91061913	11.2	89	1010.3	24	6
91061914	12.6	85	1010.3	24	8
91061915	11.3	90	1010.2	23	7
91061916	12.3	89	1010.1	22	7
91061917	11.7	85	1010.1	23	8
91061918	12.5	90	1010.4	22	7
91061919	12.1	86	1010.5	23	5
91061920	11.8	81	1010.5	23	6
91061921	11.2	81	1010.6	20	5
91061922	11.0	86	1010.2	19	4
91061923	11.0	86	1010.0	19	4
91061924	10.4	90	1009.7	20	4

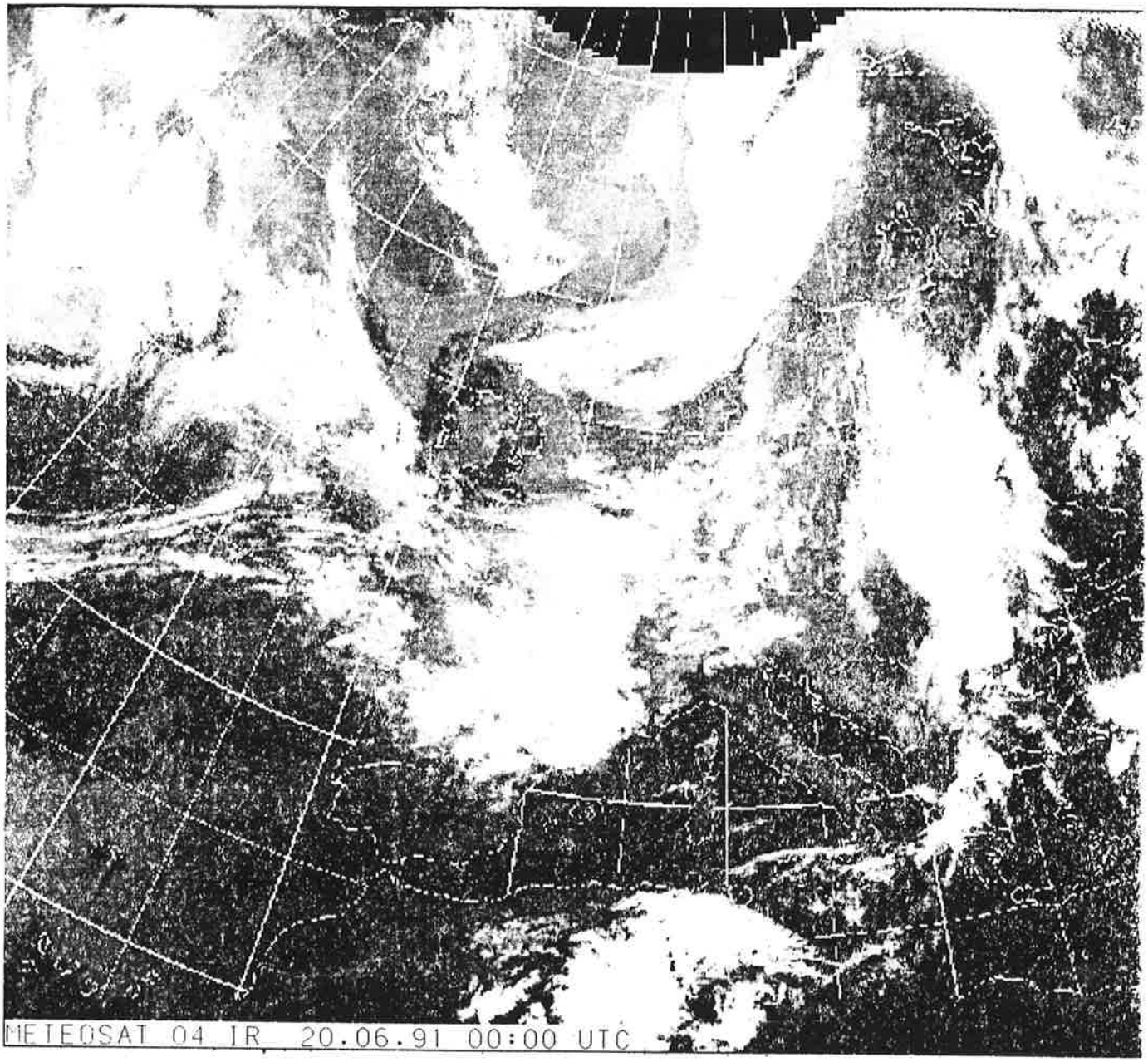

Weather Situation

The satellite picture shows a compact cloud area over the Channel, France and the north of Spain. It belongs to a frontal wave (which moved from the eastern part of the atlantic ocean to the Channel. The accompanying frontal system caused rainfalls in southern England, western France and the coast of northern Spain. In Germany, it was rather cold on Wednesday with temperatures at 12 to 20 °C . Showers and longer lasting rainfalls occurred over the coast of the North Sea.

DONDERDAG 20 JUNI 1991 1200 UTC.

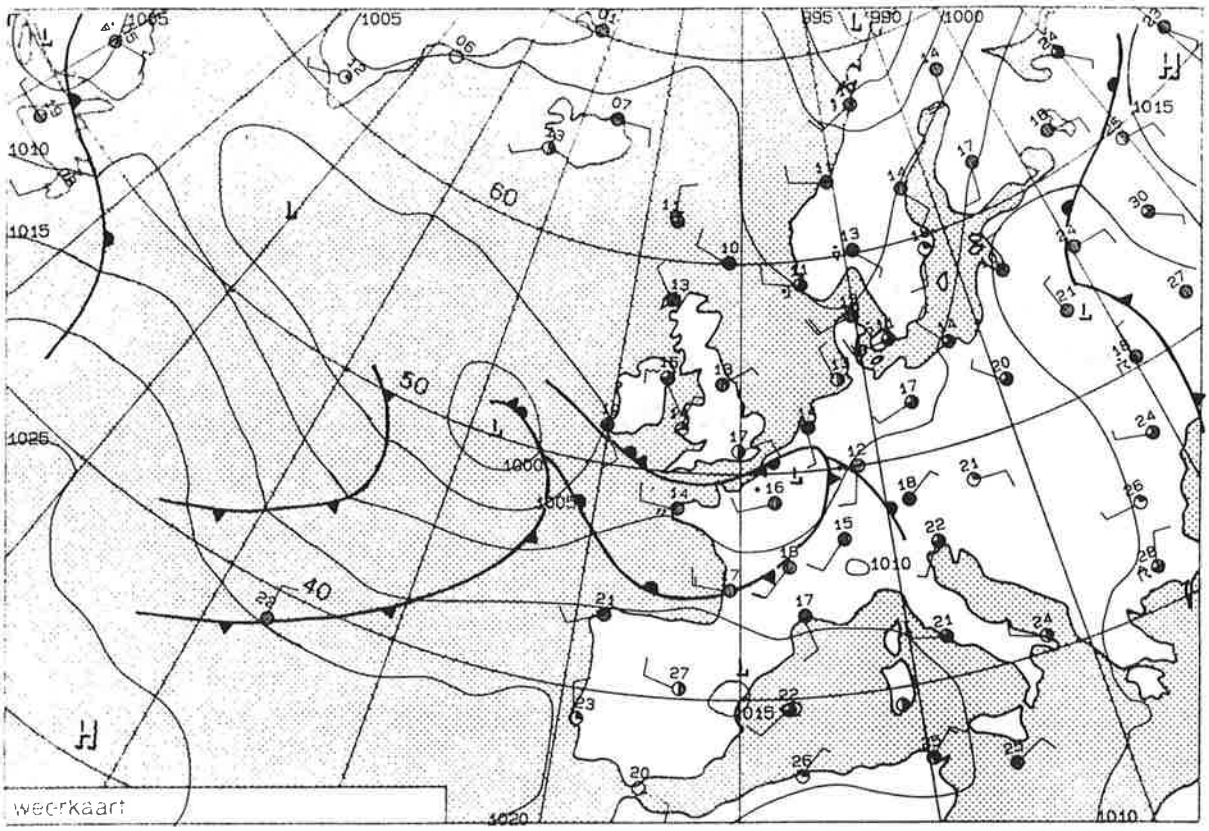

DOW 5 GEMIDDELDEN, SOMMEN EN EXTREMEN (ETMAAL 0 - 24 UUR)

20 JUNI 1991

	WINDSNELHEID UUR GEM HALVE	MAX VLAAG M/SEC.	TEMPERATUUR 10 CM GRADEN	150 CM CELSIUS	* VOCHTIGHEID DAMP DRUK MBAR	* RELA TIEF PROC	NEERSLAG HOEVEELHEID MM	DUUR UREN	* LUCHTDRUK ZEENIVEAU MBAR	* BE WOL KING 1/8
260 DE BILT										
GEM.	3	-	-	12,0	11,7	84	-	-	1008,5	6
SOM	-	-	-	-	-	-	0,0	.	-	-
MAX.	5	9	-	15,8	12,8	100	0,0	-	1011,1	8
MIN.	1	-	5,0	7,8	10,6	66	-	-	1007,3	0

yymmddhh	temp	rh	press	wd	wv
91062001	10.3	93	1009.5	22	3
91062002	9.2	97	1009.2	17	2
91062003	9.3	97	1008.9	19	3
91062004	8.8	97	1008.7	17	3
91062005	9.1	99	1008.3	18	3
91062006	9.8	97	1008.1	15	3
91062007	11.1	90	1007.9	15	3
91062008	12.1	82	1007.7	16	4
91062009	13.5	74	1007.5	17	4
91062010	13.7	74	1007.6	14	4
91062011	13.9	74	1007.5	15	5
91062012	13.7	74	1007.4	17	4

yymmddhh	temp	rh	press	wd	wv
91062013	13.9	77	1007.4	16	3
91062014	14.4	69	1007.5	14	3
91062015	14.8	72	1007.5	16	3
91062016	15.7	69	1007.6	15	4
91062017	15.2	66	1007.8	28	2
91062018	14.7	72	1008.5	19	2
91062019	14.4	75	1008.8	12	1
91062020	12.4	89	1009.4	34	2
91062021	11.4	93	1010.1	33	2
91062022	9.9	96	1010.5	0	1
91062023	8.7	99	1011.0	0	1
91062024	7.8	100	1011.2	0	1

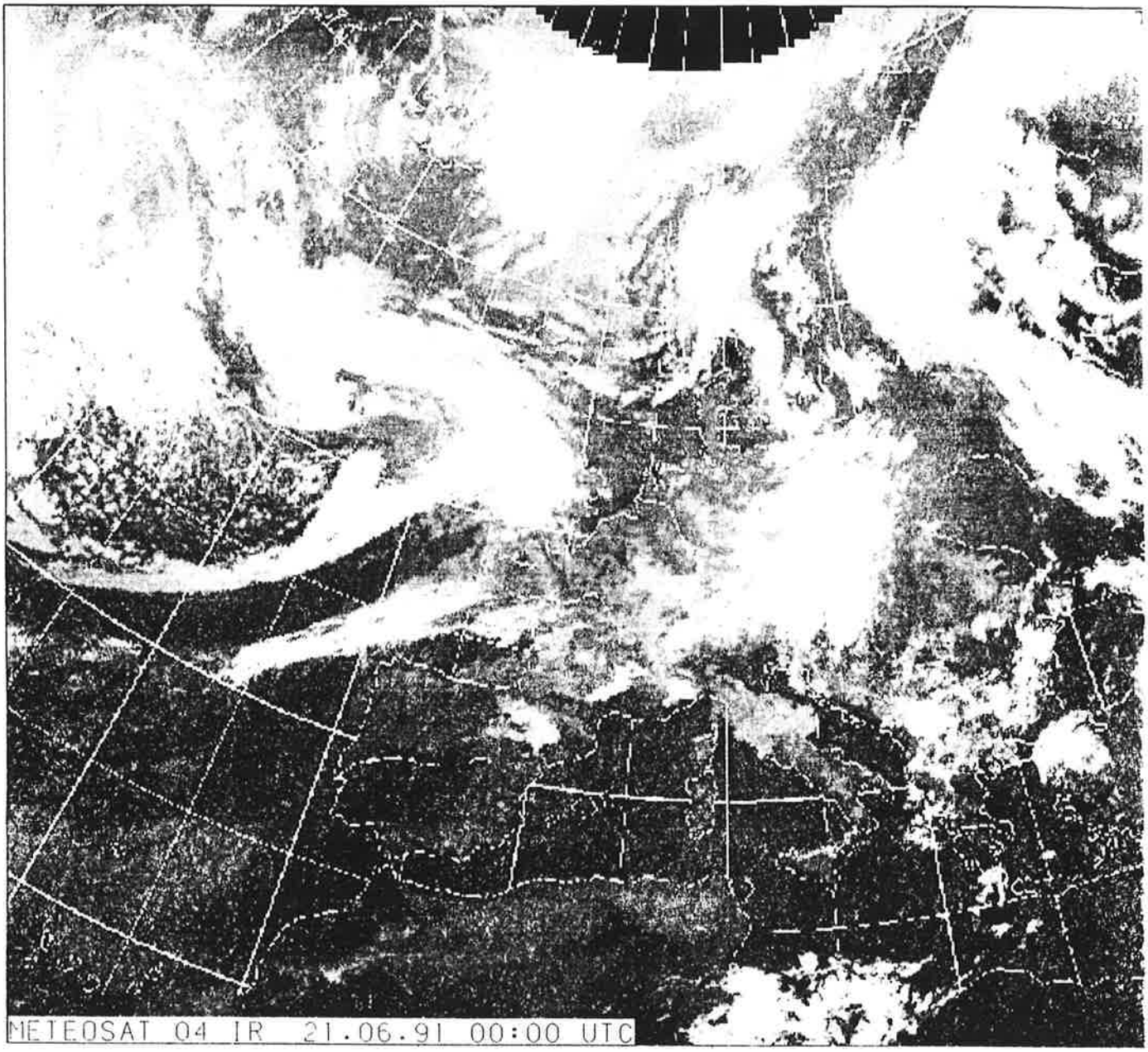

Weather Situation

On the south-eastern side of a low pressure area with its centre over the Channel, humid air coming from the atlantic ocean moved to the north-west on Thursday, ascending over the cold air from the atlantic ocean, which had moved in a few days ago. This caused the formation of a cloud and rainfall area which spread over western and middle Europe.

The satellite picture shows the rain area, dissolution of clouds over western Europe and a new cloud line over the British Isles. It belongs to the frontal system of a low pressure area north-west of Ireland.

VRIJDAG 21 JUNI 1991 1200 UTC.

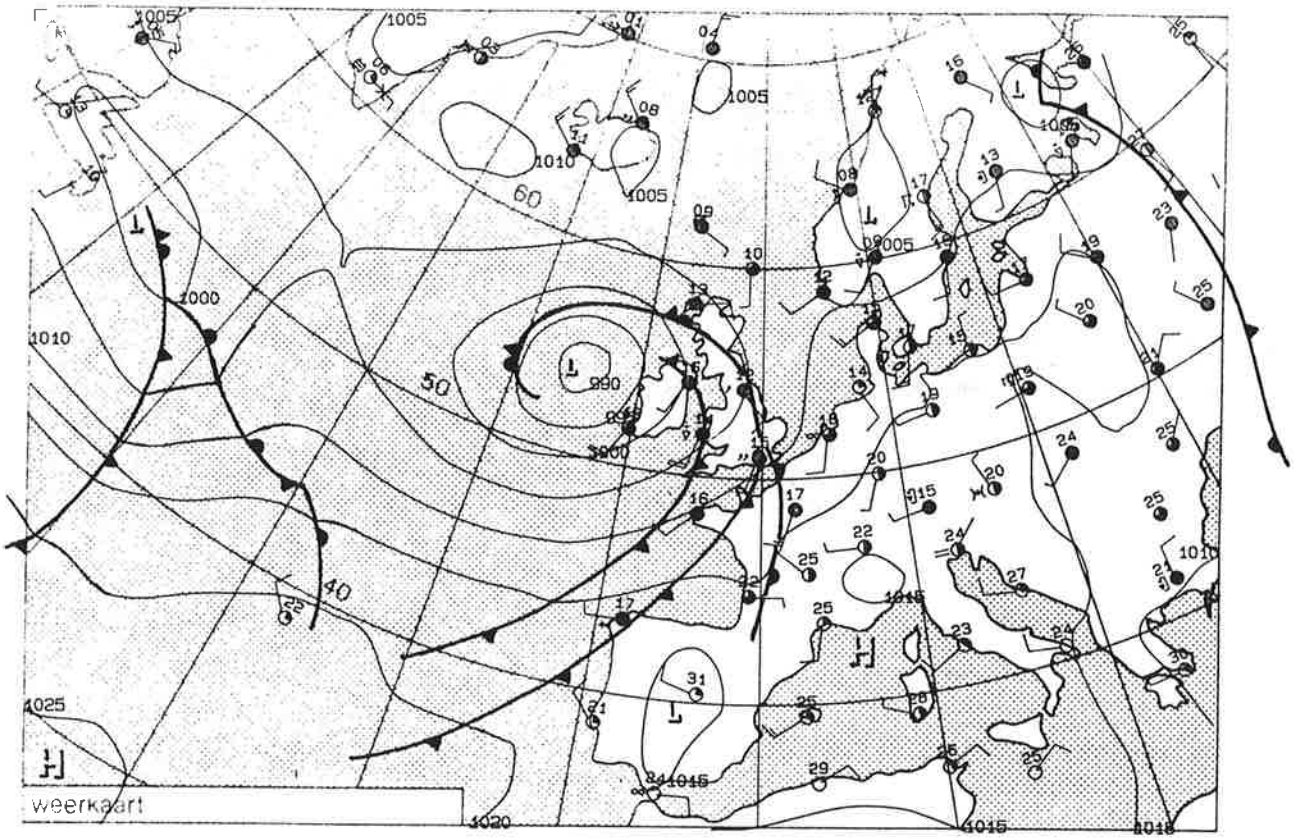

DOW 5 GEMIDDELDEN, SOMMEN EN EXTREMEN (ETMAAL 0 - 24 UUR)

21 JUNI 1991

	WINDSNELHEID UUR GEM HALVE	WINDSNELHEID MAX VLAAG M/SEC.	TEMPERATUUR 10 CM GRADEN	TEMPERATUUR 150 CM CELSIUS	* VOCHTIGHEID DAMP DRUK MBAR	* VOCHTIGHEID RELA TIEF PROC	NEERSLAG HOEVEELHEID MM	NEERSLAG DUUR UREN	* LUCHTDRUK ZEENIVEAU MBAR	* BE WOL KING 1/8
260 DE BILT										
GEM.	5	-	-	14,3	13,9	86	-	-	1011,9	5
SOM	-	-	-	-	-	-	13,6	5,7	-	-
MAX.	9	20	-	20,5	17,7	100	4,1	-	1013,2	8
MIN.	0	-	3,7	5,9	9,5	56	-	-	1010,8	0

yymmddhh	temp	rh	press	wd	wv
91062101	6.9	100	1011.4	0	0
91062102	6.5	100	1011.6	99	1
91062103	6.6	100	1011.8	11	1
91062104	6.2	100	1012.1	11	1
91062105	6.9	100	1012.6	14	1
91062106	9.0	100	1012.9	18	2
91062107	11.2	100	1013.1	16	3
91062108	12.7	98	1013.3	18	4
91062109	16.0	72	1013.3	19	5
91062110	16.6	65	1013.0	17	7
91062111	17.5	63	1012.7	18	8
91062112	18.4	62	1012.4	19	8

yymmddhh	temp	rh	press	wd	wv
91062113	19.4	59	1012.3	18	9
91062114	19.7	56	1011.9	19	8
91062115	19.6	64	1011.7	20	8
91062116	18.6	71	1011.4	19	7
91062117	17.2	87	1011.7	19	5
91062118	16.5	92	1011.5	20	7
91062119	16.0	96	1011.4	20	6
91062120	16.1	96	1011.0	19	7
91062121	16.4	94	1011.3	21	7
91062122	16.2	92	1011.2	19	6
91062123	16.2	96	1011.0	19	6
91062124	16.4	94	1010.9	21	7

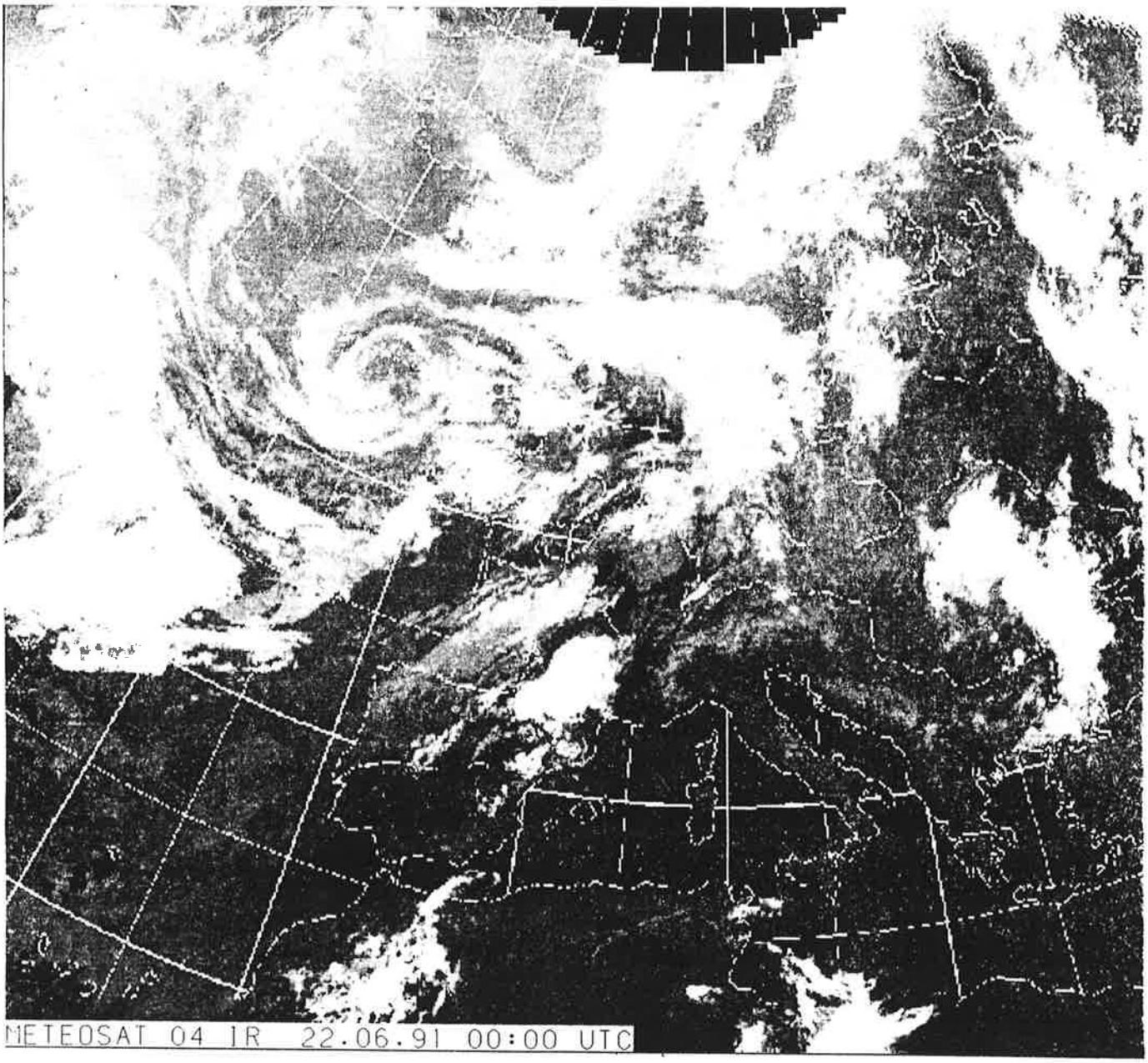

Weather Situation

The influence of an intermediate anticyclone belonging to a low pressure area north-west of Ireland caused an amelioration of the weather in Germany. During Friday night, the skies over north-western Germany cleared up and the humid and warm air caused the development of fog in the early morning. After its dissolution, the skies over the whole of Germany were overcast, partly clear. The temperatures rised to 20 °C. .The approaching frontal system of the low pressure area caused increasing clouds in noth-western Germany where rainfalls occurred in the evening.

ZATERDAG 22 JUNI 1991 1200 UTC

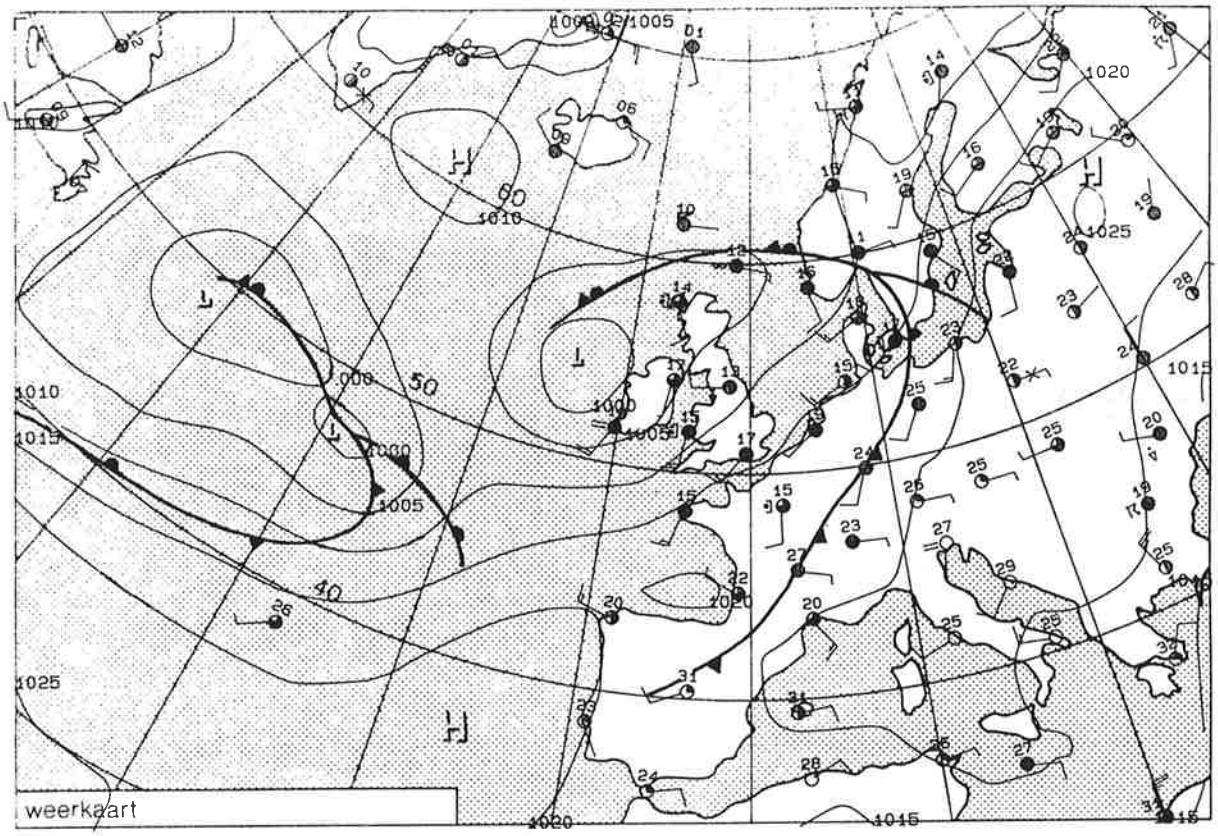

DOW 5 GEMIDDELDEN, SOMMEN EN EXTREMEN (ETMAAL 0 - 24 UUR)

22 JUNI 1991

	WINDSNELHEID UUR GEM HALVE	WINDSNELHEID MAX VLAAG M/SEC.	TEMPERATUUR 10 CM GRADEN	TEMPERATUUR 150 CM CELSIUS	VOCHTIGHEID * DAMP DRUK MBAR	VOCHTIGHEID * RELA TIEF PROC	NEERSLAG HOEVEELHEID MM	NEERSLAG DUUR UREN	LUCHTDRUK * ZEENIVEAU MBAR	BE WOL KING 1/8
260 DE BILT										
GEM.	6	-	-	15,7	13,5	77	-	-	1015,8	5
SOM	-	-	-	-	-	-	0,0	.	-	-
MAX.	11	21	-	20,5	16,8	97	0,0	-	1018,8	7
MIN.	1	-	7,9	10,9	12,4	61	-	-	1011,5	1

yymmddhh	temp	rh	press	wd	wv
91062201	15.7	94	1011.6	25	6
91062202	14.5	87	1012.4	24	6
91062203	12.8	90	1012.7	23	7
91062204	13.0	89	1013.0	22	6
91062205	13.3	85	1013.6	23	7
91062206	14.0	83	1014.2	23	8
91062207	14.7	78	1015.0	24	10
91062208	15.6	77	1015.7	24	9
91062209	16.6	69	1015.6	24	11
91062210	17.1	68	1016.0	24	11
91062211	18.2	66	1016.3	24	9
91062212	19.1	63	1016.4	23	9

yymmddhh	temp	rh	press	wd	wv
91062213	18.8	63	1016.4	21	7
91062214	19.3	66	1016.4	23	7
91062215	18.7	64	1016.6	26	5
91062216	19.0	62	1016.8	25	5
91062217	19.0	61	1017.0	26	6
91062218	17.6	65	1017.1	28	6
91062219	16.8	65	1017.4	27	4
91062220	16.0	68	1017.8	26	3
91062221	12.8	90	1018.3	17	2
91062222	11.4	95	1018.6	10	1
91062223	10.9	97	1018.9	14	1
91062224	12.0	91	1018.7	16	3

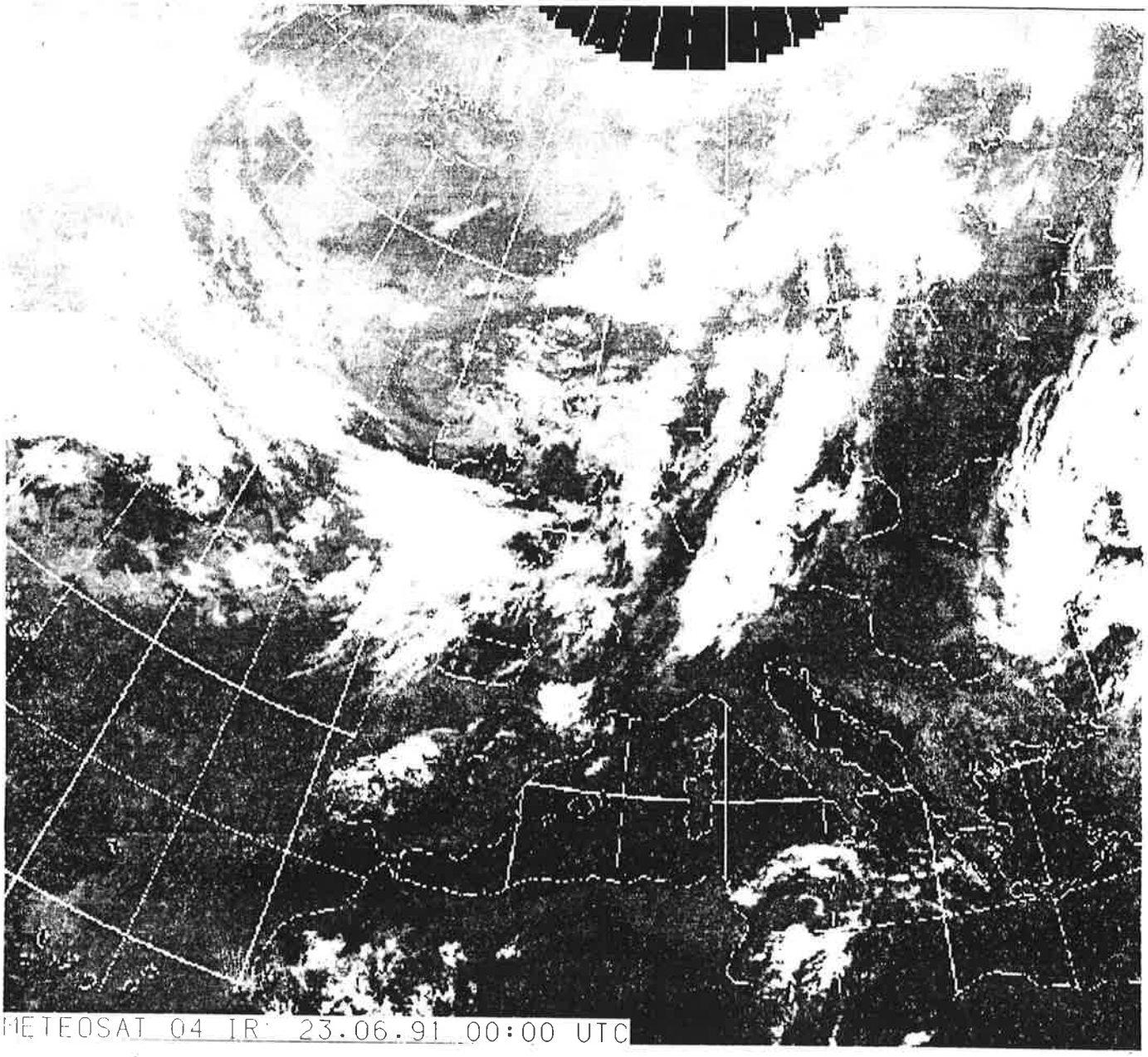

Weather Situation

The cold front of the low pressure system western of Ireland crossed nearly the whole of Germany on Sunday. The humid and warm mediterranian air which had moved in earlier was replaced by cooler and more dry air coming from the atlantic ocean. On the back of the frontal system, temperatures didn' t rise to more than 20 °C and to 10 to 13 °C during the night.

The satellite picture shows a compact cloud line over eastern and southern Germany where thunderstorms occurred during Sunday night.

ZONDAG 23 JUNI 1991 1200 UTC.

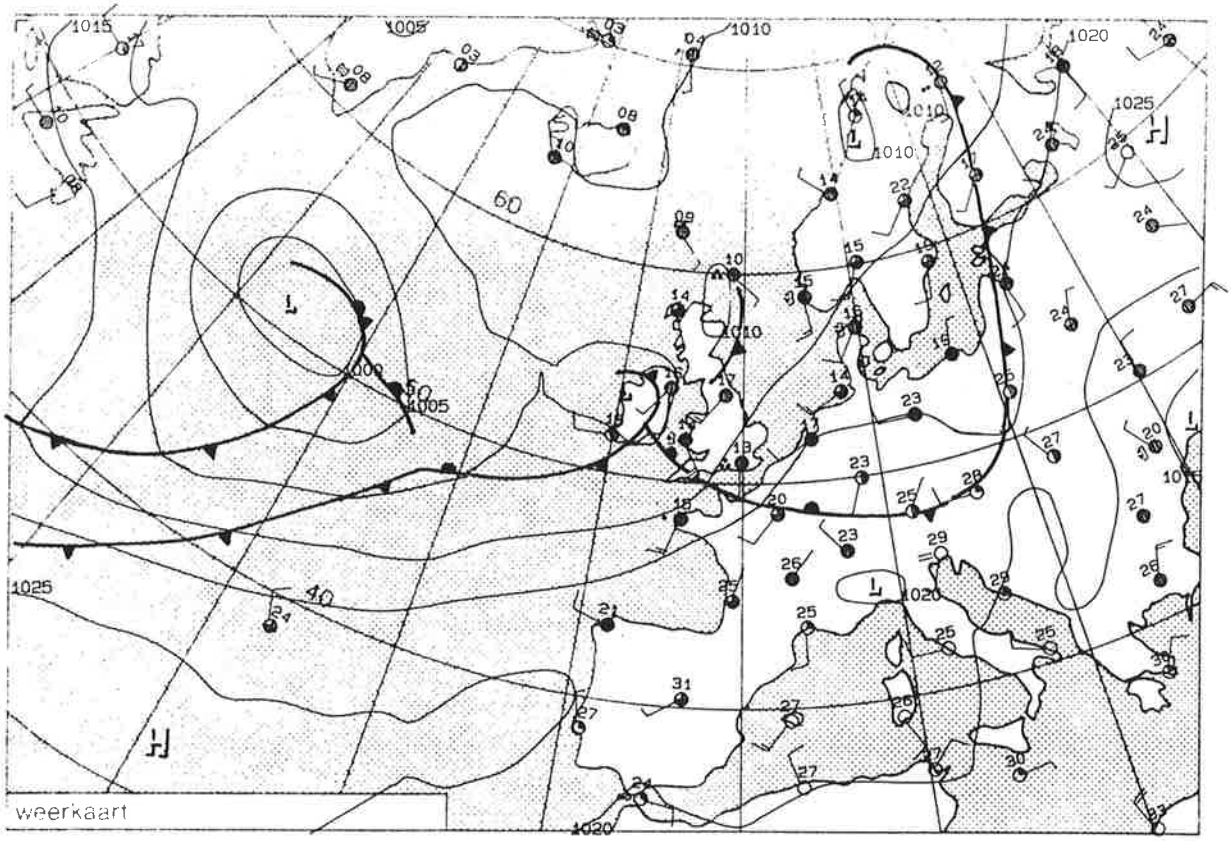

DOW 5

GEMIDDELDEN, SOMMEN EN EXTREMEN (ETMAAL 0 - 24 UUR)

23 JUNI 1991

	WINDSNELHEID UUR GEM HALVE	MAX VLAAG M/SEC.	TEMPERATUUR 10 CM GRADEN	150 CM CELSIUS	* VOCHTIGHEID DAMP DRUK MBAR	* RELA TIEF PROC	NEERSLAG HOEVEELHEID MM	DUUR UREN	* LUCHTDRUK ZEENIVEAU MBAR	* BE WOL KING 1/8
260 DE BILT										
GEM.	7	-	-	15,2	13,6	80	-	-	1018,4	7
SOM	-	-	-	-	-	-	28,2	6,6	-	-
MAX.	11	23	-	17,8	16,4	96	13,6	-	1020,7	8
MIN.	1	-	10,7	12,0	11,9	62	-	-	1012,2	4

yymmddhh	temp	rh	press	wd	wv
91062301	12.9	87	1018.1	16	4
91062302	14.2	87	1018.1	17	5
91062303	14.8	86	1018.3	20	6
91062304	14.4	88	1018.6	20	6
91062305	15.0	79	1019.2	24	7
91062306	14.6	81	1019.7	24	11
91062307	14.9	79	1020.1	23	9
91062308	15.6	73	1020.4	24	10
91062309	16.2	73	1020.4	24	10
91062310	16.5	69	1020.6	23	9
91062311	16.9	67	1020.8	23	10
91062312	16.7	63	1020.7	24	9

yymmddhh	temp	rh	press	wd	wv
91062313	17.0	63	1020.8	25	10
91062314	16.9	62	1020.4	25	7
91062315	16.8	65	1020.0	25	6
91062316	15.7	79	1019.7	24	6
91062317	15.4	73	1018.9	23	4
91062318	14.6	84	1018.4	11	1
91062319	14.4	90	1017.8	7	1
91062320	13.8	91	1017.1	13	4
91062321	13.6	94	1015.9	12	5
91062322	13.3	94	1014.1	11	7
91062323	14.3	92	1013.7	18	7
91062324	15.0	96	1012.3	21	5

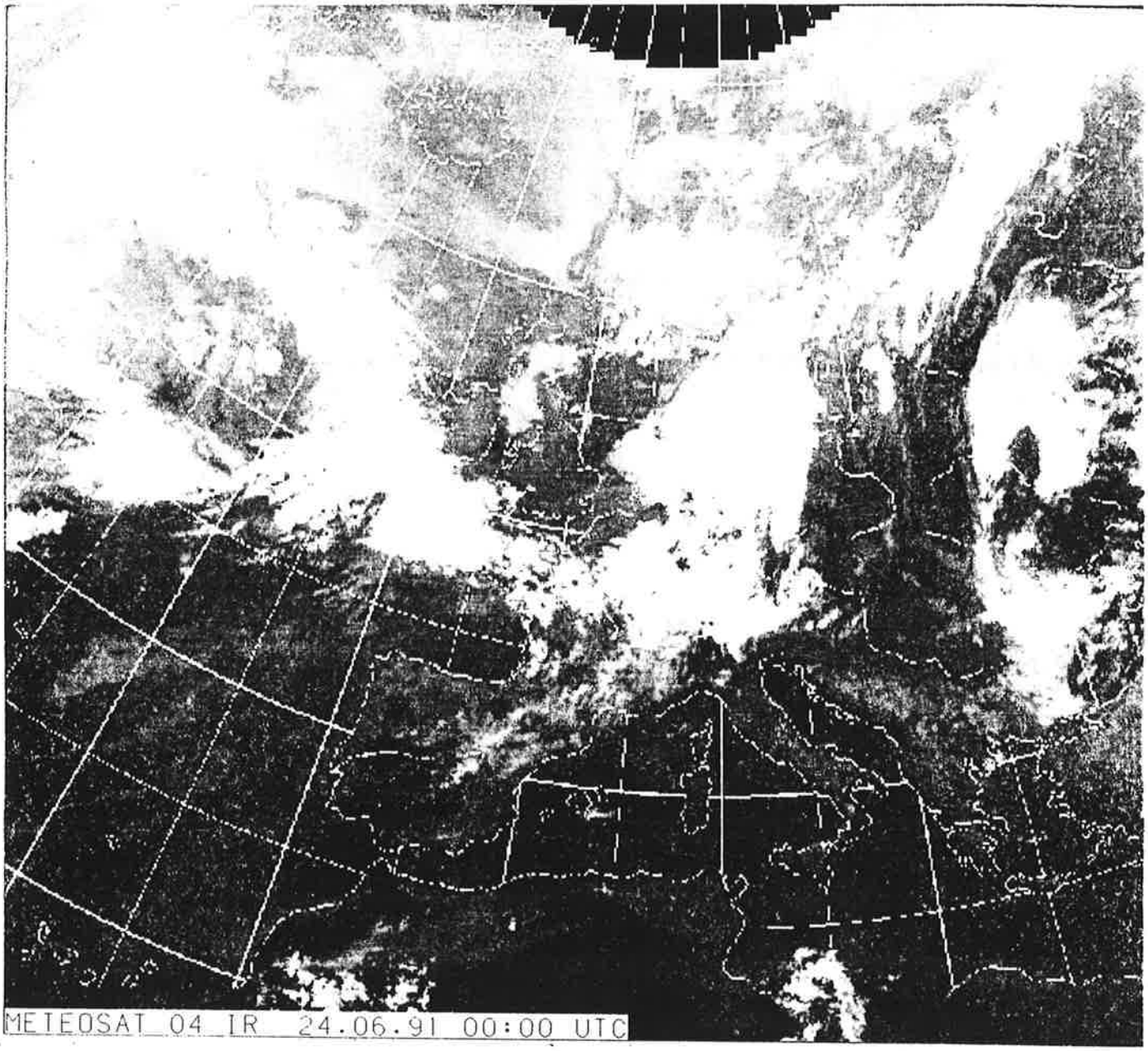

Weather Situation

On Sunday, the weather in large parts of Europe was determined by a high pressure area longing from the Azores over southern and middle Europe to the Ural. In the area of this high pressure zone it was sunny and warm. On its nothern side, the formation of a cyclone began towards noon.

The satellite picture shows the lifting area of the cyclone mentioned above over southern Scandinavia, northern Germany and the Netherlands. Another cloud area over middle Europe shows a lifting area in front of the high level trough line which arrived over western Europe.

MAANDAG 24 JUNI 1991 1200 UTC.

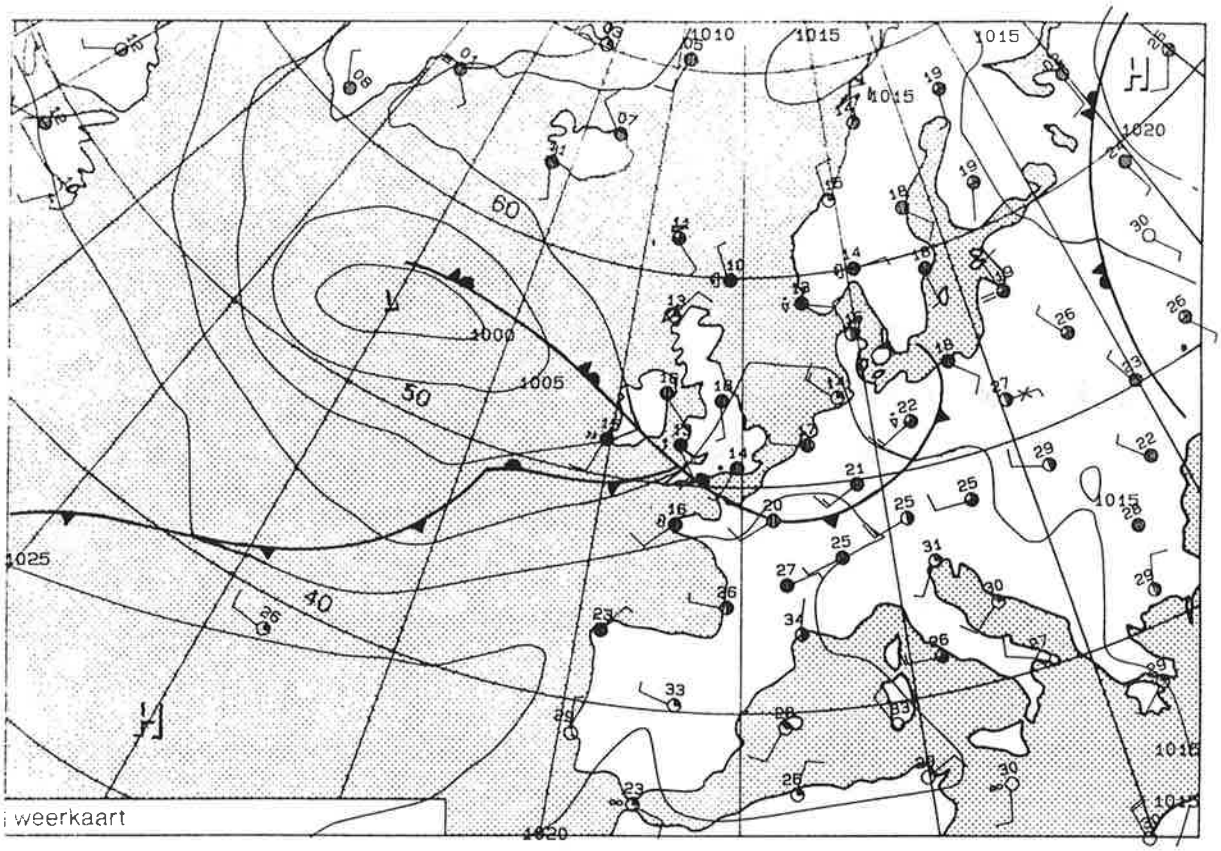

DOW 5

GEMIDDELDEN, SOMMEN EN EXTREMEN (ETMAAL 0 - 24 UUR)

24 JUNI 1991

	WINDSNELHEID UUR GEM HALVE	WINDSNELHEID MAX VLAAG M/SEC.	TEMPERATUUR 10 CM GRADEN	TEMPERATUUR 150 CM CELSIUS	* VOCHTIGHEID DAMP DRUK MBAR	* VOCHTIGHEID RELA TIEF PROC	NEERSLAG HOEVEELHEID MM	NEERSLAG DUUR UREN	* LUCHTDRUK ZEENIVEAU MBAR	* BE WOL KING 1/8
260 DE BILT										
GEM.	5	-	-	15,4	14,7	84	-	-	1016,5	8
SOM	-	-	-	-	-	-	2,5	3,3	-	-
MAX.	12	27	-	18,2	17,1	96	1,6	-	1019,2	8
MIN.	1	-	13,5	13,4	12,7	65	-	-	1011,8	7

yymmddhh	temp	rh	press	wd	wv
91062401	15.8	95	1011.9	23	11
91062402	15.0	96	1012.0	25	12
91062403	14.7	96	1012.2	25	9
91062404	14.4	95	1012.4	26	8
91062405	14.3	94	1013.0	27	7
91062406	13.4	94	1014.0	27	7
91062407	14.6	91	1015.2	32	5
91062408	15.3	85	1016.0	33	6
91062409	15.8	81	1016.7	32	7
91062410	16.5	73	1017.5	33	5
91062411	16.8	74	1018.3	32	5
91062412	16.9	70	1018.5	28	5

yymmddhh	temp	rh	press	wd	wv
91062413	17.1	70	1018.9	27	6
91062414	17.7	65	1019.2	26	6
91062415	16.8	71	1019.3	24	7
91062416	16.3	72	1019.0	25	6
91062417	16.2	69	1018.6	25	3
91062418	15.6	84	1018.5	23	3
91062419	15.0	89	1018.5	20	2
91062420	14.7	90	1018.7	20	1
91062421	14.3	91	1018.2	15	2
91062422	14.2	92	1017.6	8	2
91062423	14.0	94	1017.1	15	2
91062424	14.1	95	1016.6	16	3

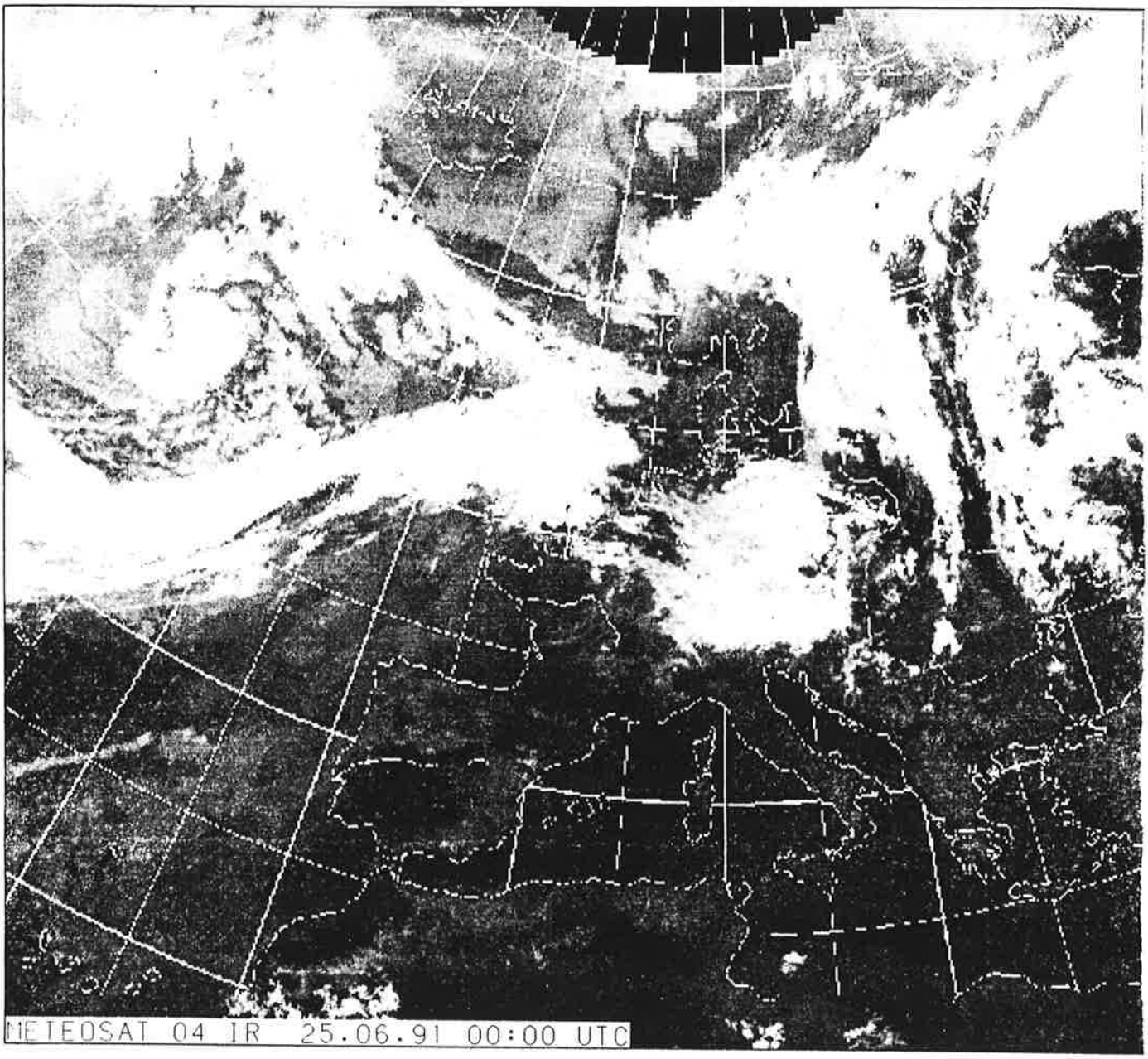

Weather Situation

The cyclone over southern England moved from the south-western North Seaa over north-western Germany to Lithuania. Its cold front crossed most of Germany and reached Poland during Monday. At the same time, an upper level trough moved easterly from the north-western part of middle Europe. With the crossing of the cold front, cold air from the atlantic ocean came to Germany, with the exception of southern Germany. The warm front of a new low pressure system in front of Ireland caused heavy rainfalls over Ireland, southern England and the Bene-Lux-Contries . The satellite picture shows the cloud area of the frontal system mentioned above.

DINSDAG 25 JUNI 1991 1200 UTC.

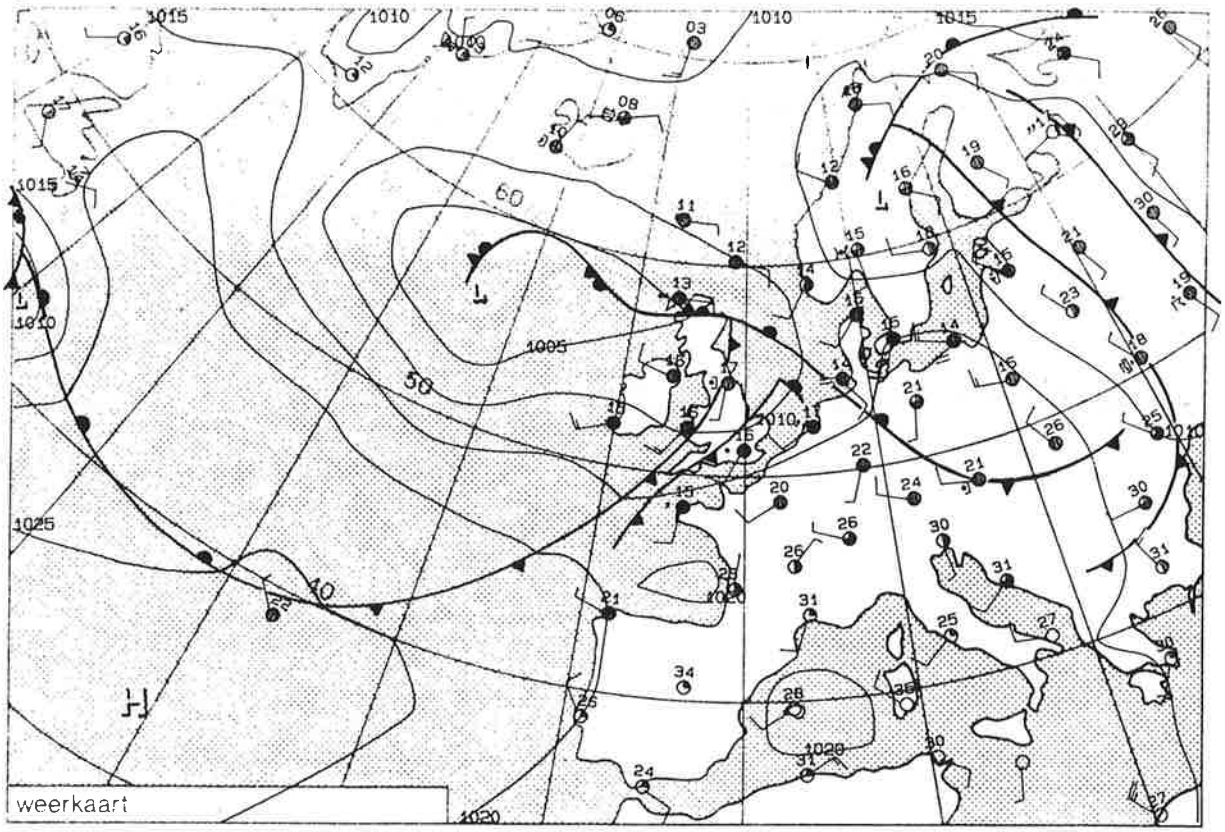

DOW 5 GEMIDDELDEN, SOMMEN EN EXTREMEN (ETMAAL 0 - 24 UUR)

25 JUNI 1991

	WINDSNELHEID UUR GEM HALVE	MAX VLAAG M/SEC.	TEMPERATUUR 10 CM GRADEN	150 CM CELSIUS	* VOCHTIGHEID DAMP DRUK MBAR	* RELA TIEF PROC	NEERSLAG HOEVEELHEID MM	DUUR UREN	* LUCHTDRUK ZEENIVEAU MBAR	* BE WOL KING 1/8
260 DE BILT										
GEM.	7	-	-	16,6	17,6	93	-	-	1013,6	8
SOM	-	-	-	-	-	-	6,7	10,2	-	-
MAX.	11	21	-	18,9	19,6	98	2,7	-	1016,0	8
MIN.	2	-	14,1	14,0	15,6	84	-	-	1009,7	7

yymmddhh	temp	rh	press	wd	wv
91062501	14.4	95	1016.0	16	3
91062502	14.4	97	1016.0	17	2
91062503	14.3	97	1016.0	16	4
91062504	14.3	98	1015.0	16	6
91062505	14.7	98	1015.0	17	5
91062506	15.2	97	1015.0	24	7
91062507	15.1	98	1015.0	23	7
91062508	15.4	95	1015.0	24	7
91062509	16.0	90	1015.0	23	9
91062510	16.3	92	1015.0	23	9
91062511	16.5	95	1015.0	23	8
91062512	17.1	90	1015.0	24	8

yymmddhh	temp	rh	press	wd	wv
91062513	18.2	90	1014.0	22	8
91062514	18.6	86	1014.0	22	8
91062515	18.2	93	1014.0	23	11
91062516	18.5	92	1013.0	22	11
91062517	18.5	88	1013.0	22	11
91062518	18.7	88	1013.0	24	8
91062519	18.2	87	1012.0	24	10
91062520	18.2	87	1012.0	22	7
91062521	18.5	84	1012.0	22	5
91062522	17.4	94	1011.0	22	7
91062523	16.7	96	1010.0	24	7
91062524	16.1	97	1010.0	24	8

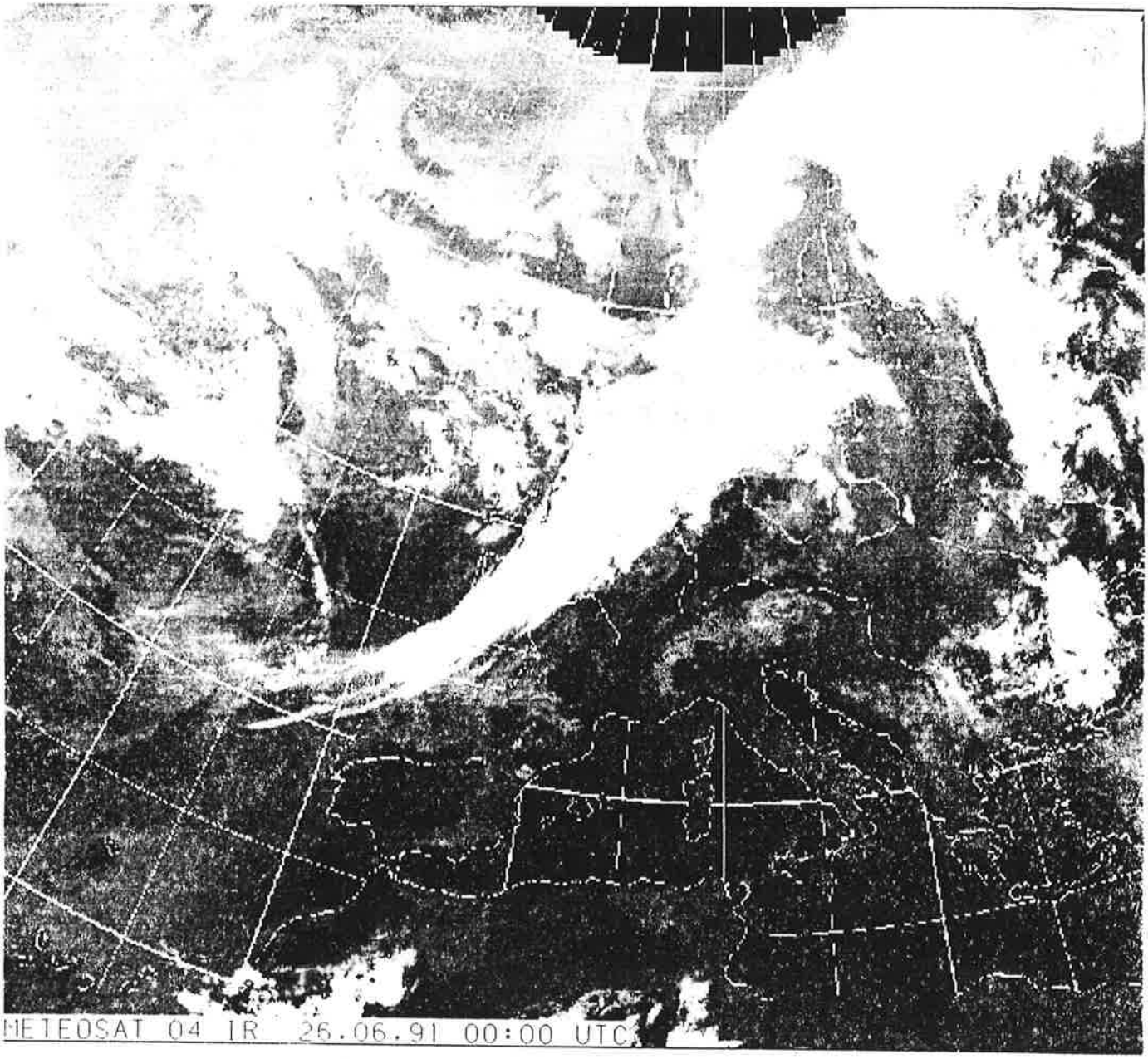

Weather Situation

The centre of the low pressure area which was north-western of Ireland on Tuesday moved to the noth-west on Wednesday. Another low pressure area was formed at the occlusion and reached the northern North Sea. Its warm front which covered the whole of Germany moved quickly towards the north-west. Germany was entirely influenced by humid and warm mediterranian air. An upper level ridge moved from England to eastern Germany but had a rather weak influence on the north. Because of the lacking sunshine, temperatures in the north were only up to 20 °C, with 15 °C at the coast. In the north-west, rainfalls with measurements of precipitation of 18 l/m² occurred in front of the cold front.

WOENSDAG 26 JUNI 1991 1200 UTC.

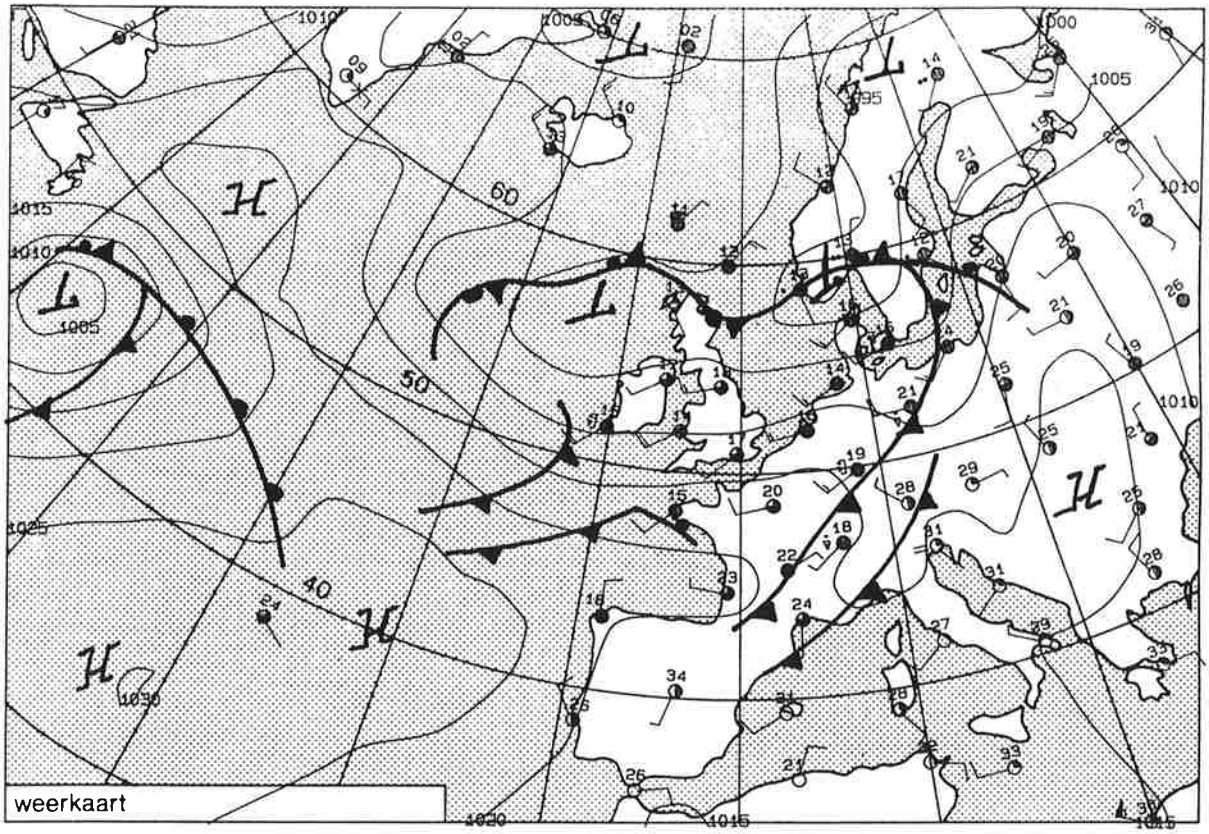

DOW 5 GEMIDDELDEN, SOMMEN EN EXTREMEN (ETMAAL 0 - 24 UUR)

26 JUNI 1991

	WINDSNELHEID UUR GEM HALVE	WINDSNELHEID MAX VLAAG M/SEC.	TEMPERATUUR 10 CM GRADEN	TEMPERATUUR 150 CM CELSIUS	VOCHTIGHEID * DAMP DRUK MBAR	VOCHTIGHEID * RELA TIEF PROC	NEERSLAG HOEVEELHEID MM	NEERSLAG DUUR UREN	LUCHTDRUK * ZEENIVEAU MBAR	BE WOL KING 1/8
260 DE BILT										
GEM.	10	-	-	15,4	13,8	79	-	-	1011,3	6
SOM	-	-	-	-	-	-	8,8	6,1	-	-
MAX.	14	30	-	18,4	17,3	96	2,1	-	1012,8	8
MIN.	5	-	12,0	12,6	10,9	57	-	-	1009,2	2

yymmddhh	temp	rh	press	wd	wv
91062601	15.9	96	1010.0	24	7
91062602	15.2	95	1009.0	25	8
91062603	14.8	96	1010.0	26	6
91062604	14.6	96	1010.0	24	7
91062605	14.4	96	1010.0	24	8
91062606	14.3	95	1010.0	24	8
91062607	14.3	96	1010.0	25	7
91062608	14.8	92	1011.0	24	7
91062609	15.5	80	1011.0	25	10
91062610	16.0	75	1012.0	25	13
91062611	15.5	77	1012.0	25	14
91062612	15.9	76	1013.0	26	13

yymmddhh	temp	rh	press	wd	wv
91062613	16.8	69	1013.0	26	12
91062614	17.1	67	1013.0	24	13
91062615	17.4	66	1013.0	25	12
91062616	17.6	61	1013.0	25	14
91062617	16.8	57	1013.0	25	14
91062618	16.5	62	1013.0	25	12
91062619	16.2	65	1013.0	24	12
91062620	15.3	72	1012.0	23	10
91062621	14.5	74	1012.0	22	9
91062622	14.4	75	1012.0	22	7
91062623	13.3	81	1011.0	21	6
91062624	12.8	84	1011.0	20	5

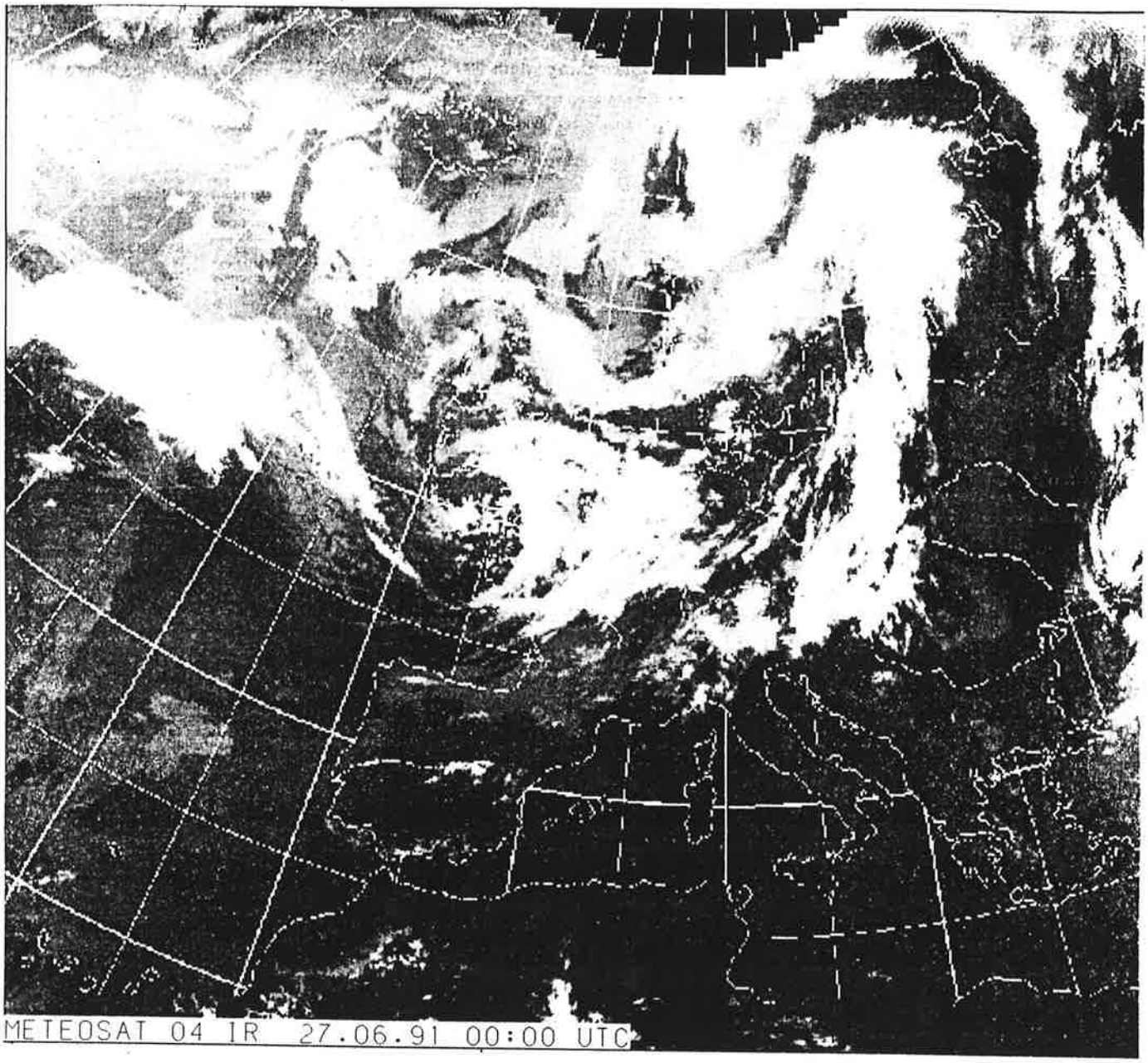

Weather Situation

The cold front which was over eastern England and the Bretagne on Wednesday moved quickly towards the east during the day. In north-western and northern Germany, it rained in the front area in the early morning. The cloudiness over the northern part of Germany diminished in the evening. The temperatures in the north were at 20 °C.

The satellite picture shows the cloud line of the cold front in the east. The skies over most of Germany are cloudless whereas in the west a new cloud area is formed which is at the front of an upper level trough.

DONDERDAG 27 JUNI 1991 1200 UTC.

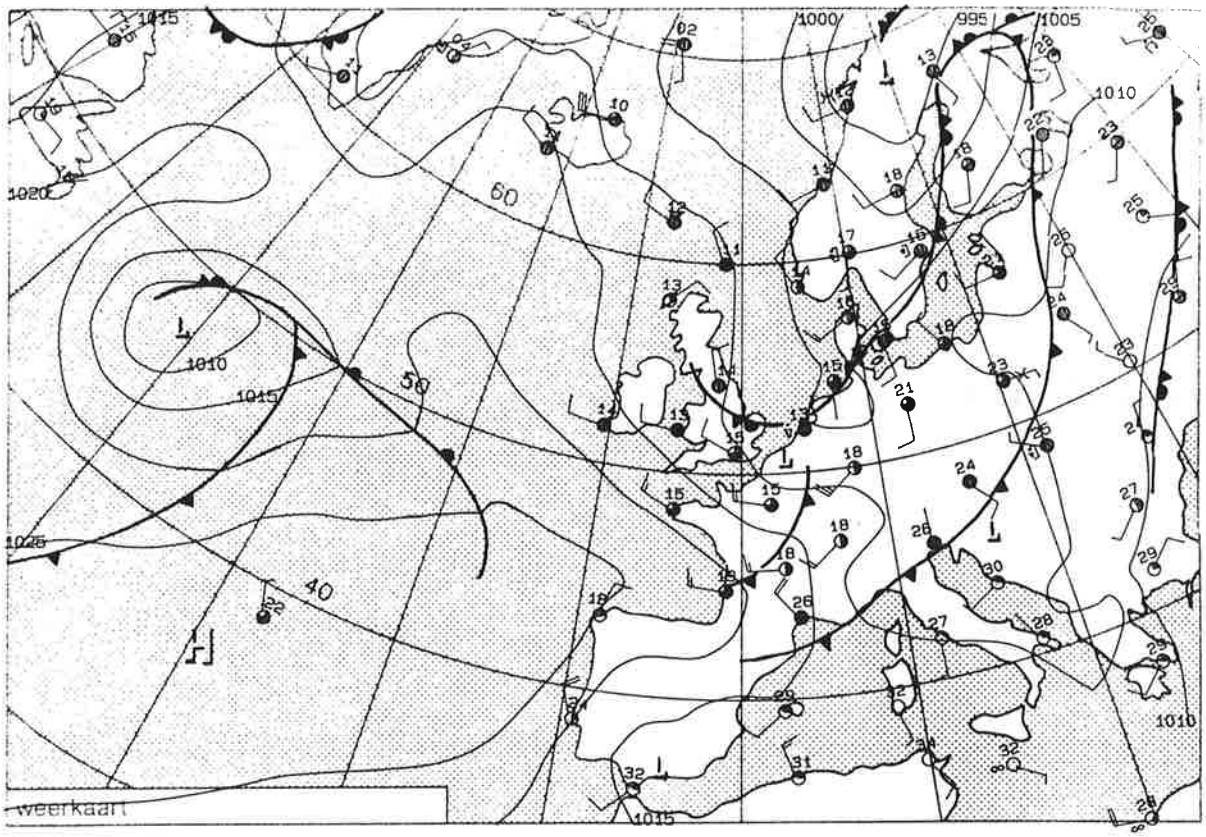

DOW 5 GEMIDDELDEN, SOMMEN EN EXTREMEN (ETMAAL 0 - 24 UUR)

27 JUNI 1991

	WINDSNELHEID UUR GEM HALVE	MAX VLAAG M/SEC.	TEMPERATUUR 10 CM GRADEN	150 CM CELSIUS	* VOCHTIGHEID DAMP DRUK MBAR	* RELA TIEF PROC	NEERSLAG HOEVEELHEID MM	DUUR UREN	* LUCHTDRUK ZEENIVEAU MBAR	* BE WOL KING 1/8
260 DE BILT										
GEM.	4	-	-	12,8	13,3	90	-	-	1007,3	8
SOM	-	-	-	-	-	-	15,1	5,9	-	-
MAX.	7	16	-	14,6	14,2	97	2,8	-	1009,9	8
MIN.	2	-	11,2	11,5	12,1	84	-	-	1004,8	7

yymmddhh	temp	rh	press	wd	wv
91062701	12.9	84	1010.0	22	5
91062702	12.5	86	1009.3	20	5
91062703	12.1	86	1008.4	19	4
91062704	11.6	90	1007.7	16	4
91062705	12.1	90	1007.6	19	4
91062706	12.0	95	1006.0	9	3
91062707	11.8	95	1006.3	21	3
91062708	11.9	97	1005.8	20	2
91062709	12.2	94	1005.0	2	2
91062710	12.4	92	1004.9	6	2
91062711	12.9	91	1005.0	31	3
91062712	13.4	86	1005.3	2	2

yymmddhh	temp	rh	press	wd	wv
91062713	13.6	89	1005.7	32	3
91062714	13.3	90	1006.0	29	4
91062715	13.0	92	1006.6	30	7
91062716	13.1	94	1006.8	31	6
91062717	13.7	89	1007.1	28	6
91062718	14.3	87	1007.5	30	6
91062719	14.1	85	1008.0	29	6
91062720	13.5	88	1008.6	29	6
91062721	13.3	88	1009.2	29	5
91062722	12.9	89	1009.7	30	6
91062723	12.7	90	1010.0	28	5
91062724	12.4	91	1010.0	27	5

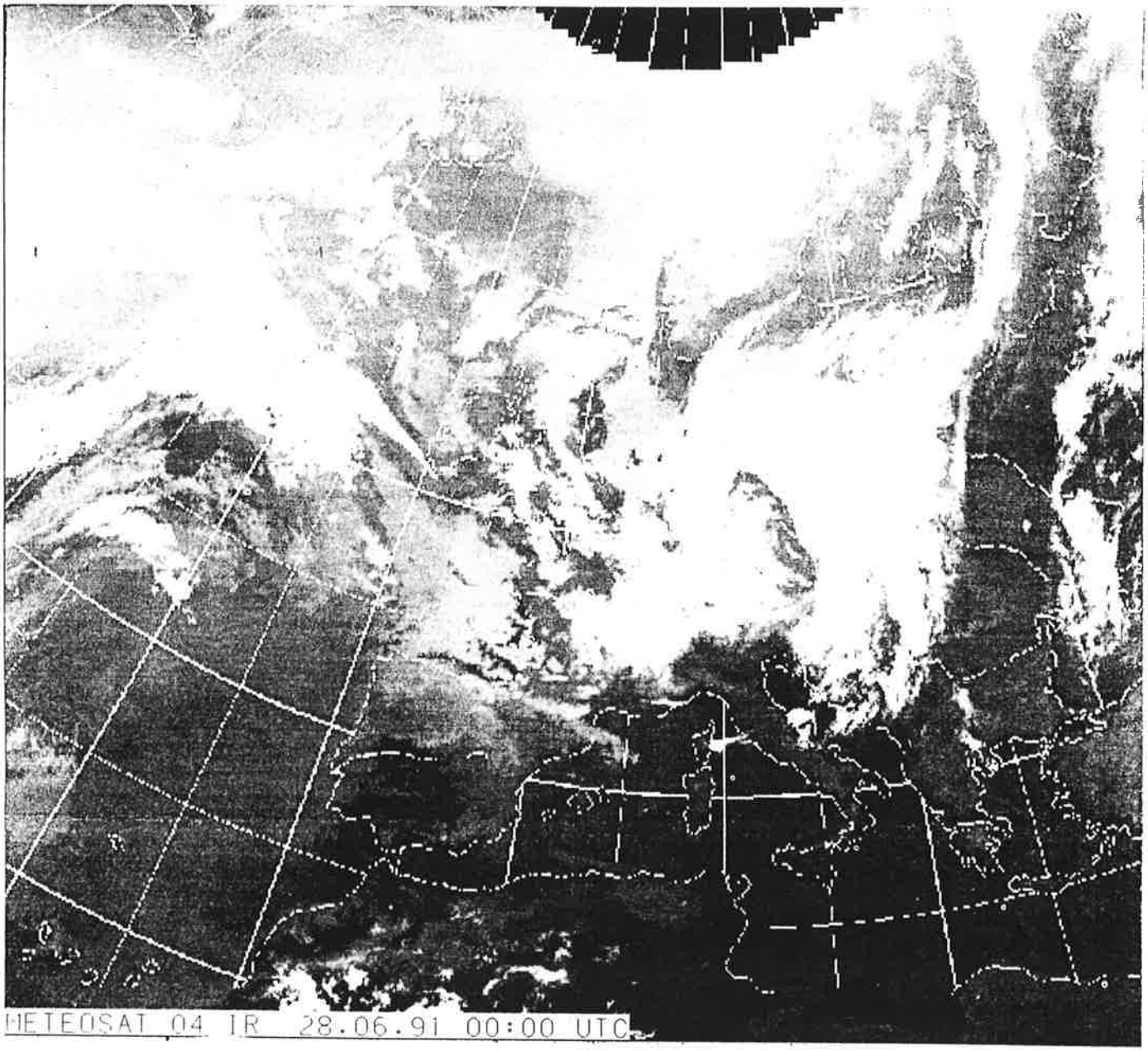

Weather Situation

A low pressure area over the British Isles moved to north-eastern France during the morning. The accompanying cyclone moved to north-western Germany. From an associated convergence line a cold front developed. In the frontal zone over Germany, heavy rainfalls occurred accompanied by strong gusts.

The satellite picture shows a cloud line in the north and the east of the Elbe and a cloud area over north-western Germany.

VRIJDAG 28 JUNI 1991 1200 UTC.

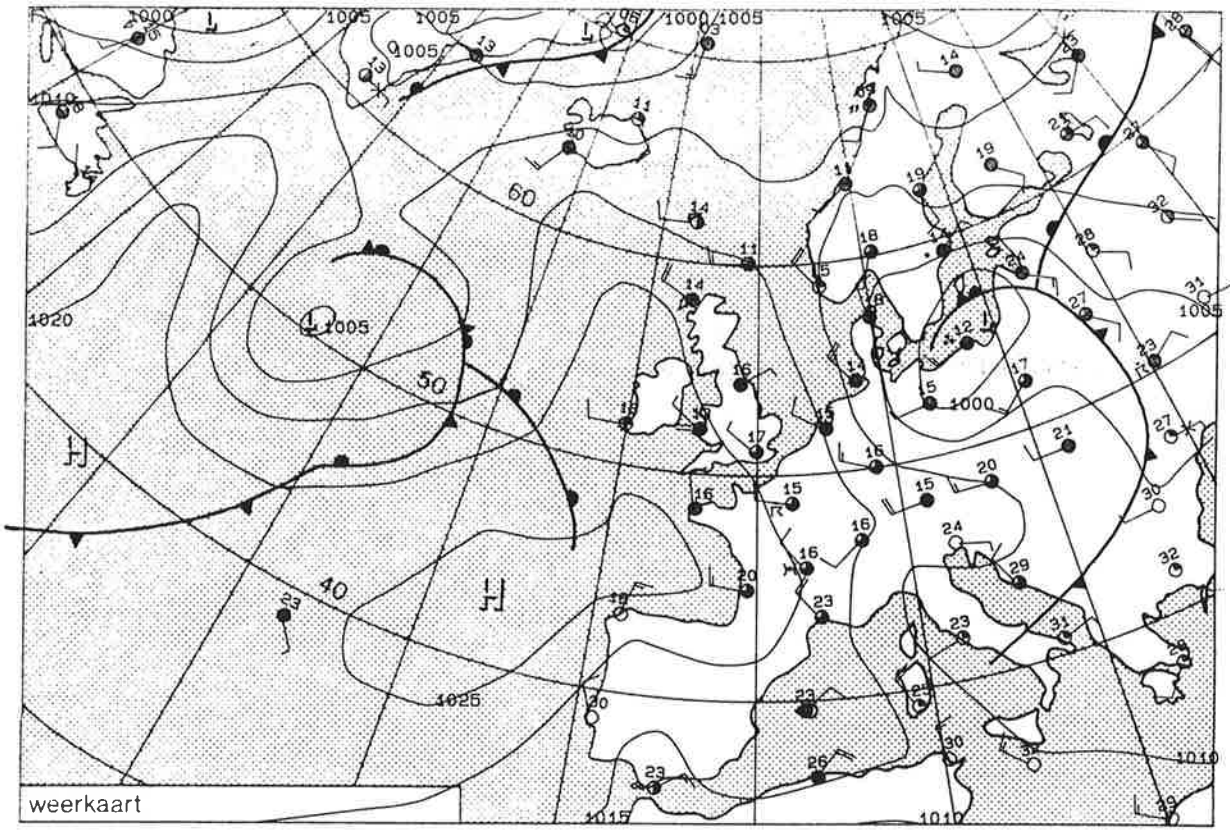

DOW 5

GEMIDDELDEN, SOMMEN EN EXTREMEN (ETMAAL 0 - 24 UUR)

28 JUNI 1991

	WINDSNELHEID UUR GEM HALVE	WINDSNELHEID MAX VLAAG M/SEC.	TEMPERATUUR 10 CM GRADEN	TEMPERATUUR 150 CM CELSIUS	* VOCHTIGHEID DAMP DRUK MBAR	* VOCHTIGHEID RELA TIEF PROC	NEERSLAG HOEVEELHEID MM	NEERSLAG DUUR UREN	* LUCHTDRUK ZEENIVEAU MBAR	* BE WOL KING 1/8
260 DE BILT										
GEM.	7	-	-	12,6	11,2	77	-	-	1014,8	6
SOM	-	-	-	-	-	-	0,1	0,1	-	-
MAX.	10	24	-	15,6	13,0	89	0,1	-	1018,3	8
MIN.	3	-	8,7	10,2	10,1	61	-	-	1010,0	2

yymmddhh	temp	rh	press	wd	wv
91062801	12.6	89	1010.3	31	5
91062802	12.4	86	1010.1	31	7
91062803	12.3	86	1010.5	31	6
91062804	11.9	86	1011.1	31	6
91062805	12.1	85	1011.5	30	6
91062806	12.4	84	1012.0	30	5
91062807	13.3	79	1012.7	32	7
91062808	12.2	82	1013.5	33	7
91062809	13.2	72	1013.8	32	7
91062810	13.2	74	1014.3	31	7
91062811	14.3	69	1014.6	31	9
91062812	14.5	61	1015.0	30	9

yymmddhh	temp	rh	press	wd	wv
91062813	13.7	73	1015.7	31	8
91062814	13.4	69	1016.3	33	10
91062815	13.9	69	1016.6	32	8
91062816	14.1	65	1017.0	32	10
91062817	12.5	73	1017.4	33	10
91062818	13.5	70	1017.5	33	7
91062819	12.6	70	1017.6	31	7
91062820	11.4	76	1017.9	30	6
91062821	10.8	81	1018.3	28	4
91062822	10.8	84	1018.3	26	3
91062823	10.7	86	1018.4	27	3
91062824	10.7	86	1018.3	26	3

5.2 Measurement periods

From the meteorological data given in section 5.1 it is apparent,that weather conditions were extremely unfavorable for lidar measurements during most of the experiment time. Very often rain or low clouds did not allow lidar operation at all. In other cases quickly changing cloud coverage made system alignment extremely difficult, since most systems need a stable atmospheric return signal for the final adjustment of the overlap between transmitted beams and receiver field of view. In addition, broken cloud decks imply that only short averaging times can be used at the expense of accuracy. Periods of homogeneous backscatter conditions were rare and hard to predict, although excellent forecast support was available from the Dutch Weather Service (KNMI). So most of the time the systems had to be operated under worst case conditions. In spite of this, a fairly large data set has been collected. Table 5.1 summarizes the measurement times of all four lidar systems. For a better overview they are repeated as graphs in fig. 5.1.

From these measurement periods some were selected already during the experiment as first priority cases for evaluation. This selection was based on the availability of helicopter data for intercomparison, simultaneous operation of all lidars, absence of clouds, or performance of horizontal intercomparisons. These priority 1 cases are listed in table 5.2 .

Table 5.1: Times of lidar operation. Days are in June 1991, times in UT For the LIT-lidar, remarks have the meanings: v = vertical, h = horizontal, vs = vertical scan

day	rivm	rivm	sa	sa	lit	lit	mpi	mpi
9					18:03	18:07 v		
9					18:17	18:20 v		
9					18:34	18:41 v		
9					18:47	18:53 v		
9					19:22	19:25 v		
10					15:57	16:00 v	19:54	20:28
10					16:55	17:02 v		
10					17:33	17:36 v		
10					17:43	17:46 v		
10					17:55	17:58 v		
10					18:22	18:29 v		
10					18:48	18:51 v		
10					18:53	18:56 v		
10					19:07	19:10 v		
10					19:24	19:27 v		
10					19:34	19:37 v		

day	rivm	rivm	sa	sa	lit	lit	mpi	mpi
11	10:24	10:26	10:00	10:41	10:24	10:43 v	06:53	07:52
11	10:34	10:36	13:25	13:47	11:01	11:04 v	08:09	08:43
11	10:42	10:44			11:48	11:51 v	09:01	10:30
11	10:47	10:48			11:56	11:59 v	11:10	12:52
11	11:05	11:07			12:31	12:34 v	13:07	13:50
11	11:15	11:18			12:46	12:49 v	14:05	14:46
11	11:20	11:23			13:54	13:57 v		
11	11:41	11:41			14:00	14:03 v		
11	11:46	11:48			14:07	17:03 v		
11	11:53	11:53						
11	11:54	11:56						
11	11:59	11:01						
11	12:35	12:36						
13	14:07	15:57	11:52	12:07	15:48	17:58 v	13:35	13:45
13	16:40	18:08	13:24	21:27	18:36	20:52 v	13:56	14:21
13	18:18	18:35	22:09	24:00	21:00	23:50 v	14:47	16:00
13	18:48	21:19					17:28	18:48
13	21:30	22:26					18:52	21:26
13							21:39	21:49
13							22:29	23:40
13							23:54	01:58
14	05:05	06:17	00:00	03:12	00:12	10:08 v	02:15	03:06
14	07:11	09:37	03:21	06:46	10:32	12:08 v	03:20	04:51
14	09:56	10:07	06:54	07:54			04:54	07:22
14			09:01	09:54			07:36	10:00
14							16:24	17:07
14							17:17	18:11
16					11:32	11:35 h	17:18	17:28
16					11:40	11:43 h		
16					11:48	11:51 h		
16					12:11	12:14 h		
16					12:24	12:27 h		
16					12:44	12:47 h		
16					13:40	13:43 h		
16					17:16	17:19 h		
16					17:30	17:33 h		
16					18:15	18:18 h		
16					18:36	18:39 h		
16					18:49	18:51 h		

day	rivm	rivm	sa	sa	lit	lit	mpi	mpi
16					18:54	18:57 h		
16					19:32	19:35 h		
16					19:41	19:44 h		
16					19:58	20:01 h		
16					20:17	20:20 h		
17	06:00	06:02	06:30	12:15	08:23	14:20 v	07:24	08:09
17	06:31	08:27					08:34	10:40
17	08:42	08:47					10:46	11:03
17	08:57	09:10					11:17	12:18
17	09:25	11:19						
17	11:54	11:56						
17	12:22	12:23						
17	19:50	20:07						
17	20:56	21:15						
18					14:26	14:29 h	17:39	17:53
18					14:35	14:38 h	17:23	17:36
18					14:57	15:17 vs	19:55	19:59
18					15:30	15:50 vs	20:04	20:40
18					16:09	16:29 vs		
18					17:38	17:58 h		
18					18:45	21:45 h		
19							19:06	19:21
19							19:23	19:38
19							19:48	20:57
20	07:21	08:47	06:48	12:22	08:54	08:57 h	06:33	06:54
20	09:02	09:37			09:12	09:15 h	06:59	09:25
20	13:03	14:33			09:53	11:35 v	09:31	13:24
20					11:39	13:23 vs		
20					15:35	16:55 vs		
20					17:31	17:56 h		
20					18:54	18:57 h		
20					19:02	19:05 h		
20					19:22	19:25 h		
21			08:24	11:05	09:02	12:34 v	07:26	08:33
21			11:47	13:05	12:39	12:42 h	08:46	10:55
21					12:46	17:41 v	11:11	14:08
21							14:21	15:43

day	rivm	rivm	sa	sa	lit	lit	mpi	mpi
22	11:39	12:16	08:30	12:00	11:05	11:21 h	08:53	09:53
22	12:32	13:23			11:27	14:15 vs	10:15	10:53
22	13:34	13:56			17:37	17:40 h	11:37	12:07
22					17:44	17:47 h	15:46	17:27
22					17:49	18:09 vs	17:30	19:28
22					18:11	20:38 h		
22					20:41	21:18 vs		
23	11:50	11:57	09:24	11:53	12:15	12:48 h	09:15	10:07
23	14:19	14:35			12:57	14:54 h	10:17	10:40
24	08:54	10:44	11:05	14:26	12:55	13:09 h	11:19	13:28
24	12:25	14:40			13:15	13:22 v	13:34	15:04
24	14:53	15:03			13:43	14:01 vs		
24					14:10	14:23 v		
24					14:25	14:43 vs		
24					14:44	16:01 v		
24					16:07	20:48 vs		
26	09:30	10:21	09:00	09:11	14:14	14:26 h	10:05	10:37
26	11:55	12:57	09:32	10:04	14:50	23:48 h	13:54	13:58
26	13:31	15:18	18:43	00:00			13:59	16:01
26	15:30	15:50					16:29	19:20
26	19:47	22:21					19:31	21:56
26	22:45	24:00					22:33	00:05
27	00:00	00:21			00:00	01:53 v		
27					15:20	15:33 h		
27					16:12	16:48 h		
27					17:41	18:21 h	20:46	21:20
28	05:59	06:53	04:38	07:00	10:37	10:46 h	03:37	04:50
28	12:35	13:51			11:01	11:17 h	06:16	07:51
28					11:19	11:36 vs	12:38	12:40
28					11:50	12:07 vs	10:51	11:48
28					13:20	13:37 vs	11:55	12:24
28					13:42	13:59 v	12:43	14:10
28					14:02	15:57 vs		
28					15:00	15:35 v		
28					15:36	15:35 vs		

Period number	Date	Time (UT)
1	91/06/11	10:00- 10:25
		11:50- 12:30
2	91/06/13	14:12- 14:21
		15:10- 15:18
		15:44- 15:48
		17:40- 17:50
		21:10- 21:20
3	91/06/26	22:35- 24:00
4 (first flight)	91/06/20	08:00- 09:00
5 (second flight)	91/06/24	12:10- 13:20
6 (third flight)	91/06/28	12:38- 13:35
7	91/06/22	15:48- 19:25
8	91/06/26	14:00- 21:53

Table 5.2: Periods of first priority

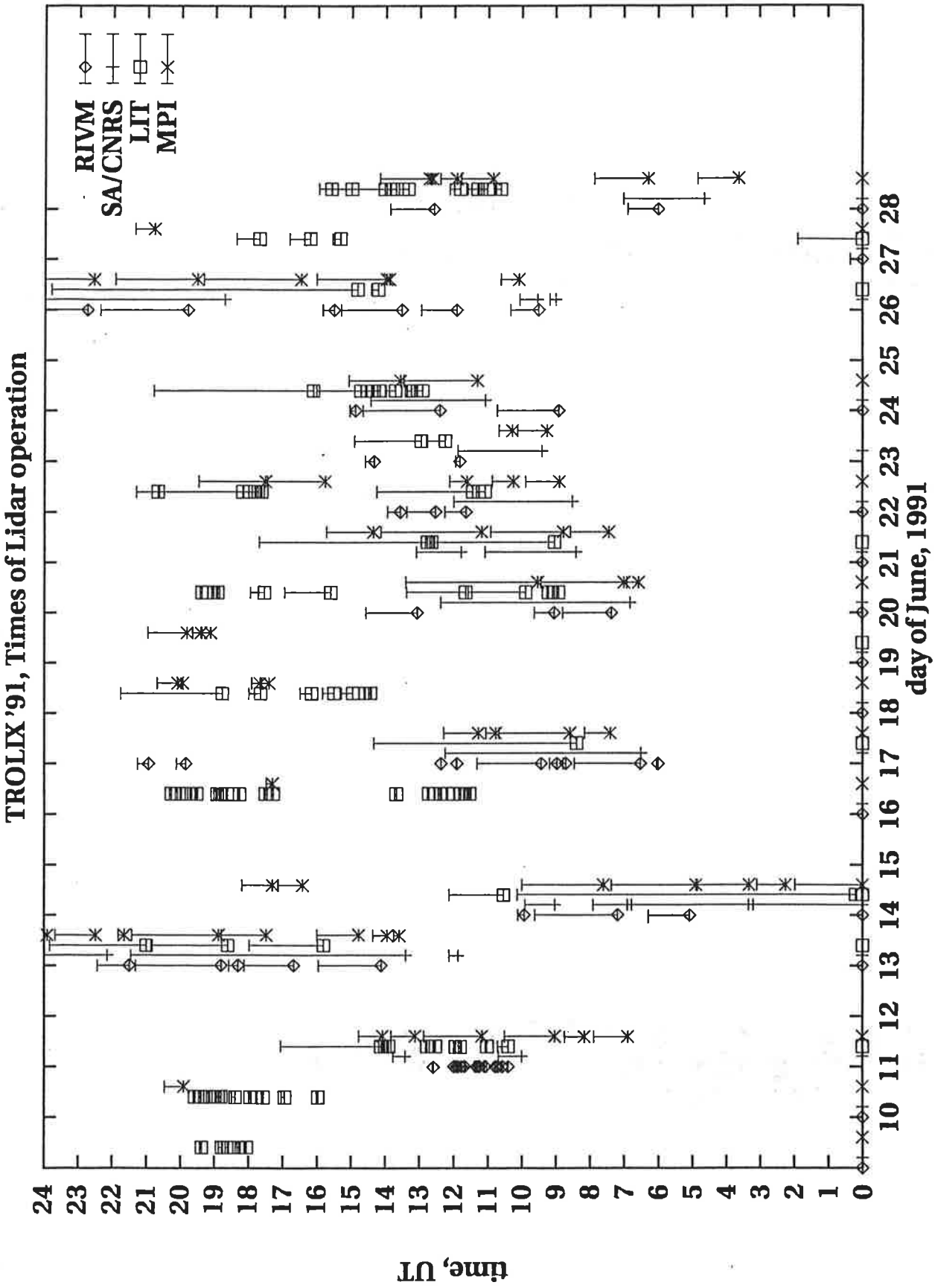

Figure 5.1: Times of lidar operation during TROLIX '91

5.3 Ozone DIAL results

5.3.1 RIVM

Discussion of acquired LIDAR signals and System performance

In figure 5.2 an example is given of a greyscale representation of the LIDAR data. The signal at 299 nm is shown, since it is the wavelength used in the system that is least absorbed by ozone. Therefore, the attenuation with range is the least and structure in the atmosphere can be discerned up till higher altitudes as compared to the other wavelengths 266 and 289 nm. In this representation a total of 13 grey tones including solid fill and not-filled is used to cover the entire dynamic range of the data in the figure. Darker shades correspond to larger values. Although the number of patterns may not be sufficient to adequately represent all details in the data, a good impression of large scale developments in time can be obtained. The resolution in the vertical direction is 30 m, which corresponds to one data sample no smoothing is applied. In the horizontal direction the width of the columns correspond to the time lapse between the start and end of the measurement. This implies that when more LIDAR returns are averaged, the column will be wider. The opposite is not true: if the measurement has been interrupted for some reason and was subsequently resumed, the column will show an increased width.

During the campaign it turned out that the system did not operate flawless in every aspect. Some problems in the emitter part of the setup were encountered with two of the wavelengths, namely 289 nm and 299 nm. For the 299 nm wavelength, the beam direction stability was not optimal. This may influence the reliability of the signal, particularly in the region where complete overlap of the laserbeam and the field of view of the telescope is just obtained. Also, data in the far field (i.e. at ranges greater than a few kilometers) may be influenced. The instability was probably caused by the mechanical construction of the attachment of the coupling mirror. Consequently, the alignment had to be checked upon always in the beginning of each measurement period and also from time to time during a session. However, the atmospheric conditions were such that optimal adjustment of the overlap between the emitted laser beams and the field of view of the telescope could not always be achieved or verified.

Previous experiences with the setup have shown that laser pulse energy at 266 nm can be stabilized to within a few percent over extended periods of time (in the order of a few hours) (see [Sune 91]). However, as it turned out, the pulse energy decreased slowly when the system was kept running for almost a full diurnal cycle. This was probably due to thermal effects in the fourth harmonic crystal in the harmonics generator of the lasers (see [Sune 91]). Higher energies could be obtained again after a period of shutdown of the lasers. Moreover, the temperature controller of the fourth harmonic crystal in the laser pumping the D_2 filled Raman cell (i.e. generating 289 nm) broke down during the campaign. This influences the energy stability considerably. However, it was found that the energy could be kept at reasonable values ($\approx$ 40 mJ after the Raman cell) if the crystal was tuned regularly. For this reason, the energy of the 289 nm signal had to be monitored from time to time. Integrating a power meter into the optical system

would require a complete realignment of the system. This was not feasible because a lot of time and clear weather conditions would be needed, both of which were not available. Therefore, the measurement cycles were interrupted from time to time for monitoring and readjustment of the 289 nm pulse energy. Another reason for decrease of energy was the slow degradation of the dichroic mirrors used for wavelength separation (see [Sune 91]). A possible cause of the damage of these mirrors is dust.

Further, some flaws existed in the detection part of the setup. First, the 299 nm signal was very weak. Since many shots were averaged, some systematic error sources would appear clearly in the averaged signals. This effect shows as an oscillation in the tail of the signal (see figure 5.3). The reason for the oscillation could not be discovered during the campaign. The problem was different from problems experienced previously with the transient digitizers [Sune 91]. Since the quality of the 299 nm signal is questionable in some cases, along with the greater sensitivity to noise of the 289/299 nm signal pair due to the small differential absorption cross-section of ozone reliable ozone measurements can possibly not be made in all cases. In almost all cases, the ringing effect starts to show at altitudes over 3 km. Since the cloud base was very often lower than that, the ringing is not a limiting factor for most of the time.

Another problem with the detection was Signal induced bias (SIB). SIB was kept to minimum by attenuation of the received optical signals. Some SIB is still present, most pronounced in the 266 nmsignal. The effect starts to show between about 1750 m and 2000 m. The SIB effect will cause an underestimation of the ozone concentration [Sune 91].

An example is shown in figure 5.3

Ozone Measurements

In the following sections the calculated ozone profiles of the periods of prime interest will be presented in grey scale format.

Ozone Measurements overview In the figures 5.4 to 5.13 the ozone values calculated for the wavelength pairs 266/289 nm and 289/299 nm are presented for the periods of prime interest listed in table , section 5.2. For the periods where a continuous sequence of measurements is not available, individual measurements are shown. Brief comments on the measurements are given in the figure subscripts. An example of LIDAR data and derived ozone profiles is shown for each period displayed. In these examples, presented as data traces, SIB correction is applied. In the ozone profiles, a combination of a continuous trace and discrete ozone values are displayed. The length of the interval of the discrete values corresponds to the interval length used in the concentration calculation. Error bars indicate the uncertainty ($\pm$ 1 σ). The trace is obtained by moving the linearization interval along the DIAL-curve (see [Sune 91]).

Remarks on Ozone profiles The ozone values presented in this report are meant to give an overview of the data. For a more elaborate inspection, additional software has to be developed first, mainly for error correction. The data presented here are only corrected for differential Rayleigh scattering. Other systematic error sources, such as SO_2, O_2, aerosols and water vapour (see [Sune 91]), are not yet accounted for. It is very well possible that timing errors have gone undetected by the processing software during the evaluation of the LIDAR data. The timing errors will give rise to erroneous ozone values in the vicinity of boundaries between atmospheric layers (see [Sune 91]. The errors can arise from the triggering mechanism used in the setup. Presently this type of error has to be manually corrected during evaluation. The signal induced errors in the 266/289 nm ozone calculation can be quite severe (see e.g. figure 5.13). In the measurements presented in grey scale format no corrective algorithm is applied. Therefore, depending on the particular conditions during the measurements, the concentration values from altitudes starting at about 1700 m and higher should be handled with care. Full overlap of the 266 nm and 289 nm signals is established at about 500 m. Full overlap of the 289 nm and 299 nm signals is achieved mostly above 1 km. As a consequence, the evaluation of ozone concentration yields erroneous values at altitudes below these limits. Mostly, the values obtained are out of scale.

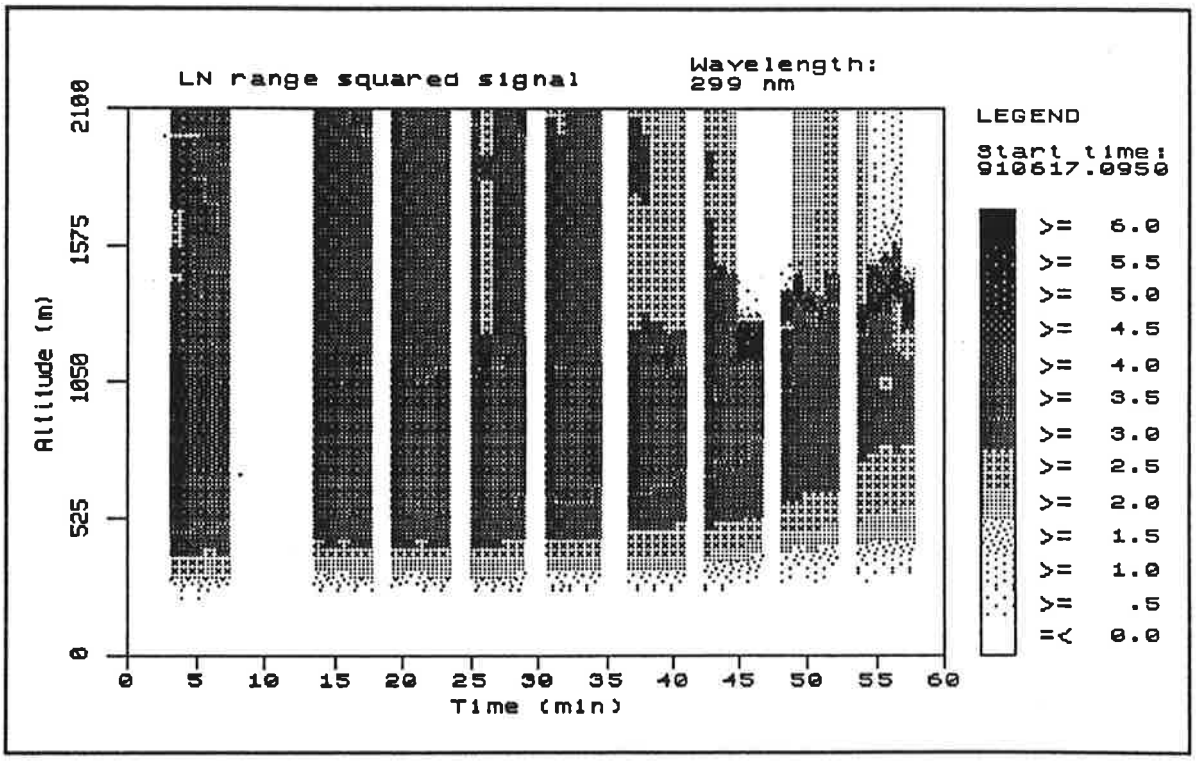

Figure 5.2: An example of LIDAR data at 299 nm.The start time of the sequence is at June 17, 1991, 09:50 U.T. Higher density of black corresponds to a stronger backscattered signal. The gaps appear where the operator has to restart a measurement. During these gaps, the laser power was measured and adjusted when necessary.

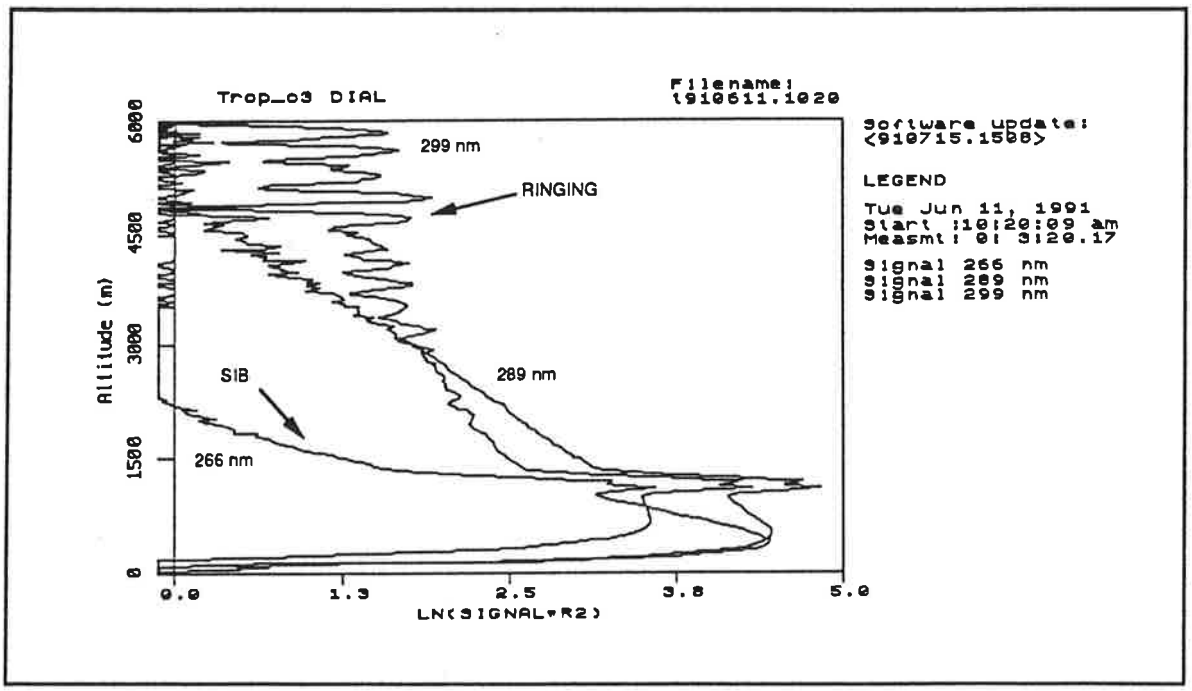

Figure 5.3: Example of data showing ringing effect and SIB.

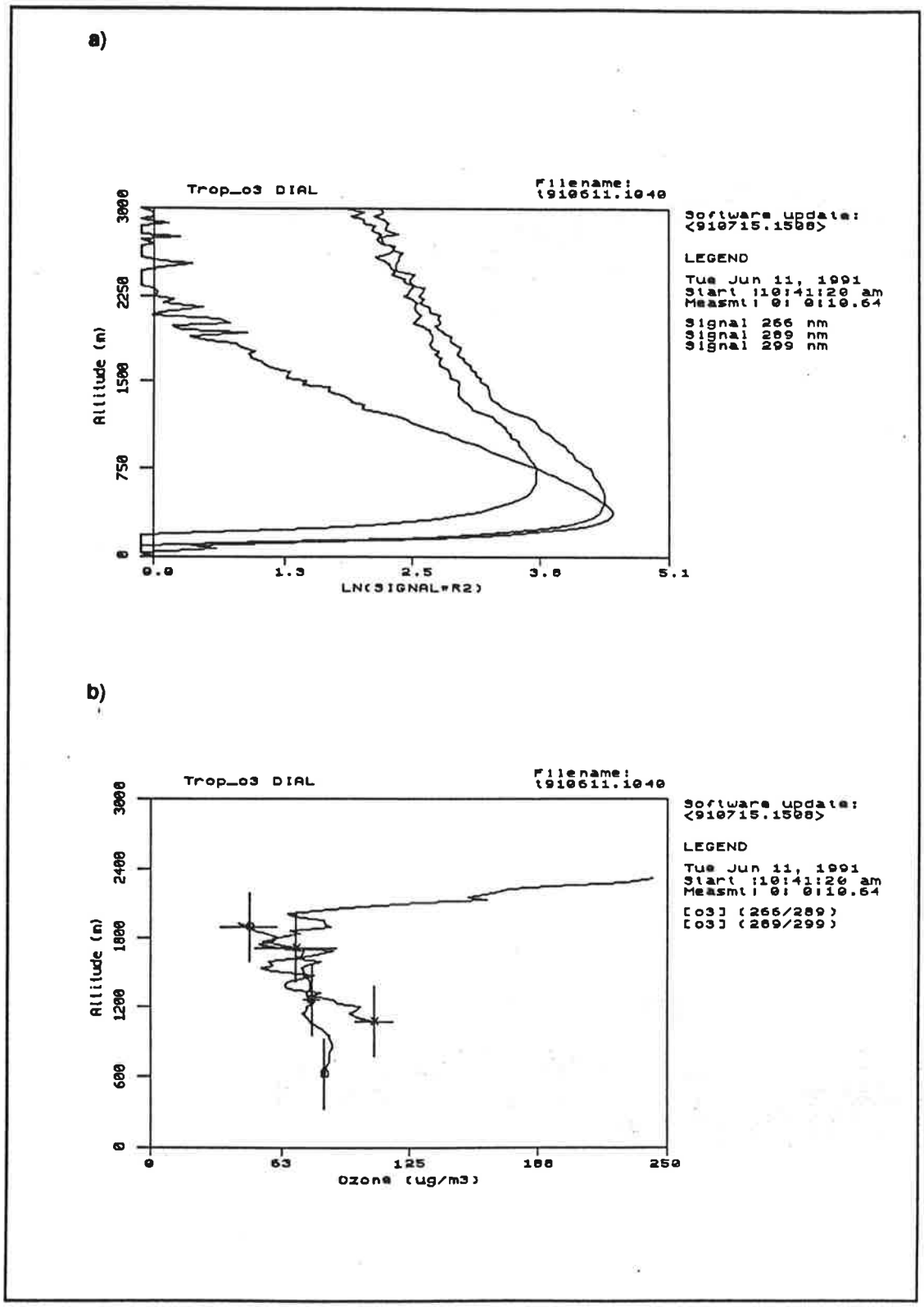

Figure 5.4: a) LIDAR returns and b) ozone profiles. In the ozone profiles the circular marker indicates the 266/289 nm data while the cross marker indicates the 289/299 nm data.

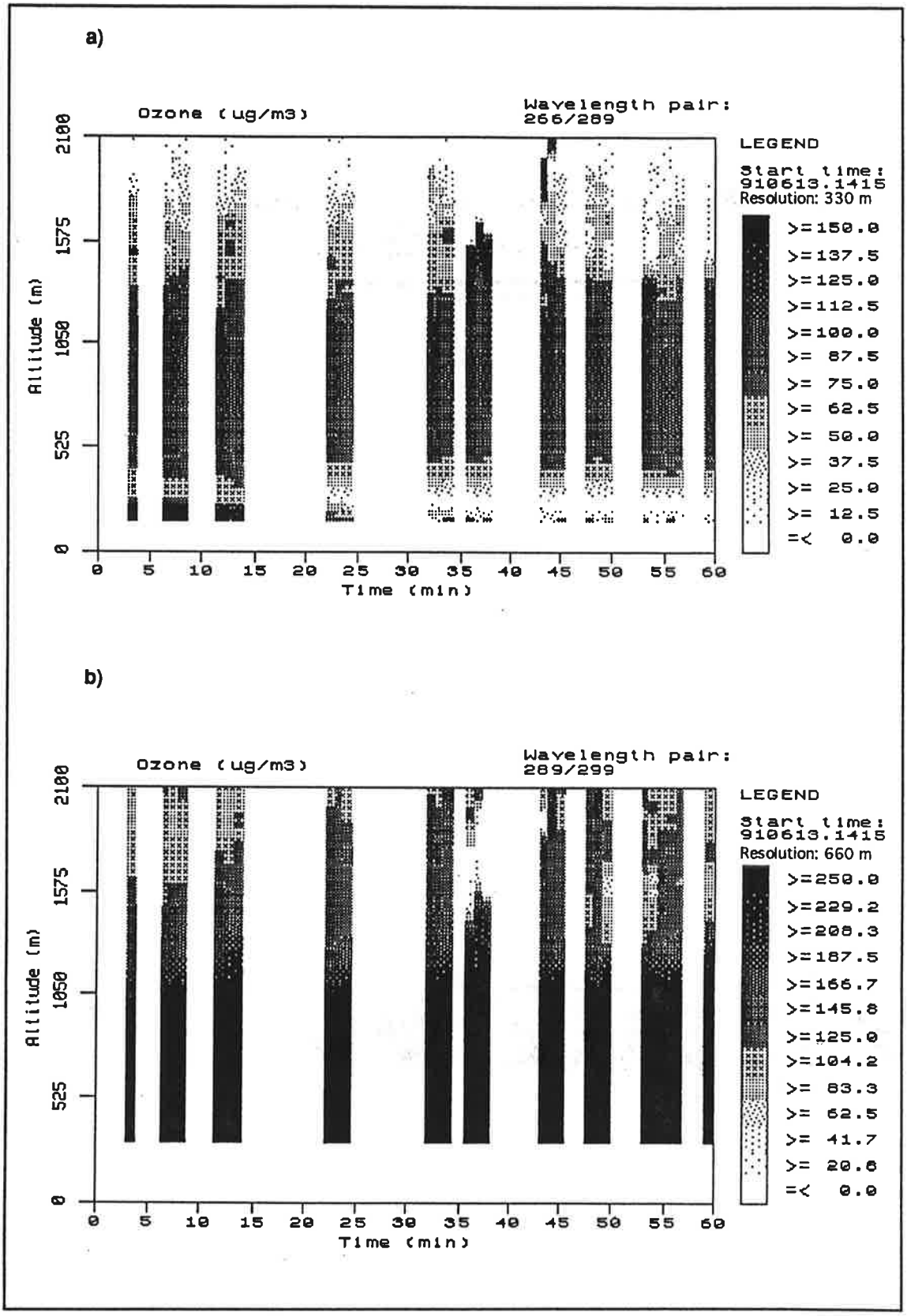

Figure 5.5: Ozone.

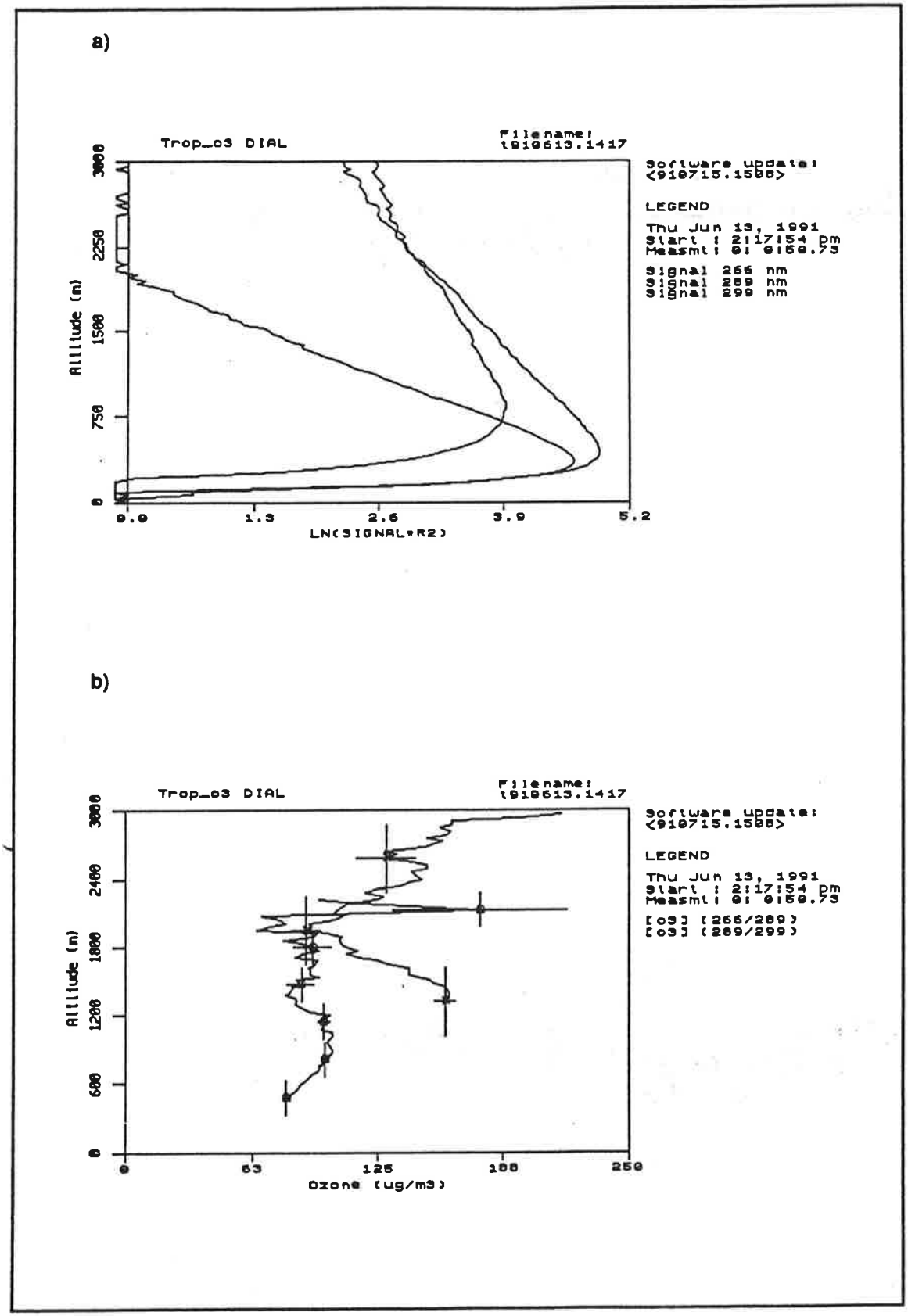

Figure 5.5: (continued) LIDAR returns and ozone profiles.

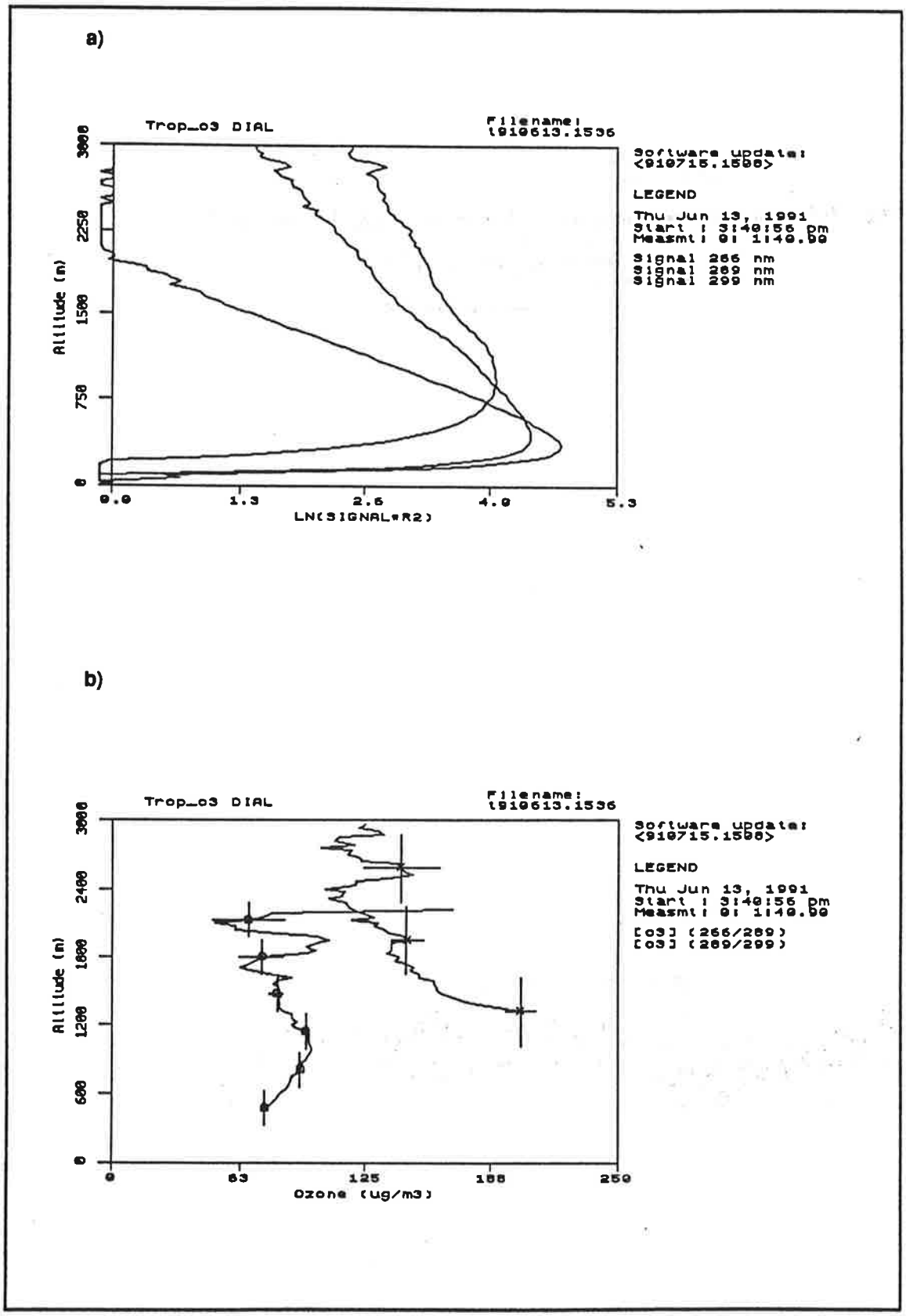

Figure 5.6: a) LIDAR returns and b) ozone profiles.

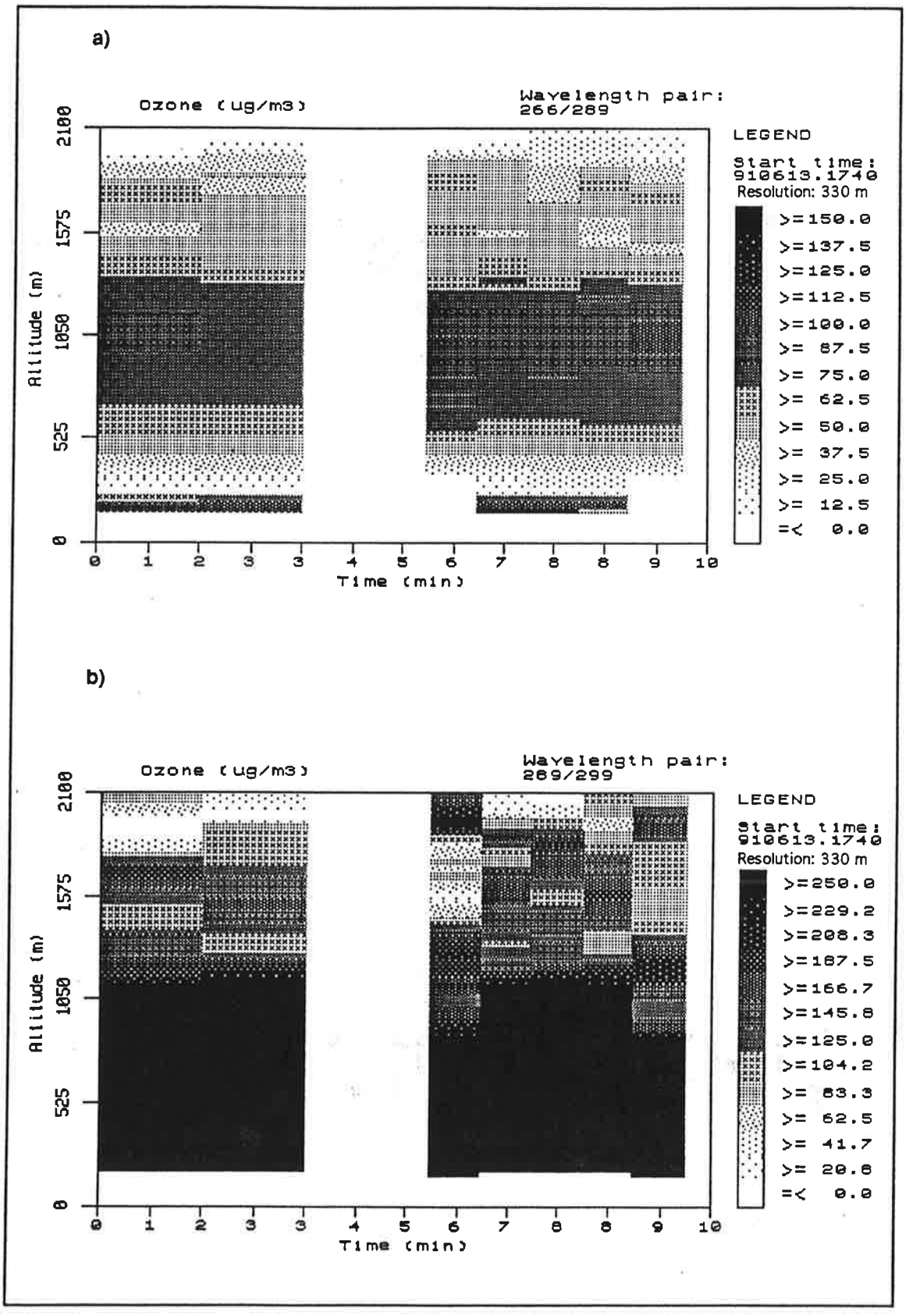

Figure 5.7: Ozone

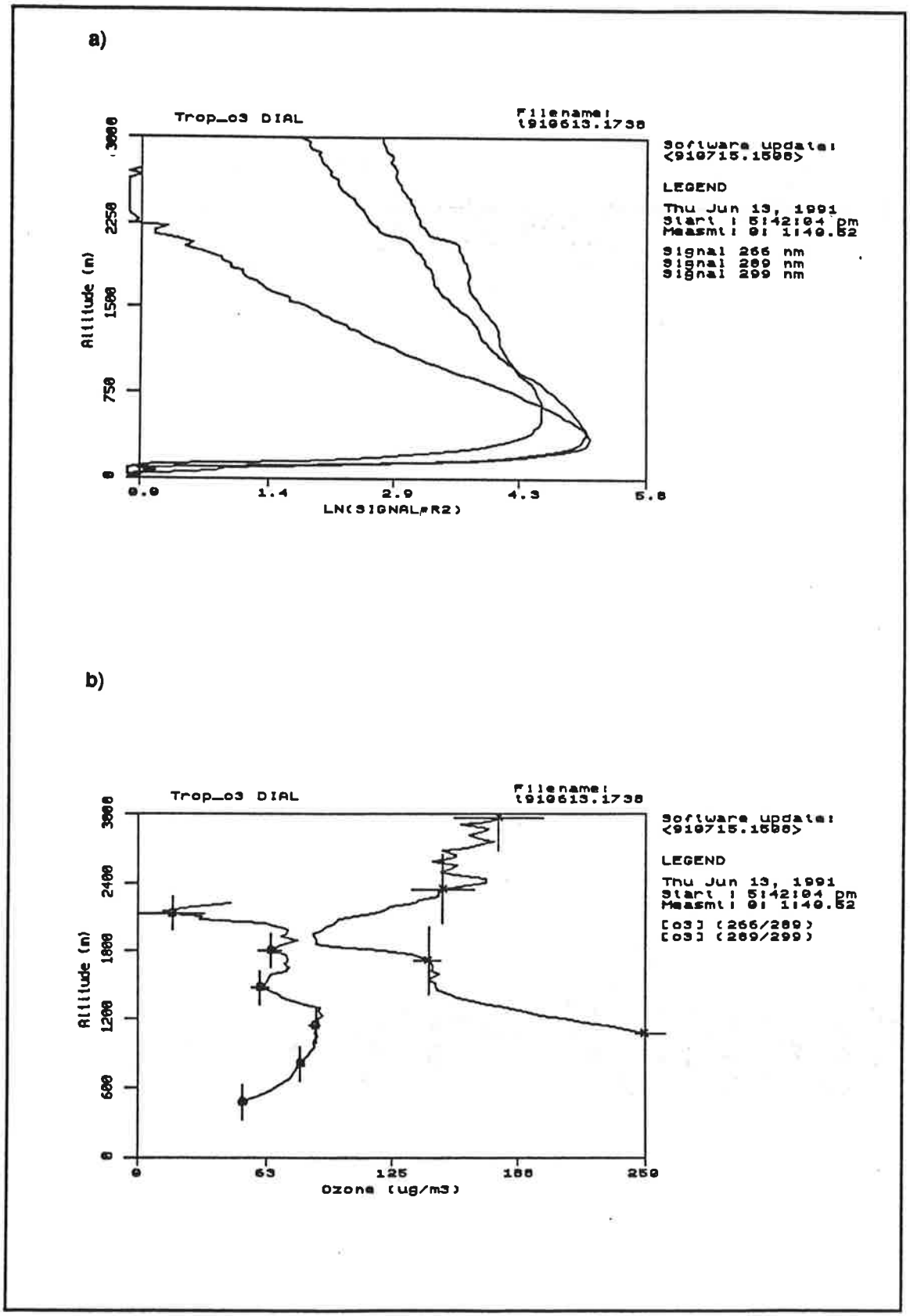

Figure 5.7: (continued) LIDAR returns and ozone profile

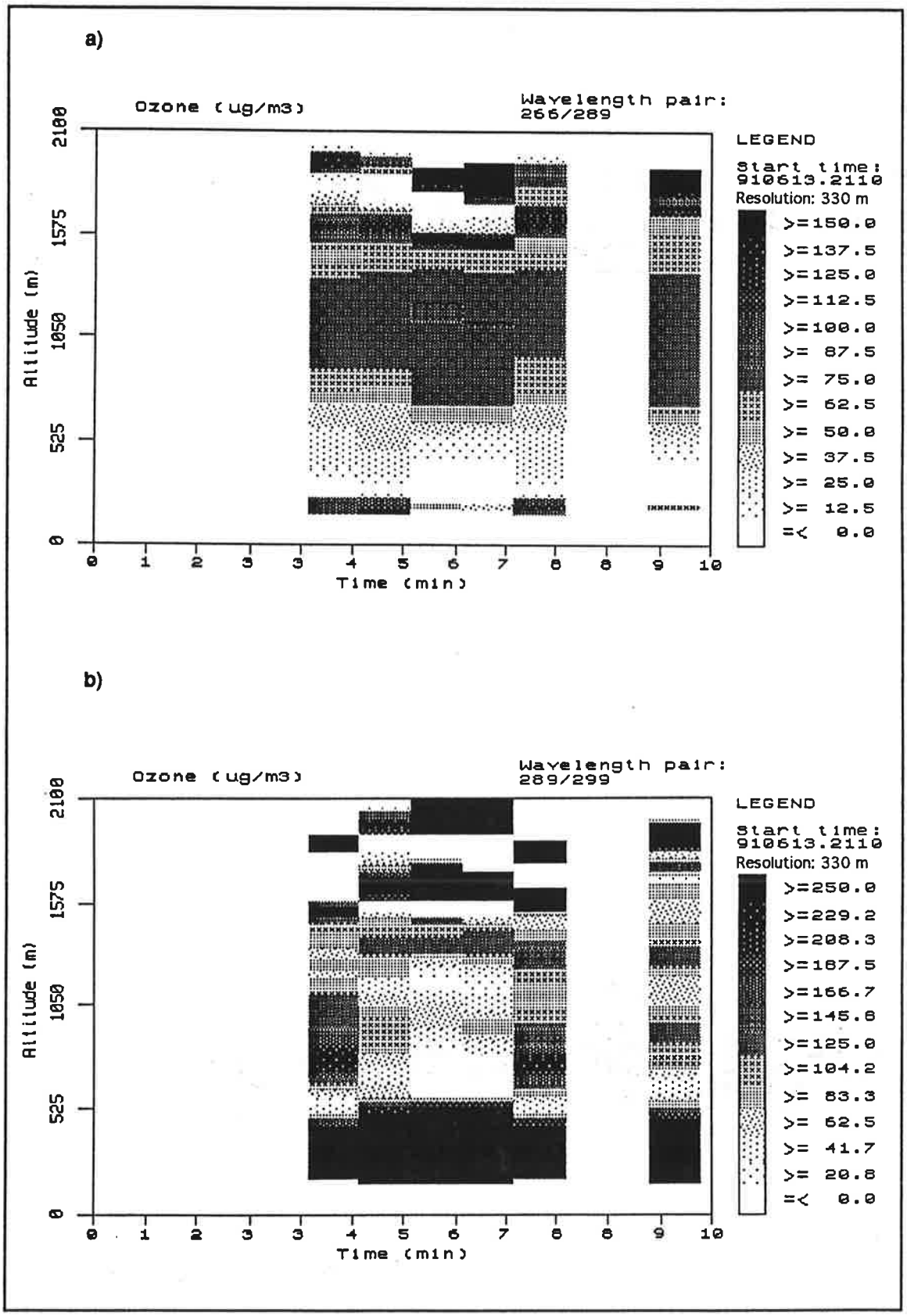

Figure 5.8: Ozone

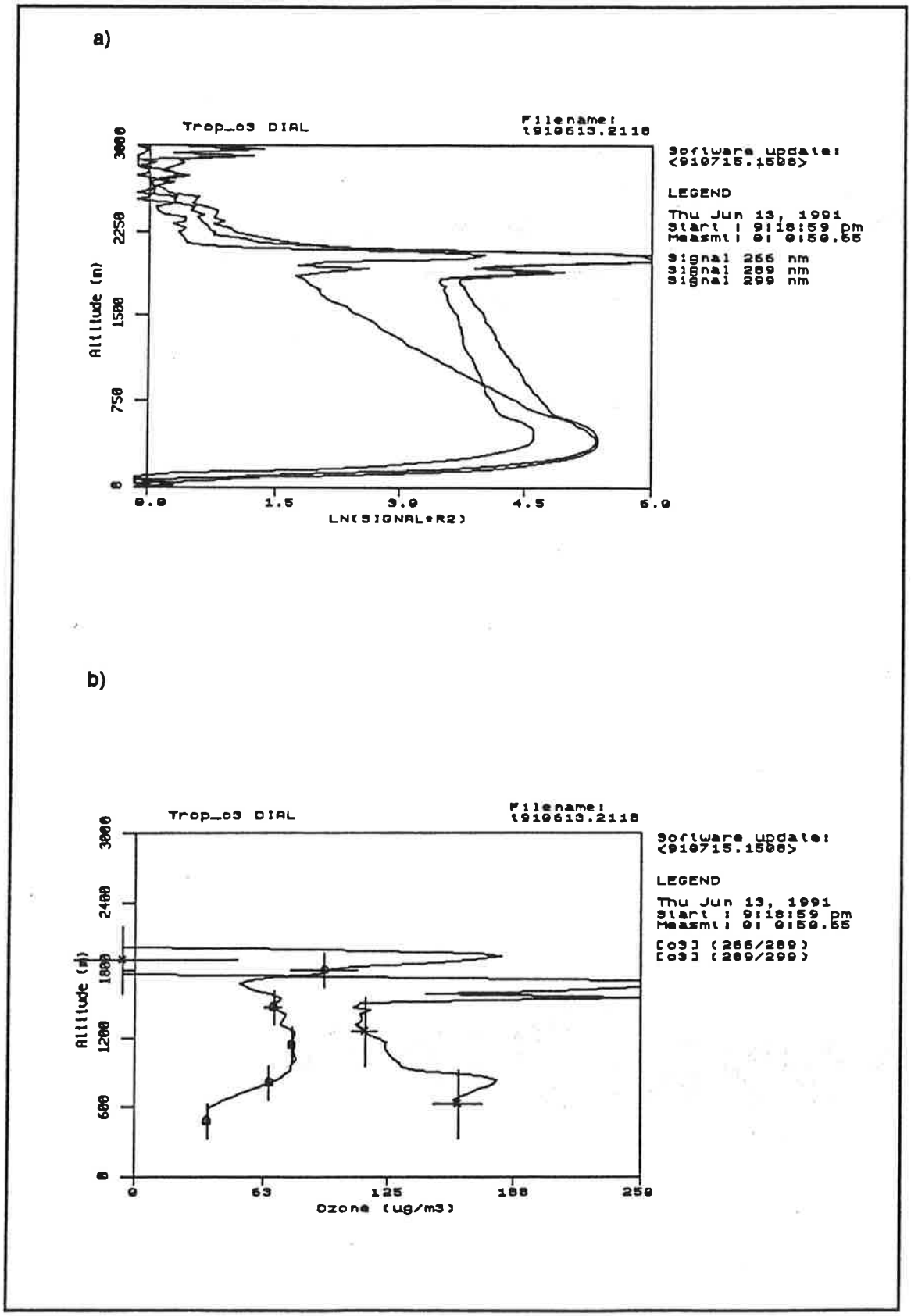

Figure 5.8: (continued) LIDAR returns and ozone profile

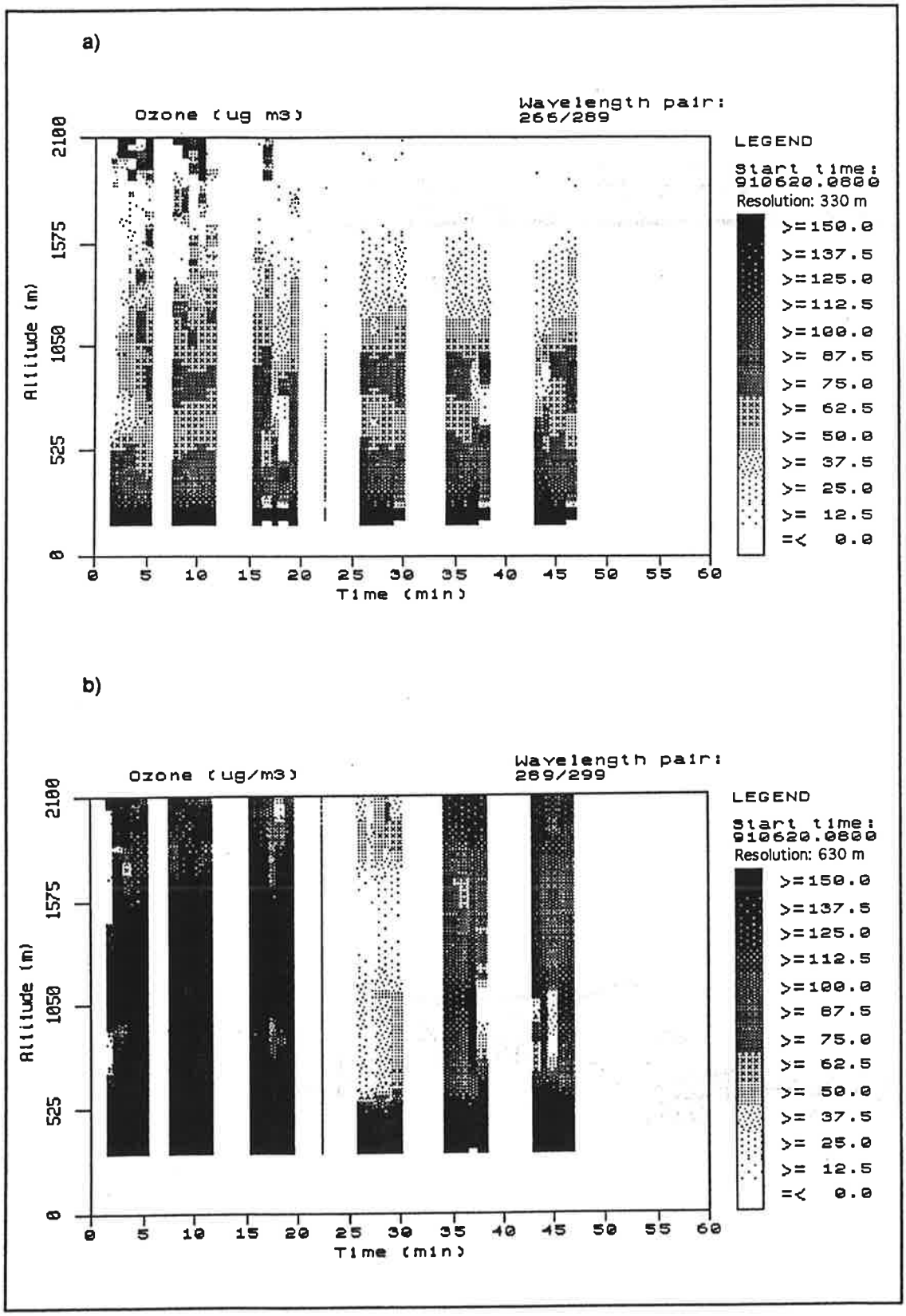

Figure 5.9: Ozone. Overlap problems in the 299 nm LIDAR return are present in the first four measurements series.

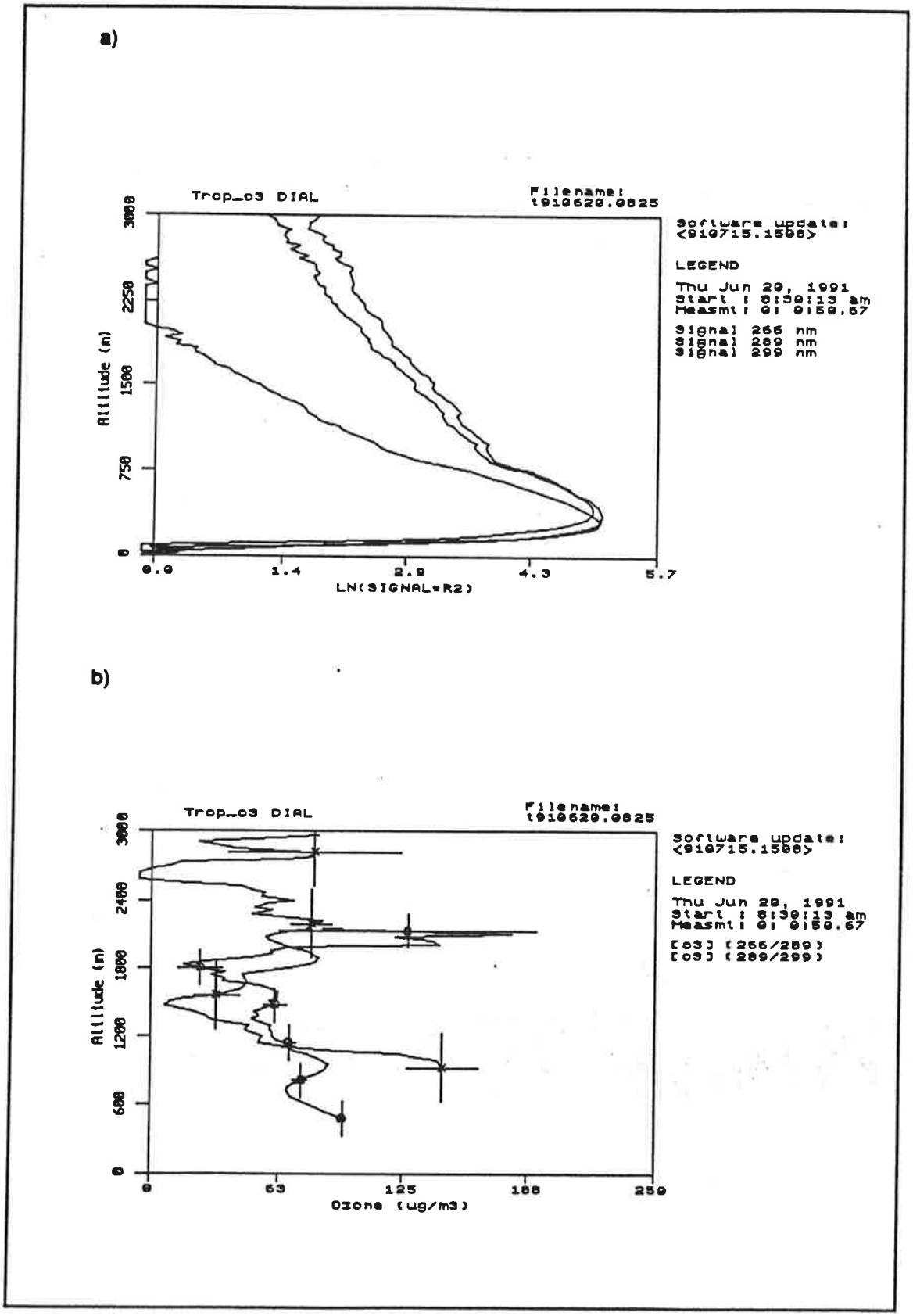

Figure 5.9: (continued) LIDAR returns and ozone profile

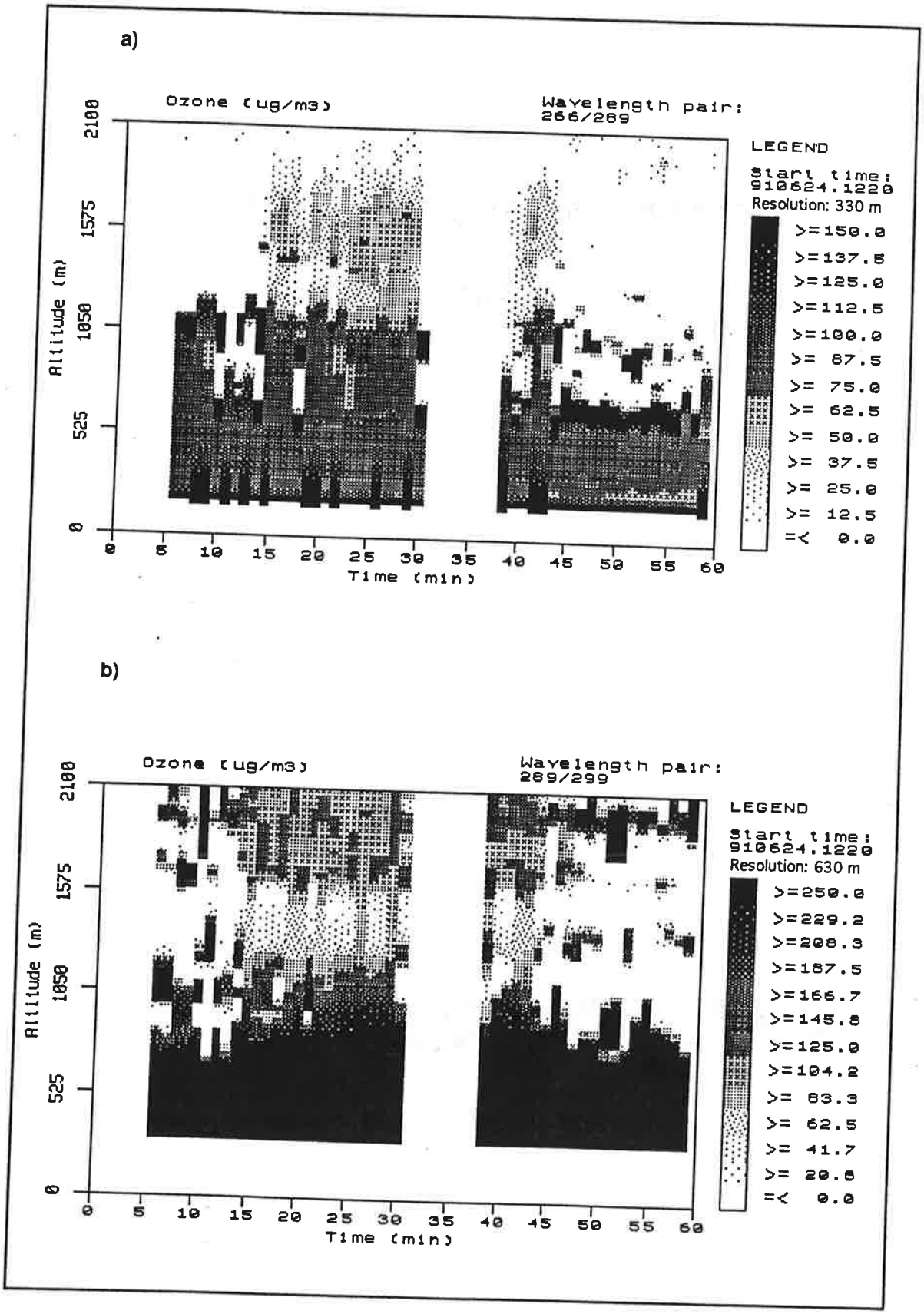

Figure 5.10: Ozone

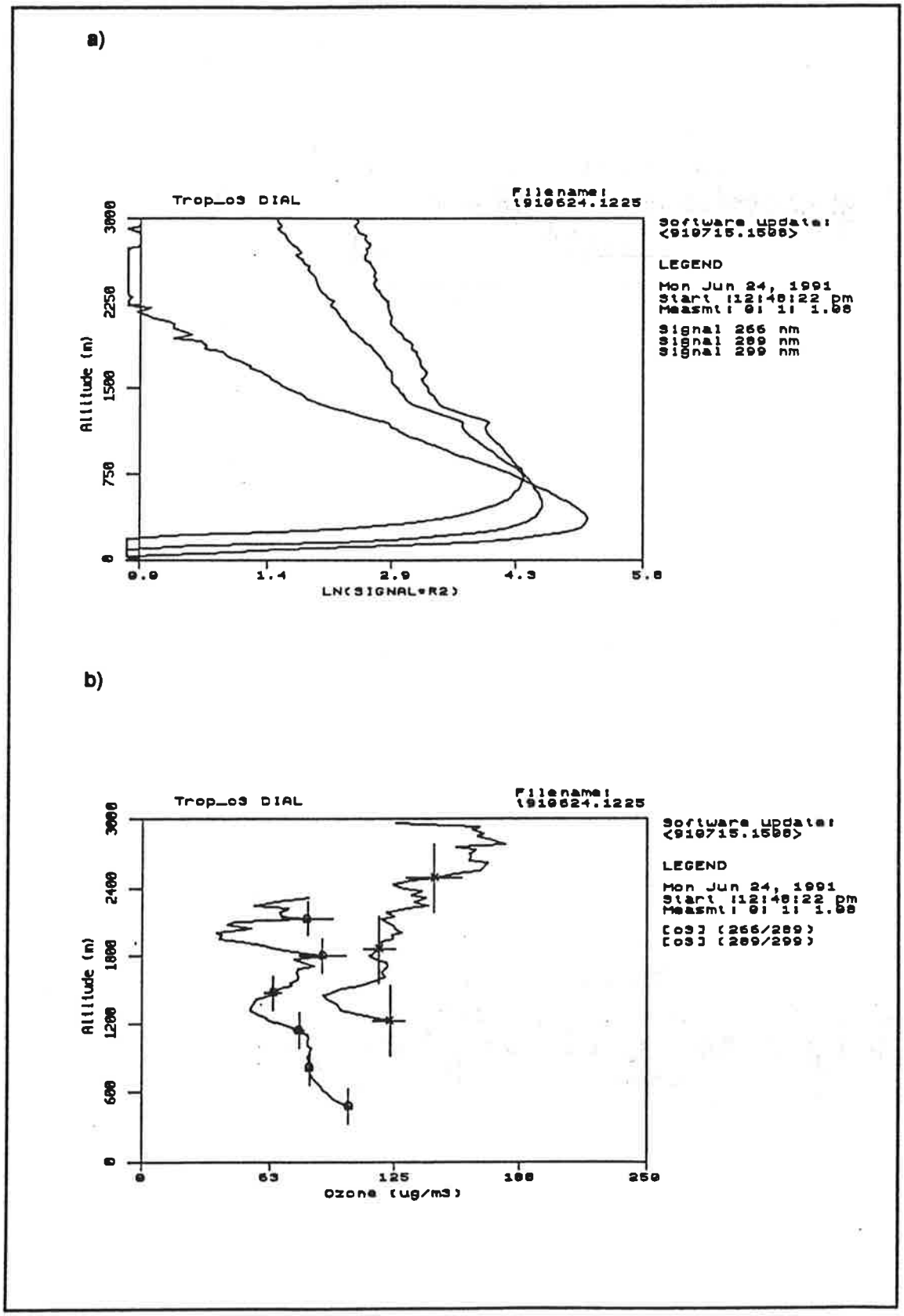

Figure 5.10: (continued) LIDAR returns and ozone profiles.

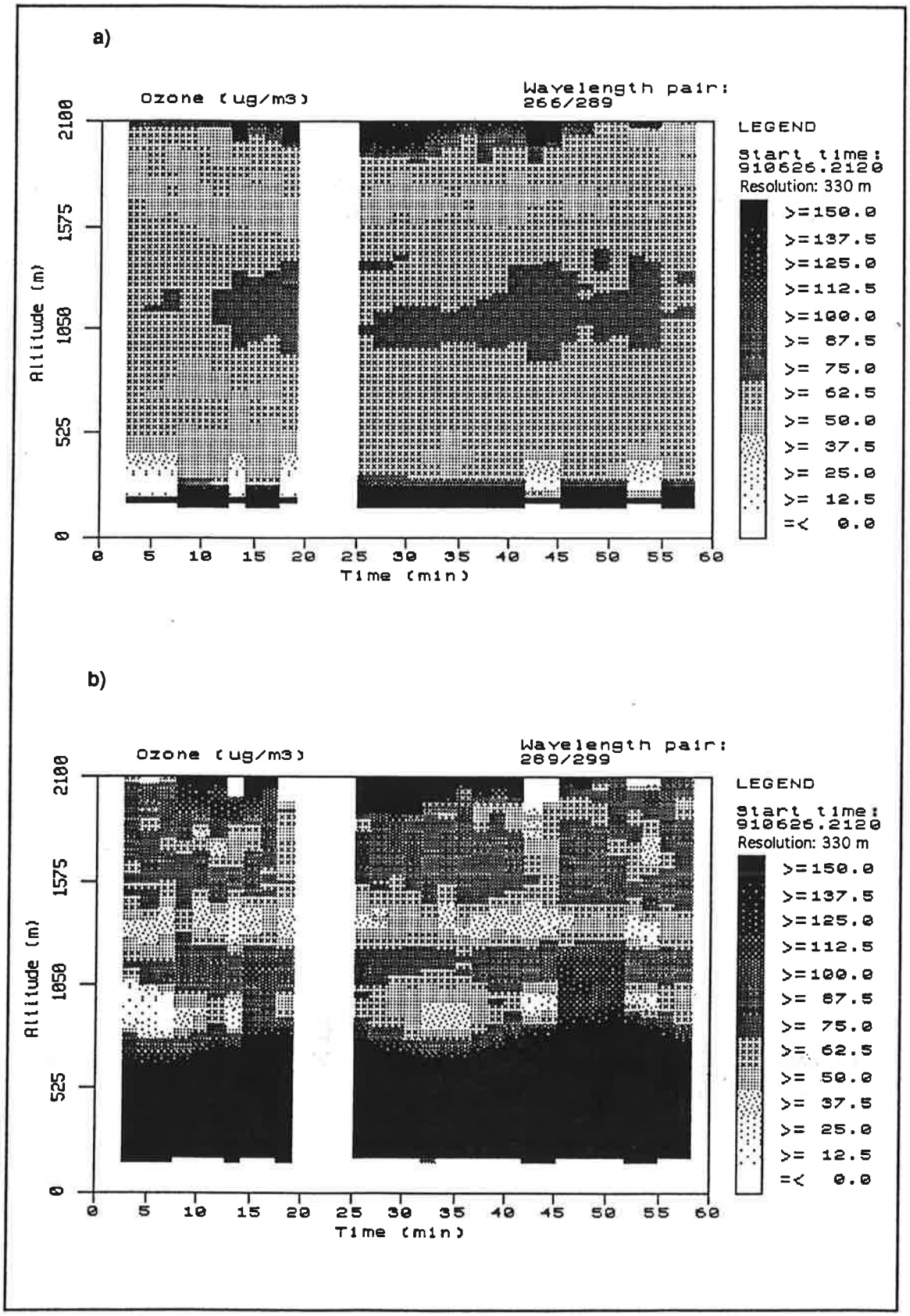

Figure 5.11: Ozone

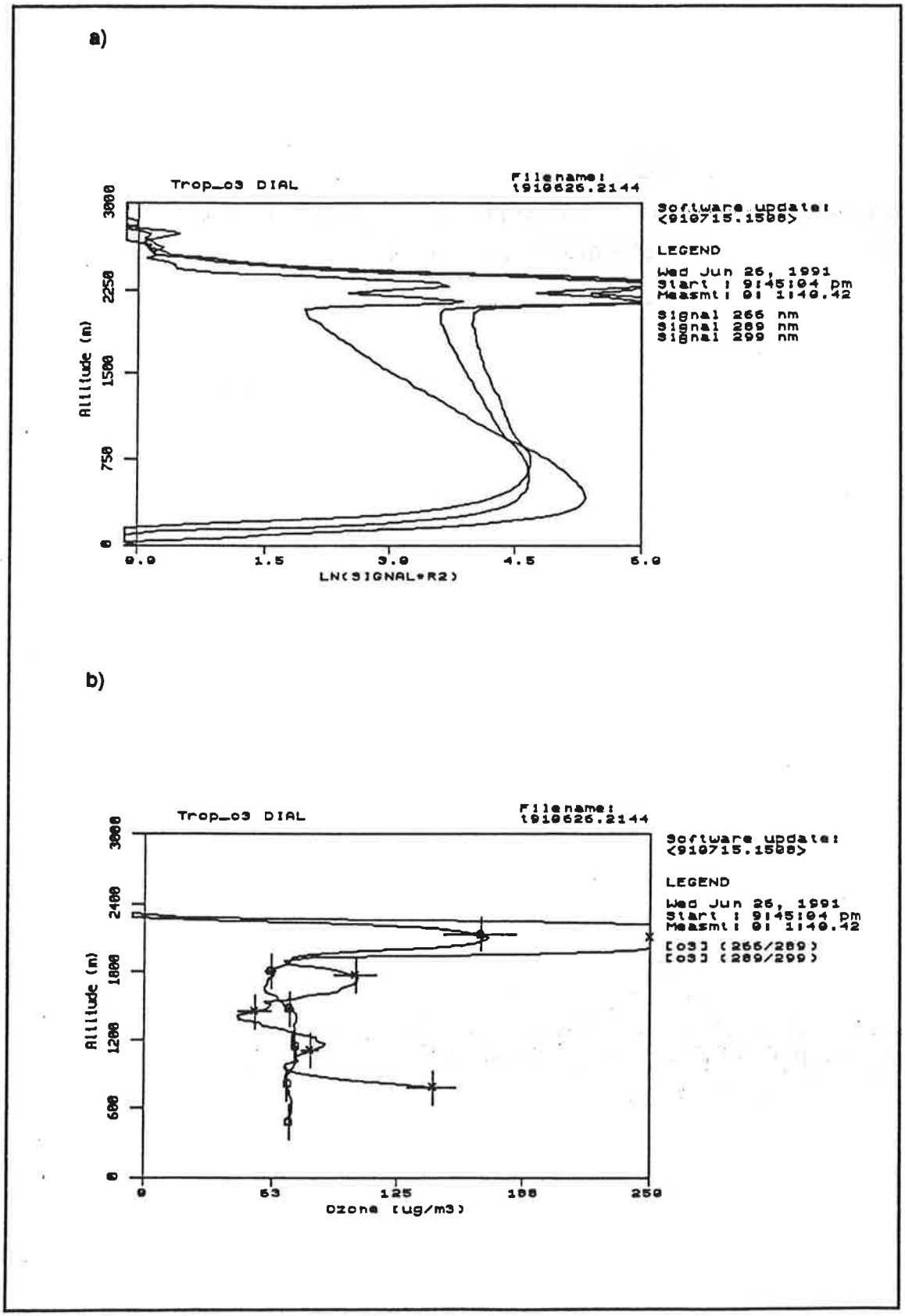

Figure 5.11: (continued) LIDAR returns and ozone profile

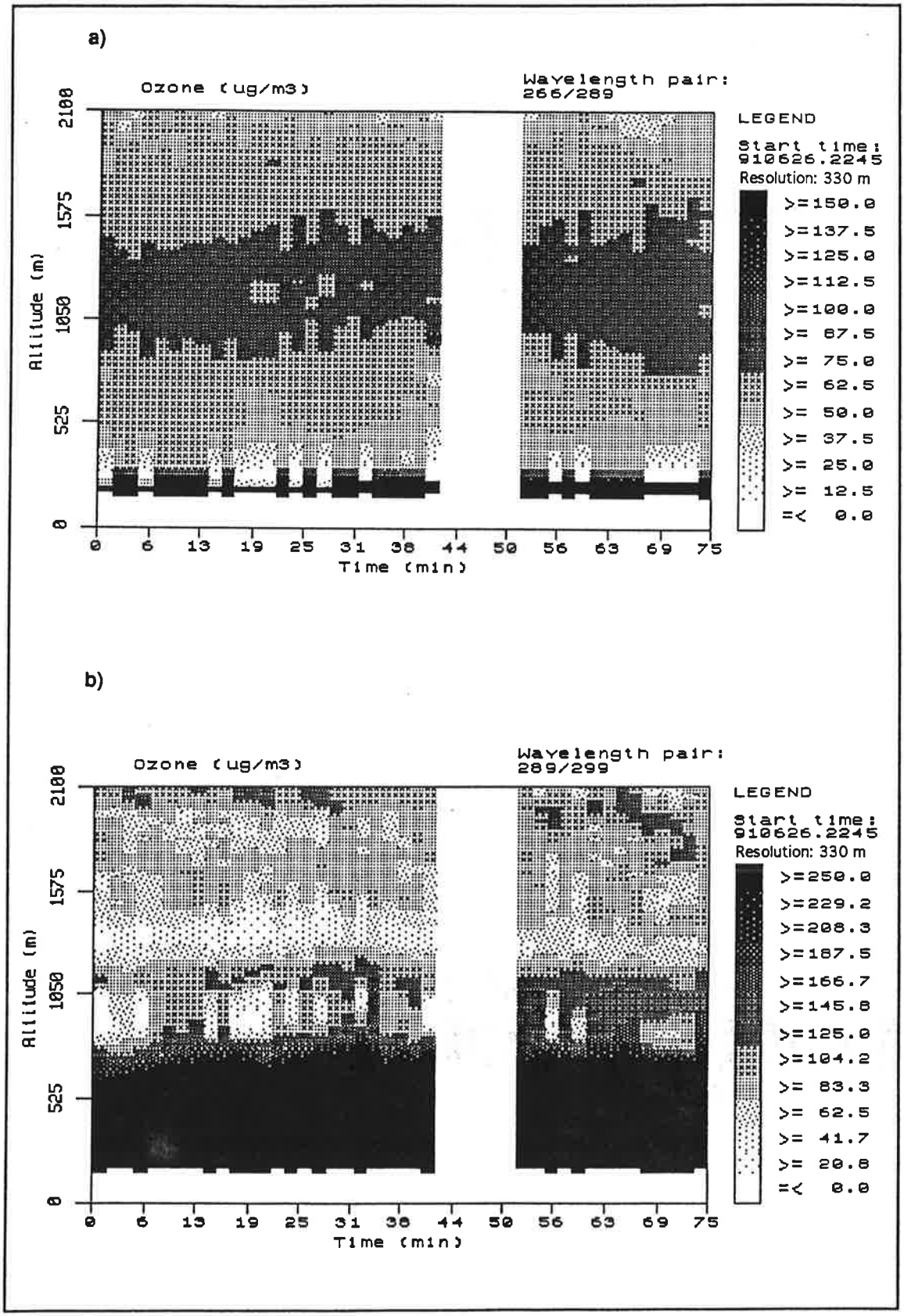

Figure 5.12: Ozone

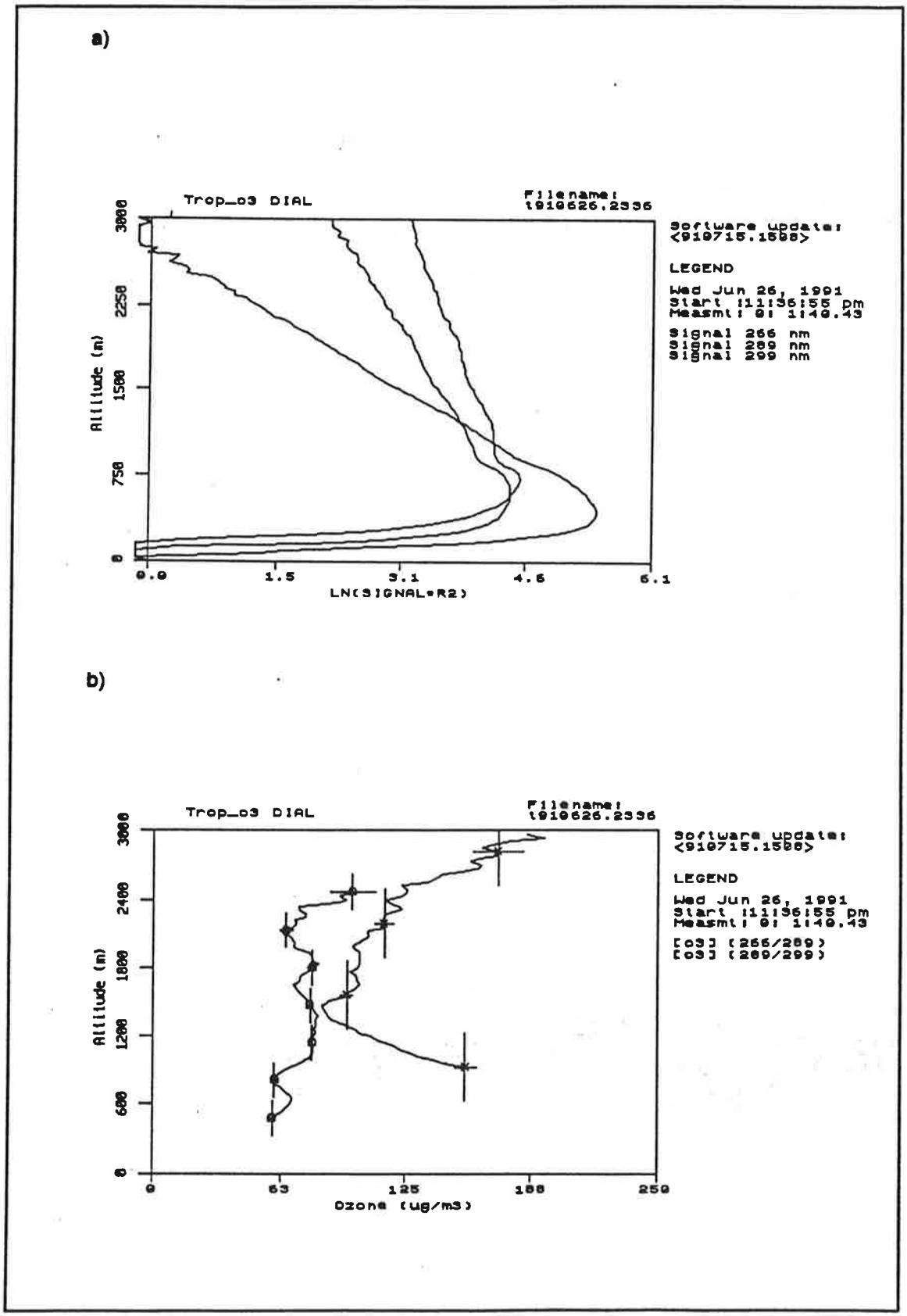

Figure 5.12: (continued) LIDAR returns and ozone profile

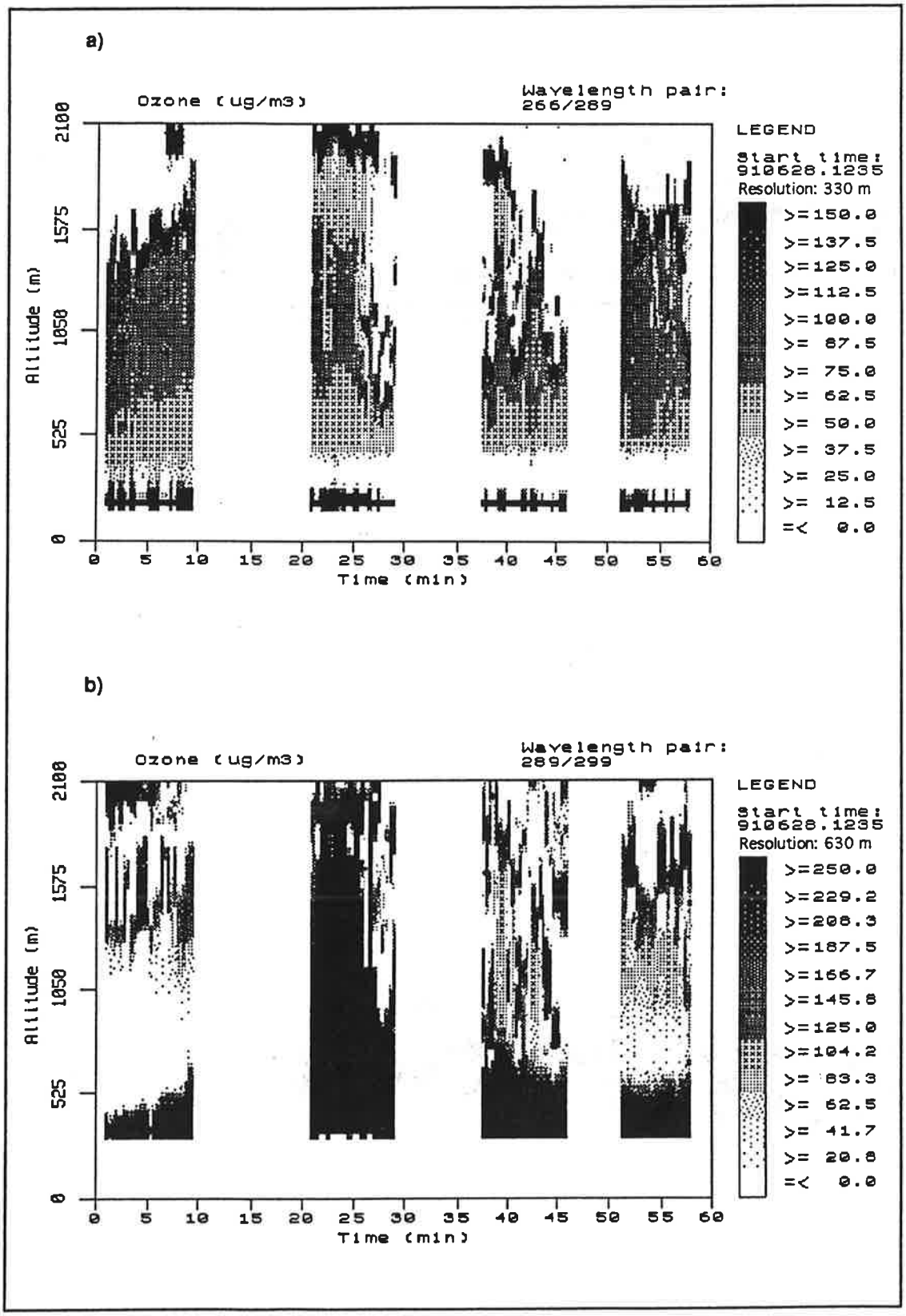

Figure 5.13: Ozone. Overlap problems are present in the 299 nm LIDAR return in the first two measurements series.

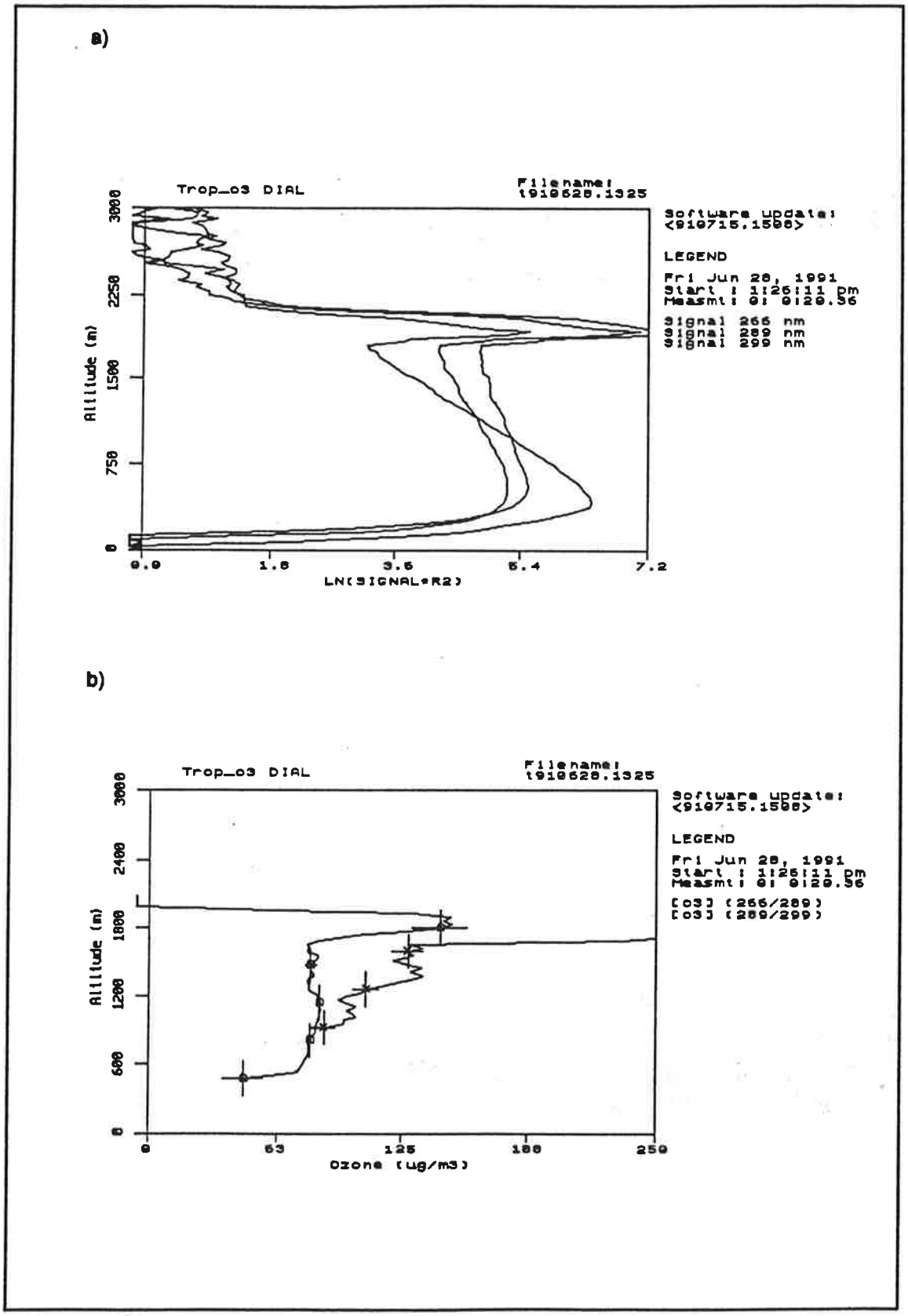

Figure 5.13: (continued) LIDAR returns and ozone profile

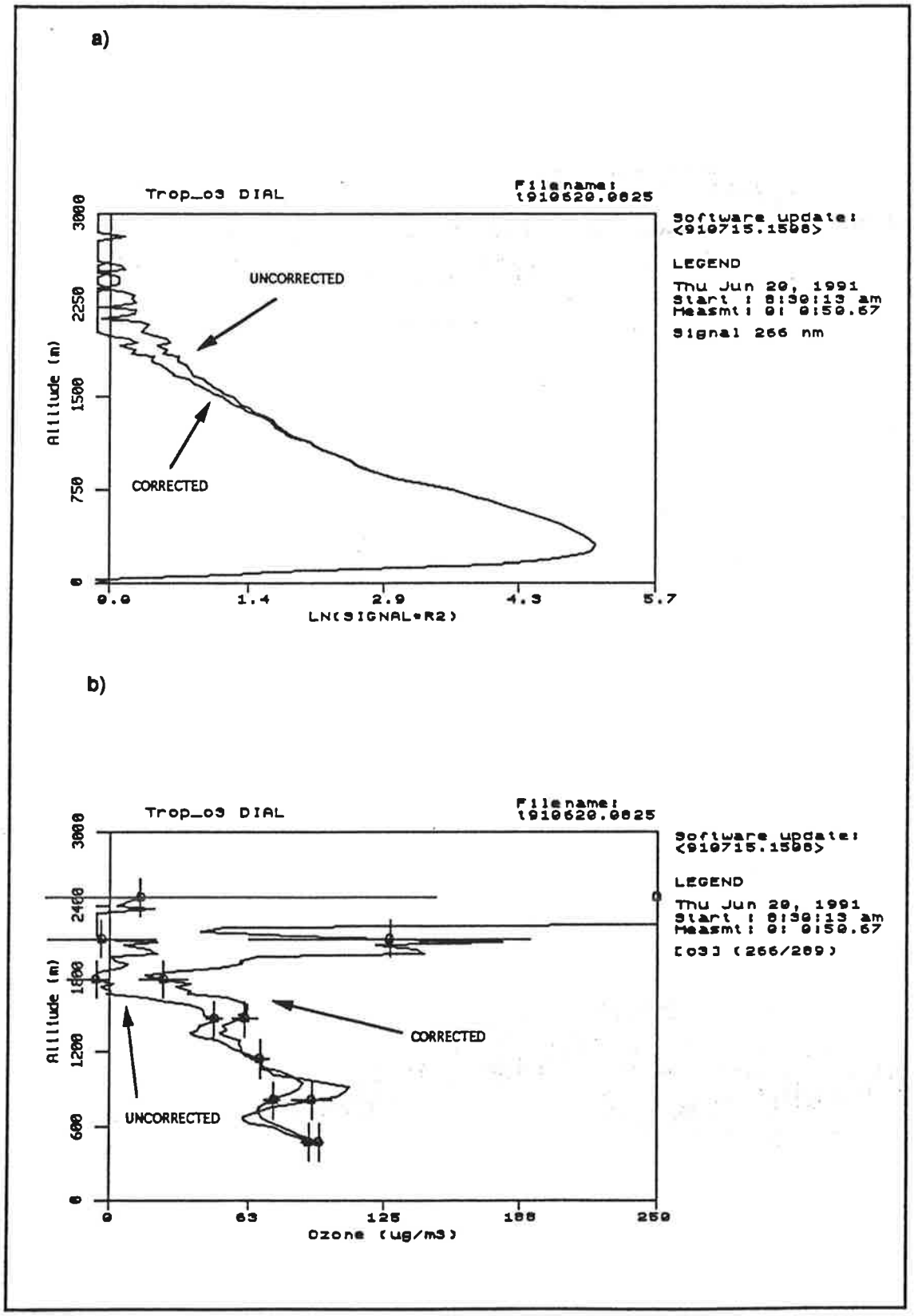

Figure 5.14: Example of SIB on concentration values. a) LIDAR return at 266 nm without and with SIB correction. b) Resulting ozone profiles from 266/289 nm wavelength pair.

5.3.2 CNRS/SA

The lidar system was operated from June 11^{th} to June 28^{th} and the measurement days and times are indicated in table 5.1 and figure 5.1. One can see that a full diurnal cycle was performed on June 13^{th} and June 14^{th}. Interruption in the data recording often corresponded to bad weather conditions (low clouds or rain) and not to technical problems. Data were collected during the first and the second helicopter flight, but the lidar was already disassembled for the last one in the afternoon of the 28^{th} of June.

Although the lidar system was providing useful data during the whole campaign, several problems were found during the operation of this new lidar. Some were expected, such as the presence of a signal induced noise or the difficulty to align the various beams so that ozone retrieval would be always possible between 300 m and 500 m:

-an example of the signal induced noise is shown in figure 5.15 where the logarithm of the signal is represented as a function of range. After the signal maximum at 3 km due to the cloud layer, one would expect a constant value representing the background signal. But one can see that the signal continues to decrease following approximately an exponential function (ln(S) decreases approximately as a linear function). However using an exponential function is not completely satisfactory to subtract this noise from the signal, a 4^{th} order polynomial function was found to be more appropriate to obtain experimental slope values close to the theoretical one. The theoretical slopes can be calculated for each wavelength separately using an atmospheric density model and using ozone values as derived from the DIAL equation or from ECC sondes for the days where there were available.

- the relative alignment of the 266 nm and 299 nm laser beams was always rather good since the two beams were generated by the same laser. Differences in the overlap function between the receiver and the transmitter were then only related to differences in the beam divergences. The resulting effect on ozone retrieval above 300 m was then found to be small ($< 5\ \mu g \cdot m^{-3}$). The relative alignment of the 289 nm beam with the other ones was more critical since it is generated by a different Raman cell. It was checked regularly by both maximizing the return signal at larger ranges and having the peak value at an altitude near 200 m. Because of the presence of elevated clouds, the second criteria was often used to determine the quality of the alignment. However this was sometimes misleading when high aerosol loads were present in the lower layers or when the laser beam's spatial properties changed.

Some unexpected problems encountered were: a minor problem related to the lifetime of the Raman cell windows, and the presence of a noise source on the 299 nm analog channels. Burning of the Raman cell windows by the input laser beam occured several times during the campaign due to the presence of an oily substance on the window's inner side. This will be solved by a better cleaning of the stainless steel tube and of the input valve of the cell. Noise interferences in the analog channels are shown in figure 5.16 where one can see spikes in the 299 nm signal generated in the waveform recorder. The frequency of the occurrence of the largest spikes is of the order of 250 kHz corresponding to a 600 m period wave structure superimposed on the 299 nm signal.

Results

Overview of the lidar data Before presenting greyscale representations of the ozone lidar profiles for the days of the priority list, two examples of 1 min ozone profiles are presented in figure 5.17 to obtain a better illustration of the profile quality. We selected two rather clear periods at the beginning and the end of the campaign. Three wavelength pairs have been used to compute the ozone concentrations from the analog signals: 266/289 nm, 289/299 nm, 266/299 nm. In addition to the profiles deduced from the analog channel, the profiles derived from the 289 nm and 299 nm photocounting channels are indicated.

There are rather large differences between the 289/299 nm pair and the other pairs below 1 km. This behavior has been often observed for our data recorded during the TROLIX campaign. Observation of the slopes $dln(S \cdot R^2)/dR$ for both wavelengths 289 nm and 299 nm (figure 5.18) shows the presence of a region of enhanced absorption below 1 km on June 26^{th}. It supports the idea of an aerosol interference region on this day, but it is not the case for June 13^{th}. These differences could then be related both to a misalignment of the 289 nm and 299 nm laser beams and to aerosol interferences in the boundary layer. Above 1 km, the agreement depends on the intensity of the 289 nm signal which was not very large in the evening of June 26^{th} (decrease of the laser output power or misalignment of the 289 nm beam tilted away from the telescope axis). The decrease in the 289 nm intensity results in an overestimation of the 289 nm slope when the signal induced noise effect is corrected.

The 266/299 nm pair is the least sensitive one to misalignment since these two beams are emitted from the same Raman cell. Overlap between the photocounting and the analog mode is not observed since the gain of the analog amplifier was set to a rather small value. The choice of the analog gain value is always a trade-off between generating large input signals on the waveform recorder and avoiding ringing on the output of the amplifier. The photocounting mode allows ozone measurements between 2 and 4 km.

Time series of the ozone vertical distributions are presented in figure 5.19 to 5.25 for the selected time period excepted for the first day due to difficulty in reading the data back from the tape and the last day when our lidar system was being disassembled. Results for the two wavelength pair 266/289 nm (or 266/299 nm) and 289/299 nm are presented except for June 24^{th} when the 289 nm signal was completely misaligned. The ozone profiles in these time series are integrated over a 1 min. time interval and they were not corrected for aerosol interferences.

On June 13^{th} in the afternoon, ozone concentrations shows a positive gradient in the boundary layer up to 1.2 km. Sudden drops or increases in the ozone values in the 14:00-15:00 time series are not representative since these correspond to time periods when the PMT gain was adjusted: 14:20 for the 266/289 nm pair, and from 14:25 to 14:45 for the 289/299 nm pair. The weather pattern was characterized by isolated cloud structures and large instabilities as expected behind a cold front. Presence of clouds generated erroneous values above 1.2 km in the 289/299 nm pair around 15:07, 15:20 and 15:35. Comparing the two wavelength pairs shows clearly a layer of high ozone values on the 289/299 nm

pair near 0.7 km which does not appear on the 266/289 nm data. This discrepancy was already discussed in the previous paragraph.

On June 20^{th}, the cloudiness was characteristic of the leading part of the warm front with a cloud deck at 2.5 - 3 km and a boundary layer extended not higher than 0.8 to 1 km with often poor transmission during the measuring period: 08:18/08:20, 08:24/08:28, 08:35/08:43. The agreement between the two wavelength pairs is better than for the previous case although the large variability of the cloud structure appears to be more important in the ozone profiles derived from the 289/299 nm pair. It is clear that this pair will be more sensitive to aerosol interferences necessarily present between the periods of cloud formation at the top of the boundary layer. Nevertheless a rise in the altitude of the ozone maximum associated with the development of the boundary layer can be seen in both displays. It is interesting to observe that this increase of the boundary layer depth corresponds also to a rise in the ozone values recorded at ground level.

On June 24^{th}, the ozone temporal evolution is derived only from the 266/299 nm pair. The cloudiness was rather important as for June 20^{th} since the meteorological situation was similar. A cloud deck was always present at 1.1 km (except from 08:45 to 08:50) with an additional cloud layer present at 0.7 km around 12:30 and from 12:50 to 13:05. The ozone maximums calculated at 1.0 km or 0.6 km are likely to be related to the large positive aerosol gradients below the clouds.

On June 26^{th}, the ozone temporal evolution is presented for the three wavelength pairs. A cloud layer is present near 2 km until 22:40 and the rest of the evening is characterized by a clear sky. The ozone data derived from the 289/299 nm pair are erroneous as the 289 nm channel was probably misaligned. This is seen also in the ozone derived from the 266/289 nm pair which shows larger values than for the 266/299 nm pair. Electronical noise was also present in the 299 nm analog channel for some of the data recorded between 23:00 and 24:00. It is seen in the data as periods of large ozone values both in the 266/289 nm and 289/299 nm time series.

Intercomparison with in-situ measurements On June 20^{th} and on June 24^{th}, comparisons were made with an ECC sonde and a UV absorption spectrometer both mounted in an helicopter flying around the institute. For the first day, lidar data have been averaged from 08:20 to 08:40 excluding the file with a very low transmission in the lower layer. For the second day, lidar data were averaged from 12:47 to 12:51 during the short time where good transmission was obtained through the cloud layer. The lidar data have been corrected of the aerosol interferences by the Klett method as it will be explained in the next section. The lidar profiles are represented in figure 5.26 with the results of the in-situ measurements. One can see that the 266/289 nm or 266/299 nm profiles are in good agreement with the in-situ data up to 1 km, but show larger values (differences of 10-20 $\mu g \cdot m^{-3}$) between 1 and 1.5 km for June 20^{th}. Even if one includes the 5 $\mu g \cdot m^{-3}$ error due to the 266 nm signal absorption by oxygen, this difference remains unexplained and may be due to low frequency noise on the 266 nm channel. The comparison with the 289/299 nm pair shows poor agreement below 500 m indicating the strong influence of the laser beam alignment on the ozone retrieval. Above 500 m the overall agreement

is satisfactory, but the 600 m low frequency oscillation indicated above seems to create a distortion of the ozone profile which shows differences of 10 $\mu g \cdot m^{-3}$ with in -situ data.

Aerosol correction To account for the aerosol interferences, one can estimate the aerosol backscatter coefficient profile, $\beta_p(r)$, from the 299 nm analog signal S(r). According to Klett's formulation, the lidar differential equation, including the effect of Rayleigh scattering $\beta_R(r)$ can be written as:

$$dS'/dr = d\beta/\beta dr - 2\beta/C \tag{5.1}$$

where $\beta = \beta_R + \beta_p$, and C is the aerosol backscatter to extinction ratio.

$$S'(r) - S'(r_m) = S(r) - S(r_m) - 16\pi/3 \int_r^{r_m} \beta_R(1 - 3/8\pi C)dr - 2\int_r^{r_m} \alpha_{oz} dr \tag{5.2}$$

where α_{oz} is the ozone (or SO_2) extinction coefficient and r_m is a reference altitude at the highest altitude possible (i.e. where the signal to noise ratio is still large enough). The solution of equation 4.2 is given by:

$$\beta(r) = exp(S'(r) - S'(r_m))/\{1/\beta_m + 2\int_r^{r_m} exp(S'(r) - S'(r_m))dr/C\} \tag{5.3}$$

where β_m is an initial value for β at the altitude r_m. The parameter values selected were: $r_m = 2.1$ km and $\beta_m = 0.018$ km^{-1} considering that the inversion procedure is then insensitive to the choice of β_m below 1.8 km. The Rayleigh scattering coefficient is derived from the same density model which is used for the correction of the Rayleigh absorption in the lidar processing algorithm. The ozone extinction coefficient is calculated from the ozone profile estimated by the lidar before the aerosol correction. Errors in the ozone profile do not change β(r) significantly since the latter depends mainly on the integrated ozone absorption. The most critical parameter is the backscatter to extinction ratio S which is supposed to be range independent and is set to 0.02 corresponding to a middle value between urban condition with a 70% relative humidity (S=0.01) and maritime condition with similar humidity (S=0.06) [Shet 79]. To calculate the aerosol backscatter coefficient at the other wavelengths (266 nm and 289 nm), one must specify a wavelength λ dependence for the aerosol backscatter and extinction coefficient which is chosen to vary as $\lambda^{-0.9}$ for both coefficients. This value corresponds to the largest spectral variation of the aerosol backscatter coefficient which may range between $\lambda^{-0.1}$ and λ^{-1}.

The aerosol backscatter coefficient profiles at 299 nm are represented in figure 5.27 and 5.28 for the two days where the intercomparisons with the in-situ measurements were performed. For the first day, one can observe the presence of a thin cloud layer at 0.7 km which is the top of the boundary layer. On the second day, the boundary layer is more developed and its top corresponds to the sharp gradient at 1.25 km. The ozone profiles were corrected from the aerosol interferences (extinction and scattering) for both wavelength pairs on June 20^{th}, but only on the pair 266/299 nm for June 24^{th}. As

expected the correction remains small (less than 10 $\mu g \cdot m^{-3}$) for the 266/289 or 266/299 pair owing to the large ozone differential absorption. For the 289/299 nm, the correction is much larger, especially at the altitude of the large aerosol gradient where it can be as large as 40 $\mu g \cdot m^{-3}$. The contribution of the extinction within the boundary layer is two times smaller and it is interesting to note that the misalignment error can be hidden by an aerosol interference on June 20^{th}. However it should be remembered that this aerosol correction may be overestimated due to the large spectral variation chosen for the aerosol backscatter coefficient. It is clear that more work is needed to initialize the aerosol correction algorithm: determination of C and of the spectral variations of the backscatter and extinction coefficient. The results on aerosol correction shown in this report are then considered only as preliminary.

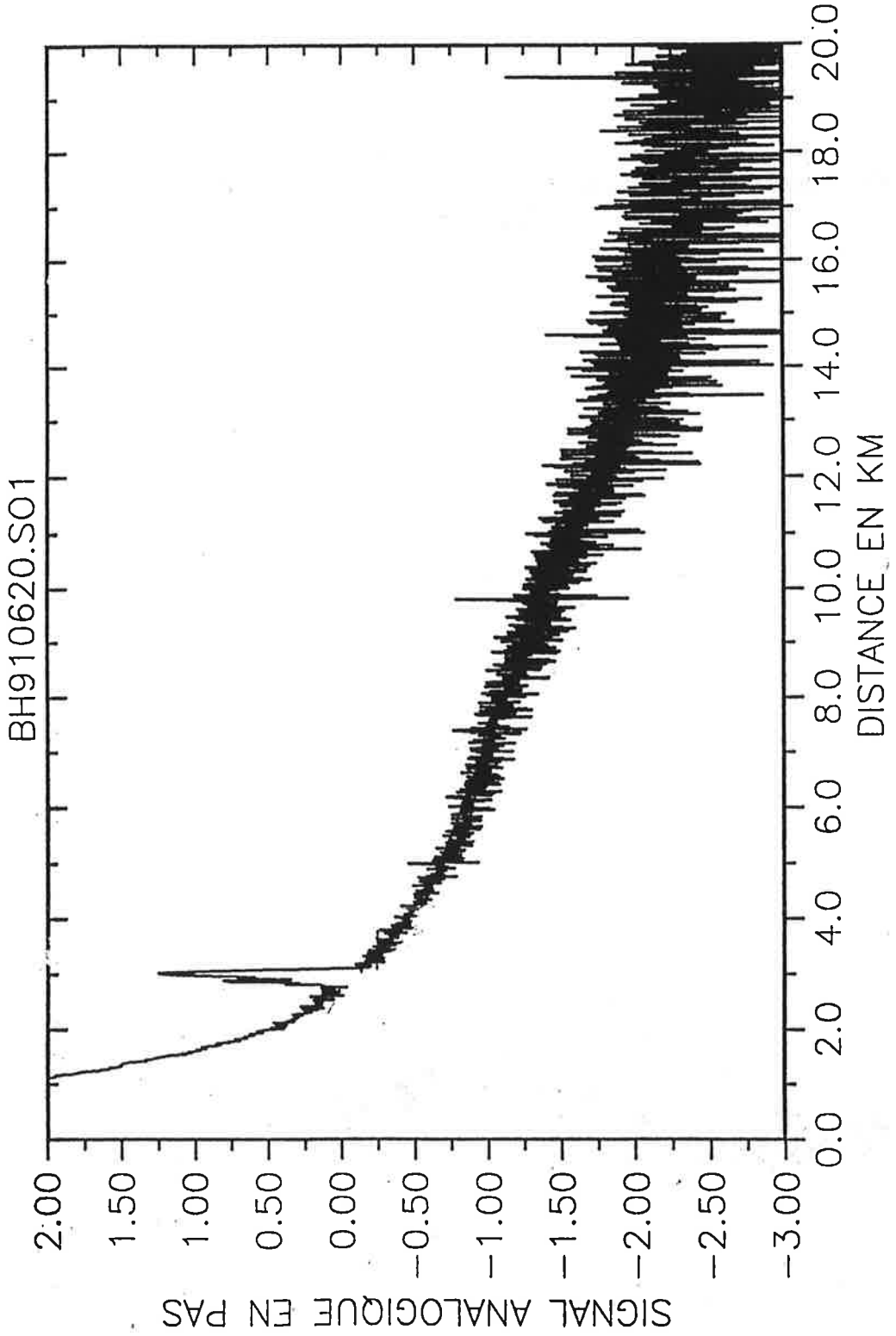

Figure 5.15: Natural logarithm of the raw analog signal at 289 nm versus range

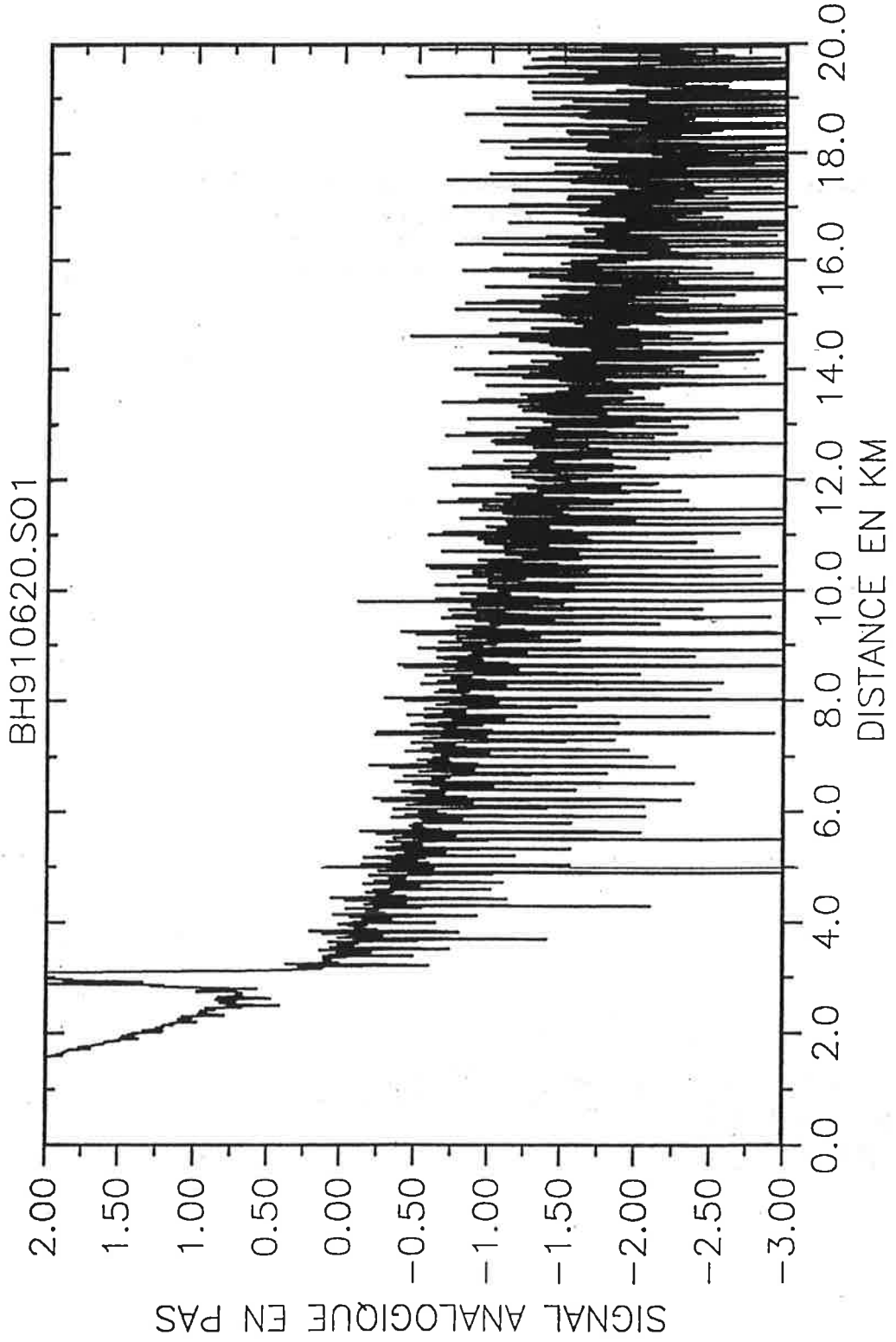

Figure 5.16: Natural logarithm of the raw analog signal at 299 nm versus range

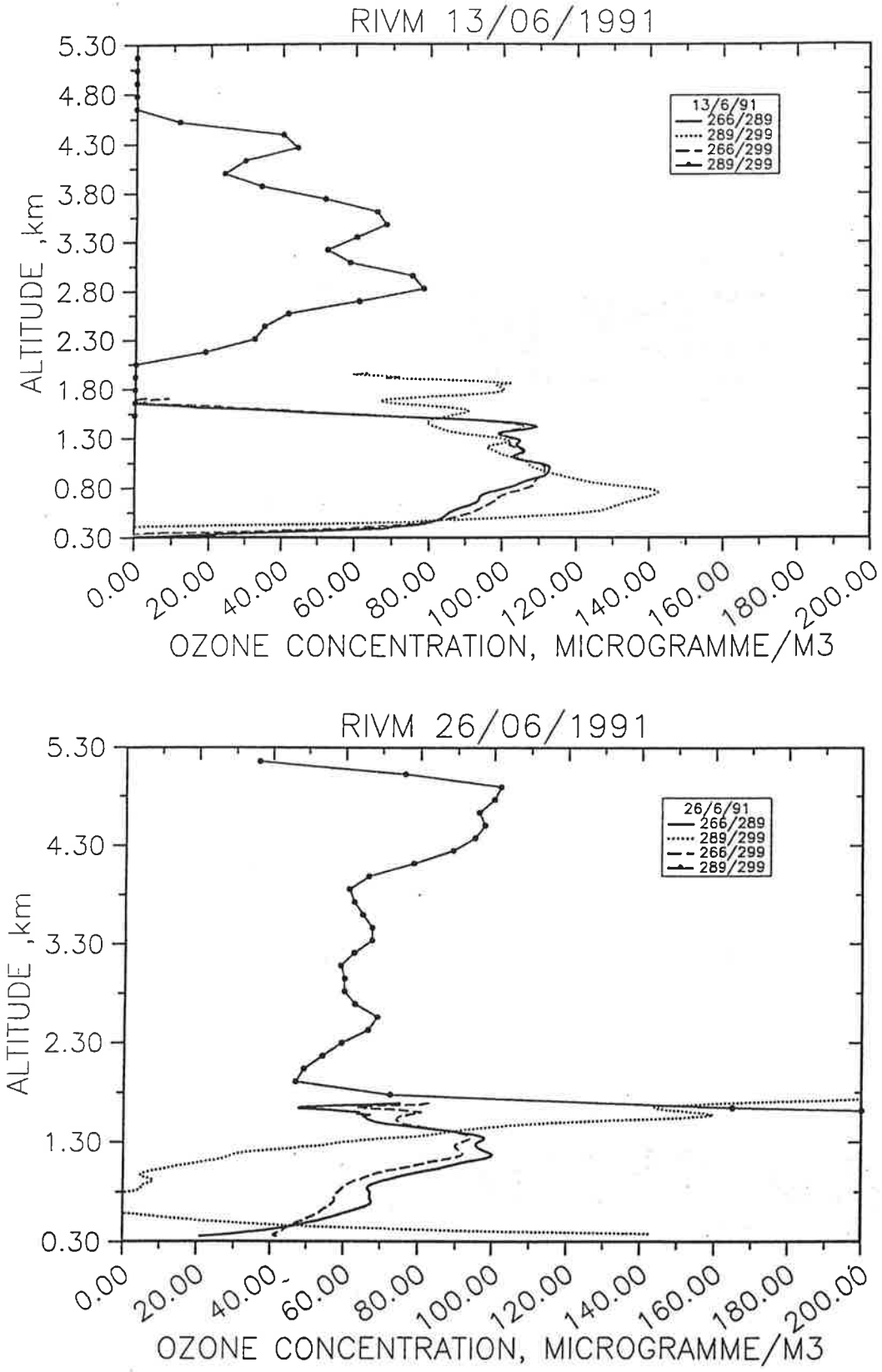

Figure 5.17: Ozone profiles measured by the CNRS lidar for several wavelength pairs using analog detection (below 2 km) and photocounting detection (above 2 km).

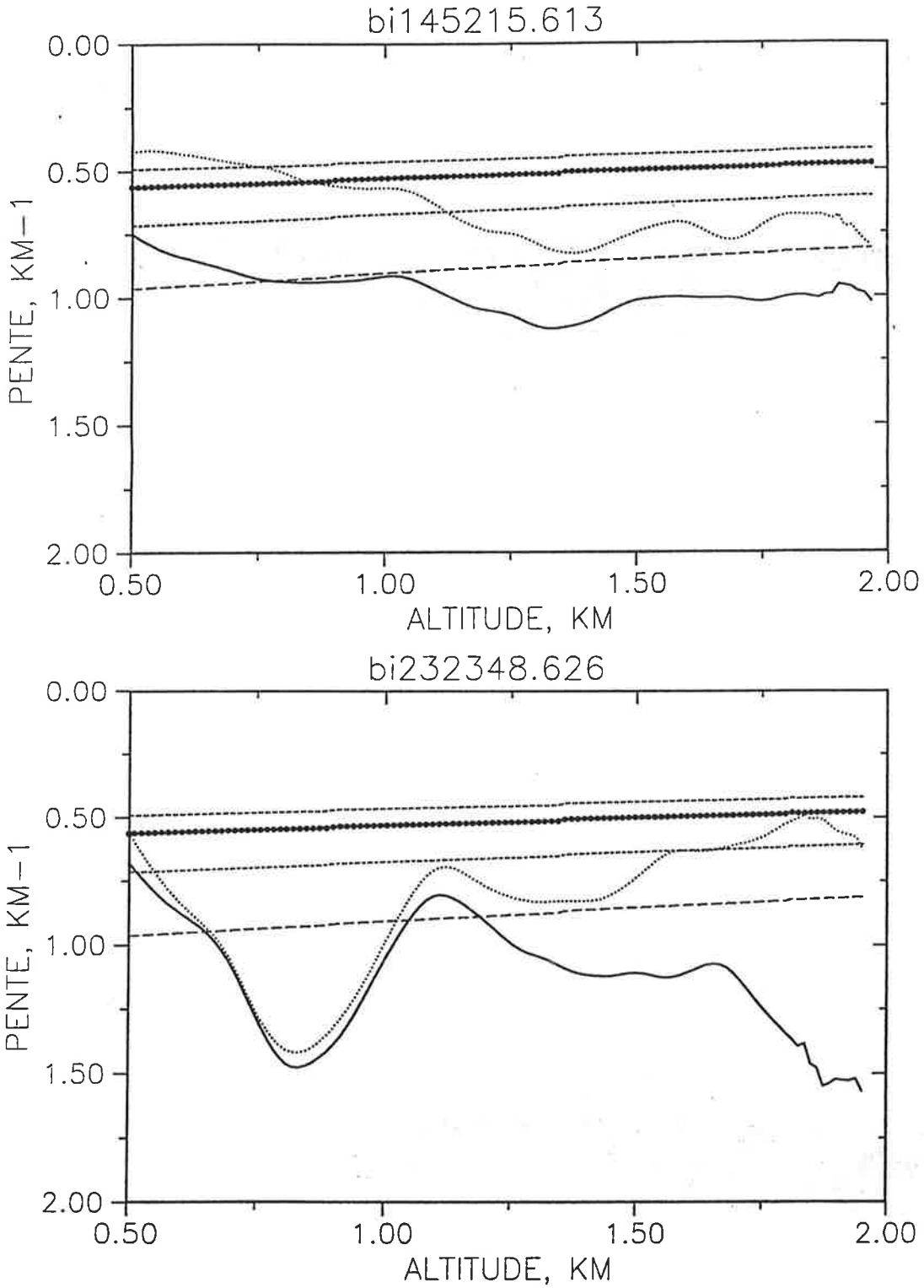

Figure 5.18: Slopes of the 289 and 299 nm signals corrected from Rayleigh absorption for the two ozone profiles shown in figure 5.17. The two straight lines in the upper part of the figure represent the theoretical slopes for the wavelength 299 nm and for two constant ozone mixing ratios (40 ppb and 60 ppb). The other two straight lines are the theoretical slopes for the wavelength 289 nm and for the same ozone mixing ratios.

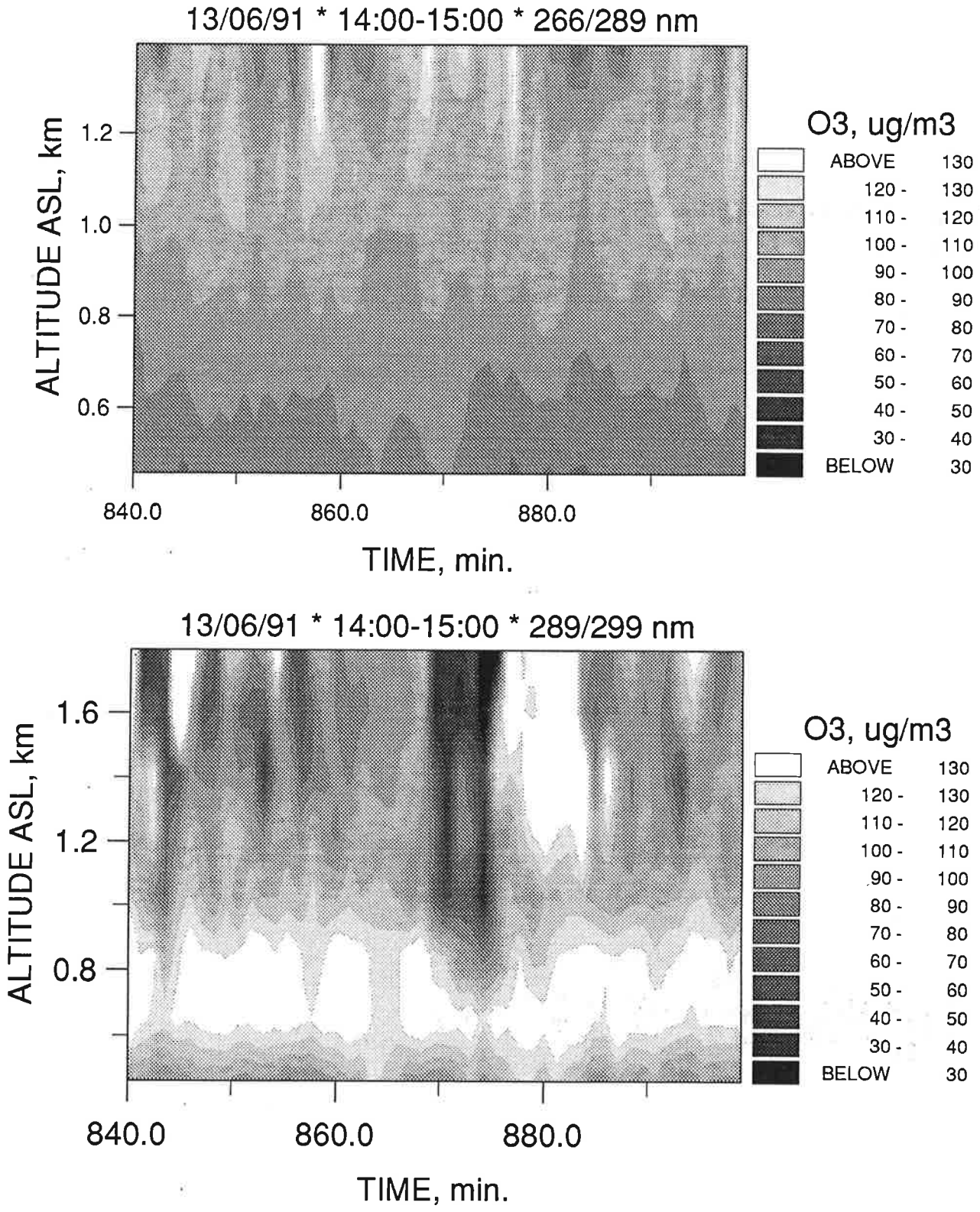

Figure 5.19: Ozone vertical distribution in $\mu g \cdot m^{-3}$ recorded on June 13, 1991 for the wavelength pair 266/289 nm (upper display) and 289/299 nm (lower display).

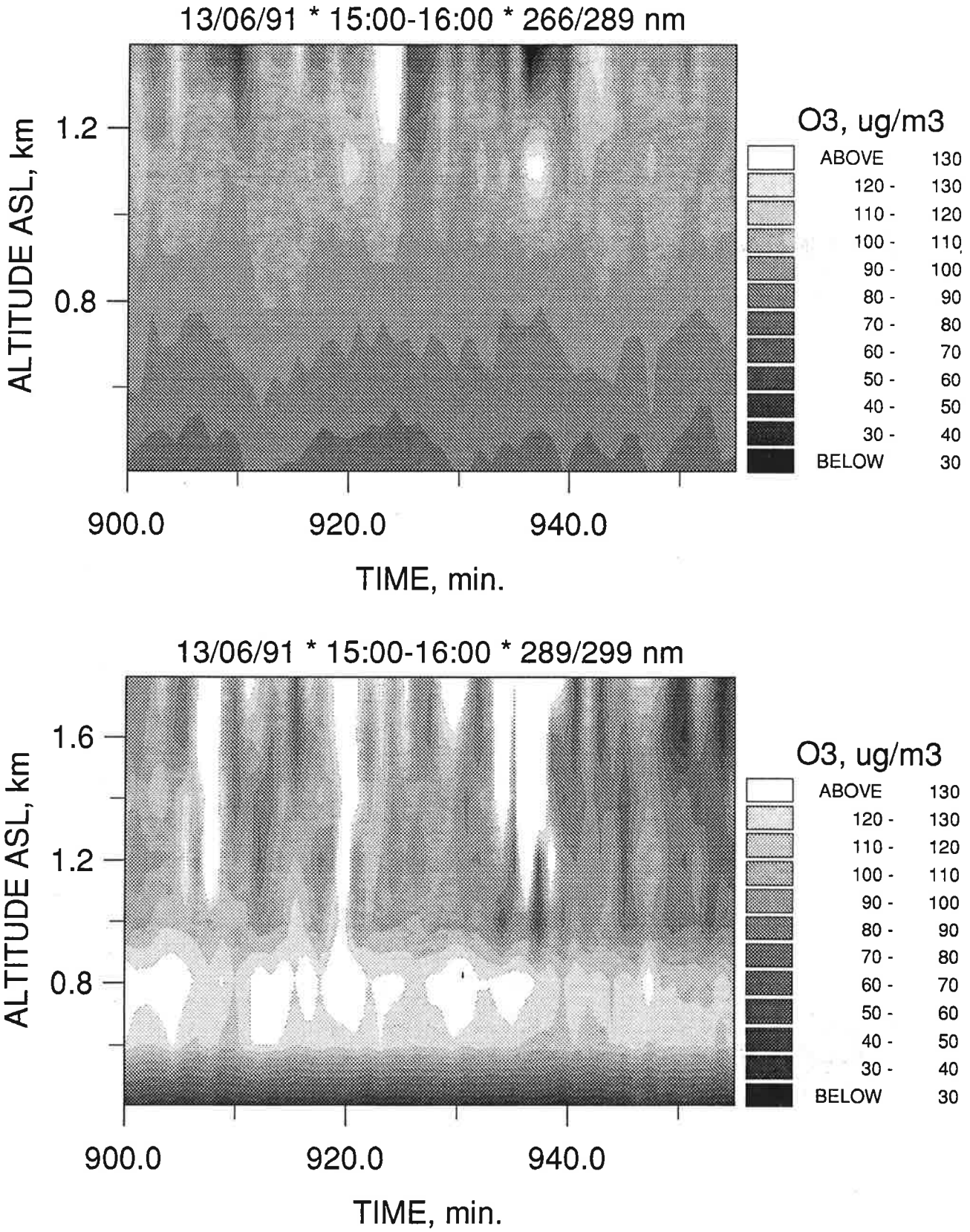

Figure 5.20: Ozone vertical distribution in $\mu g \cdot m^{-3}$ recorded on June 13, 1991 for the wavelength pair 266/289 nm (upper display) and 289/299 nm (lower display).

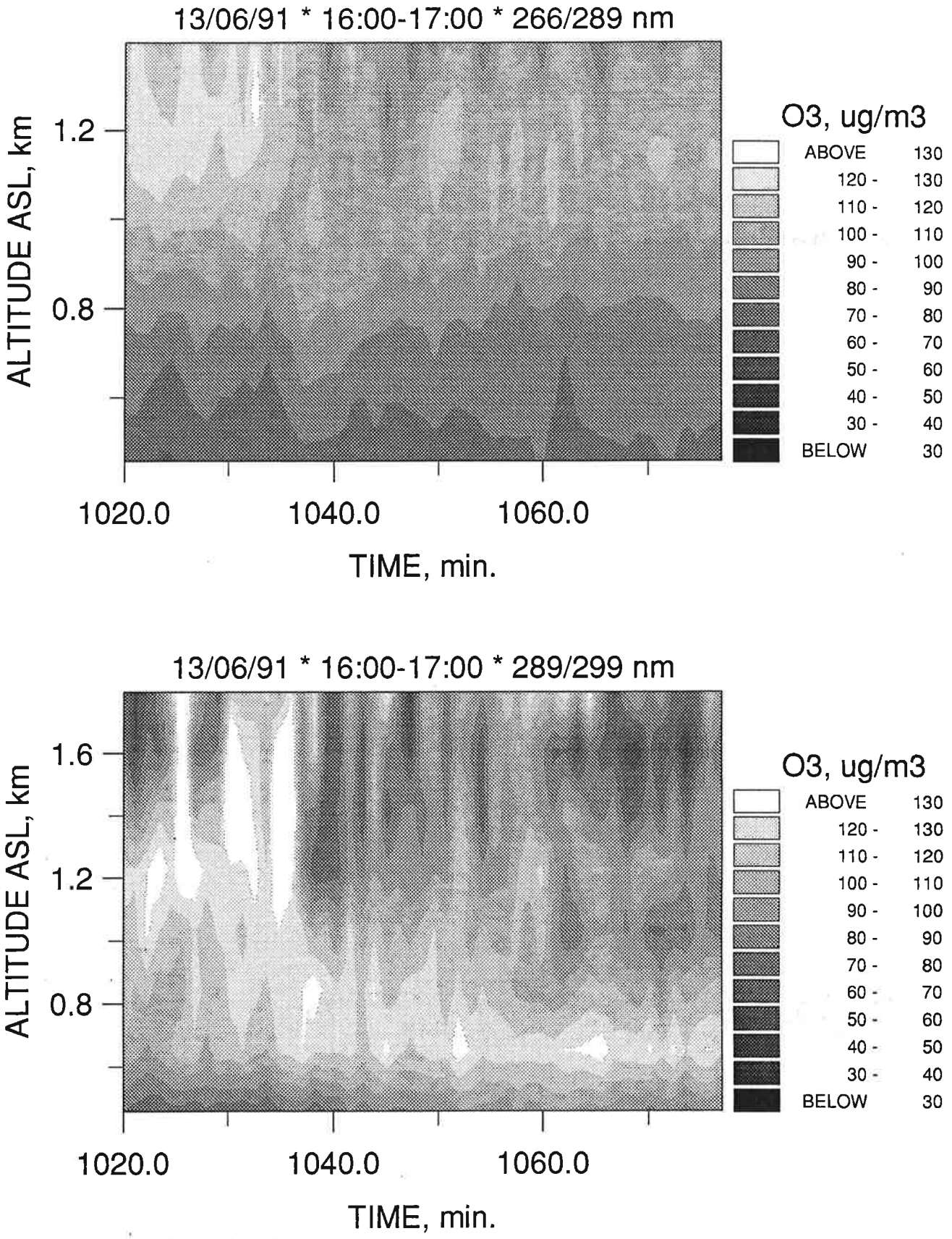

Figure 5.21: Ozone vertical distribution in $\mu g \cdot m^{-3}$ recorded on June 13, 1991 for the wavelength pair 266/289 nm (upper display) and 289/299 nm (lower display).

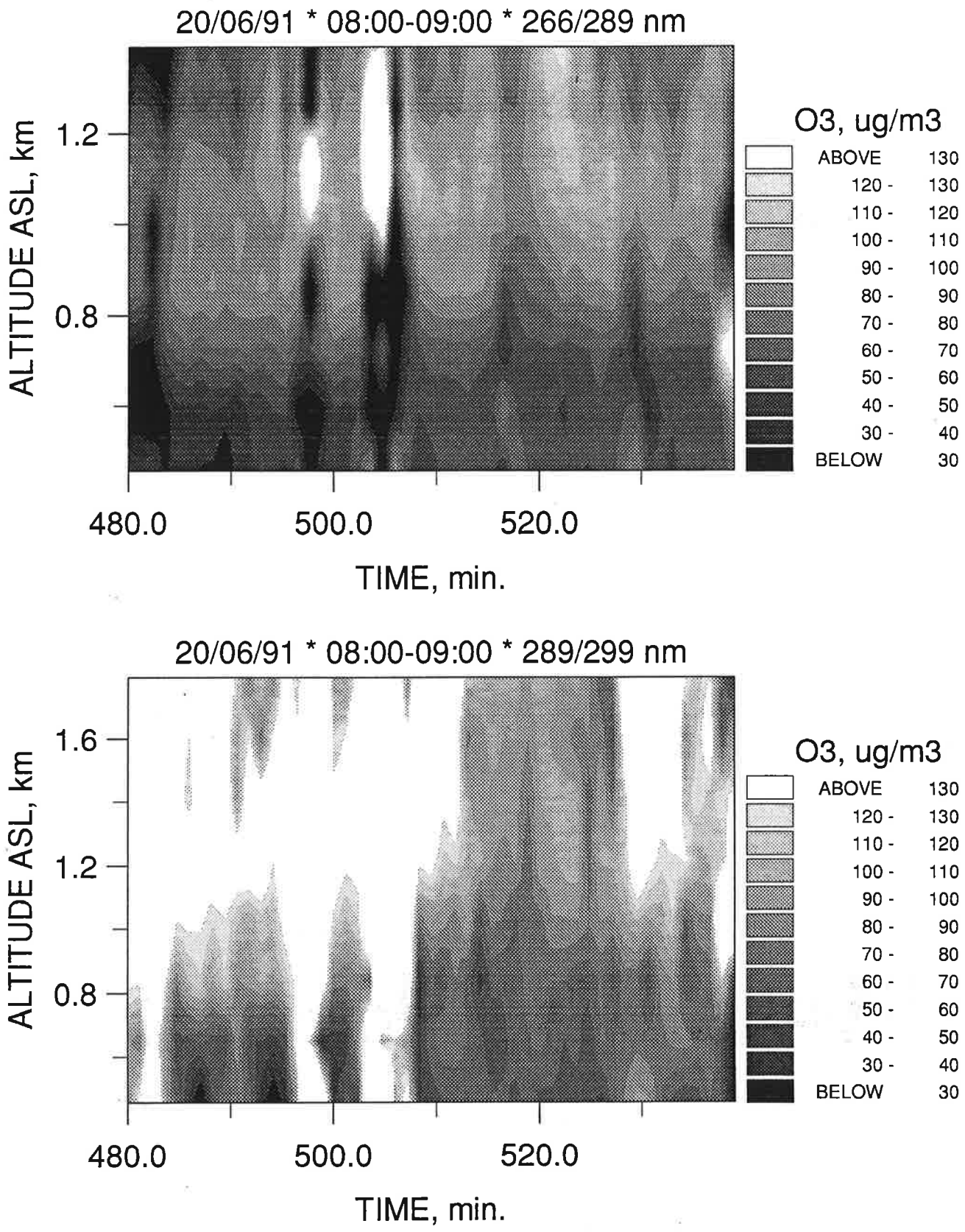

Figure 5.22: Ozone vertical distribution in $\mu g \cdot m^{-3}$ recorded on June 20, 1991 for the wavelength pair 266/289 nm (upper display) and 289/299 nm (lower display).

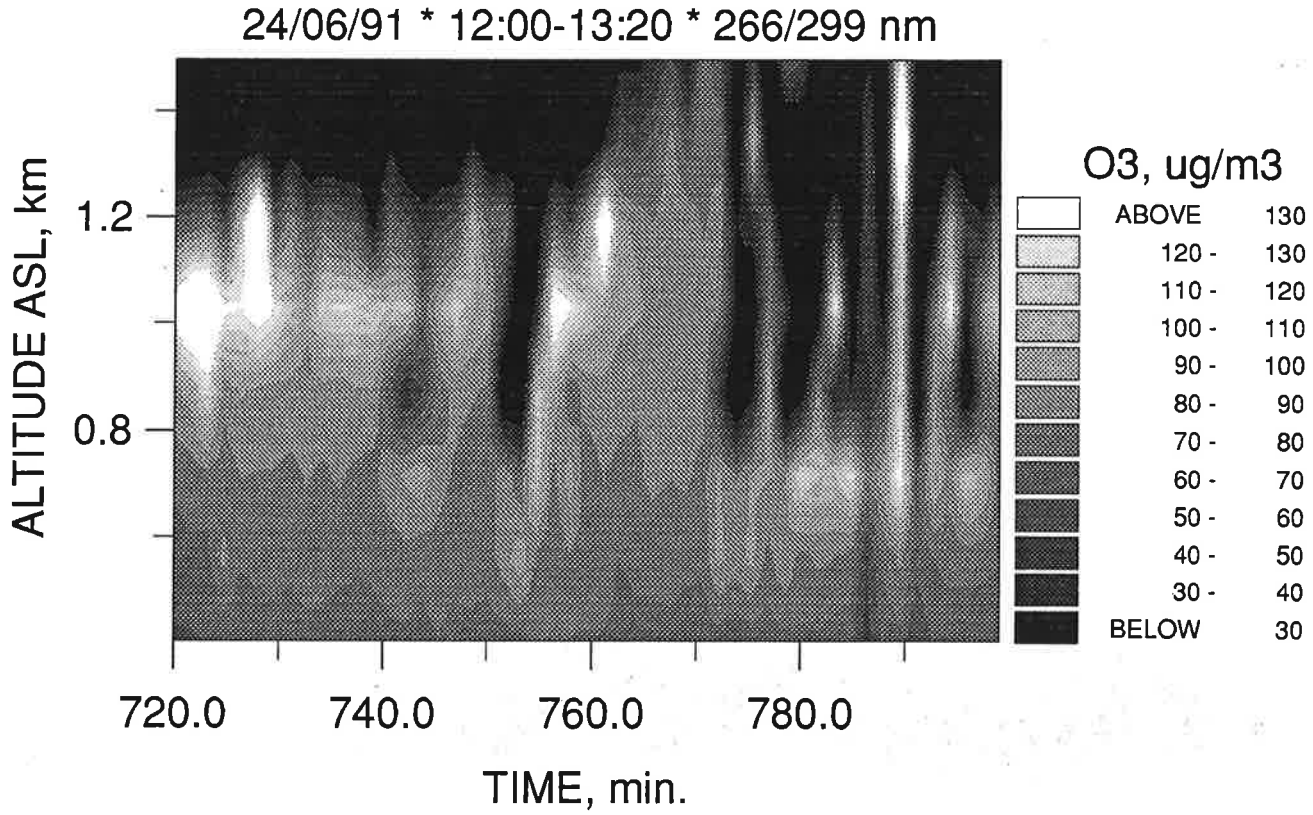

Figure 5.23: Ozone vertical distribution in $\mu g \cdot m^{-3}$ recorded on June 24, 1991 for the wavelength pair 266/299 nm.

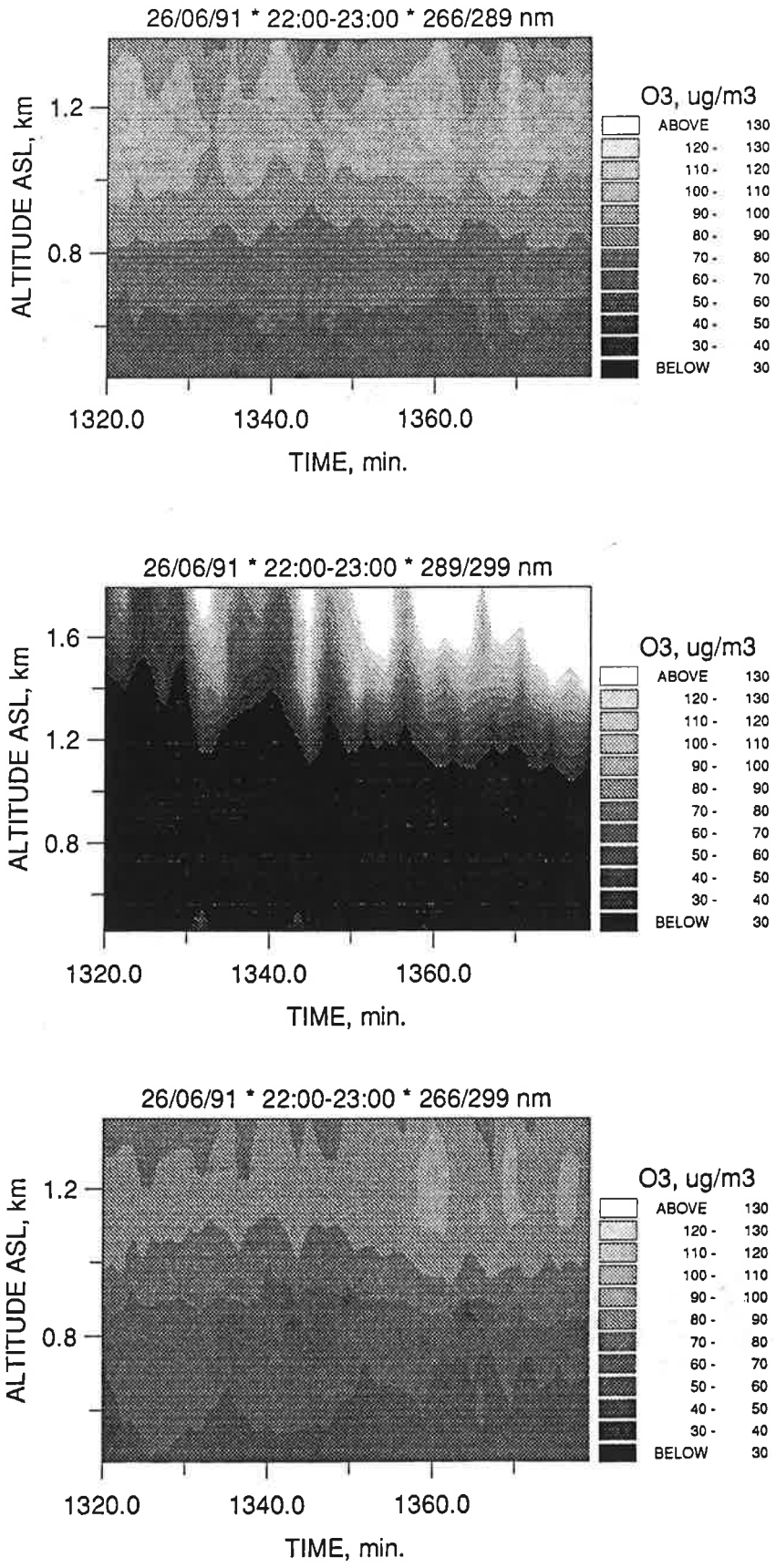

Figure 5.24: Ozone vertical distribution in $\mu g \cdot m{-}3$ recorded on June 26, 1991 for the wavelength pair 266/289 nm (upper display), 266/299 nm (middle display) and 289/299 nm (lower display).

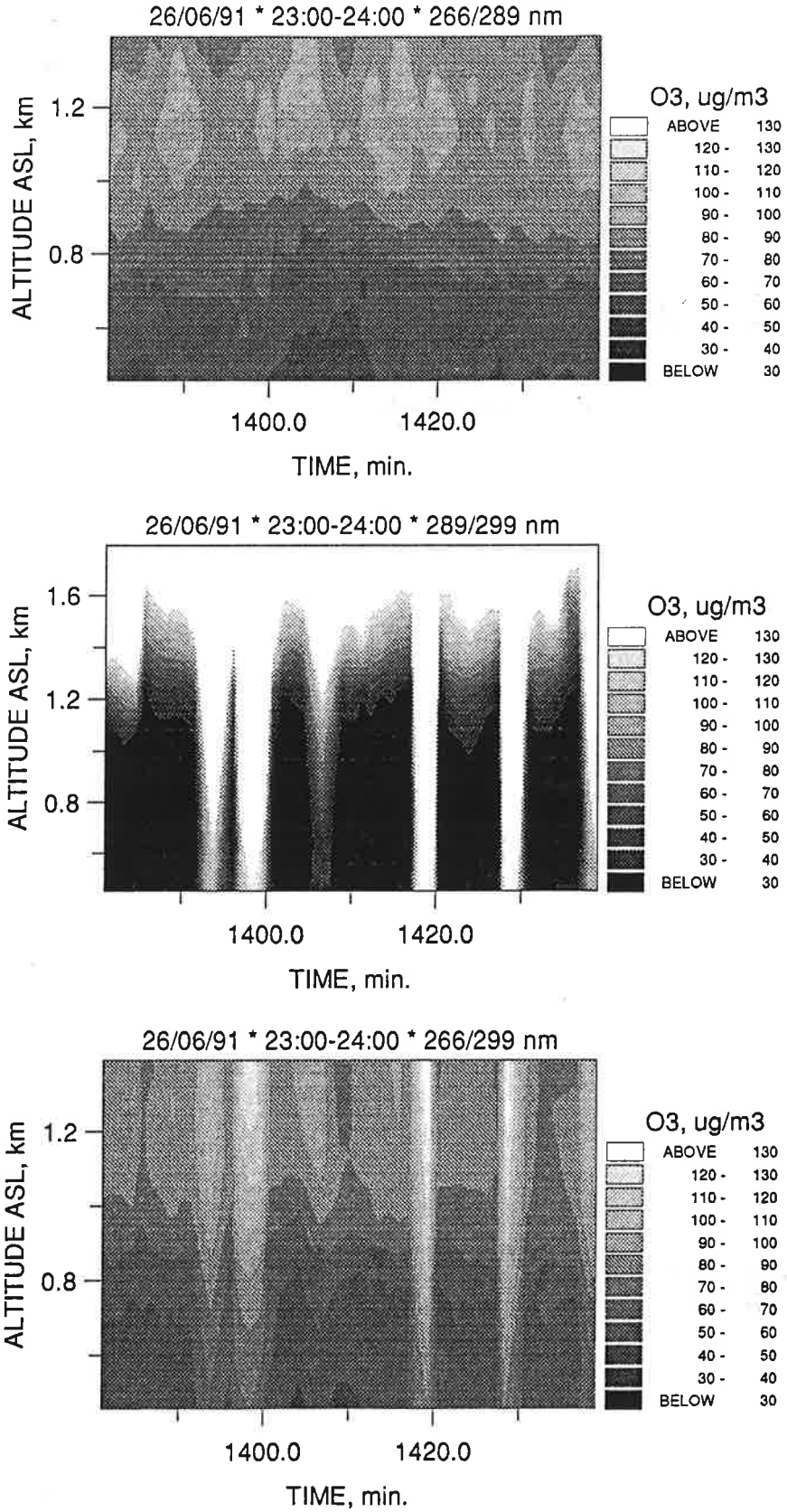

Figure 5.25: Ozone vertical distribution in $\mu g \cdot m^{-3}$ recorded on June 26, 1991 for the wavelength pair 266/289 nm (upper display), 266/299 nm (middle display) and 289/299 nm (lower display).

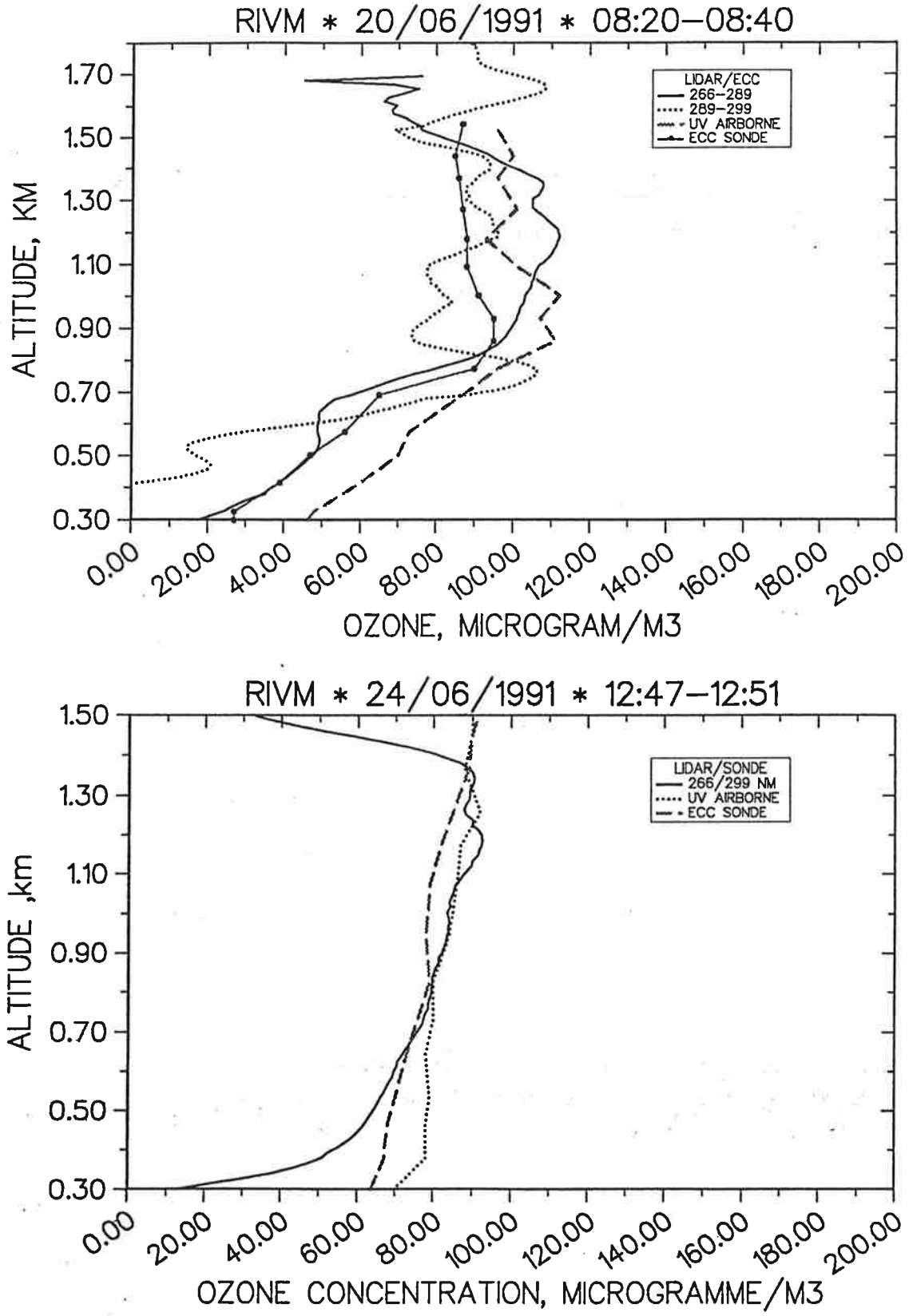

Figure 5.26: Comparison of ozone vertical profiles measured by the CNRS lidar , ECC sonde and UV absorption on June 20, 1991 and on June 24, 1991.

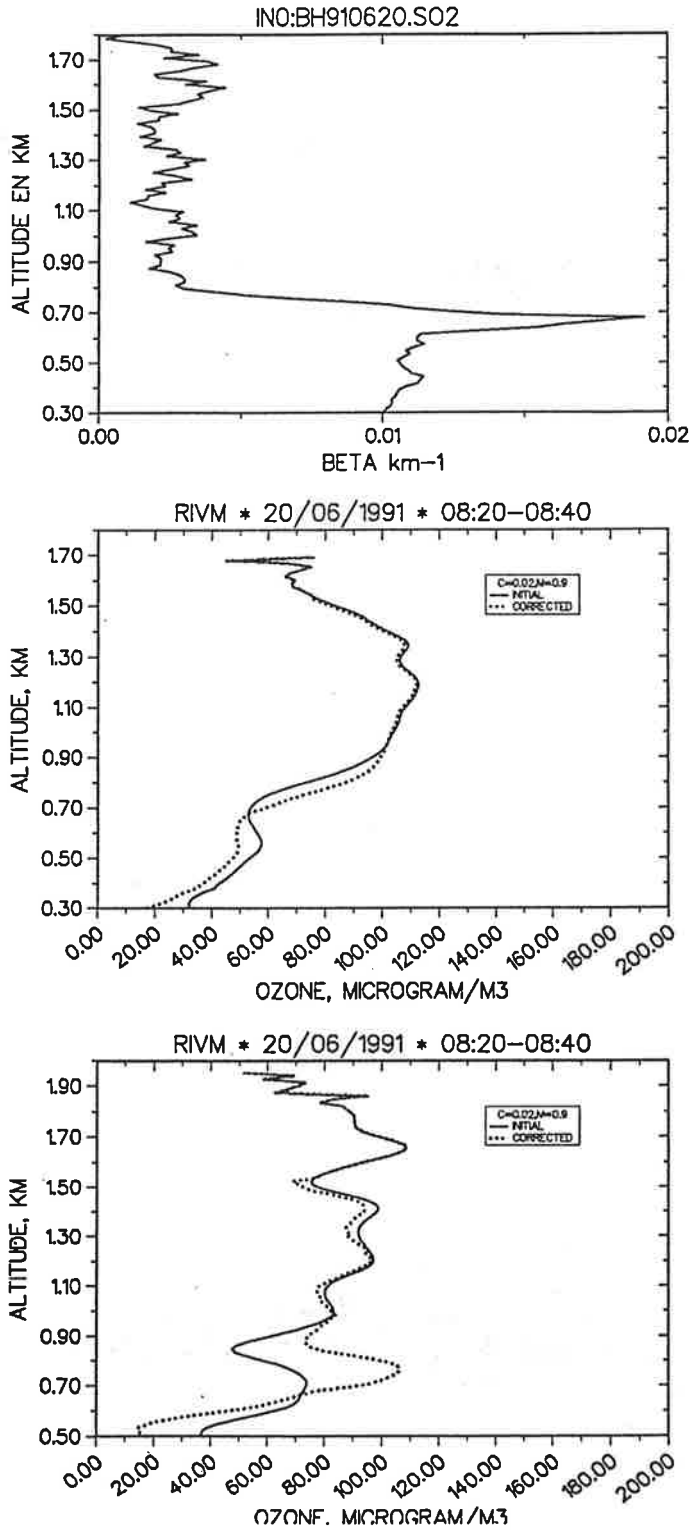

Figure 5.27: Aerosol backscatter coefficient at 299 nm devived from the CNRS lidar signal on June 20^{th} intercomparison (upper figure) Ozone profiles before and after the aerosol interferences correction for the wavelength pair 266/289 nm (middle figure) an .d 289/299 nm (lower figure). Correction is performed with a backscatter to extinction ratio of 0.02 and a $\lambda^{-0.9}$ wavelength dependency.

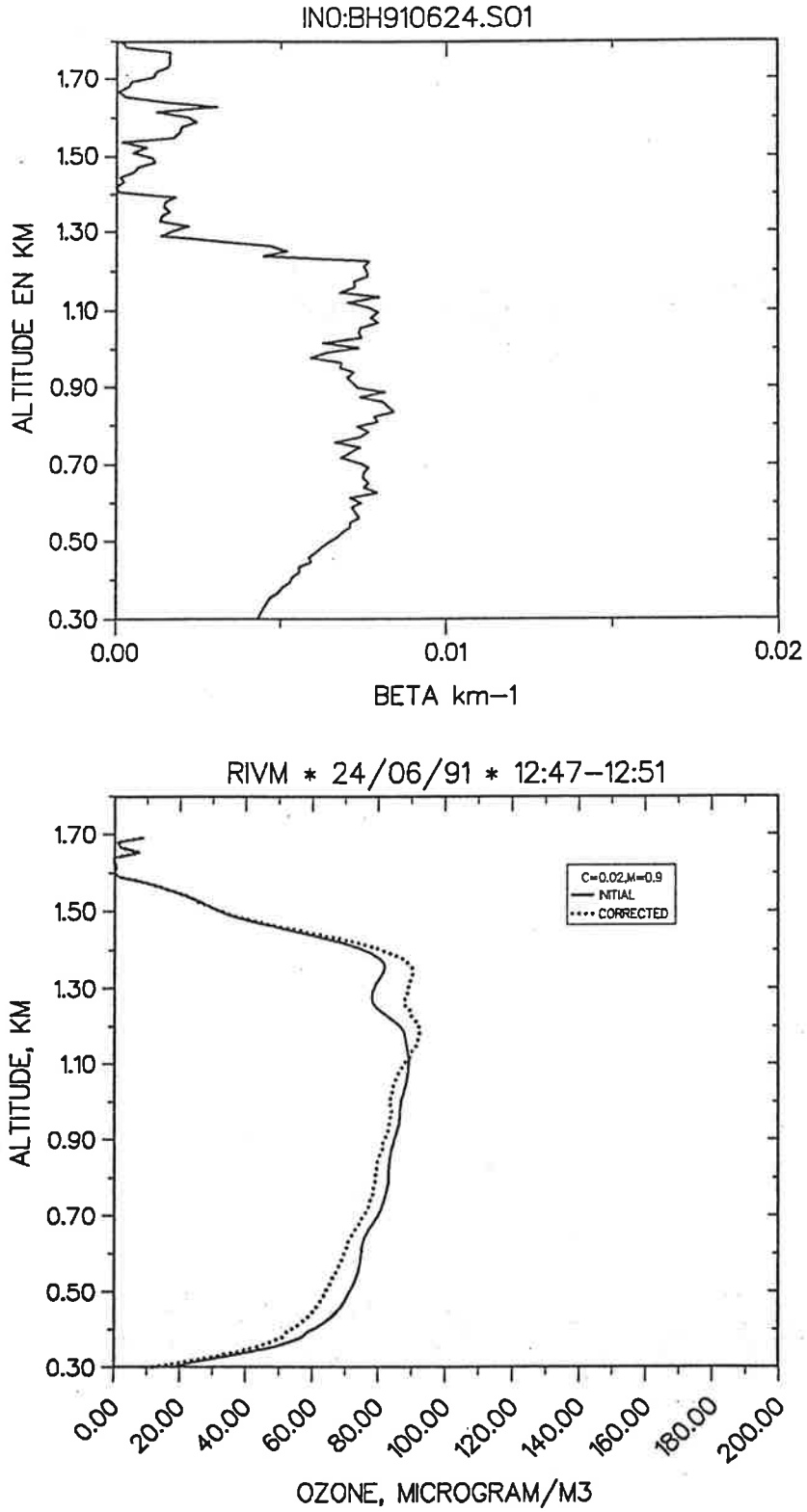

Figure 5.28: Aerosol backscatter coefficient at 299 nm derived from the CNRS lidar signal on June 24^{th} intercomparison (upper figure) Ozone profiles before and after the aerosol interferences correction for the wavelength pair 266/299 nm (lower figure). Correction is performed with a backscatter to extinction ratio of 0.02 and a $\lambda^{-0.9}$ wavelength dependency.

5.3.3 LIT

Measurement examples / Intercomparisons Figures 5.29 -5.34 show some examples of evaluated data. The ozone concentrations have been compensated for differential Rayleigh extinction but not for possible aerosol effects. Due to the fairly low pulse energy generated by the frequency doubled dye laser, the ozone profile could normally not be evaluated above 1.2-1.5 km. We experienced problems at higher altitudes, probably due to signal-induced background (SIB) from the near-field scattering. Different settings of the gain modulation function were investigated, but only with smaller effects on the SIB, which indicates that the problem is due to overload of the photocathode. Another limiting factor is the low dynamic range (8-bit) of the digitizing system. This made it difficult to avoid saturation of the A/D converter during situations when low thin clouds drifted in during a measurement.

Figure 5.29 shows an example of a vertical measurement, where the upper part shows the logarithm of the range-corrected lidar signals averaged over 3 minutes at the two wavelengths together with the logarithm of the ratio. It should be noted that the overlap starts already at 300 meters or lower - the form of the lidar signals is due to the gain modulation. The lower part displays the retrieved ozone profile from 5 consecutive measurements up to 1500 m height with a range-resolution of 100 m. Figure 5.30 shows an example of a vertical scan from ground and up to about 45 degrees elevation, which during this measurement was enough to reach the cloud base. The measurement consists of 10 different directions during a total time of 17 minutes. From this type of scan a vertical profile essentially from the ground can be inferred with a vertical projection, as seen in the left part of the figure. The vertical resolution in this type of measurement will also be higher.

Figure 5.31 and 5.32 show the result of an intercomparison between the DIAL data and the results from the ECC-sonde during helicopterflight 1 and 2. The DIAL values are here evaluated with 100 m resolution around the altitude of the helicopter for different times. The DIAL measurement time was 3 minutes. Some of the measurements were disturbed by clouds, and in this case the previous or following measurement has been used to give the value at the appropriate altitude. During helicopter flight 2 some of the values are deduced from a vertical scan. Intercomparisons were also performed between the results of DIAL and DOAS measurements over the same horizontal paths. The interesting fact in comparisons between these techniques is that the measurements can be made in the same air volume - no presumption of the homogeneity of the air over the path is needed. Both of the techniques utilize the optical absorption, but whereas DIAL only employs two wavelengths with rather large separation, the DOAS technique uses small higher order structures on the ozone absorption profile in a wavelength interval. DOAS will normally not be affected by extinction due to aerosol scattering. A study of aerosol effects and validation of correction procedures in DIAL measurements can thus be made. DOAS also has the advantage of being able to measure a number of other gases simultaneously.

Figures 5.33 and 5.34 show results of intercomparisons which were made during TROLLIX 91 with a DOAS system from IVL, Göteborg, and where the DIAL results are only corrected for differential Rayleigh extinction. Experiments with a double path DOAS were also performed in order to measure a true transmission spectrum in the wavelength regions employed by the DIAL systems.

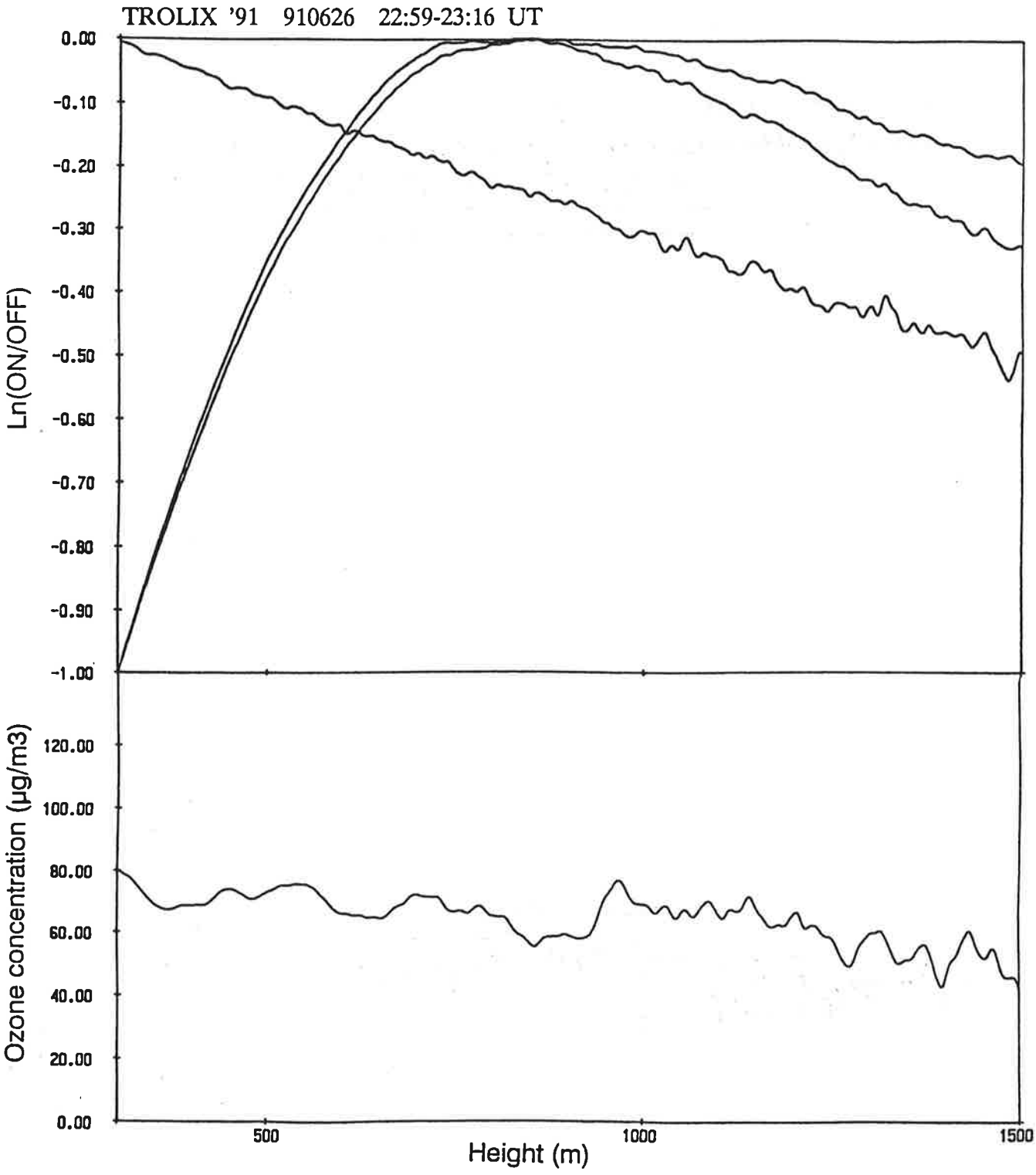

Figure 5.29: Logarithmic range-corrected lidar signals and ratio curve for the 278.7/286.3 nm wavelength pair. The retrieved vertical ozone profile is shown in the lower part of the figure.

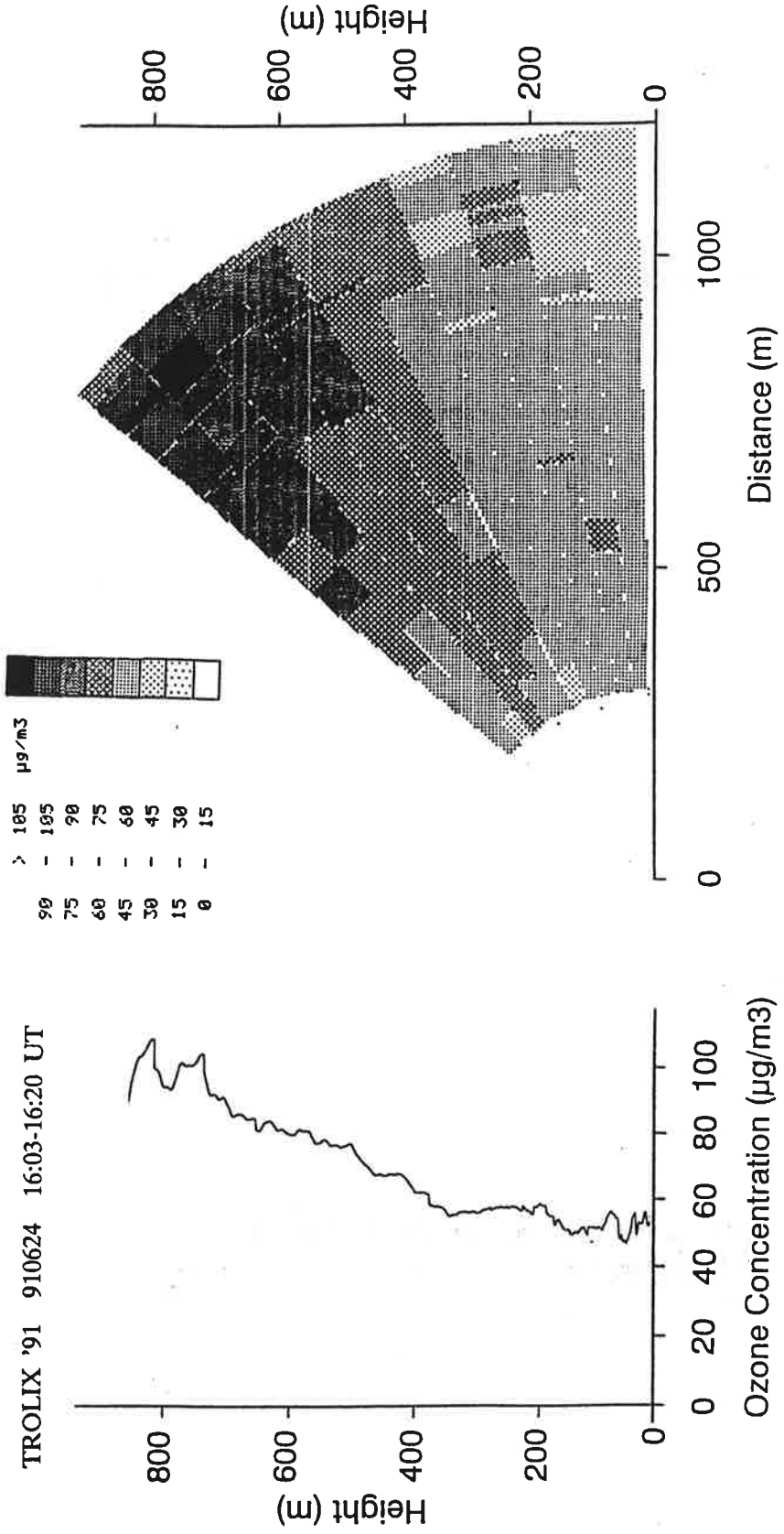

Figure 5.30: Ozone distribution deduced from a vertical scan.

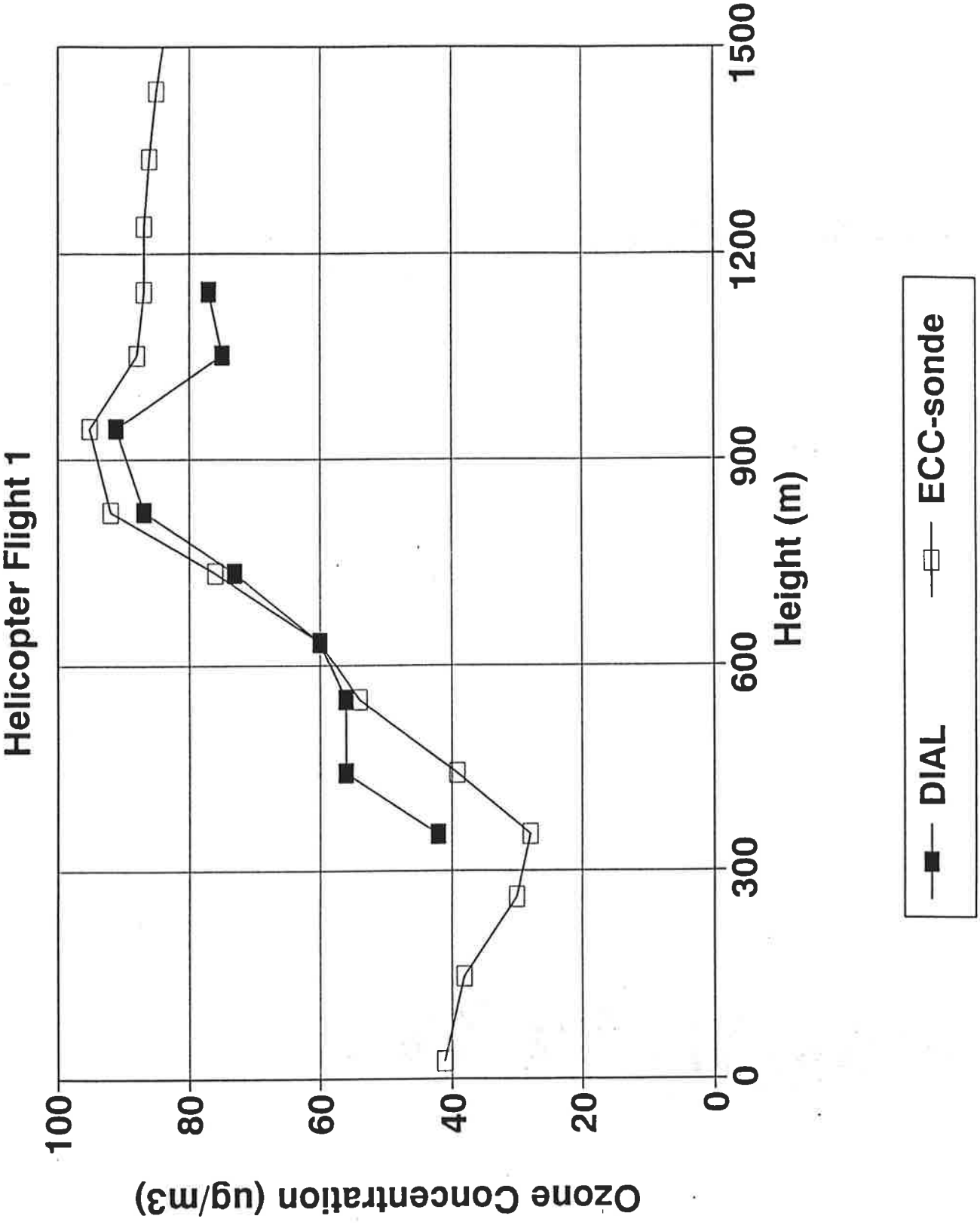

Figure 5.31: Ozone vertical profile measured by the DIAL and ECC sonde during helicopter flight 1.

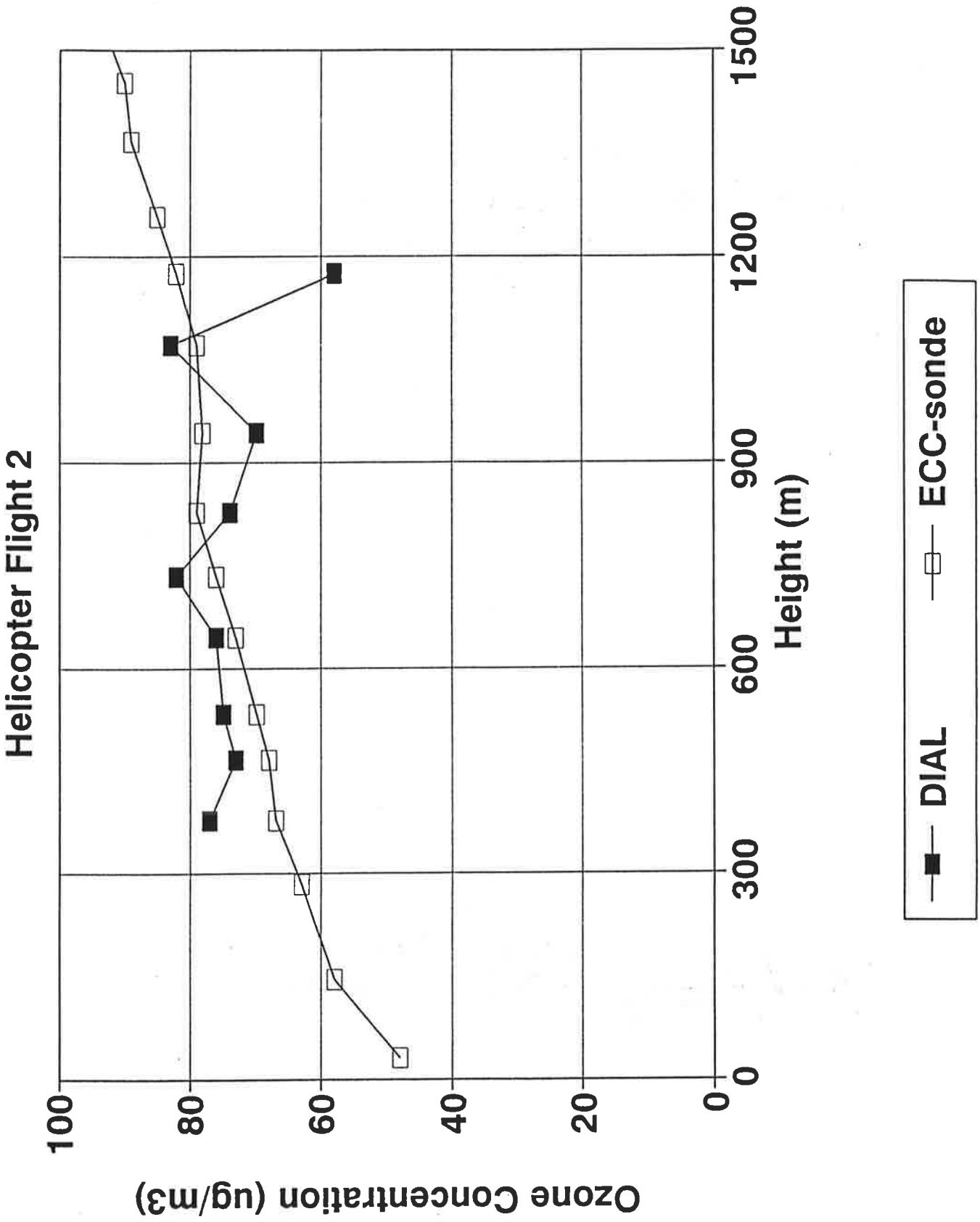

Figure 5.32: Ozone vertical profile measured by the DIAL and ECC sonde during helicopter flight 2.

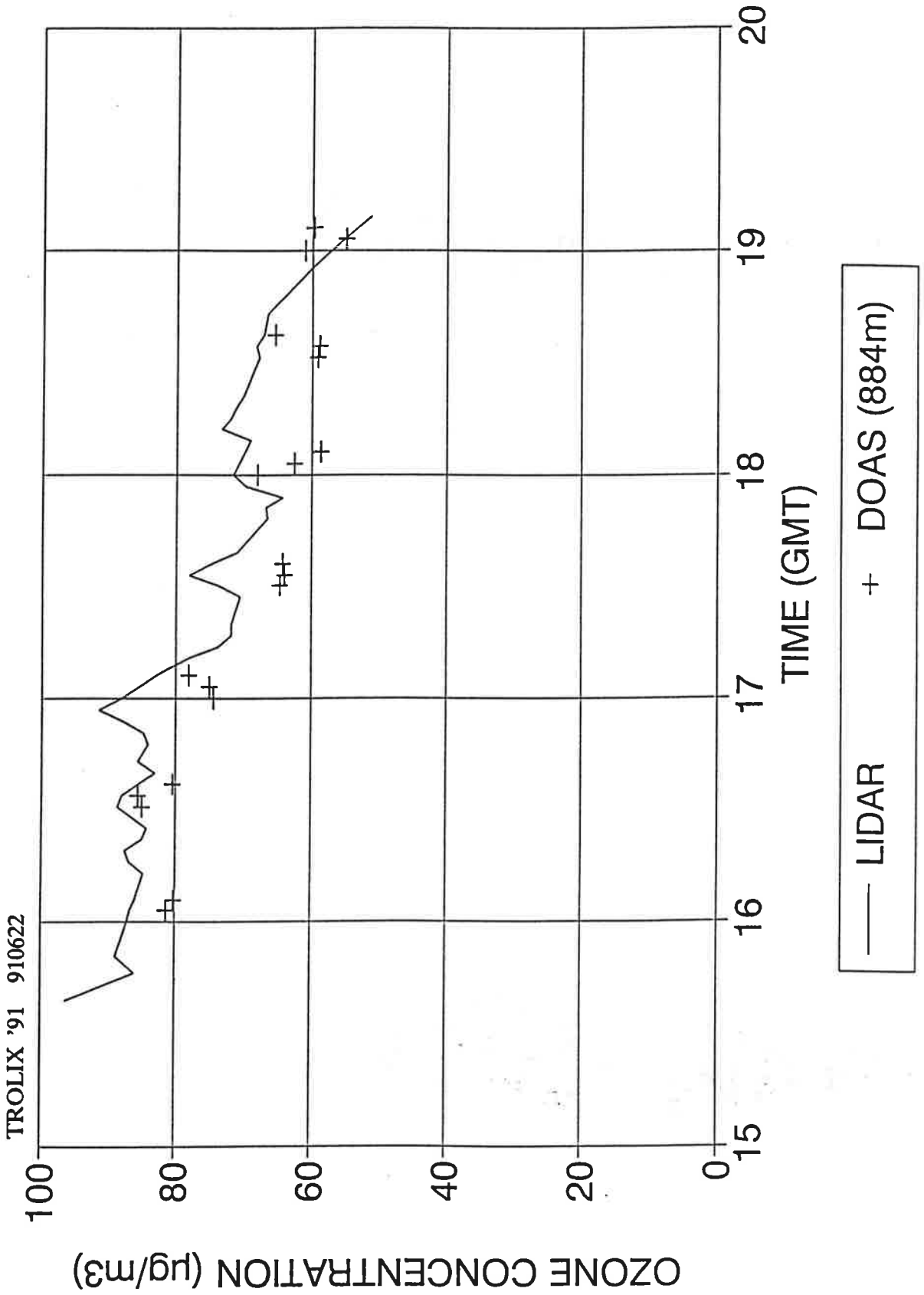

Figure 5.33: Intercomparison between DIAL and DOAS measurements of ozone over an horizontal path.

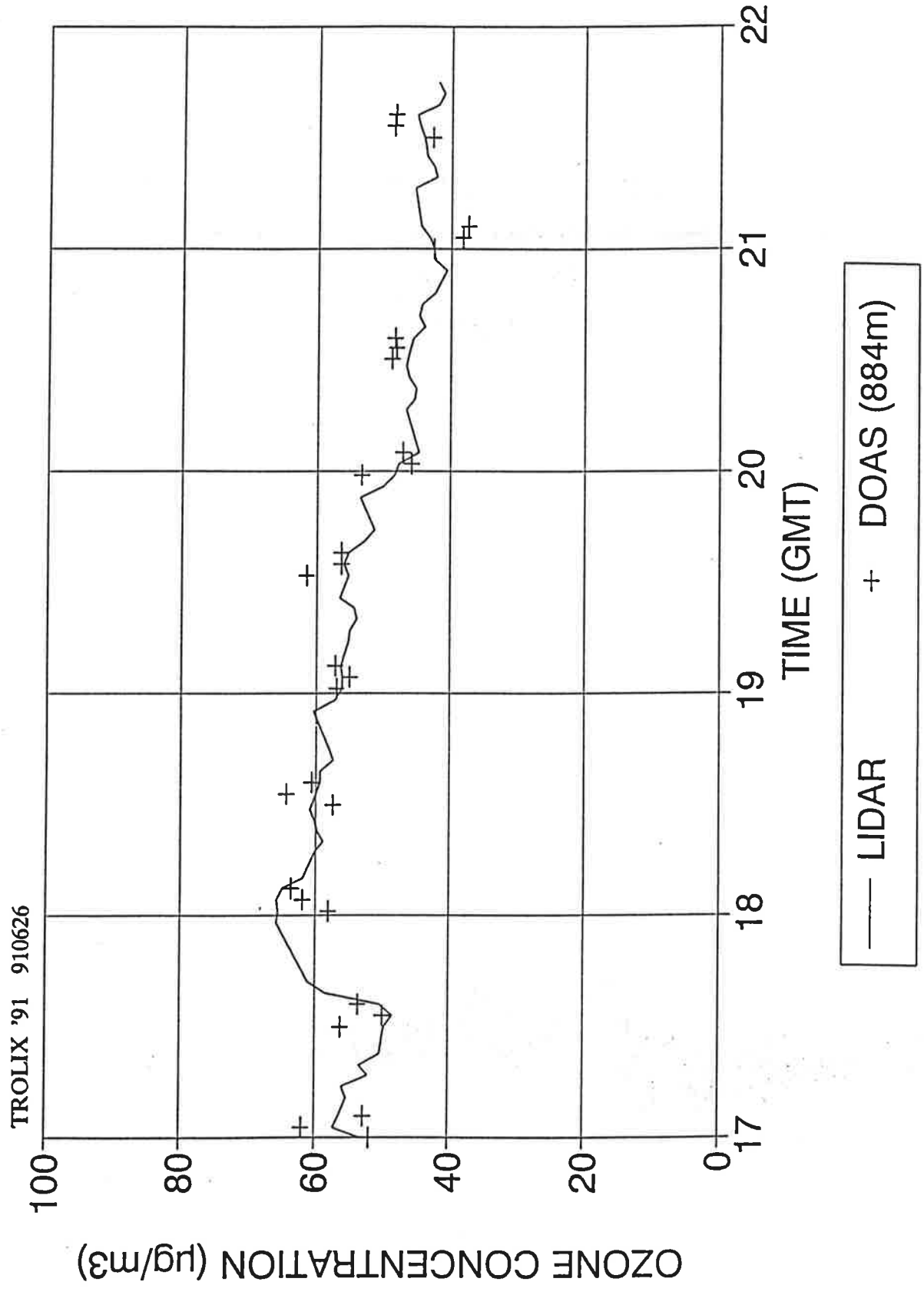

Figure 5.34: Intercomparison between DIAL and DOAS measurements of ozone over an horizontal path.

5.3.4 MPI

The lidar system, housed in a standard 20' container, was brought to the measurement location 3 days before the first measurements were planned, and was ready for the first measurements in the evening of June 10, almost as scheduled. During this campaign a total of 70 hours of measurements were made with the system, restricted mainly by the bad weather conditions mentioned above. The minor technical problems which occurred with the system were mostly due to the unexpectedly short lifetime of the laser windows. In addition, a problem with the Brewster windows of the Raman cells occurred, which could be fixed in short time.

More principal problems were encountered with the transient digitizers, which were noticed only during the evaluation. In one channel, almost exclusively used for the 277 or 268 nm signal, apparently a bit error occurred which made evaluation of signals smaller than $\approx$ 20 LSB (least significant bit) dubious.

The other problem detected during the experiment was, that the beam divergence was only slightly less than the field of view of the telescope, so that correct adjustment was very difficult, and measurements at low heights were impossible. The difficult alignment procedure was particularly troublesome under inhomogeneous atmospheric conditions, when signals were changing fast. Unfortunately, this happened quite often during this experiment.

The combination of both effects restricted the usable range from $\approx$ 700 m to somewhere between 1200 and 2000 m, depending on atmospheric conditions. The upper limit was not a real restriction for most intercomparisons, but the lower limit clearly restricted the range of overlap with other systems and helicopter measurements.

Data for priority cases

Horizontal measurements

Horizontal measurements are particularly suitable for intercomparisons, since ground level in situ measurements can be used as a reference, and since the atmosphere often is nearly horizontally homogeneous over the lidar range, at least for sufficiently long averaging intervals. This can be used to separate the problems due to aerosol interference from other problems.

Fig. 5.35 shows the range corrected signals for 248, 277, and 313 nm for a selected period during the horizontal intercomparison on June 22, together with a display of the actual signals on a very expanded scale to demonstrate the range were the signals are so low that data acquisition problems show up clearly. This appears to happen for signal levels below $\approx$170 LSB absolute, or 20 LSB relative to the offset level, at a range of $\approx$ 1100 m in this example. Full overlap between laser beams and telescope field of view is beyond 400 m. At ranges between these two limits the decrease of $ln(P \cdot r^2)$ is linear, as expected for a horizontally homogeneous atmosphere. From the slope of these lines, the total extinction coefficient can be calculated, consisting of extinction due to Rayleigh

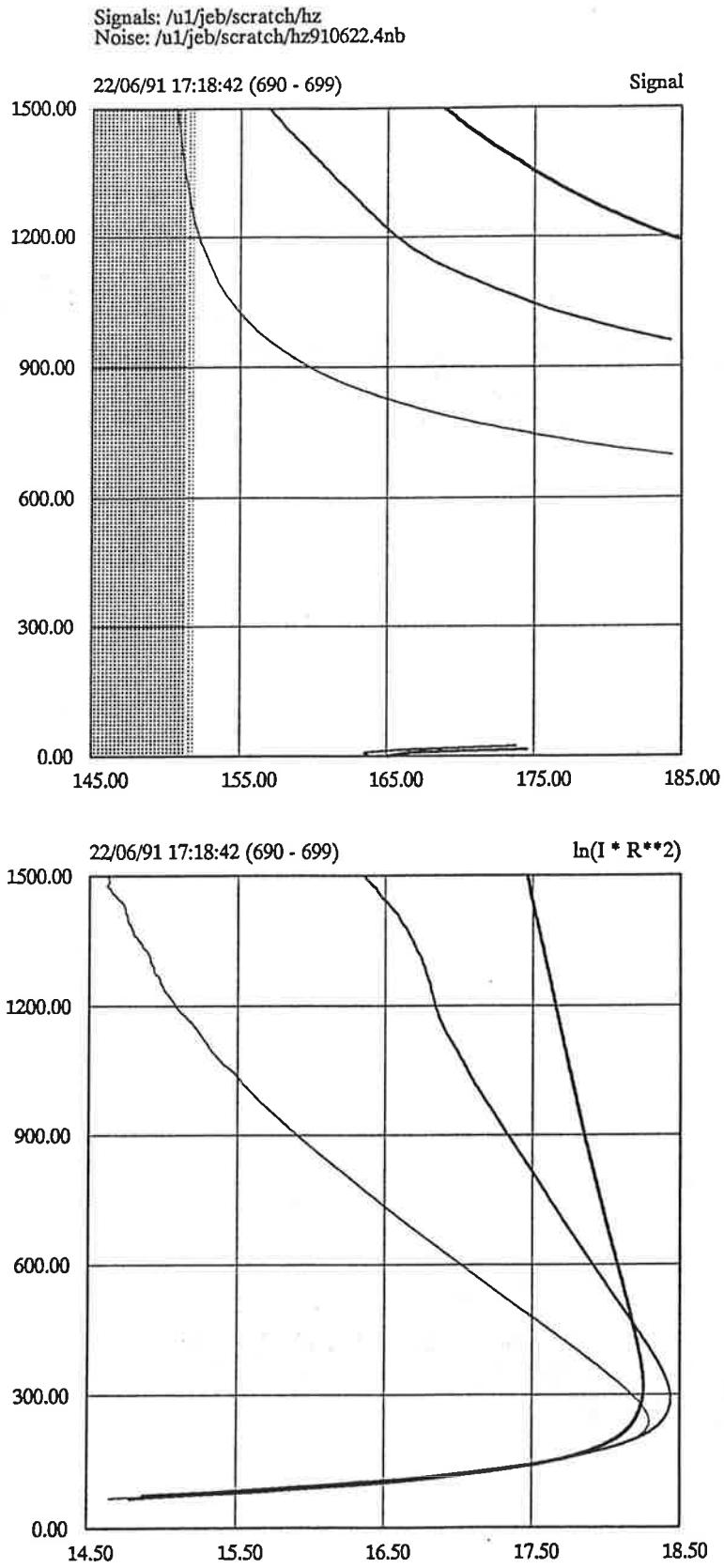

Figure 5.35: Original lidar signals on expanded scale (top), for the wavelengths of 248, 277, 313 nm, and the corresponding range corrected signals on a logarithmic scale (bottom). Lidar pointing horizontally. 1991/06/22 17:18 UT.

scattering α_R, aerosol scattering α_a, ozone absorption α_{O_3}, and eventually absorption by other gases (e.g. SO_2, O_2). For the 313 nm wavelength, ozone absorption is almost negligible ($\alpha_{O_3} < 8 \cdot 10^{-6} m^{-1}$ for an ozone density of 100 $\mu g \cdot m^{-3}$) and absorption by other gases is assumed negligible, too. Since Rayleigh extinction can be calculated using a standard atmospheric model for the density, the aerosol extinction coefficient can be retrieved from the measured slope. The results of this calculation are presented in fig. 5.36, together with results of the Klett method for the same data set. The calibration range for the Klett method was chosen as 1350-1500 m, with a start factor of $\frac{\beta_a}{\beta_R} = 0.6$, and a lidar ratio of $S = 25$. The extinction values vary considerably with time, this is reflected in both the values obtained by the slope method and the Klett method. For the latter, this is only true for the extinction values calculated for the close ranges. On the far end, close to the calibration range, the values remain constant. This is an artifact of the calibration procedure, since $\frac{\beta_a}{\beta_R}$ was held constant (a priori there is no better knowledge for these values). The agreement between the results of the two independent methods is excellent for the closest range of 400 m, but of course less satisfactory at the far end.

Fig. 5.37 shows the log of the ratio of the 277 to the 313 nm signal, and the 248 to the 313 nm signal, as a function of range. The slope of this curve corresponds to the differential extinction coefficient, and hence to ozone concentration after correction for differential Rayleigh extinction, differential aerosol extinction, and possibly differential absorption by other gases. The simplest evaluation procedure for this case is a linear "fit by eye", and a correction as indicated above. This is done for the two wavelength pairs, and the resulting ozone densities agree fairly well, and are quite close to the result of a nearby in situ measurement (MPI UV-photometer, see section 4.10.3). It should be noted, however, that the concentration retrieved from the 277 - 313 nm wavelength pair is 12% higher than the other values.

In figure 5.38 the results for a standard evaluation of these horizontal measurements is given, with no correction applied but differential Rayleigh extinction. Shown are the results for a range of 625 - 775 m, with a time resolution of 15 min (matched to the DOAS-system of IVL running simultaneously), for both wavelength pairs 248 - 313 nm and 277 - 313 nm. The results of the photometric ozone monitor (MPI) are included for comparison. The results show the same time dependence, but absolute values are not too satisfactory. In particular, the results of the 277 - 313 nm pair are $25 - 30 \mu g \cdot m^{-3}$ higher than the monitor values. Correction for aerosol differential extinction would lower these values by $\approx 5 \mu g \cdot m^{-3}$, so still a considerable difference remains. The origin of this difference is not quite clear yet, but it seems to be existent for all measurements. So a orrection seems to be appropriate.

In a similar way the results of a second horizontal intercomparison performed on June 26 1991 are shown in fig. 5.39. This time the lidar measurements used the deuterium wavelengths of 268 and 292 nm. For this measurement, the agreement is excellent, on the average the difference between the monitor and the lidar values is only 2.3 $\mu g \cdot m^{-3}$. The only corrections which have been applied are for differential Rayleigh extinction and oxygen absorption at 268 nm.

Further intercomparisons with DOAS and the Lund lidar will be given in section 6.

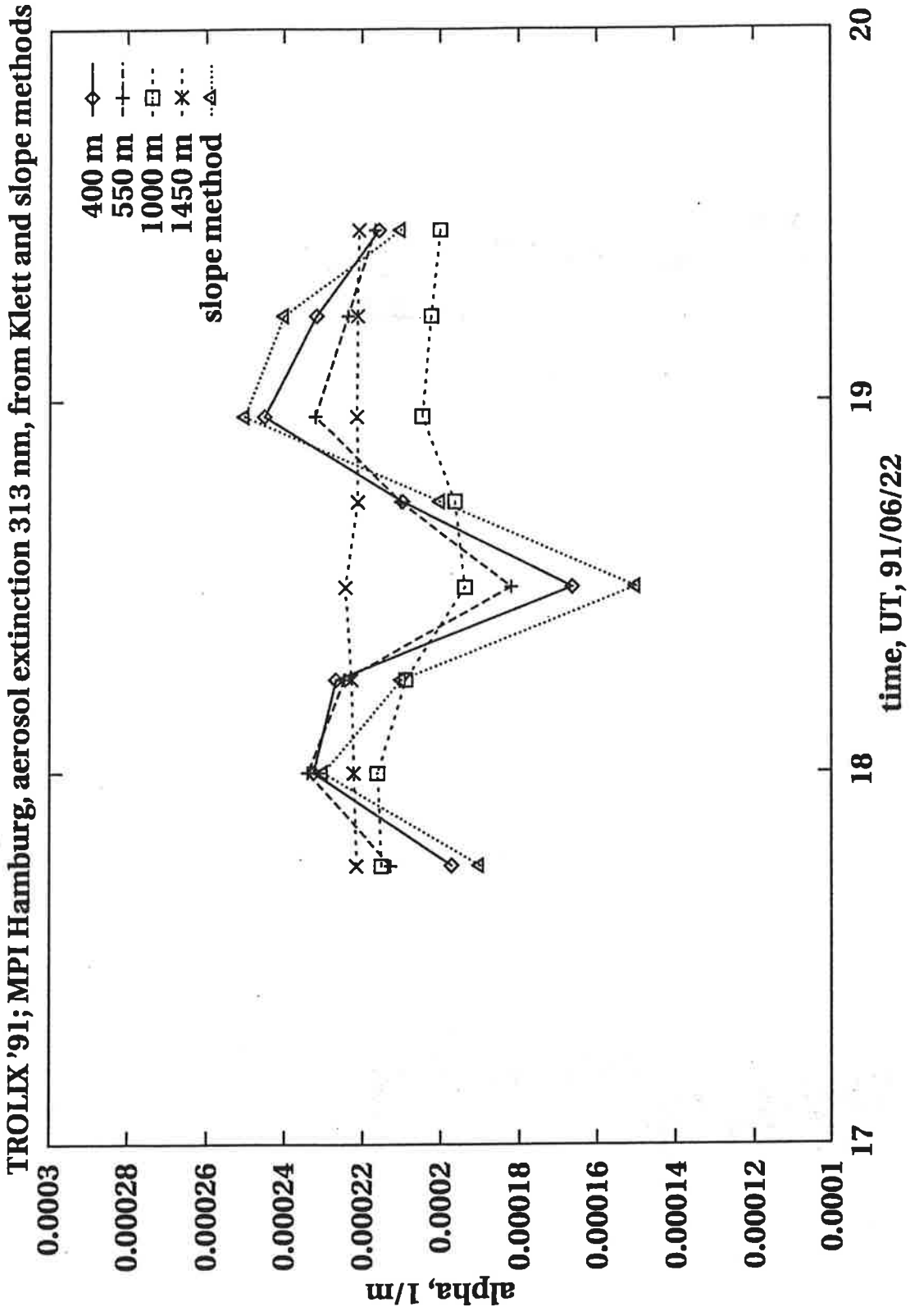

Figure 5.36: Aerosol extinction coefficients retrieved from lidar signals at 313 nm, using the slope method and a Klett algorithm. Lidar pointing horizontally. 1991/06/22

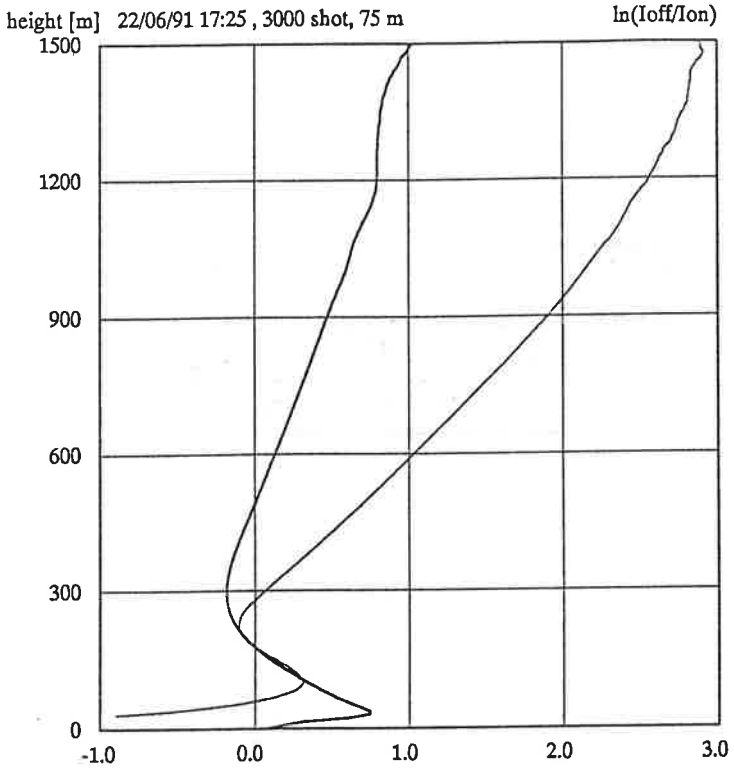

Horizontal measurement, H_2 Raman-shifter
$\lambda_0 = 248nm$, $\lambda_1 = 277nm$, $\lambda_2 = 313nm$
3000 shot average (7 min), 75 gliding average

Wavelength pair 277 - 313nm :			
measured extinction coefficient	α	=	$0.573km^{-1}$
Rayleigh correction	α_R	= −	$0.078km^{-1}$
Aerosol correction	α_{Aer}	= −	$0.026km^{-1}$
SO_2 correction ($15ppbV$)	α_{SO_2}	= −	$0.031km^{-1}$
effective extinction coefficient	α_{eff}	=	$0.438km^{-1}$
$\Longrightarrow$ Ozone density	ρ_{Oz}	=	$73\mu g \cdot m^{-3}$

Wavelength pair 248 - 313nm :			
measured extinction coefficient	α	=	$1.514km^{-1}$
Rayleigh correction	α_R	= −	$0.191km^{-1}$
Aerosol correction	α_{Aer}	= −	$0.052km^{-1}$
Oxygen correction	α_{Ox}	= −	$0.400km^{-1}$
effective extinction coefficient	α_{eff}	=	$0.871km^{-1}$
$\Longrightarrow$ Ozone density	ρ_{Oz}	=	$65\mu g \cdot m^{-3}$

Ozone monitor:	ρ_{Oz}	=	$65\mu g \cdot m^{-3}$

Figure 5.37: $ln(I_{off}/I_{on})$ for the wavelengths pairs 277/313 nm and 248/313 nm versus range. Simple evaluation included.

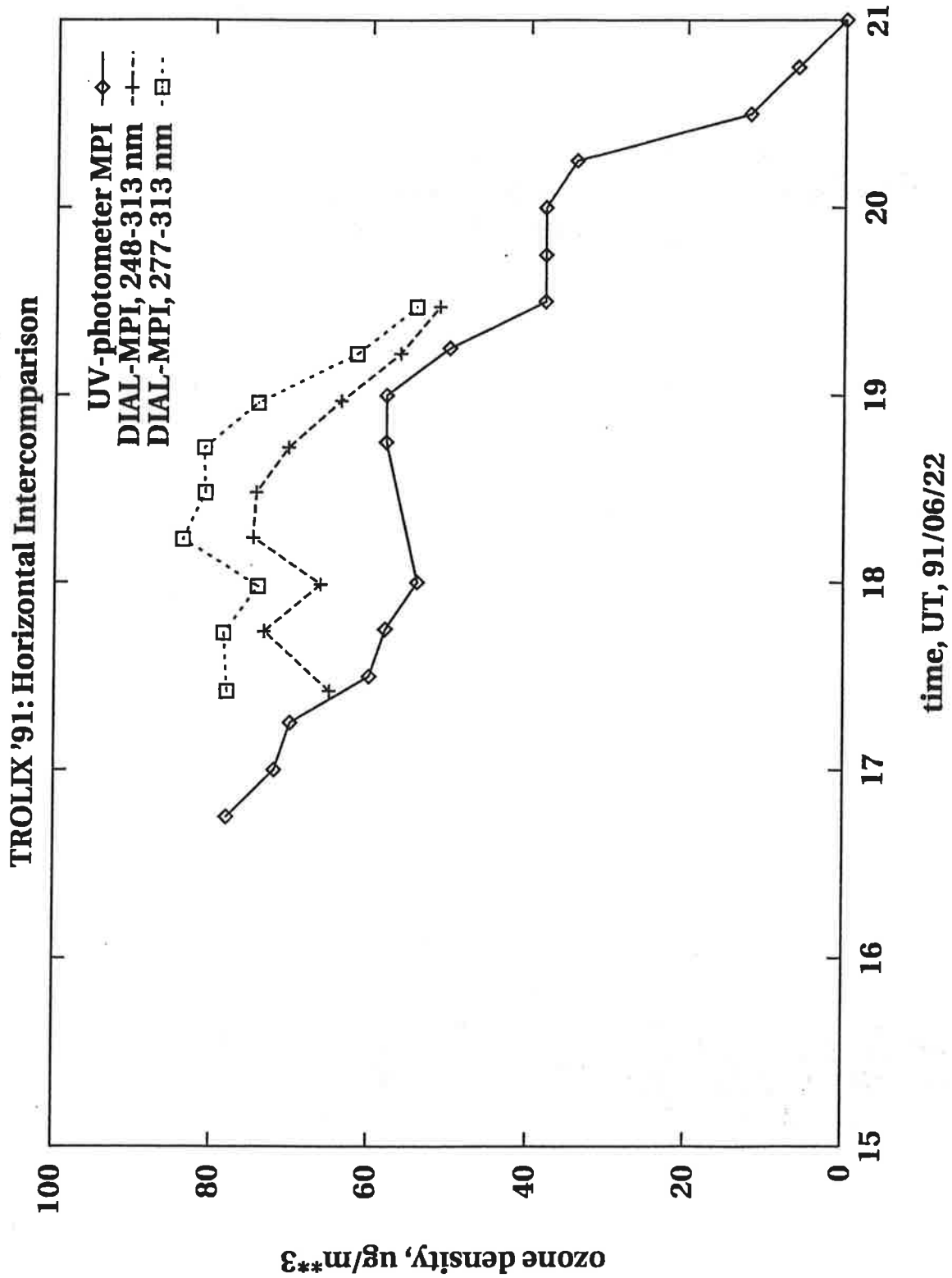

Figure 5.38: Horizontal lidar measurements for two different wavelength pairs compared to a standard ground level photometric ozone monitor.

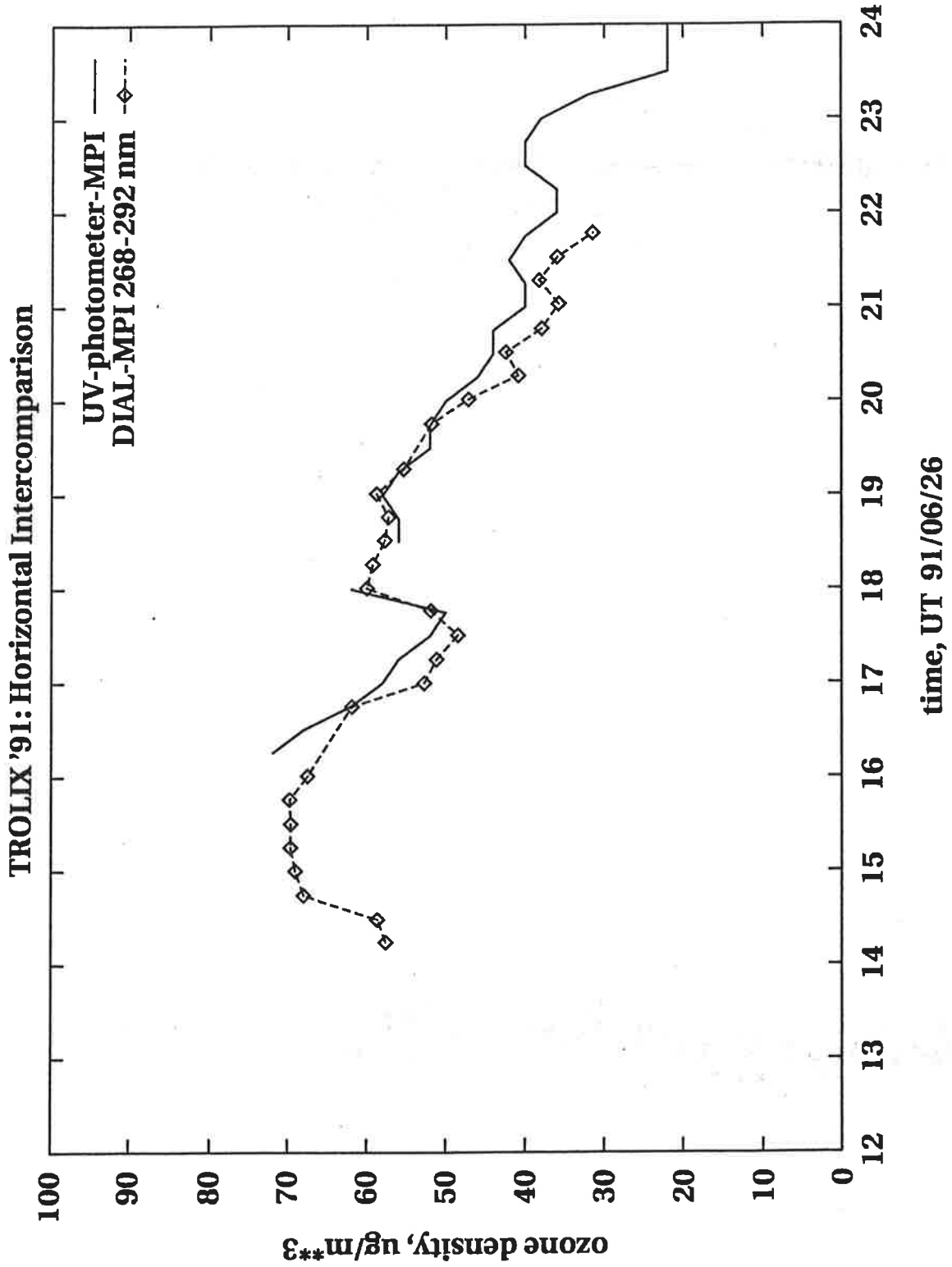

Figure 5.39: Results of a horizontal lidar measurement using the deuterium wavelengths 268 and 292 nm.

Flight intercomparisons

Of the three flight intercomparisons performed, MPI lidar data are available only for flight 1 and 3. For flight 2 the beams were not adjusted properly, so there are no usable results.

Fig. 5.40 shows the time-height-distribution of the range corrected 313 nm signal during the time of the flight intercomparison as a pseudo-3D plot. During most of the time a thick haze or cloud layer exists around 800 m, sometimes blocking the beam completely. A broken cloud layer exists at about 2500 m. As the best interval for intercomparison the period from 08:25 - 08:40 UT has been chosen, which is free from low clouds. For this period, the corresponding ozone profile is presented in fig. 5.41, with and without aerosol correction. Several values for the free parameters in the aerosol retrieval have been tried, for the extinction to backscatter ratio S, the start factor $\frac{\beta_a}{\beta_R}$ at calibration range, and the exponent of the wavelength dependence of the aerosol backscatter and extinction coefficient. For a better overview in fig. 5.42 only the differences between the corrected and the uncorrected values are shown. With the given range of input parameters for the aerosol retrieval, which is considered to span about the most reasonable values, the different retrievals generally yield differences of less than 10 $\mu g \cdot m^{-3}$, at the top of the boundary layer up to 20 $\mu g \cdot m^{-3}$.

Fig. 5.43 shows the corresponding profiles of the aerosol backscatter coefficient. From this it is apparent, that a value of $\frac{\beta_a}{\beta_R} = 1$ at the calibration range of 2100 - 2300 m certainly is too high, the increase of β_a with height beyond the top of the boundary layer at $\approx 700m$ is rather unlikely. For the more probable value of $\frac{\beta_a}{\beta_R} = 0.1$ at calibration range the profile looks more reasonable. The differences in the profile for an extinction to backscatter ratio of 25sr and 35sr are not significant. This is regarded as the "best" solution.

Fig. 5.44 shows the time height-distribution of the range corrected signal for flight 3 on June 28. It is quite obvious, that the conditions were really inhomogeneous with quite a number of low clouds. For evaluation, the period from 12:53 - 13:03 UT was chosen, the longest period with no clouds below 2 km. The averaged profiles for the range corrected signal at 313 nm, and the aerosol backscatter for this period are shown, too. In figure5.45 the corresponding ozone profile is shown. In this case it is particularly difficult to choose a good estimate for $\frac{\beta_a}{\beta_R}$ at any possible calibration height, so the aerosol correction certainly is not complete. This is particularly serious at the top of the boundary layer at about 900 m. Beyond 1500 m height the 277 nm signal is too low for proper evaluation.

Intercomparisons with other instruments are presented in section 6.

Vertical measurements

In figures 5.46 through 5.57 results of vertical measurements for the selected priority 1 cases are given. For each selected period a time-height- distribution for the aerosol backscatter coefficient retrieved from the 313 nm signal is presented as a pseudo-3D plot, together with one or two typical profiles giving the absolute scale. The corresponding

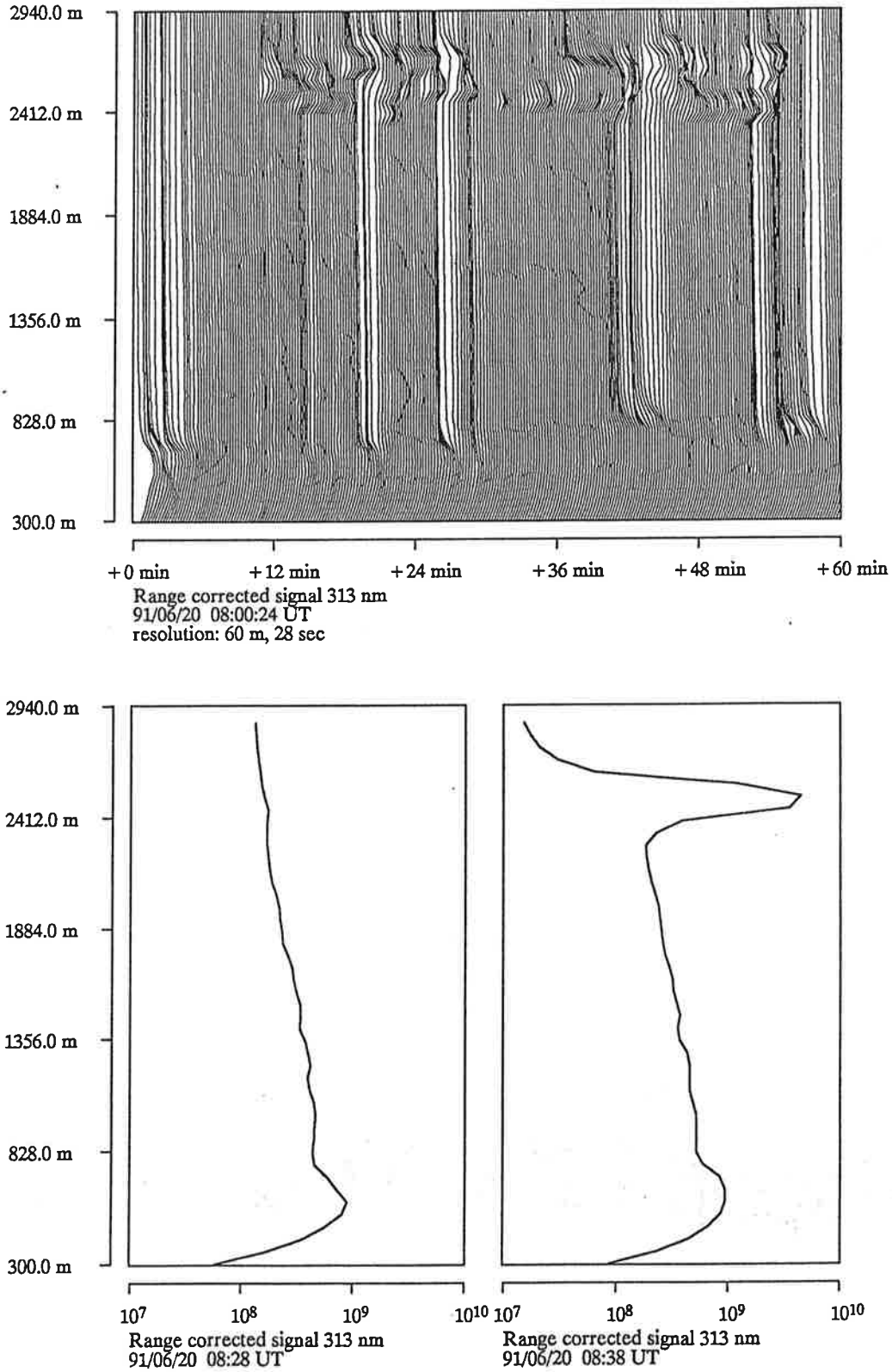

Figure 5.40: Time-height-distribution of the range corrected 313 nm signal. 1991/06/20 08:00-09:00 UT.

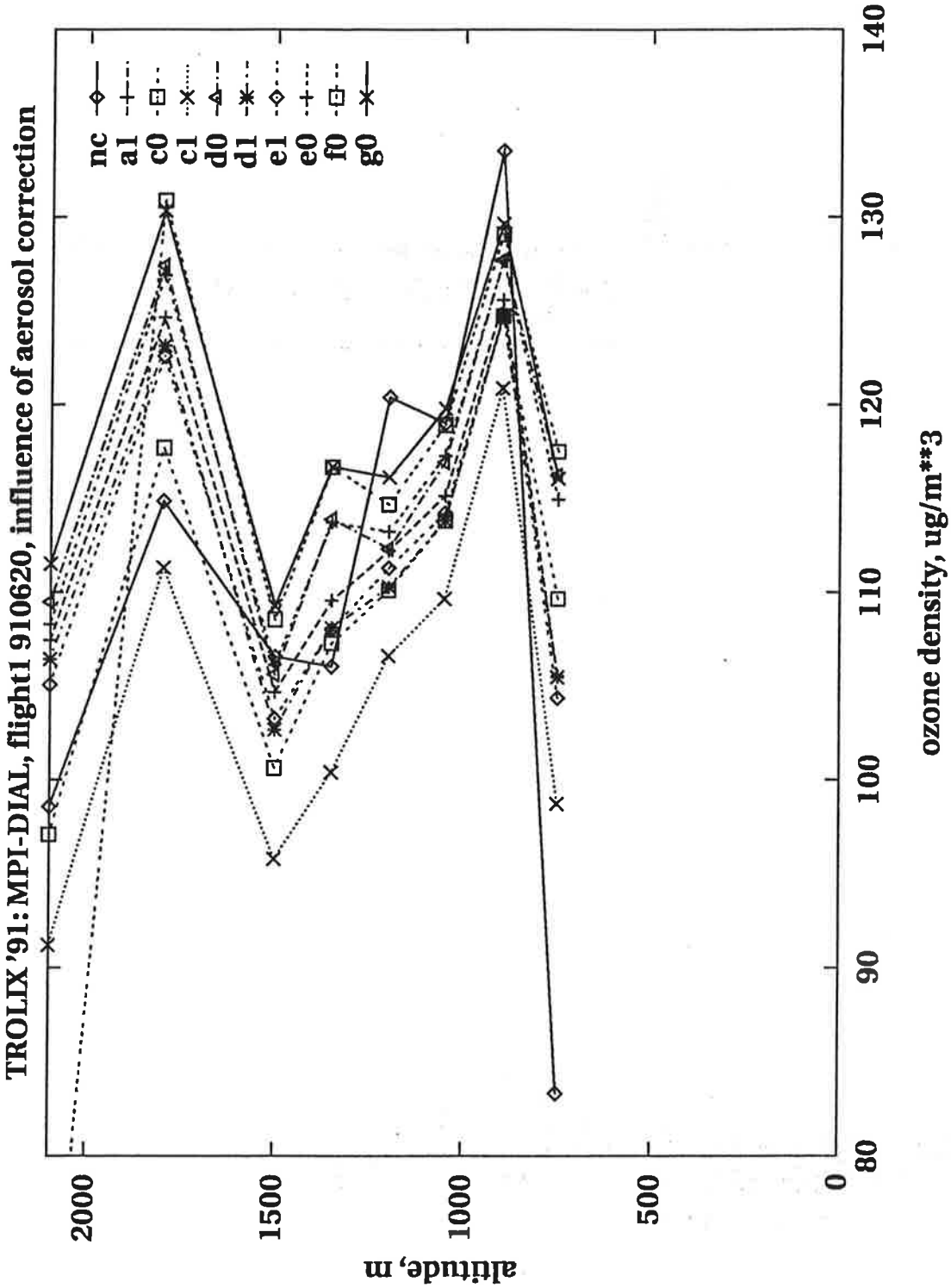

Figure 5.41: Ozone profiles for the flight intercomparison, 91/06/20 08:25-08:40 UT. nc is the uncorrected curve, in the labeling the letters have the meaning a:$\beta_{cal} = 0.1$, $S = 25$, c:$\beta_{cal} = 1.0$, $S = 25$, d:$\beta_{cal} = 0.1$, $S = 35$, e:$\beta_{cal} = 0.2$, $S = 25$, f:$\beta_{cal} = 0.0$, $S = 25$, g:$\beta_{cal} = 0.1$, $S = 15$. The number (0 or 1) indicates the exponent of the λ-dependence of the aerosol backscatter and extinction, λ^0 and λ^{-1}, respectively.

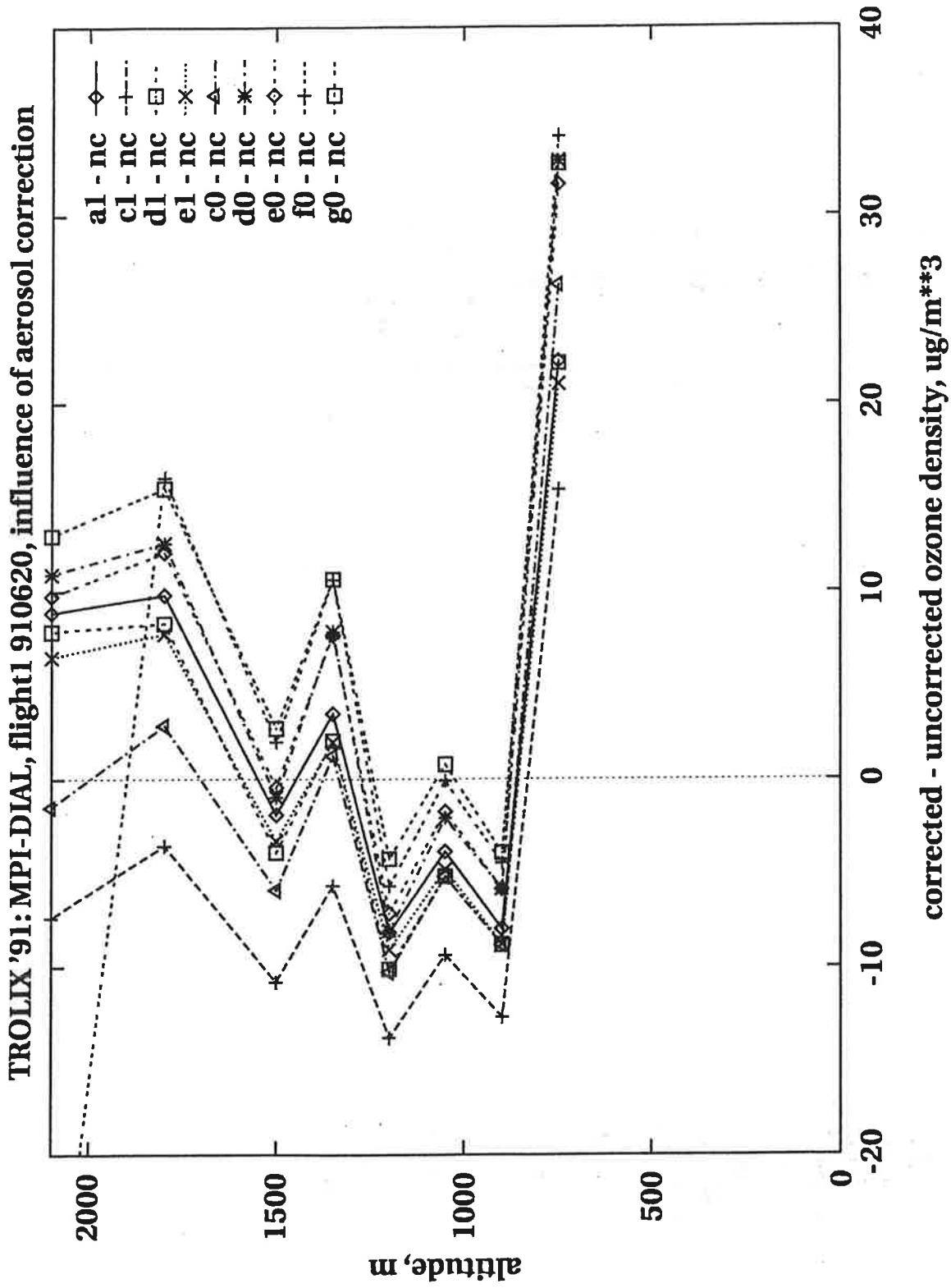

Figure 5.42: Aerosol corrections for the flight intercomparison, 91/06/20 08:25-08:40 UT. nc is the uncorrected curve, in the labeling the letters have the meaning a:$\beta_{cal} = 0.1$, $S = 25$, c:$\beta_{cal} = 1.0$, $S = 25$, d:$\beta_{cal} = 0.1$, $S = 35$, e:$\beta_{cal} = 0.2$, $S = 25$, f:$\beta_{cal} = 0.0$, $S = 25$, g:$\beta_{cal} = 0.1$, $S = 15$. The number (0 or 1) indicates the exponent of the λ-dependence of the aerosol backscatter and extinction, λ^0 and λ^{-1}, respectively.

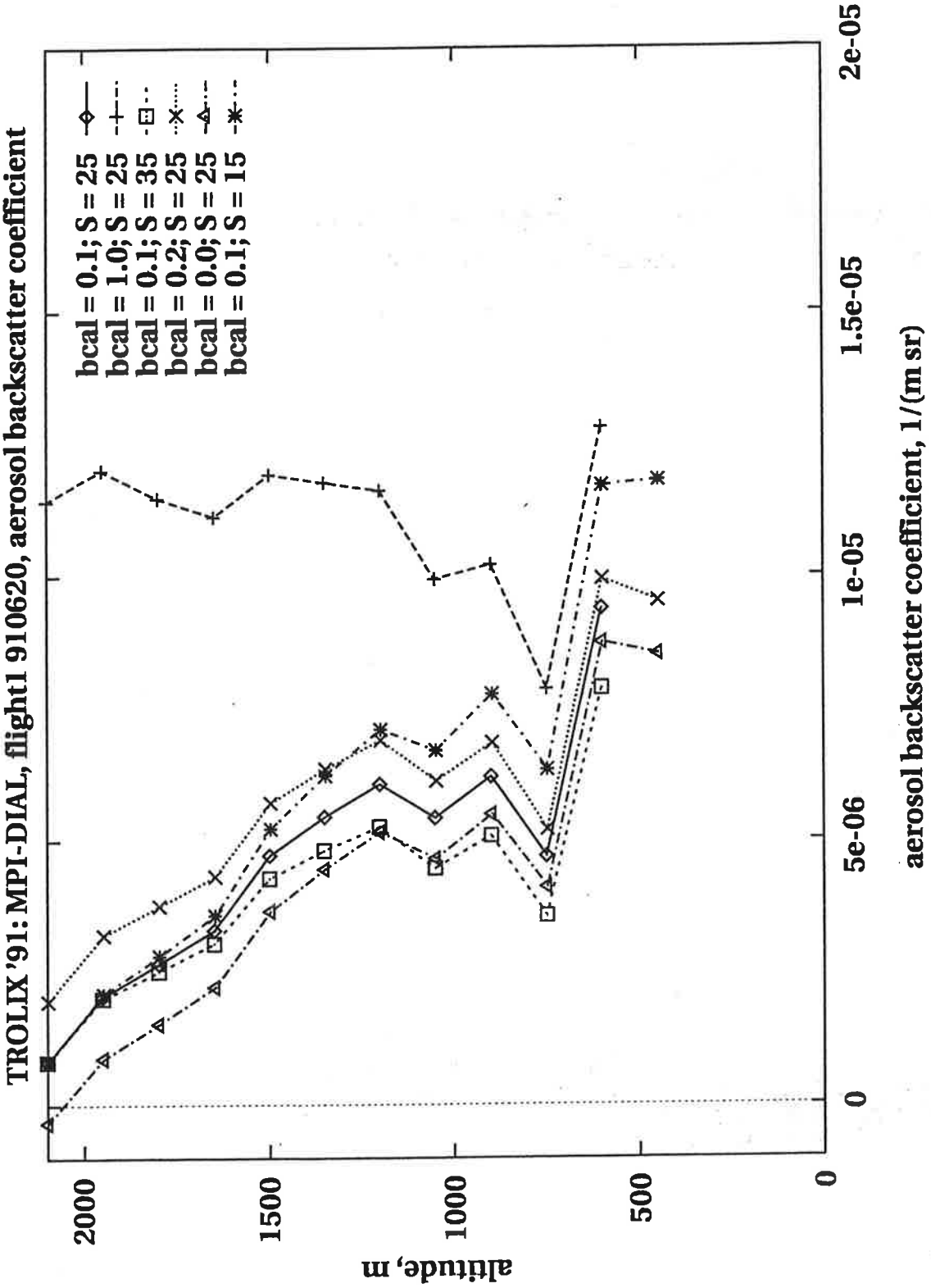

Figure 5.43: Aerosol backscatter coefficient for the flight intercomparison, 91/06/20 08:25-08:40 UT. Retrieval from 313 nm signal using a Klett-algorithm with different parameters.

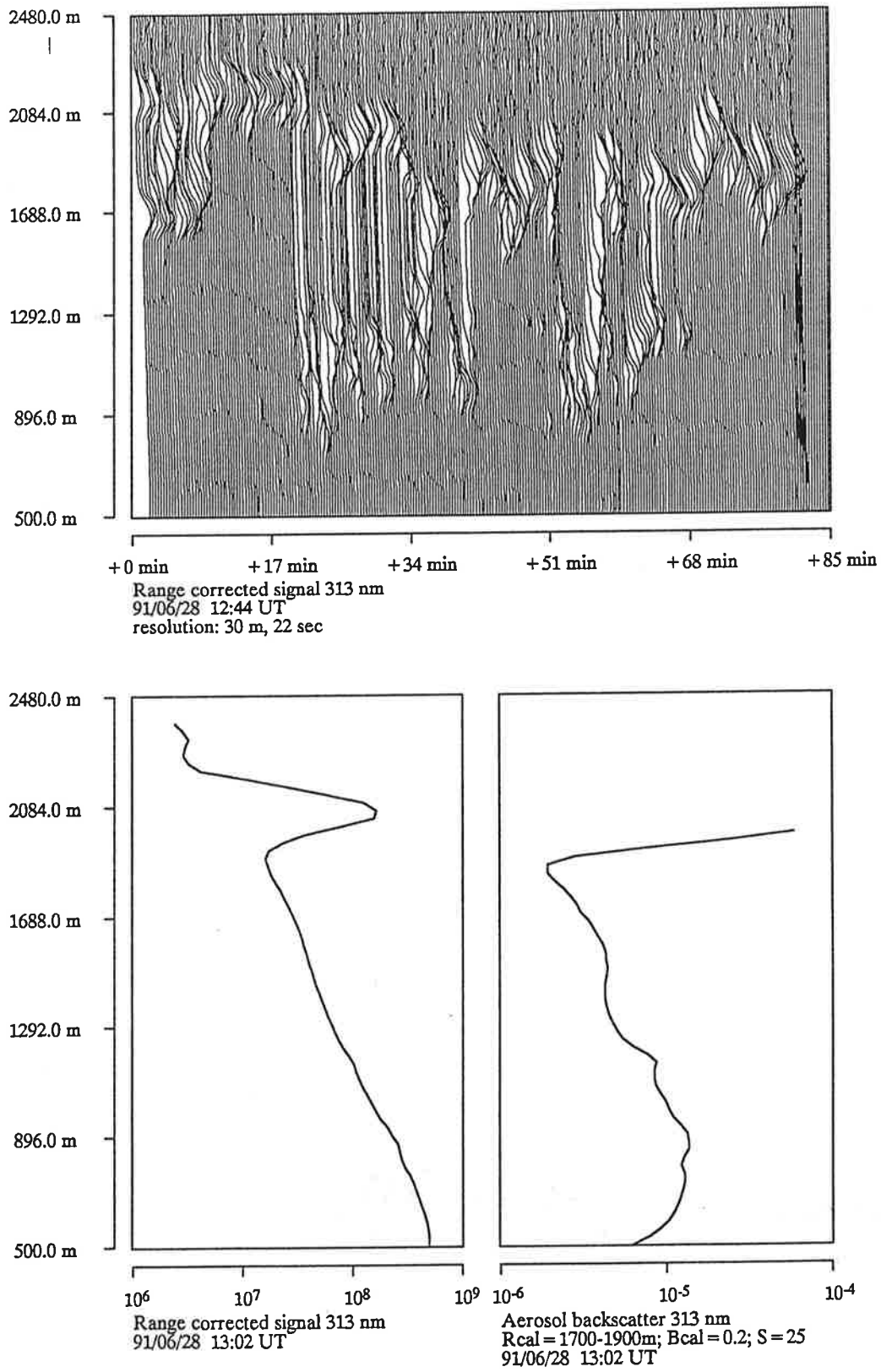

Figure 5.44: Range corrected signal for the flight intercomparison. Averaged profile (12:53 - 13:02 UT) in arbitrary units in the lower left, corresponding aerosol backscatter retrieval in the lower right.

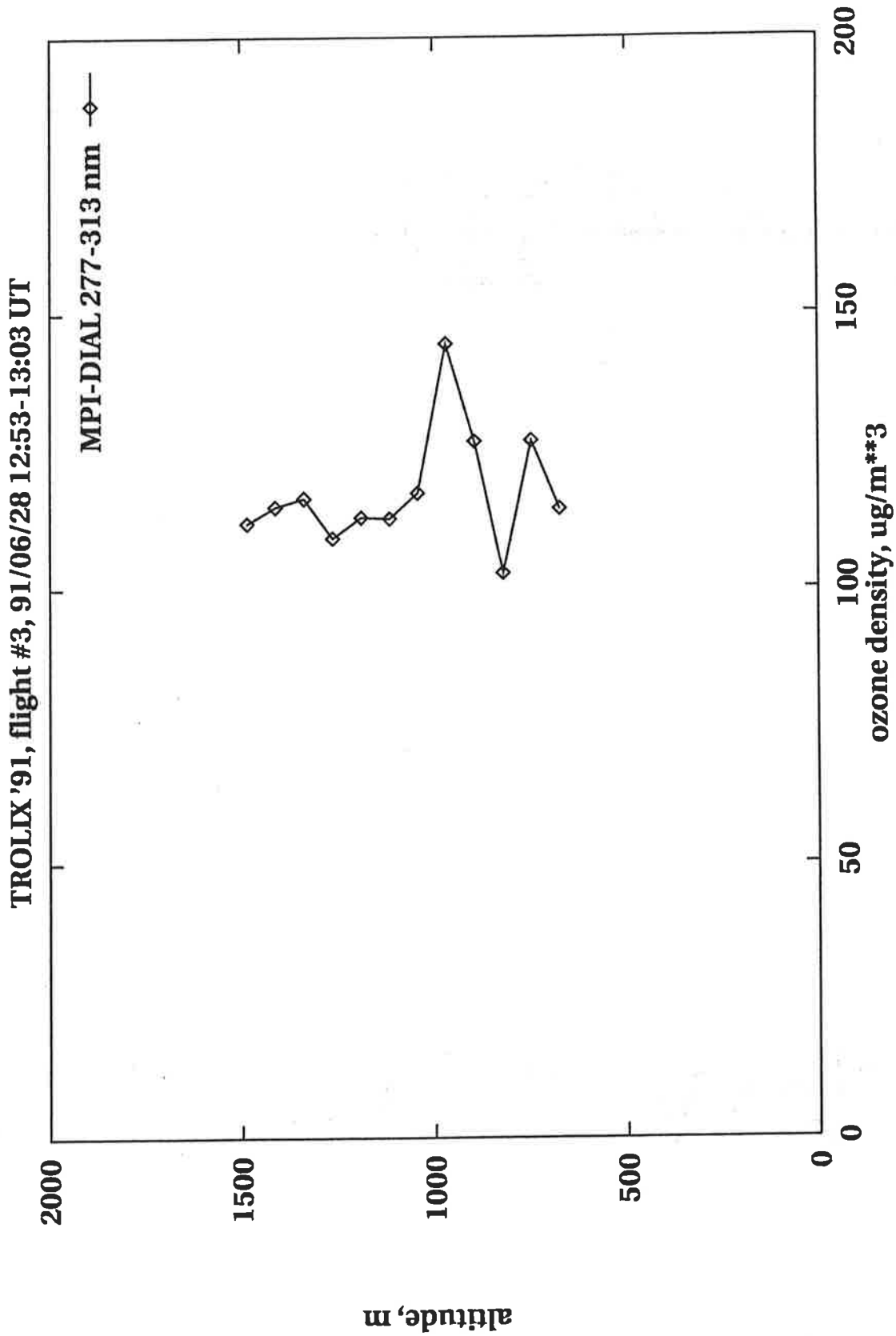

Figure 5.45: Ozone profile for flight intercomparison, 91/06/28, 12:53-13:03 UT.

ozone results are corrected for differential Rayleigh extinction, and differential aerosol backscatter and extinction, assuming a wavelength dependence of $(\frac{\lambda}{\lambda_0})^{-1}$.

On June 11, the aerosol backscatter profiles show a well developed boundary layer up to $\approx 1400m$, with few small cumulus clouds at its top. The gradients in the aerosol backscatter are moderate ($< 1{\cdot}10^{-7} sr^{-1} m^{-2}$, except for clouds), hence aerosol correction is not too important ($< 15\mu g{\cdot}m^{-3}$). Large corrections occur only at the top of the boundary layer. The bending to low ozone values at low heights of the corrected profiles is an artifact of the aerosol retrieval. Since overlap between transmitted beam and receiver field of view is not quite complete at these heights, the associated smaller signal is interpreted as a low backscatter value and hence as a gradient in aerosol backscatter. In the uncorrected profiles this does not show up, since the overlap function is the same for both wavelengths and thus is divided out in the DIAL equation. It is only via the correction for differential aerosol backscatter that this effect enters into the results. It is obvious, that in this region the corrected profiles should not be taken.

Ozone concentration in the boundary layer is clearly higher than in the free tropospheric layer above, approximately $100 - 120\mu g \cdot m^{-3}$ and $60 - 70\mu g \cdot m^{-3}$, respectively.

On June 13, measurements start in the afternoon around 14:00 UT. Again there is a well developed boundary layer, up to $\approx 2km$. In the first selected period, there are several clouds in the beginning, with cloud base around 1400 m, while the second half is cloudfree. The corresponding backscatter distribution is shown in fig. 5.50. In the second selected period, from 14:50-15:50 UT, fig 5.51 cumulus convection extends up to about 2.6 km, with two clearly distinct layers at 1.4 and at 2.4 km. For the 1^{st} priority case 15:44-15:48 UT, beyond 2.4 km there is a cloud with very high aerosol backscatter, making an ozone evaluation in that height impossible.

In the period from 17:35-18:35, see fig 5.52 the clouds have disappeared, and the boundary layer height is about 2.1 km, but with still considerable aerosol backscatter beyond that level (which is quite natural, since we have seen the cumulus convection reaching up to that level in the preceding period).

For the last period, fig 5.53, there is a cloud layer at about 1.5 km height, so again there is no ozone evaluation possible beyond that level. Aerosol correction is somewhat difficult in this case, since it is hard to find a good starting value at some calibration height. Therefore only an uncorrected profile is calculated (there are no regions of strong backscatter gradients in the evaluation range, so the error should be small).

Averaged ozone profiles for the periods indicated in fig. 5.54 are not very different and all of them show enhanced ozone concentration in the boundary layer, again, as for June 11, $\approx 100 - 120\mu g \cdot m^{-3}$ and $\approx 40 - 60\mu g \cdot m^{-3}$, respectively. It is remarkable, that there was almost no change in the ozone distribution over a period of seven hours, including sunset.

For the 1^{st}-priority period on June 26, 22:35-24:00 UT, no aerosol backscatter values have been calculated, since in this case the deuterium wavelengths 248, 268, and 292 nm have been used. So all signals are affected by ozone absorption, and the aerosol retrieval algorithm we are presently using fails. From the 292 nm signal, however, it can be concluded that there was a stable stratification for all the time, with layer boundaries

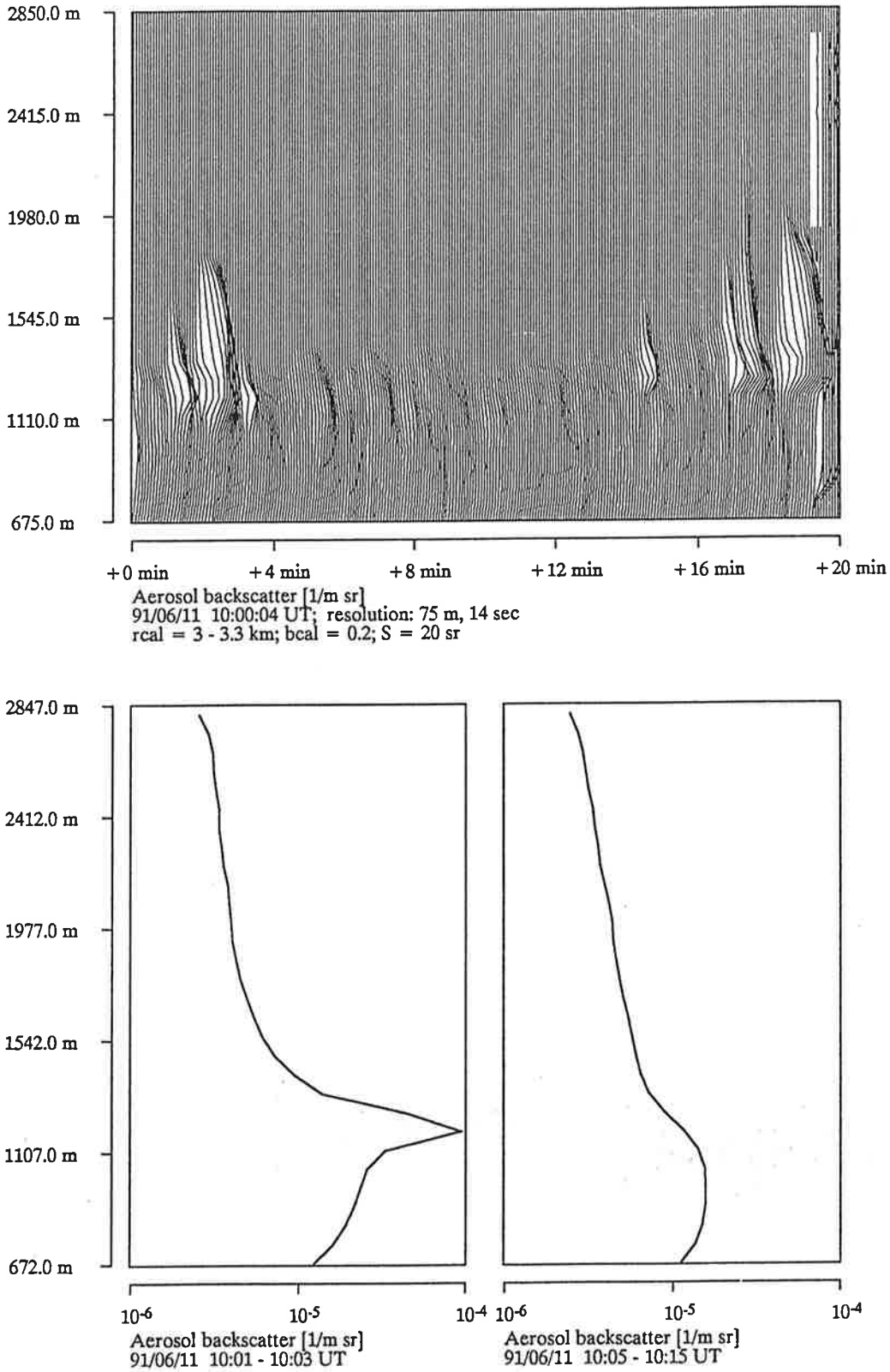

Figure 5.46: Time height distribution of aerosol backscatter coefficient retrieved from 313 nm signal. Selected profiles given below for absolute scaling.

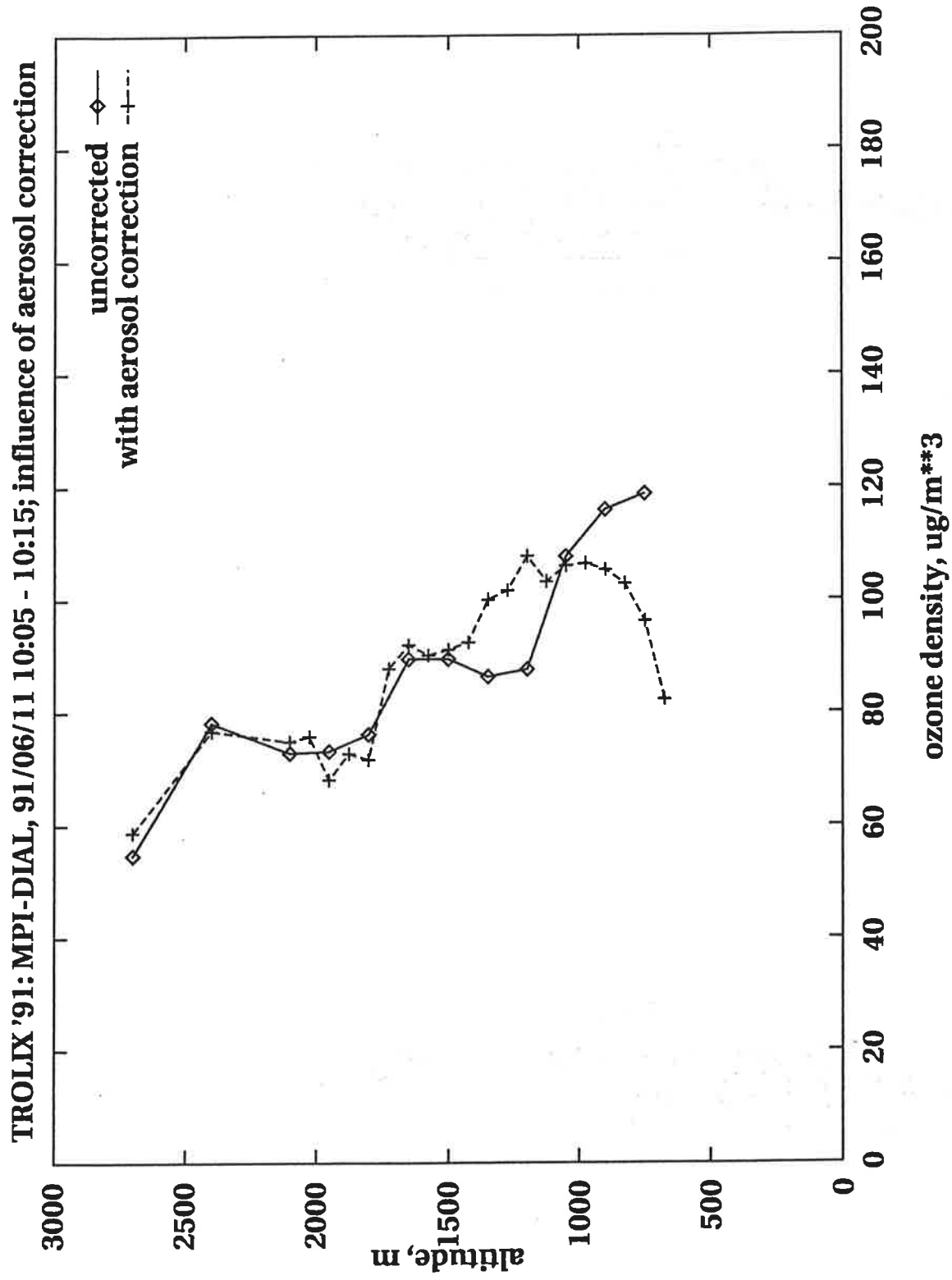

Figure 5.47: Ozone profiles with and without aerosol correction for 91/96/11, 10:05-10:15 UT.

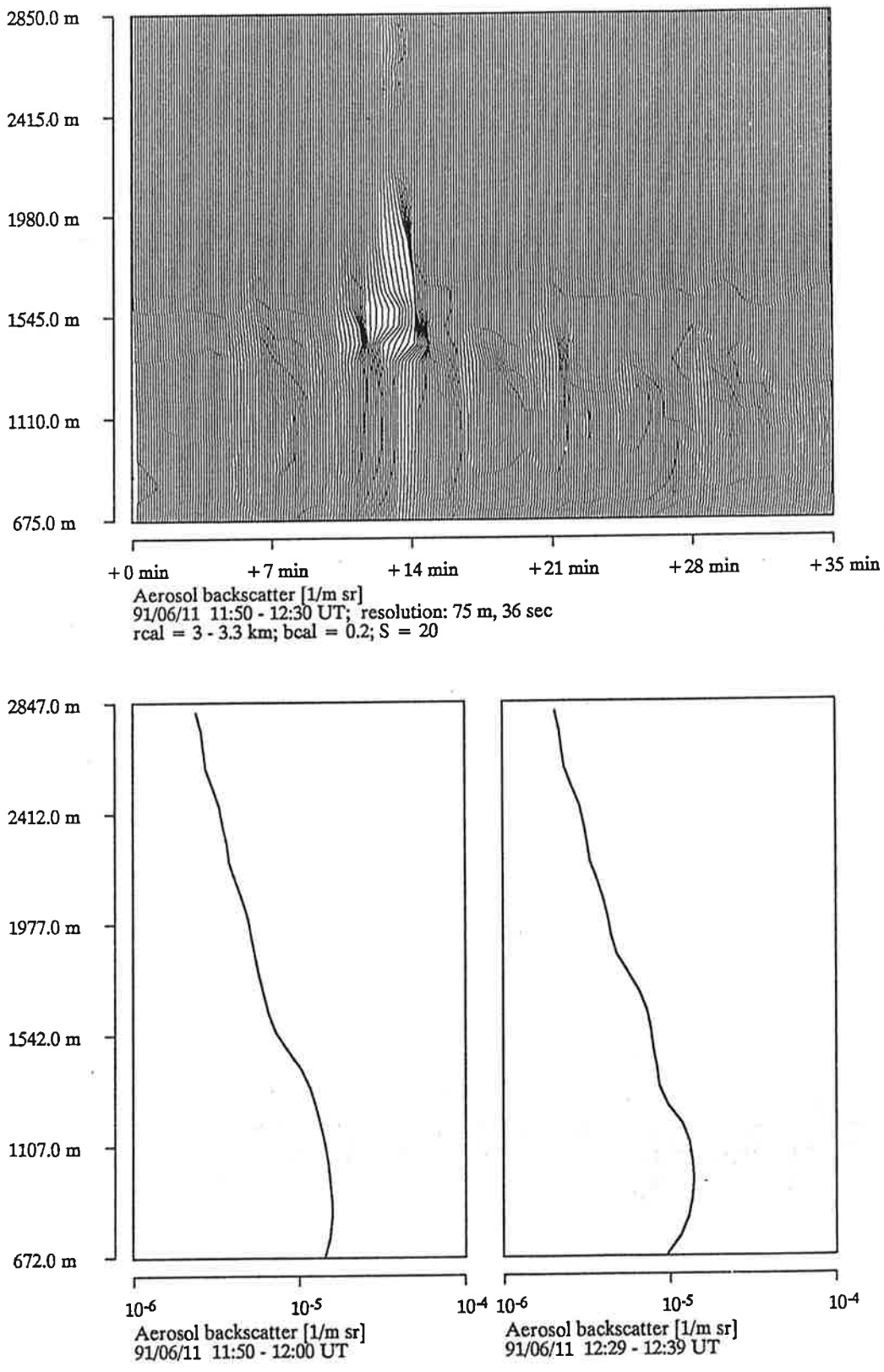

Figure 5.48: Time height distribution of aerosol backscatter coefficient retrieved from 313 nm signal. Selected profiles given below for absolute scaling.

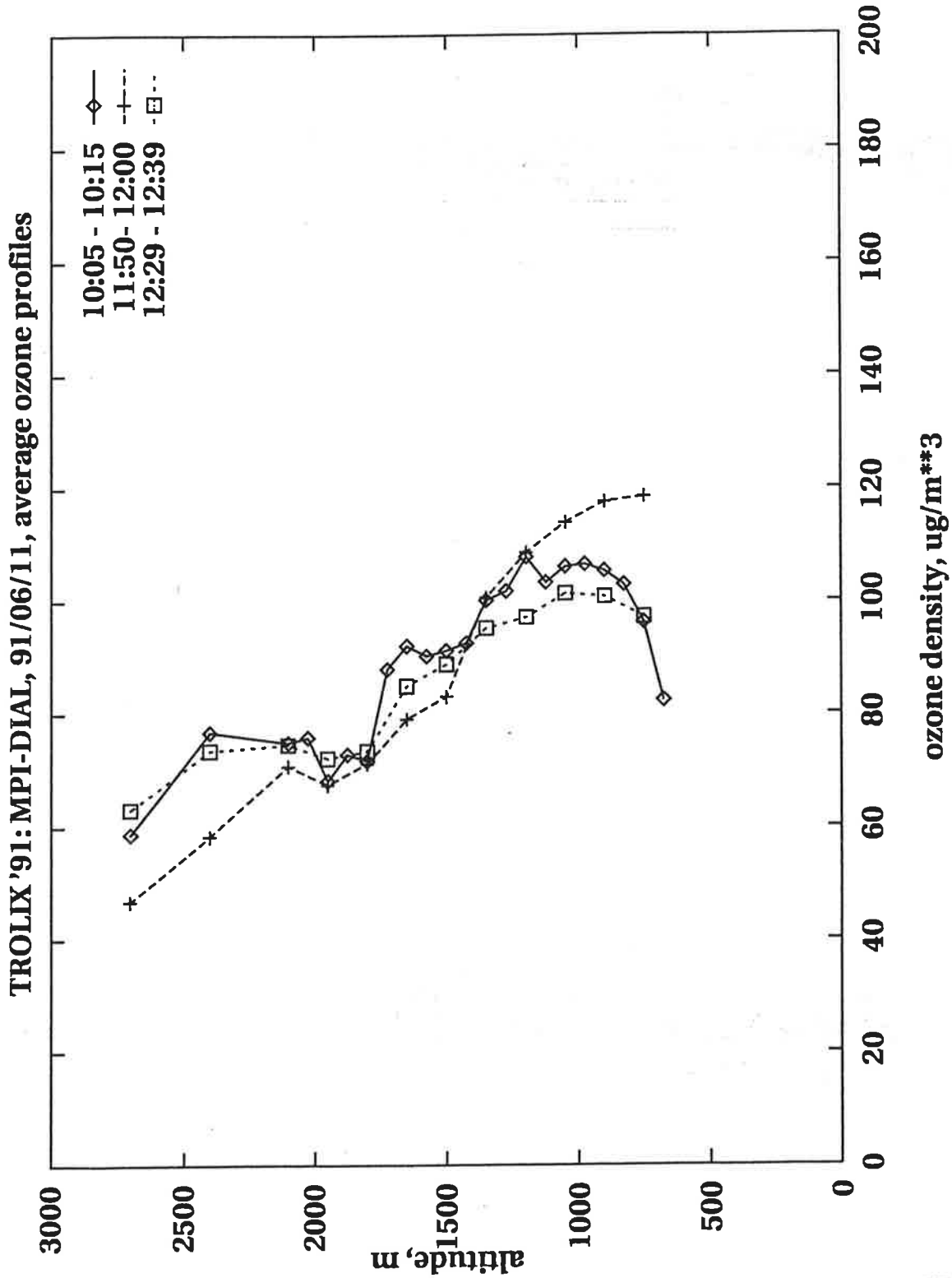

Figure 5.49: Ozone profiles with aerosol correction for 91/06/11.

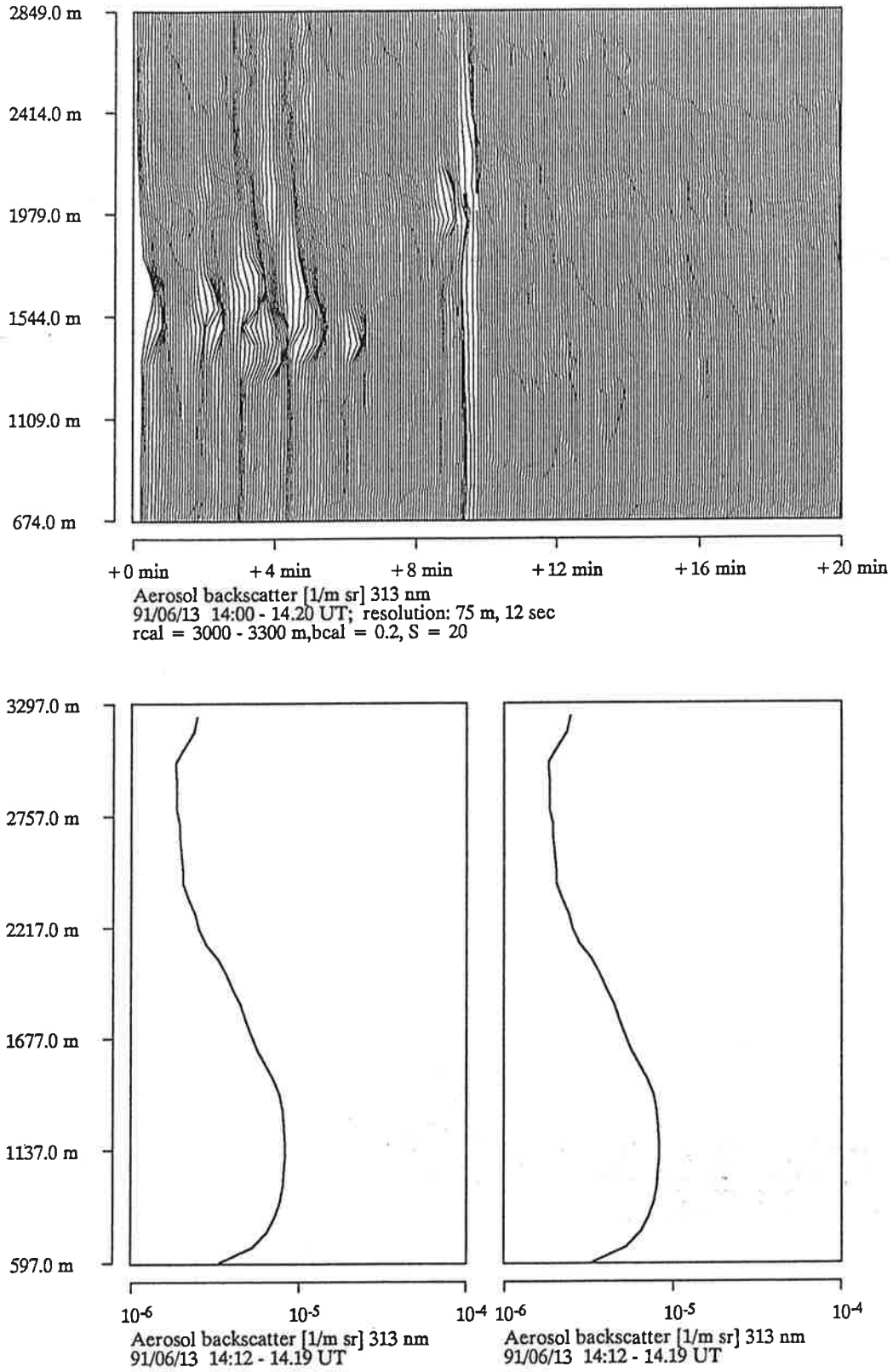

Figure 5.50: Time height distribution of aerosol backscatter coefficient retrieved from 313 nm signal. Selected profiles given below for absolute scaling.

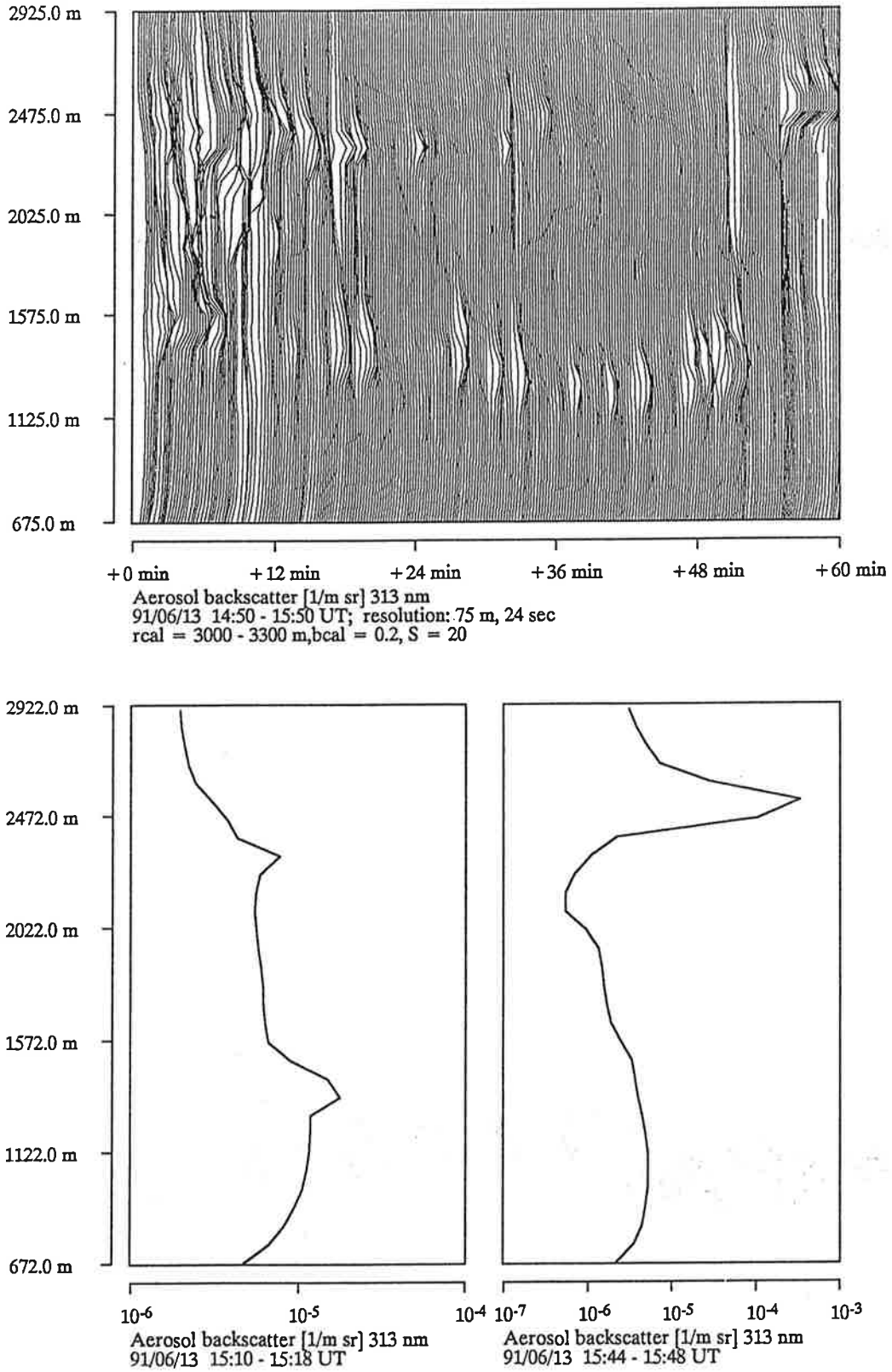

Figure 5.51: Time height distribution of aerosol backscatter coefficient retrieved from 313 nm signal. Selected profiles given below for absolute scaling.

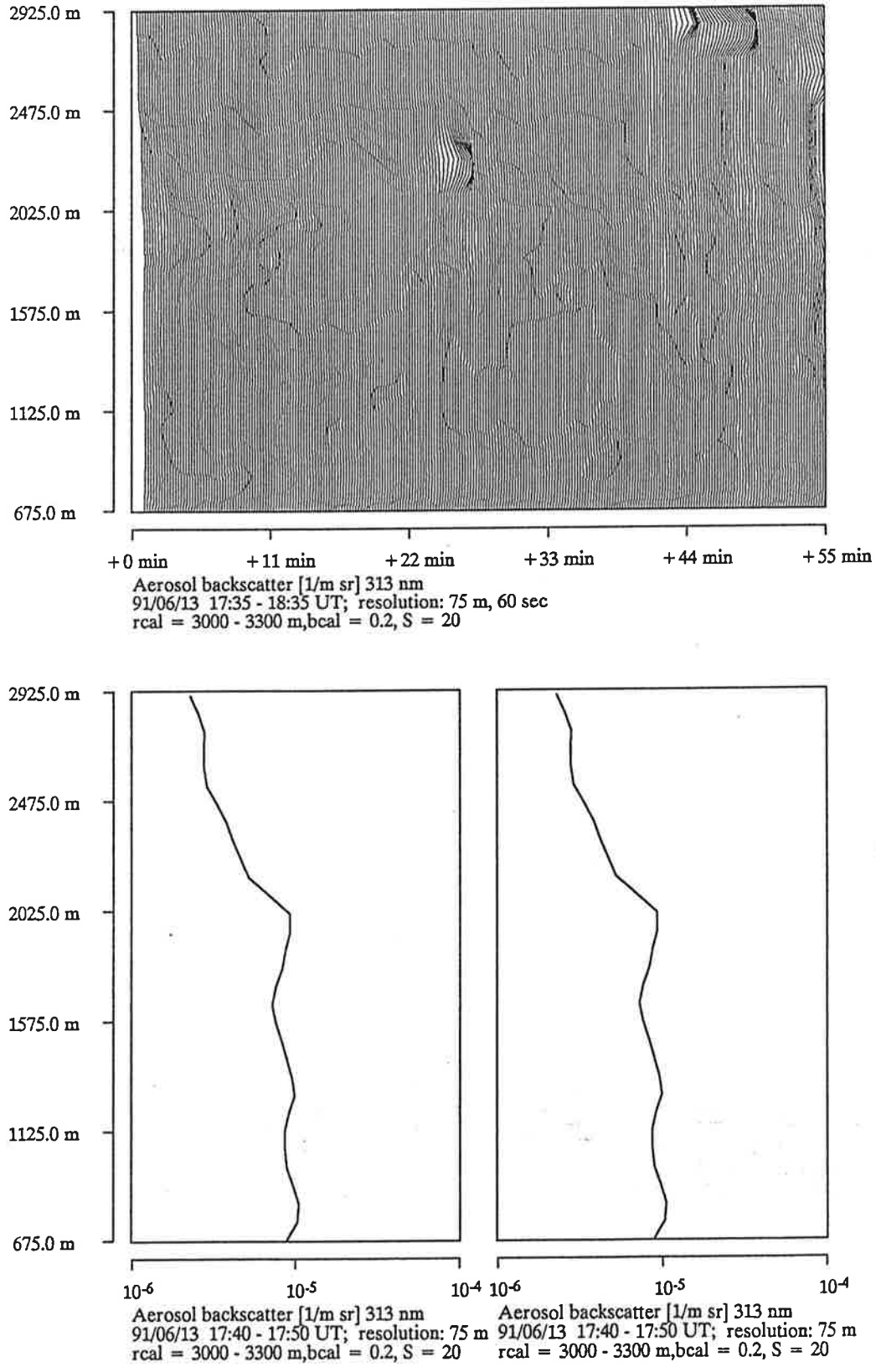

Figure 5.52: Time height distribution of aerosol backscatter coefficient retrieved from 313 nm signal. Selected profiles given below for absolute scaling.

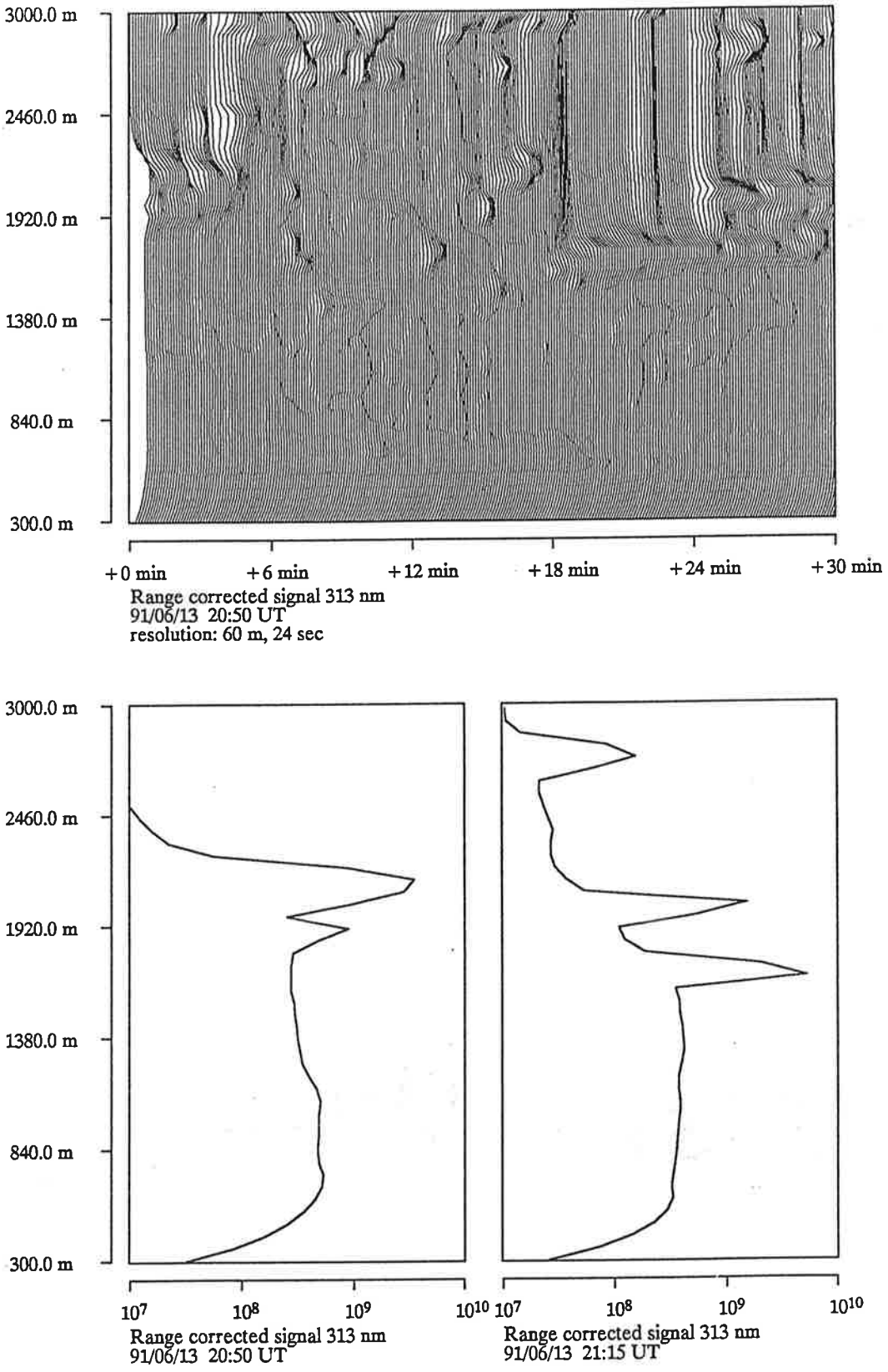

Figure 5.53: Time height distribution of range corrected signal at 313 nm.

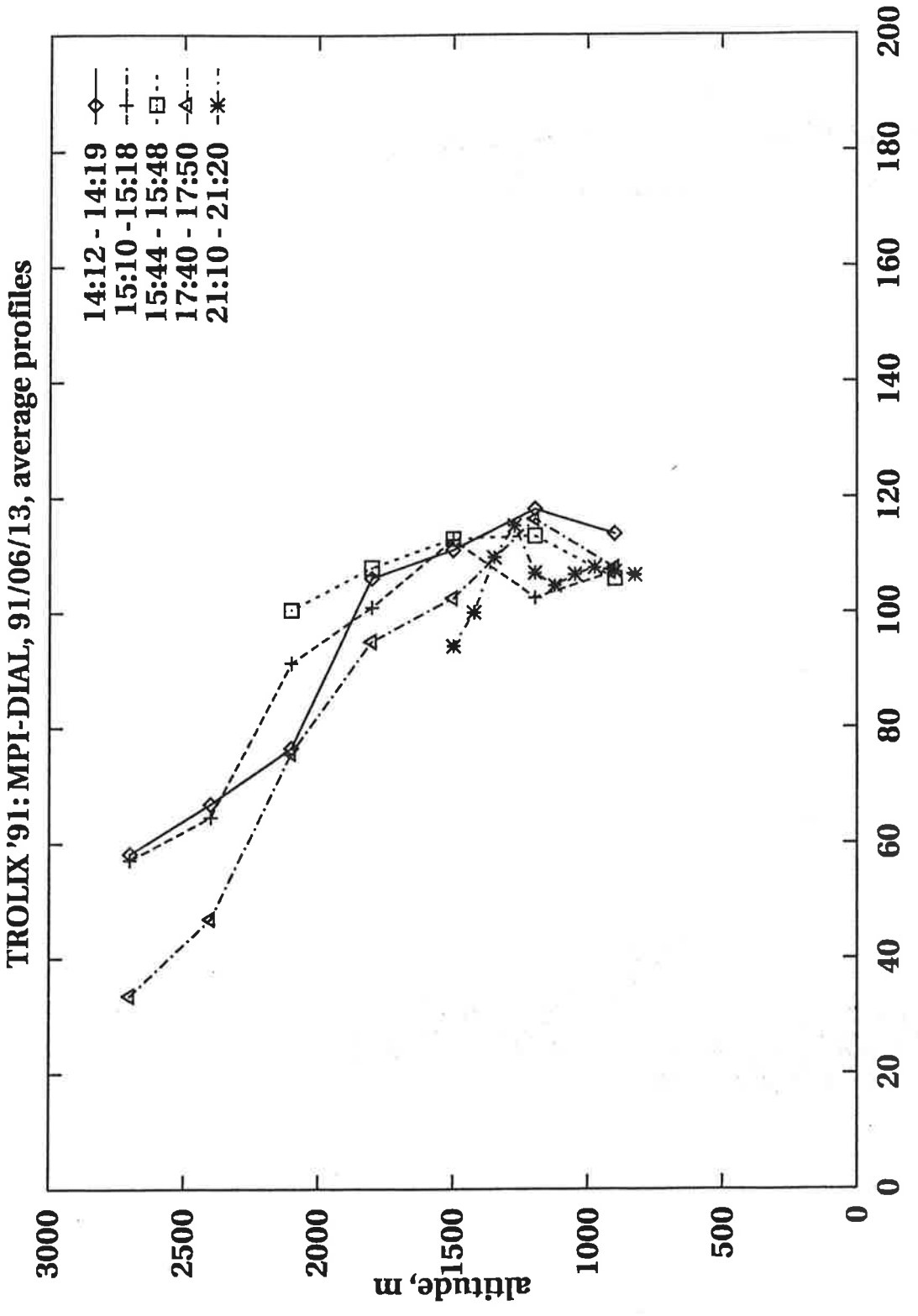

Figure 5.54: Average ozone profiles for selected periods on 91/06/13.

at $\approx 0.7km$, $\approx 1.4km$, and $\approx 1.9km$. Only two averaged profiles are shown in fig. 5.55 as examples.

Fig. 5.56 shows ozone profiles averaged over 10 min. for the whole period. The prominent structure between 1200 and 1600 m is a consequence of the data acquisition problem described above. So data beyond 1200 m are considered nonreliable. However, if an average is taken over the whole height interval of this disturbance, a reasonable for the ozone concentration is found. This is illustrated in fig. 5.57. Still ozone values beyond 1200 m should be taken with some care, because of the low on-line signal, but sufficient height averaging appears to be a workaround for this problem.

The deuterium wavelengths are particular suited to obtain high resolution measurements in the first few hundred meters. This is demonstrated in fig. 5.58, where a variance spectrum is calculated from the whole time series of about 1.5 hours, for an altitude of 630 m. This height had been selected because it stayed in the same layer for the complete period, so the influence of aerosol gradients could be minimized. Evaluations have been performed with different time and height resolution, some of them are shown in fig. 5.58. All variance spectra decrease with increasing frequency, over a fairly large frequency range approximately according to a -5/3 power law, but reach an almost constant level at the high frequency end. This level depends on the height resolution. Apparently at the high frequency end the spectra are dominated by instrumental noise, which is better averaged out for poorer height resolution. Since the noise spectrum for this process can only be white (consecutive measurements are completely independent), the noise level can be estimated from the lowest statistically significant level of the power spectrum. A line for a power spectral density corresponding to $2\mu g \cdot m^{-3}$ is indicated in the figure, which is a little less than the estimated rms noise for the measurement with 120 m vertical and 12 sec temporal resolution. For 30 m vertical resolution, the noise level is increased to about $6\mu g \cdot m^{-3}$. Increasing the average time to 36 sec does not affect most of the variance spectrum, see fig. 5.59. Only at the highest frequencies the level is decreased approximately by a factor of 2. This is in good agreement with the theoretically expected noise reduction by a factor of $\sqrt{3}$.

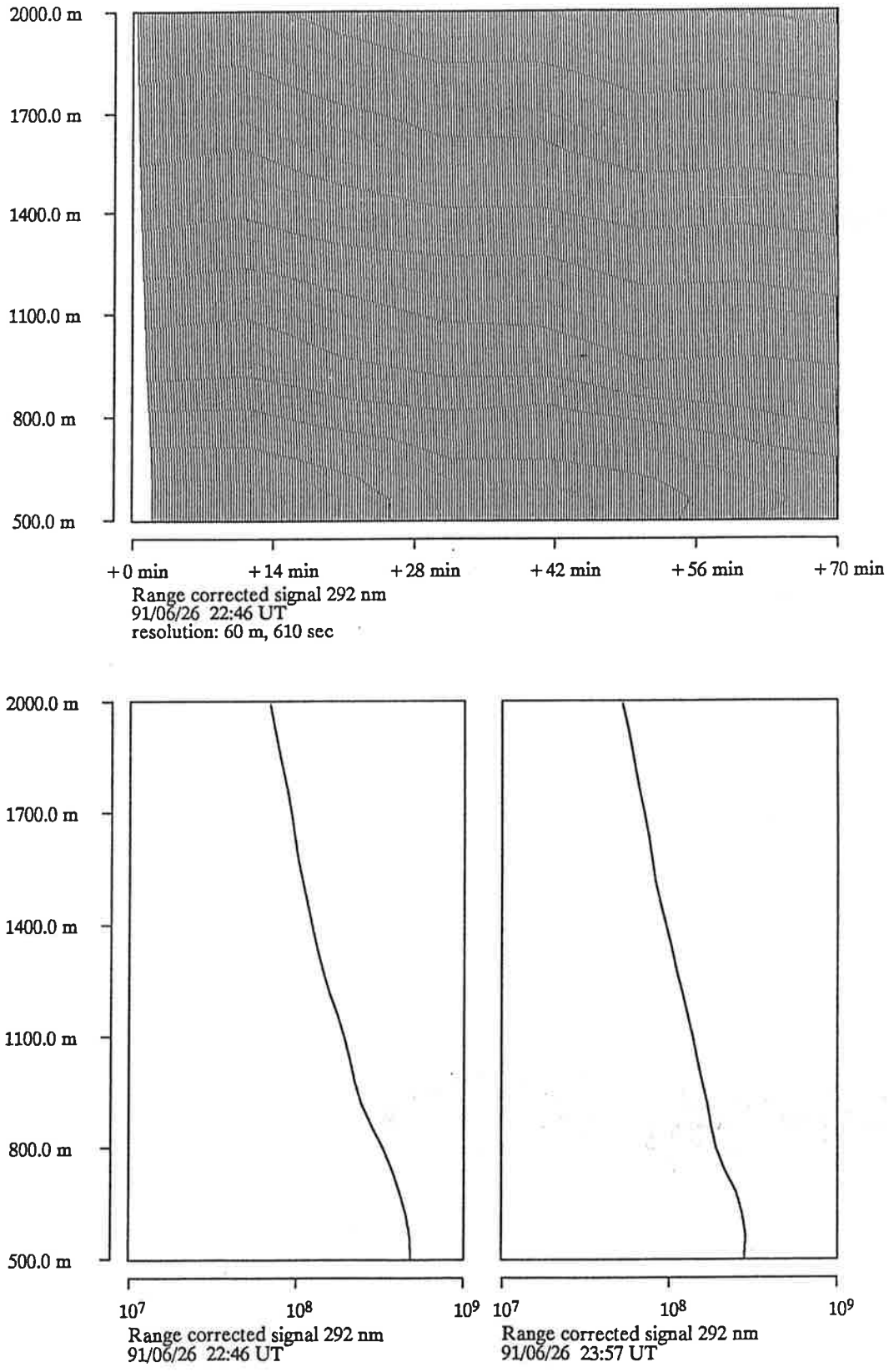

Figure 5.55: Time height distribution and selected profiles for the 292 nm range corrected signal. 91/06/26.

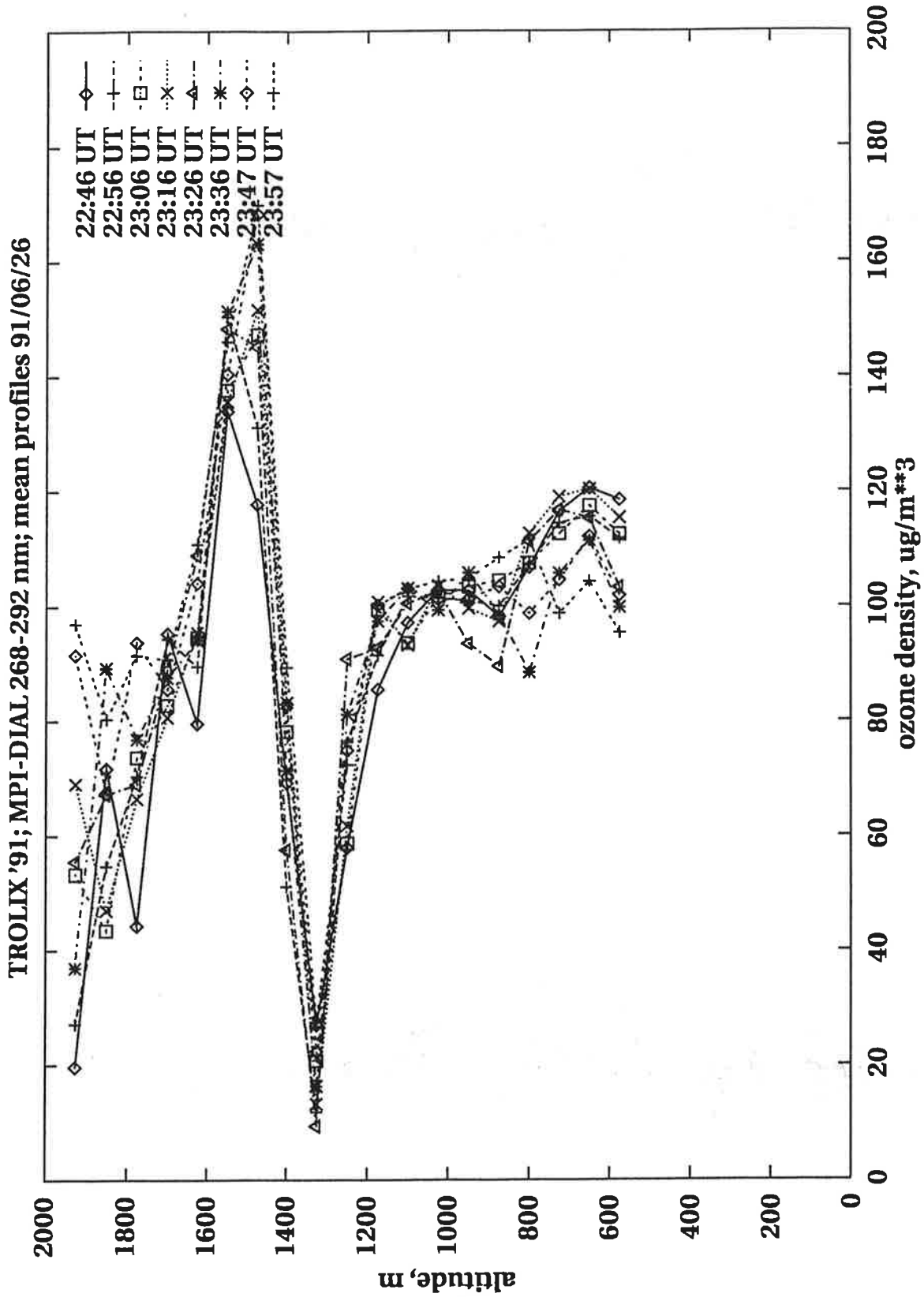

Figure 5.56: Average ozone profiles for selected periods on 91/06/26.

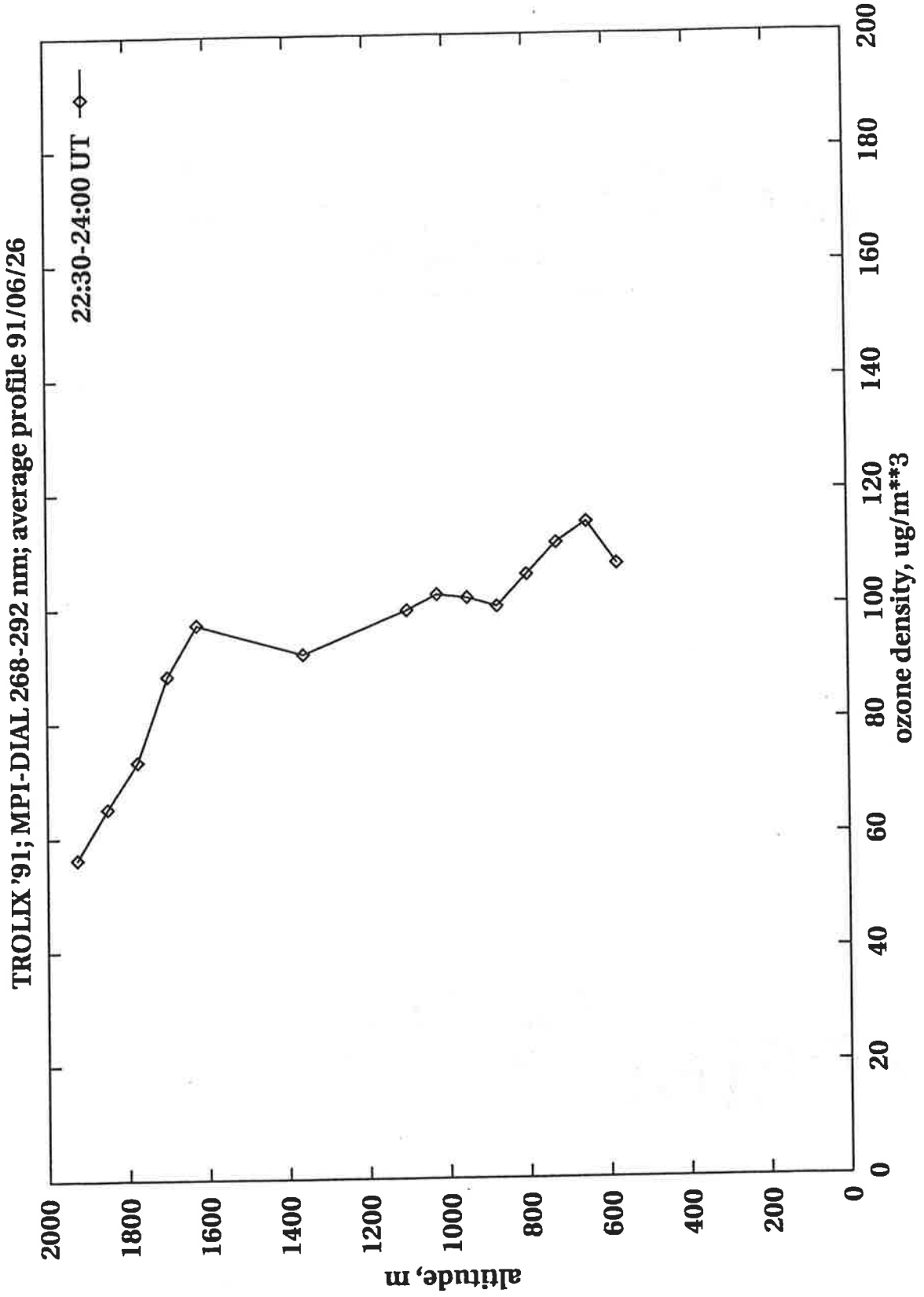

Figure 5.57: Average ozone profile 91/06/26.

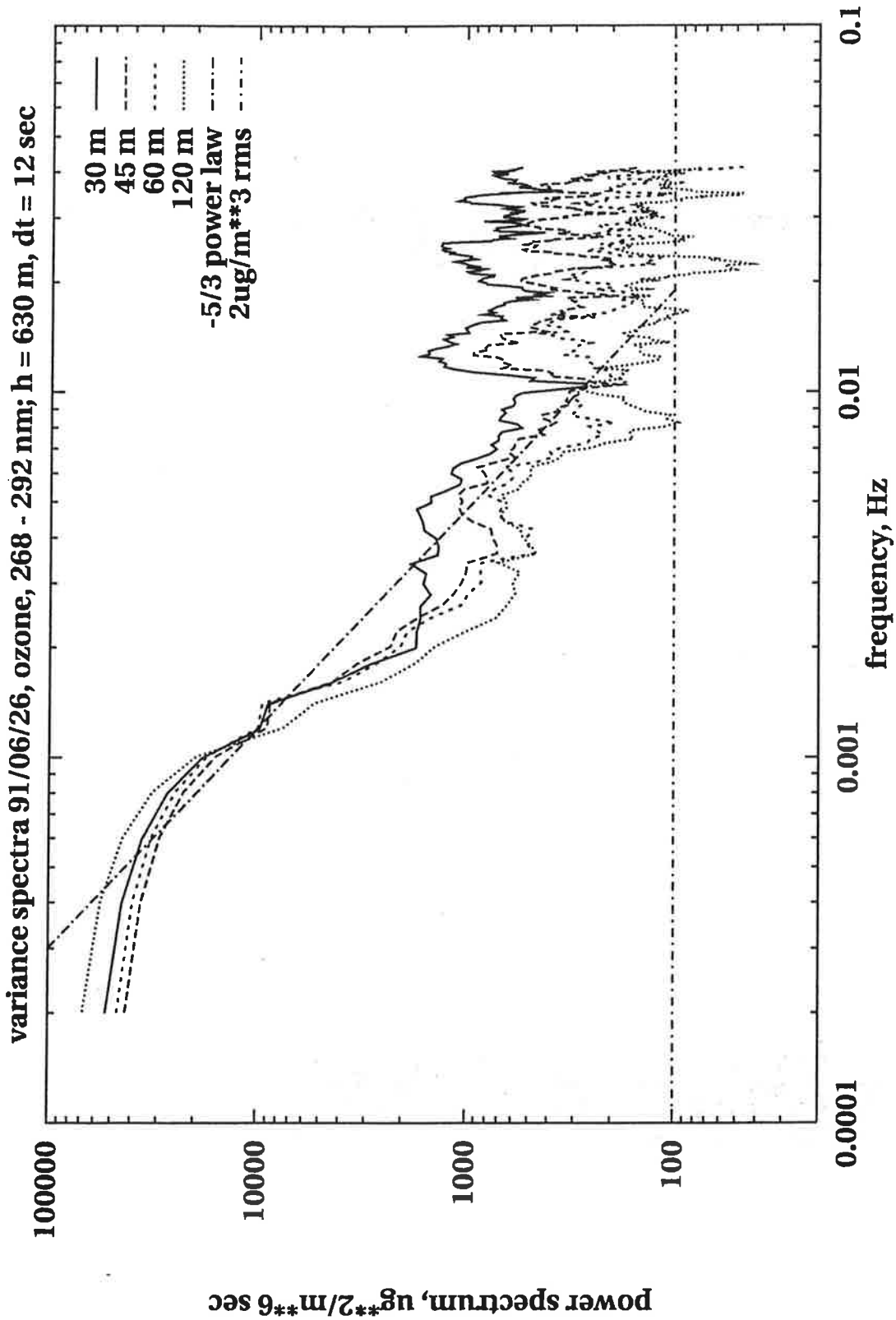

Figure 5.58: Variance spectrum of ozone density for different height resolutions. 91/06/26 22:35-24:00 UT.

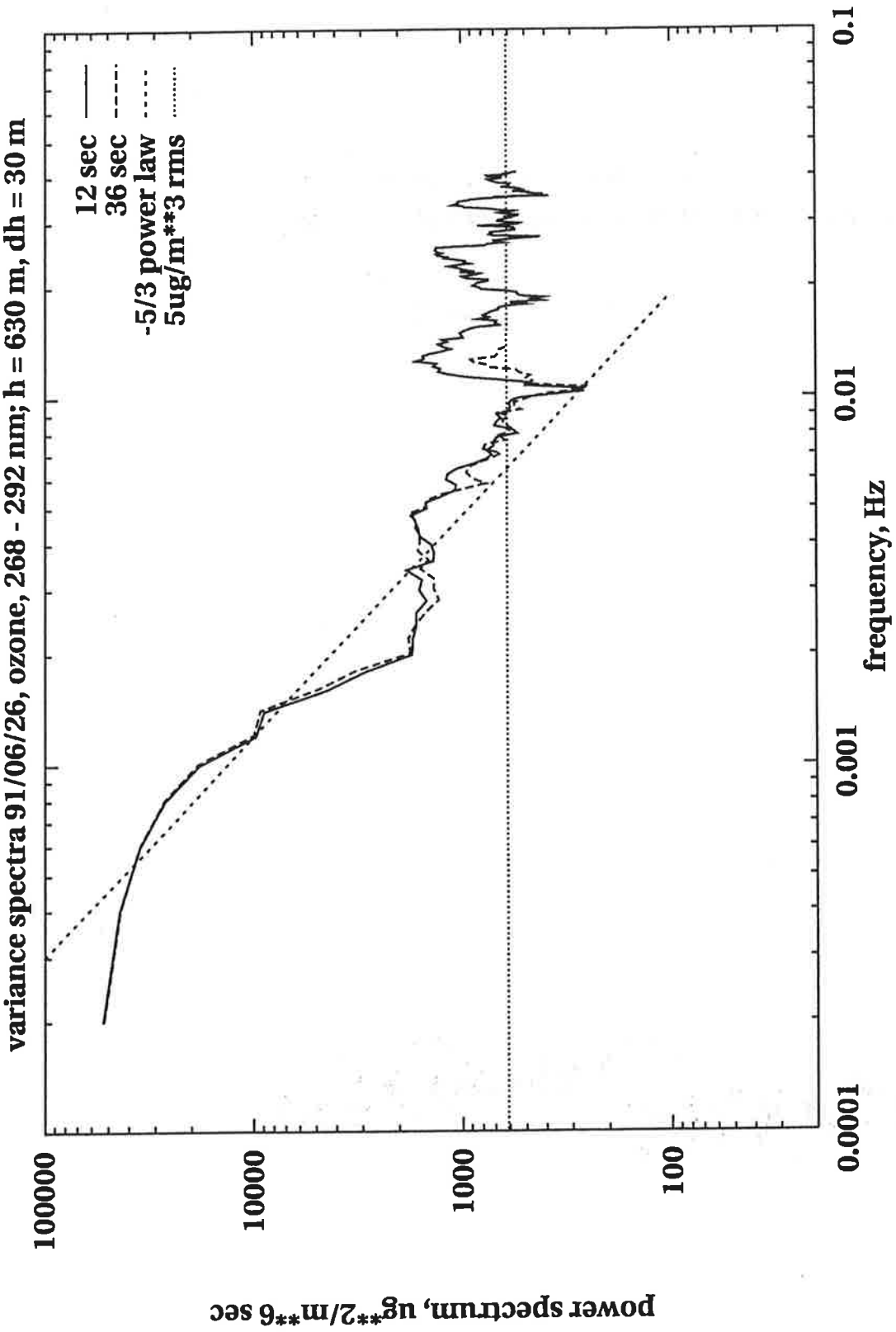

Figure 5.59: Variance spectrum of ozone density for different time resolutions. 91/06/26 22:35-24:00 UT.

5.4 Results of helicopter flights

5.4.1 Flight procedure

The flights were carried out by a helicopter flying at constant altitude in circles with a radius of about 500 m at altitude intervals of 100 m starting at 200 m. A minimum presence of a few minutes at each altitude is necessary.

During take off (and landing), the analyzers were disconnected from the main FEP tube and connected to a filter filled with activated coal to prevent exhaust gases reaching the analyzers (see figure 5.61). Between the flights the FEP tube was stored with the tube ends sealed.

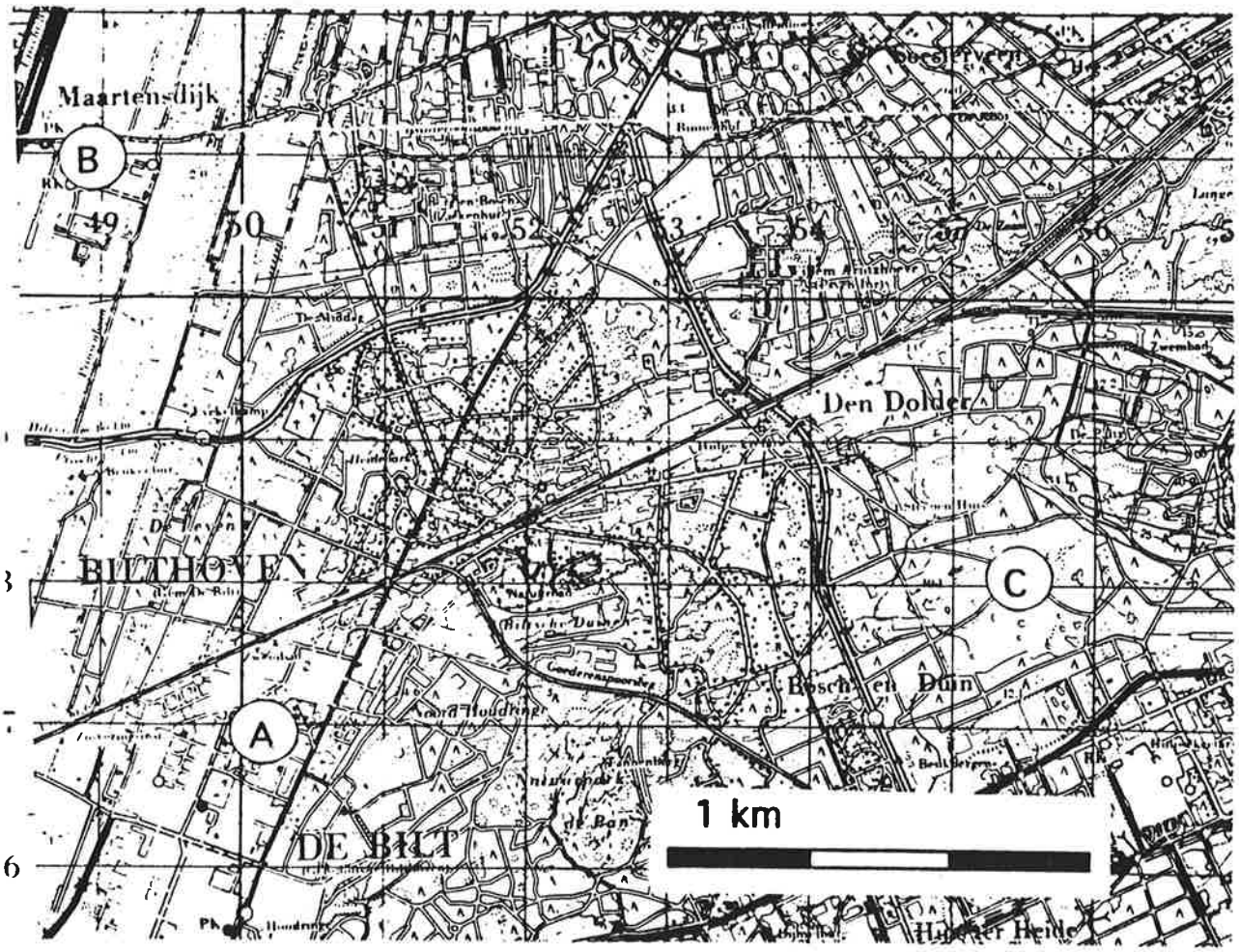

Figure 5.60: Flight locations: A - Trolix site at Bilthoven; B - Maartensdijk; C - Soesterberg.

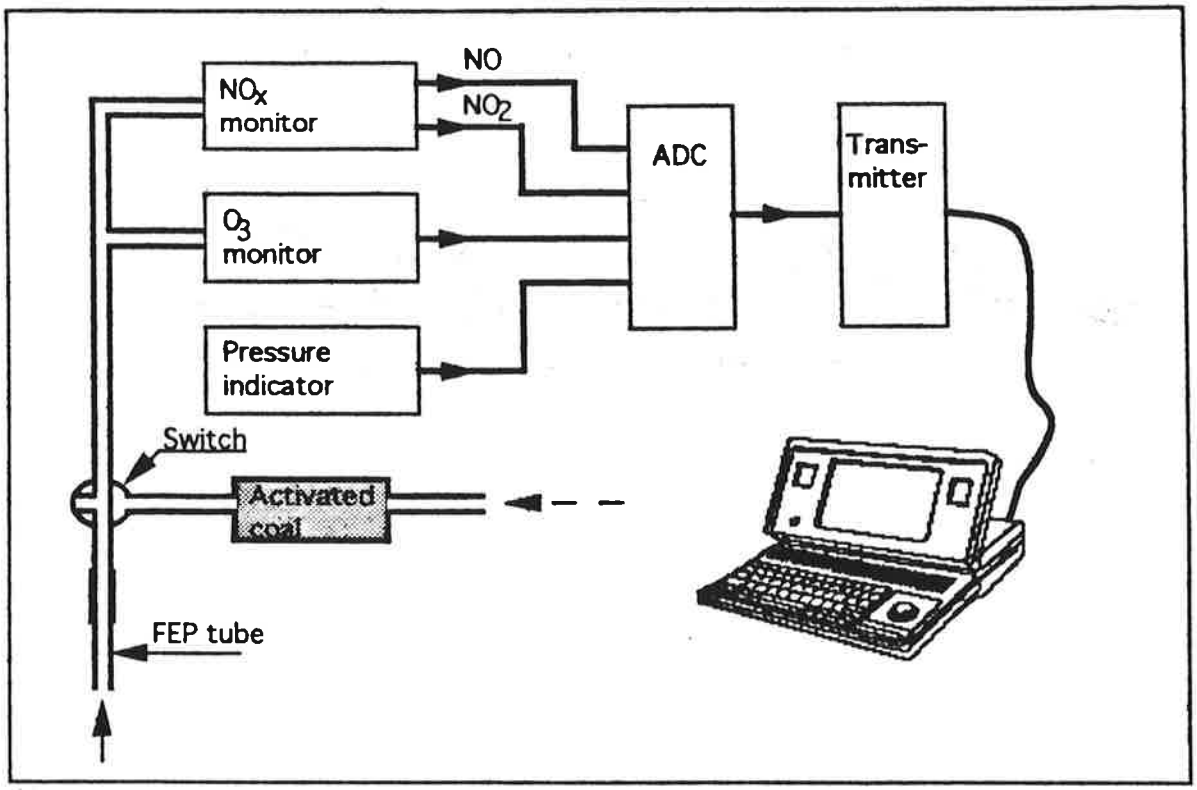

Figure 5.61: Measurement setup

5.4.2 Results

For the purpose of direct comparison $\mu\ g \cdot m^{-3}$ is used as the unit for O_3, NO and NO_2. Successive measurements taken at the same altitude have been averaged. However, the individual response time of the instruments is taken into account by using one of two data points for the ozone data and one of four data points for the NO_x measurements. The average and standard error of the mean at each altitude are given for the various components (Altitude, Ozone, Nitrogen oxide and Nitrogen dioxide). The altitude is defined by the pressure following the expression (temperature = 283 K):

Table 5.3 shows flight times and locations, tables 5.4 - 5.6 give the different component concentrations for the three flights as a function of height. The concentrations given are mean values with standard error of the mean.

Altitude	= 8270 ln (P_0/P_h) - H_p (m)
where P_o	= local pressure at ground level,
P_h	= local pressure at altitude H,
H_p	= difference in height between pressure indicator and gas sampling point (10 m).

The time standard used was UT (Universal Time) .

Date of flight	Starting time (UT)	Stopping time (UT)	Flight location
91/06/20	7:56	8:55	Bilthoven
91/06/24	12:15	13:07	Maartensdijk
91/06/28	13:39	14:27	Soesterberg

Table 5.3: Summary of the flights.

5.4.3 Discussion

The precision of the airborne O_3 measurements turned out to be less than expected from instrument specifications and calibration results. Individual measurement readings at a constant altitude show a large variation.

At the present stage we think this is caused by the pressure-correcting algorithm in the monitor used to convert absolute values to ppb. The pressure variations occurring as a consequence of the inevitable altitude variations of the helicopter probably cause large oscillations in the pressure-corrected ppb values. This assumption is strengthened by the observation that O_3 values during climbing or descent were permanently off scale.

In future experiments care should be taken to prevent adverse influences from the pressure correcting algorithm. Instead, absolute O_3 values directly from the UV absorption should be used.

Time UT	Altitude [meter]	Airborne $[\mu g \cdot m^{-3}]$			Number of data-points
		O_3	NO	NO_2	
7:56:40 -8:03:40	250 +/- 3	43 +/- 4	8 +/- 1	31 +/- 2	32
8:04:30 -8:09:30	326 +/- 2	48 +/- 2	12 +/- 1	42 +/- 1	27
8:10:50 -8:13:30	415 +/- 5	60 +/- 4	8 +/- 1	32 +/- 1	13
8:14:30 -8:15:50	502 +/- 4	70 +/- 5	4 +/- 1	21 +/- 1	9
8:16:10 -8:18:50	575 +/- 4	73 +/- 6	2 +/- 1	22 +/- 1	14
8:19:15 -8:21:40	692 +/- 1	87 +/- 4	2 +/- 1	13 +/- 1	12
8:22:50 -8:25:10	774 +/- 1	96 +/- 6	-1 +/- 1	2 +/- 1	11
8:26:20 -8:28:50	860 +/- 3	111 +/- 4	-1 +/- 1	2 +/- 1	16
8:29:40 -8:32:40	929 +/- 2	107 +/- 3	-2 +/- 1	4 +/- 1	15
8:33:30 -8:35:40	1002 +/- 4	112 +/- 7	-2 +/- 1	1 +/- 1	8
8:36:30 -8:38:40	1093 +/- 3	101 +/- 6	-1 +/- 1	0 +/- 1	9
8:39:40 -8:42:30	1181 +/- 2	93 +/- 6	-1 +/- 1	2 +/- 1	14
8:43:30 -8:46.20	1272 +/- 2	101 +/- 4	-1 +/- 1	2 +/- 1	18
8:47:20 -8:50:00	1370 +/- 4	96 +/- 7	-1 +/- 1	-1 +/- 1	13
8:51:20 -8:52:10	1439 +/- 1	100 +/- 9	-1 +/- 1	1 +/- 1	6
8:53:00 -8:55:10	1542 +/- 2	95 +/- 5	-1 +/- 1	2 +/- 2	10

Table 5.4: Flight 1, 20 June 1991 near Bilthoven (RIVM) location A.

Time U.T.	Altitude [meter]	Airborne $[\mu g \cdot m^{-3}]$			Number of data-points
		O_3	NO	NO_2	
12:15:40 -12:17:40	271 +/- 2	68 +/- 4	0 +/- 2	20 +/- 4	9
12:19:30 -12:21:20	358 +/- 3	78 +/- 5	1 +/- 1	14 +/- 2	12
12:22:10 -12:25:30	443 +/- 2	78 +/- 4	0 +/- 1	13 +/- 2	17
12:27:00 -12:30:10	503 +/- 6	78 +/- 4	-2 +/- 1	15 +/- 2	15
12:31:10 -12:32:50	592 +/- 3	80 +/- 5	1 +/- 1	12 +/- 1	11
12:33:50 -12:36:20	675 +/- 3	77 +/- 6	0 +/- 1	12 +/- 1	12
12:37:20 -12:39:50	765 +/- 2	80 +/- 4	1 +/- 1	11 +/- 1	16
12:40:50 -12:42:40	853 +/- 2	80 +/- 6	2 +/- 1	9 +/- 1	12
12:44:00 -12:46:10	940 +/- 1	84 +/- 5	1 +/- 1	9 +/- 1	14
12:47:10 -12:48:50	1024 +/-2	85 +/- 6	2 +/- 1	8 +/- 1	11
12:49:50 -12:52:10	1116 +/- 4	87 +/- 5	1 +/- 1	7 +/-1	15
12:53:50 -12:55:10	1187 +/- 5	87 +/- 6	1 +/- 1	7 +/- 1	9
12:56:10 -12:58:30	1280 +/- 4	93 +/- 5	0 +/- 1	4 +/-1	10
12:59:00 -13:02:30	1374 +/- 3	88 +/- 3	-1 +/-1	1 +/- 1	22
13:03:10 -13:05:30	1486 +/- 3	91 +/- 2	-1 +/- 1	0 +/- 1	15
13:06:00 -13:07:30	1558 +/- 8	90 +/- 2	-1 +/- 1	-1 +/- 1	10

Table 5.5: Flight 2, 24 June 1991 near Maartensdijk location B.

Time U.T.	Altitude [meter]	Airborne $[\mu g \cdot m^{-3}]$			Number of data-points
		O_3	NO	NO_2	
2:39:50 -12:42:30	234 +/- 4	46 +/.4			17
12:44:00 -12:46:20	414 +/- 6	57 +/- 3			10
12:46:40 -12:48:50	489 +/- 2	59 +/-3			14
12:49:30 -12:51:30	605 +/- 5	58 +/- 6			9
12:51:50 -12:54:00	704 +/- 4	57 +/- 2			14
12:54:40 -12:55:40	815 +/- 3	57 +/- 2			7
12:58:10 -12:59:20	963 +/- 4	62 +/- 6			8
12:59:50 -13:02:00	1063 +/- 1	64 +/- 1			14
13:03:00 -13:05:10	1193 +/- 4	87 +/- 3			14
13:07:20 -13:09:50	1688 +/- 4	92 +/- 4			16
13:12:30 -13:13:00	1404 +/- 4	100 +/ 5			4
13:21:10 -13:22:30	463 +/- 2	99 +/- 6			9
13:24:10 -13:27:10	298 +/- 3	82 +/- 7			9

Table 5.6: Flight 3, 28 June 1991 near Soesterberg location C. No NO_x data available due to disconnected tube.

5.4.4 ECC-sonde results

Discussion of the meteorological measurements

The figures 5.62 and 5.63 show the temperature versus the altitude. Especially for the second flight a temperature inversion at about 1200 m is clearly discernible, which is capping the boundary layer. Above this height the free troposphere begins. Relating to the first flight a temperature anomaly lies between 700 and 970 m. As the first flight took place in the morning, the temperature inversion was distinctly lower and the structure of the planetary boundary layer was less pronounced during the ascent phase. The theoretical value of the dry adiabatic lapse rate Γ_d runs to about $\Gamma_d = -10\ Kkm^{-1}$, but it has a smaller amount in reality. From the radio sonde measurements average values of $\approx -8,5\ Kkm^{-1}$ and $-8,7\ Kkm^{-1}$ are determined which indicate a well mixed boundary layer. In the first flight a lapse rate $\Gamma_d = -7,3\ Kkm^{-1}$ continues above the boundary layer. Figures 5.64 and 5.65 show the relative humidity versus height. The relative humidity changes with temperature according to

$$F(T) = F(T_o) \cdot \exp(6,2343 \cdot 10^{-2} \cdot (T_o - T)) \tag{5.4}$$

(T_o stands for the temperature in a reference height Z_o e.g. at ground) assuming that the H_2O-mixing ratio remains constant as expected in a convectively mixed atmosphere. In this case the relative humidity should increase slowly exponentially (quasi linearly) for a temperature decreasing linearly with height. The humidity profiles qualitatively follow this trend.The peplopause is indicated within the temperature-humidity-map (Fig. 5.66 and 5.67) by a clear drop of the relative humidity, which illustrates that this air does not come from the convective mixed boundary layer. Within the lower height range ($\approx 400m$) the humidity values correspond to about the values after equation (5.4). For this region the temperature gradient corresponds to the theoretical amount of $-10\,Kkm^{-1}$, too. Within the layer above, the air is dryer than expected after (5.4) and also the temperature gradient is smaller than its theoretical value. Obviously dry air has been entrained into this region and for the second flight also somewhat warmer air. For the first flight the temperature profile indicates that a distinct temperature inversion builds up during the 40 minutes of flight time.

Evaluation of the ozone sonde measurements

Figures 5.68 and 5.69 show the ozone concentration averaged over 100 m ranges in dependence on height for both launches. Below 600-700 m, the convectively well mixed region, the ascent and descent profiles differ distinctly from eachother. The ascent values of O_3 are about 5-10 ppbv less than the descent values. This discrepancy could have different reasons. The ECC-sondes have been started in the morning between 08.00 and 09.00 UT and early afternoon between 12.00 and 13.00 UT, that means near the morning minimum and close to the broad daytime maximum of the longtime averaged daily ozone course. But the simultaneously measured ground ozone concentrations of the nearby measuring station in Bilthoven show a distinct increase of the ozone concentration of about 10 ppbv

h^{-1} just during the morning hours of June 20^{th} and a possibly weaker ozone gradient of about 5 ppbv h^{-1} during the afternoon of June 24^{th} in conformity with the results of the ECC-sondes. The SO_2-burden, measured in Bilthoven, too, was not high enough and the slope of the time gradient not steep enough to explain the discrepancy between the ascent and decent values. A maximum correction for the two flights of $+5ppbv$ and $3ppbv\,O_3$ respectively can be estimated. The NO_2 correction has the same order in magnitude, but the opposite sign, so that both influences partly compensate eachother. The average value of the ozone gradient with height is 0.015 - 0.02 ppbv/m, much greater than explicable by dry deposition. Because of the close photochemical relation between O_3 and NO_x, NO_2 has to be regarded as oddoxygen. NO is the primary emitted constituent of NO_x. Afterwards it is relatively fast oxidized by O_3 to NO_2. Taking into consideration the reverse reaction of the photodissociation of NO_2 (J_{NO_2}) , the equilibrium formula

$$J_{NO_2}[NO_2]_t = l_{O_3-NO}\,[O_3]_t\,[NO]_t \tag{5.5}$$

and the two conservation equations

$$[O_3]_t + [NO_2]_t = constant \tag{5.6}$$

and

$$[NO]_t + [NO_2]_t = constant \tag{5.7}$$

follow.

l_{O3-NO} is the reaction rate of $NO+O_3 \rightarrow NO_2+O_2$. The only effective oddoxygen loss is given by reactions with OH especially by the reaction $NO_2 + OH + M \xrightarrow{k} HNO_3 + M$ with $k[M] \approx 1.1\,x\,10^{-11} cm^3 s^{-1}$ within the boundary layer. The characteristic chemical time amounts several hours till few days. This process is slow compared with the time to reach the equilibrium(5.5). Thus the sum of $[O_3]$ and $[NO_2]$ has to be considered rather than $[O_3]$ alone, which will be possible using the data from the NO_X-monitor on board the helicopter . Further conclusions should be drawn in connection with the other experiments of TROLIX-91 which were carried out simultaneously.

Height range [m]	Average height [m]	Ozone [ppb]	Ozone [µg/m^3]	Datapoints
0 - 100	27 ± 20	20 ± 0	41 ± 0	5
> 100 - 200	148 ± 42	19 ± 0	38 ± 0	2
> 200 - 300	264 ± 13	15 ± 3	30 ± 6	68
> 300 - 400	353 ± 15	14 ± 3	28 ± 6	49
> 400 - 500	444 ± 23	20 ± 4	39 ± 8	32
> 500 - 600	550 ± 32	28 ± 2	54 ± 4	28
> 600 - 700	634 ± 22	31 ± 1	60 ± 2	16
> 700 - 800	734 ± 14	40 ± 3	76 ± 6	25
> 800 - 900	823 ± 26	49 ± 1	92 ± 2	33
> 900 - 1000	945 ± 34	51 ± 2	95 ± 4	43
>1000 - 1100	1052 ± 20	48 ± 1	88 ± 2	21
>1100 - 1200	1145 ± 15	48 ± 1	87 ± 2	28
>1200 - 1300	1239 ± 18	48 ± 1	87 ± 2	35
>1300 - 1400	1337 ± 20	48 ± 1	86 ± 2	34
>1400 - 1500	1436 ± 25	48 ± 1	85 ± 2	28
>1500 - 1600	1513 ± 22	48 ± 1	84 ± 2	21
>1600 - 1700	1613 ± 11	48 ± 1	84 ± 2	21

Table 5.7: Flight 1 (ascent): 91/06/20, ECC-sonde

Height range [m]	Average height [m]	Ozone [ppb]	Ozone [µg/m^3]	Datapoints
0 - 100	40 ± 25	28 ± 1	57 ± 2	19
> 100 - 200	153 ± 28	30 ± 1	60 ± 2	8
> 200 - 300	250 ± 32	28 ± 1	56 ± 2	6
> 300 - 400	348 ± 37	29 ± 0	57 ± 0	5
> 400 - 500	446 ± 27	31 ± 1	60 ± 2	3
> 500 - 600	556 ± 31	31 ± 2	60 ± 4	4
> 600 - 700	647 ± 26	29 ± 2	56 ± 4	4
> 700 - 800	755 ± 40	34 ± 2	65 ± 4	3
> 800 - 900	866 ± 38	42 ± 2	79 ± 4	2
> 900 - 1000	957 ± 26	48 ± 1	89 ± 2	2
>1000 - 1100	1040 ± 26	47 ± 1	86 ± 2	2
>1100 - 1200	1152 ± 41	45 ± 2	82 ± 4	4
>1200 - 1300	1255 ± 28	48 ± 1	86 ± 2	3
>1300 - 1400	1360 ± 24	46 ± 1	82 ± 2	5
>1400 - 1500	1446 ± 30	47 ± 1	83 ± 2	5
>1500 - 1600	1555 ± 32	46 ± 1	80 ± 2	6
>1600 - 1700				

Table 5.8: Flight 1 (descent): 91/06/20, ECC-sonde

Height range [m]	Average height [m]	Ozone [ppb]	Ozone [µg/m^3]	Datapoints
0 - 100	32 ± 34	24 ± 5	48 ±10	6
> 100 - 200	147 ± 35	29 ± 0	58 ± 0	3
> 200 - 300	284 ± 16	32 ± 3	63 ± 6	40
> 300 - 400	377 ± 21	34 ± 2	67 ± 4	26
> 400 - 500	467 ± 25	35 ± 2	68 ± 4	31
> 500 - 600	534 ± 16	36 ± 2	70 ± 4	45
> 600 - 700	646 ± 20	38 ± 1	73 ± 2	29
> 700 - 800	734 ± 21	40 ± 2	76 ± 4	29
> 800 - 900	827 ± 21	42 ± 3	79 ± 6	31
> 900 - 1000	944 ± 40	42 ± 2	78 ± 4	48
>1000 - 1100	1072 ± 27	43 ± 2	79 ± 4	27
>1100 - 1200	1174 ± 19	45 ± 1	82 ± 2	25
>1200 - 1300	1256 ± 20	47 ± 2	85 ± 4	29
>1300 - 1400	1367 ± 22	50 ± 2	89 ± 4	23
>1400 - 1500	1453 ± 16	51 ± 2	90 ± 4	34
>1500 - 1600	1561 ± 20	54 ± 1	94 ± 2	30
>1600 - 1700	1641 ± 17	52 ± 1	90 ± 2	13

Table 5.9: Flight 2 (ascent): 91/06/24, ECC-sonde

Height range [m]	Average height [m]	Ozone [ppb]	Ozone [µg/m^3]	Datapoints
0 - 100	34 ± 29	34 ± 1	68 ± 2	15
> 100 - 200	181 ± 27	36 ± 3	72 ± 6	24
> 200 - 300	218 ± 20	38 ± 1	75 ± 2	19
> 300 - 400	366 ± 35	39 ± 0	76 ± 0	3
> 400 - 500	453 ± 37	40 ± 1	78 ± 2	4
> 500 - 600	552 ± 31	40 ± 0	77 ± 0	2
> 600 - 700	651 ± 40	40 ± 1	76 ± 2	3
> 700 - 800				
> 800 - 900	848 ± 41	42 ± 1	79 ± 2	3
> 900 - 1000	960 ± 37	43 ± 0	80 ± 0	3
>1000 - 1100	1068 ± 32	44 ± 1	81 ± 2	3
>1100 - 1200	1145 ± 26	44 ± 0	80 ± 0	2
>1200 - 1300	1245 ± 42	48 ± 2	87 ± 4	3
>1300 - 1400	1356 ± 34	51 ± 1	91 ± 2	3
>1400 - 1500	1462 ± 34	51 ± 1	90 ± 2	3
>1500 - 1600	1556 ± 28	51 ± 1	89 ± 2	2
>1600 - 1700	1616 ± 12	50 ± 3	86 ± 5	6

Table 5.10: Flight 2 (descent): 91/06/24, ECC-sonde

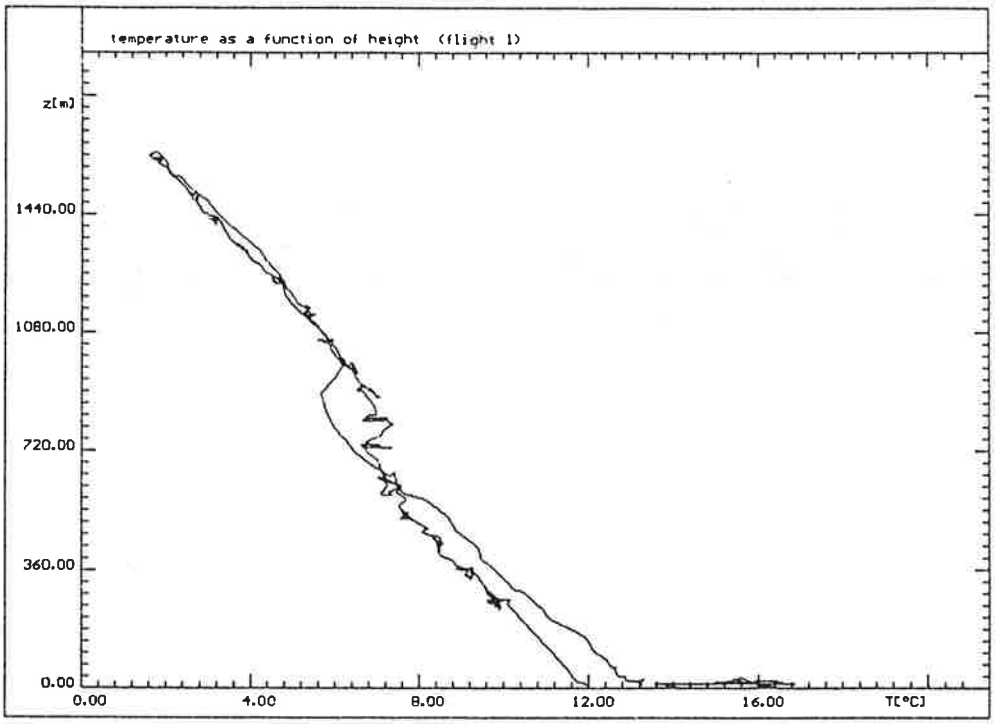

Figure 5.62: temperature as a function of height (flight 1)

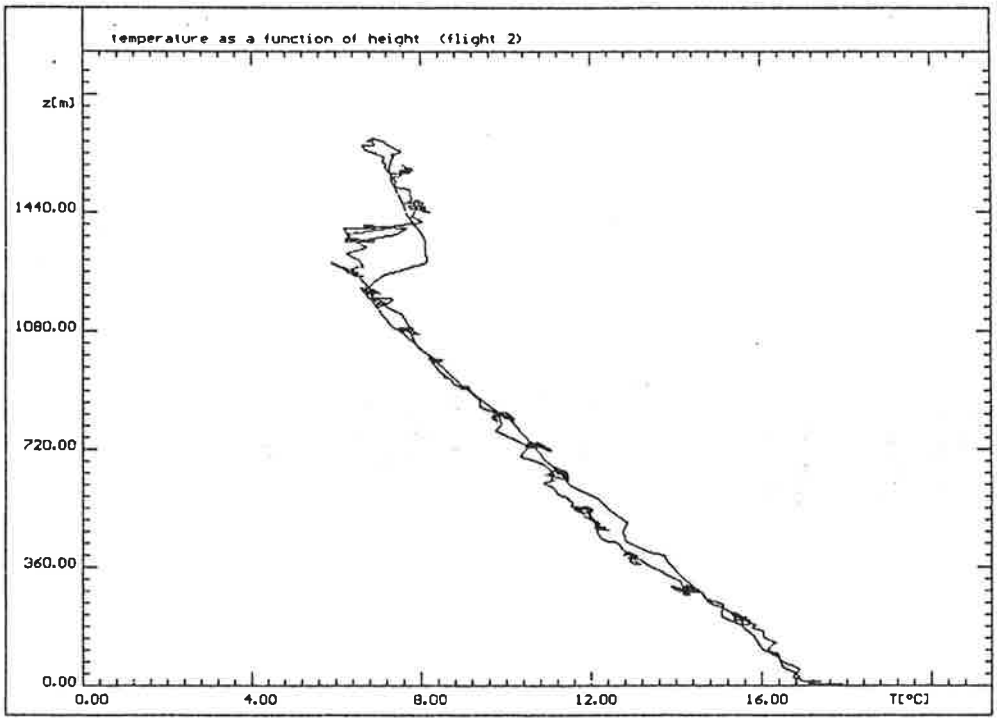

Figure 5.63: temperature as a fuction of height (2)

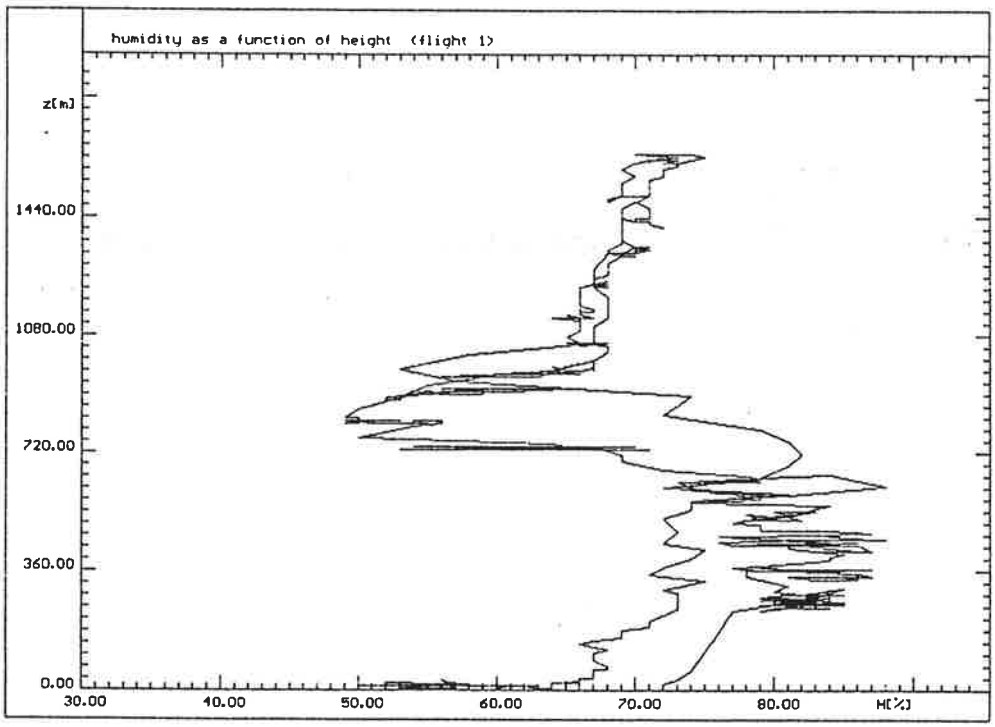

Figure 5.64: humidity as a function of height (flight1)

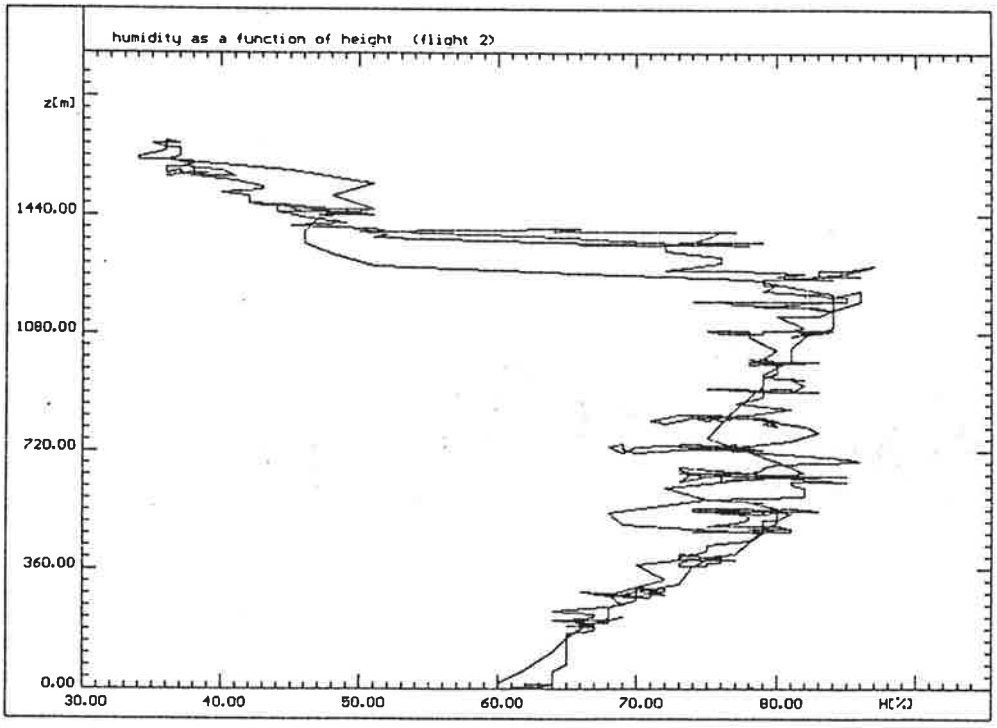

Figure 5.65: humidity as a function of height (flight 2)

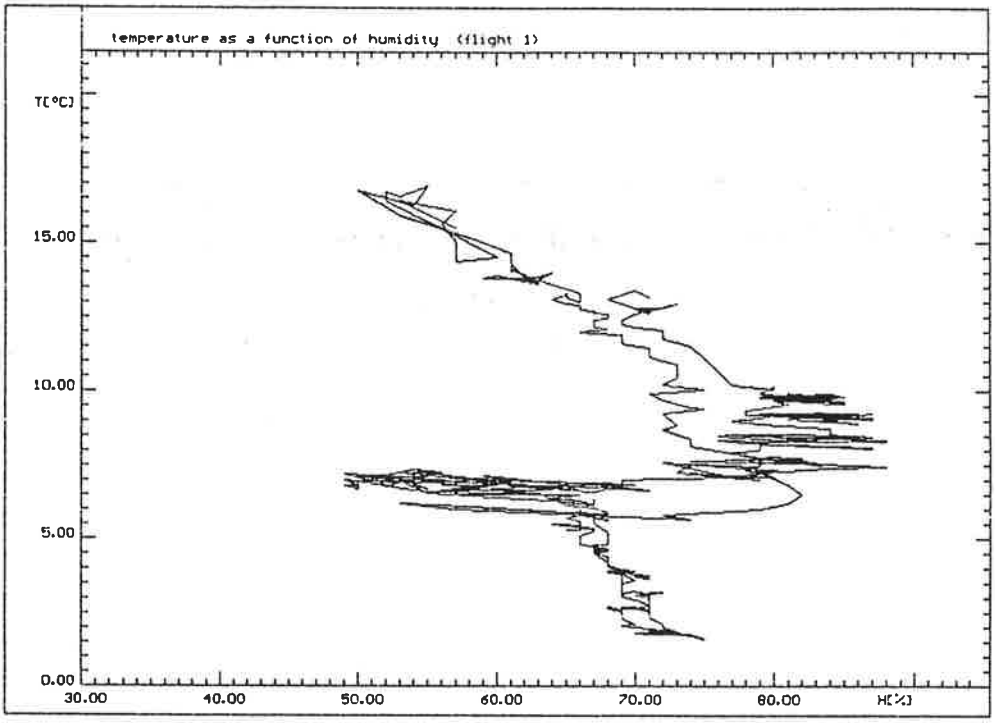

Figure 5.66: temperature as a function of humidity (flight 1)

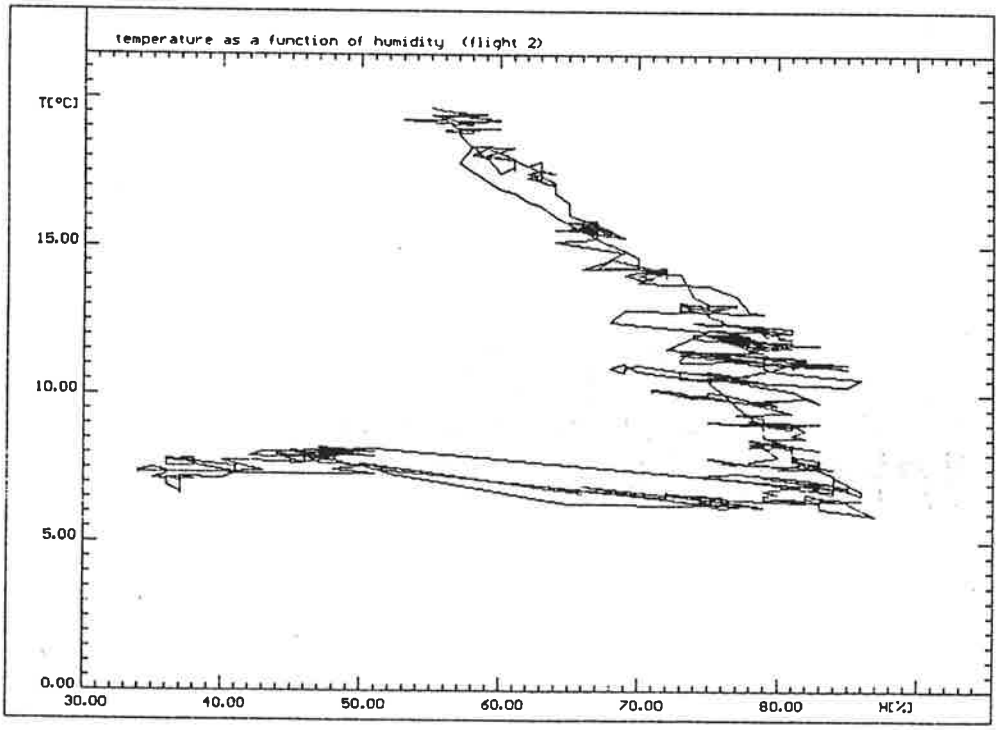

Figure 5.67: temperature as a function of humidity (flight 2)

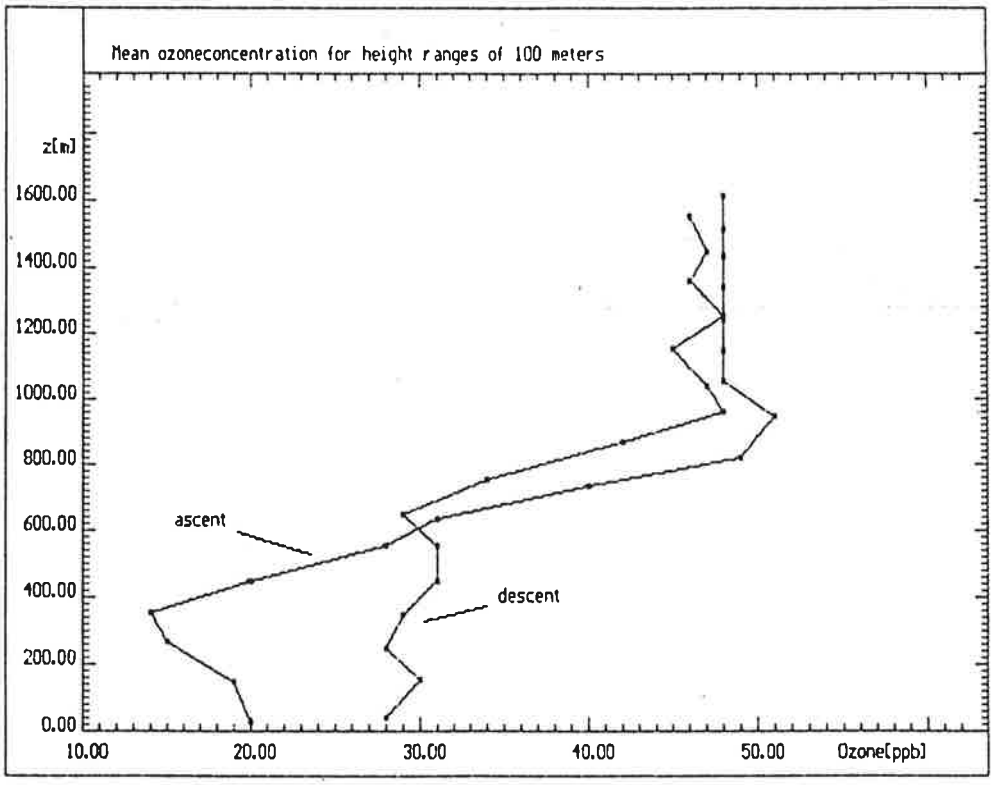

Figure 5.68: TROLIX-91: Helicopterflight 1, 91/06/20, ECC-sonde. Mean ozoneconcentraion for height ranges of 100 meters

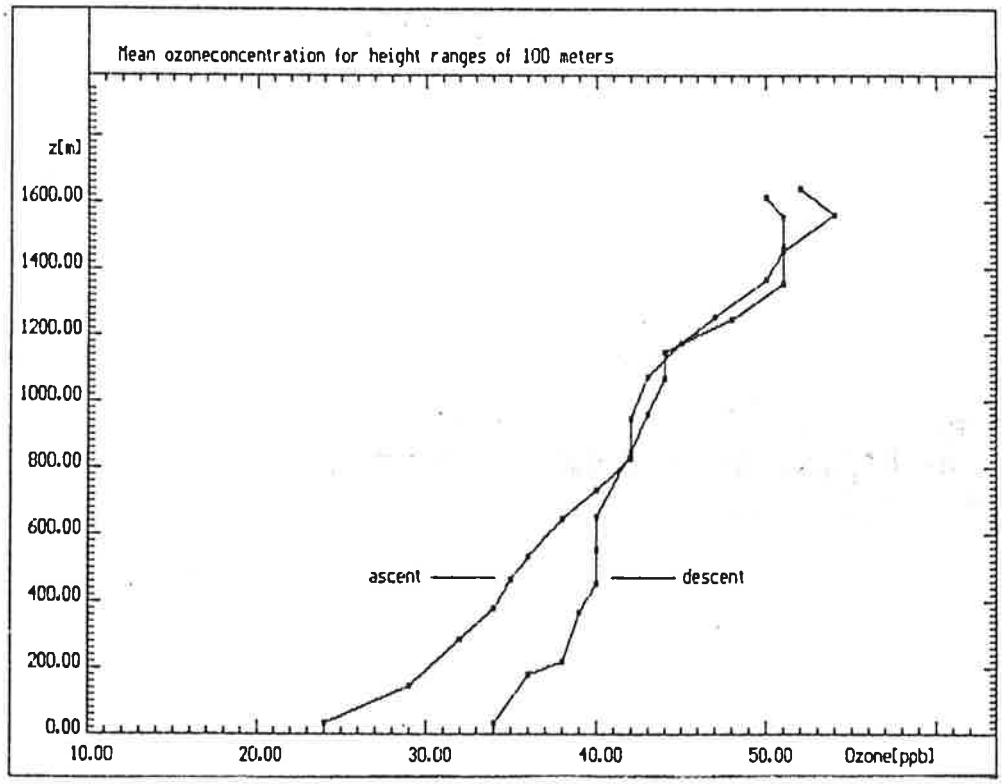

Figure 5.69: TROLIX-91: Helicopterflight 2, 91/06/24, ECC-sonde. Mean ozoneconcentration for height ranges of 100 meters

5.5 Backscatter at $1.06\mu m$

5.5.1 Trolix '91 PBL Lidar measurements overview

This chapter will survey the PBL Lidar measurements taken. In the next chapter, special attention will be paid to measurements during periods of prime interest, defined at the end of the campaign (see table 5.2).

The PBL Lidar system operates continously once the computer program has been started. During the campaign the system usually operated with 210 s between successive bursts. During some periods, however, it operated with smaller time gaps.

Table 5.11 gives an overview of all measurement periods, as well as the time resolution for the boundary layer height calculation of each data file.

5.5.2 Analysis of prime interest periods

All measurements during periods of prime interest have been evaluated. Boundary layer heights were calculated over 15-min periods (table 5.71). Figure 5.70 shows an example of a backscatter signal, corrected for geometric attenuation. Figure 5.71 shows a back-scatter signal over a 6-h period.

Start of measurement Date / Trolix Time*	End of measurement Date / Trolix Time*	Time resolution (s)	Data filename
10-06-91 / 00.00	12-06-91 / 11.12	225	V15801
12-06-91 / 11.42	13-06-91 / 13.33	225	V16301
13-06-91 / 13.35	14-06-91 / 22.34	15	V16402
14-06-91 / 11.43	14-06-91 / 12.15	225	V16501
14-06-91 / 12.16	17-06-91 / 06.22	225	V16502
17-06-91 / 07.18	18-06-91 / 14.39	35	V16801
18-06-91 / 14.49	19-06-91 / 06.35	55	V16901
19-06-91 / 06.54	19-06-91 / 12.23	30	V17001
19-06-91 / 12.48	20-06-91 / 05.58	30	V17002
20-06-91 / 05.59	20-06-91 / 14.41	15	V17102
20-06-91 / 14.49	21-06-91 / 07.42	225	V17103
21-06-91 / 07.43	21-06-91 / 14.34	15	V17201
21-06-91 / 14.35	22-06-91 / 09.58	225	V17202
22-06-91 / 11.52	23-06-91 / 14.06	15	V17301
22-06-91 / 14.08	24-06-91 / 06.52	225	V17302
24-06-91 / 07.32	24-06-91 / 09.25	225	V17501
24-06-91 / 09.27	24-06-91 / 15.15	15	V17502
24-06-91 / 15.16	26-06-91 / 08.42	225	V17503
26-06-91 / 08.42	27-06-91 / 00.29	15	V17704
27-06-91 / 00.29	27-06-91 / 07.58	225	V17802
27-06-91 / 08.49	28-06-91 / 05.27	225	V17801
28-06-91 / 05.28	28-06-91 / 15.32	15	V17902
28-06-91 / 15.34	01-07-91 / 14.20	225	V17903

* Trolix Time = GMT

Table 5.11: Overview of PBL Lidar measurement periods

Date (period)	Filename	Trolix Time (GMT)	Boundary layer height (m)
11-06-91 (1)	V15801	10.00 - 10.15	1100 ± 80
		10.15 - 10.30	1100 ± 80
		11.45 - 12.00	1100 ± 80
		12.00 - 12.15	1300 ± 80
		12.15 - 12.30	1200 ± 80
13-06-91 (2)	V16402	14.00 - 14.15	1350 ± 80
		14.15 - 14.30	1100 ± 80
		15.00 - 15.15	1250 ± 80
		15.15 - 15.30	1250 ± 160
		15.30 - 15.45	1200 ± 160
		15.45 - 16.00	1000 ±80
		17.30 - 17.45	700 ± 40
		17.45 - 18.00	800 ± 40
		21.00 - 21.15	700 ± 40
		21.15 - 21.30	450 ± 40
26-06-91 (3)	V17704	22.30 - 22.45	800 ± 80
		22.45 - 23.00	800 ± 80
		23.00 - 23.15	800 ± 80
		23.15 - 23.30	850 ± 80
		23.30 - 23.45	750 ± 80
		23.45 - 24.00	700 ± 80

Table 5.12: PBL for prime interest periods

Date (period)	Filename	Trolix Time (GMT)	Boundary layer height (m)
20-06-91 (4)	V17102	08.00 - 08.15	450 ± 80
		08.15 - 08.30	450 ± 80
		08.30 - 08.45	650 ± 80
		08.45 - 09.00	500 ± 80
24-06-91 (5)	V17502	12.00 - 12.15	650 ± 80
		12.15 - 12.30	800 ± 80
		12.30 - 12.45	700 ± 80
		12.45 - 13.00	700 ± 80
		13.00 - 13.15	700 ± 80
		13.15 - 13.30	700 ± 80
28-06-91 (6)	V17902	12.30 - 12.45	1000 ± 80
		12.45 - 13.00	950 ± 80
		13.00 - 13.15	750 ± 80
		13.15 - 13.30	900 ± 80
		13.30 - 13.45	800 ± 80

Table 5.12: continued

Date (period)	Filename	Trolix Time (GMT)	Boundary layer height (m)
22-06-91 (7)	V17302	15.45 - 16.00	800 ± 160
		16.00 - 16.15	850 ± 160
		16.15 - 16.30	1100 ± 160
		16.30 - 16.45	950 ± 160
		16.45 - 17.00	900 ± 160
		17.00 - 17.15	1100 ± 160
		17.15 - 17.30	1000 ± 160
		17.30 - 17.45	900 ± 160
		17.45 - 18.00	950 ± 80
		18.00 - 18.15	950 ± 80
		18.15 - 18.30	900 ± 80
		18.30 - 18.45	600 ± 80
		18.45 - 19.00	500 ± 80
		19.00 - 19.15	450 ± 80
		19.15 - 19.30	550 ± 80
26-06-91 (8)	V17704	14.00 - 15.00	850 ± 80
		15.00 - 16.00	950 ± 80
		16.00 - 17.00	1000 ± 80
		17.00 - 18.00	1100 ± 80
		18.00 - 19.00	1100 ± 80
		19.00 - 20.00	1000 ± 80
		20.00 - 21.00	1200 ± 80
		21.00 - 22.00	950 ± 80

Table 5.12: continued

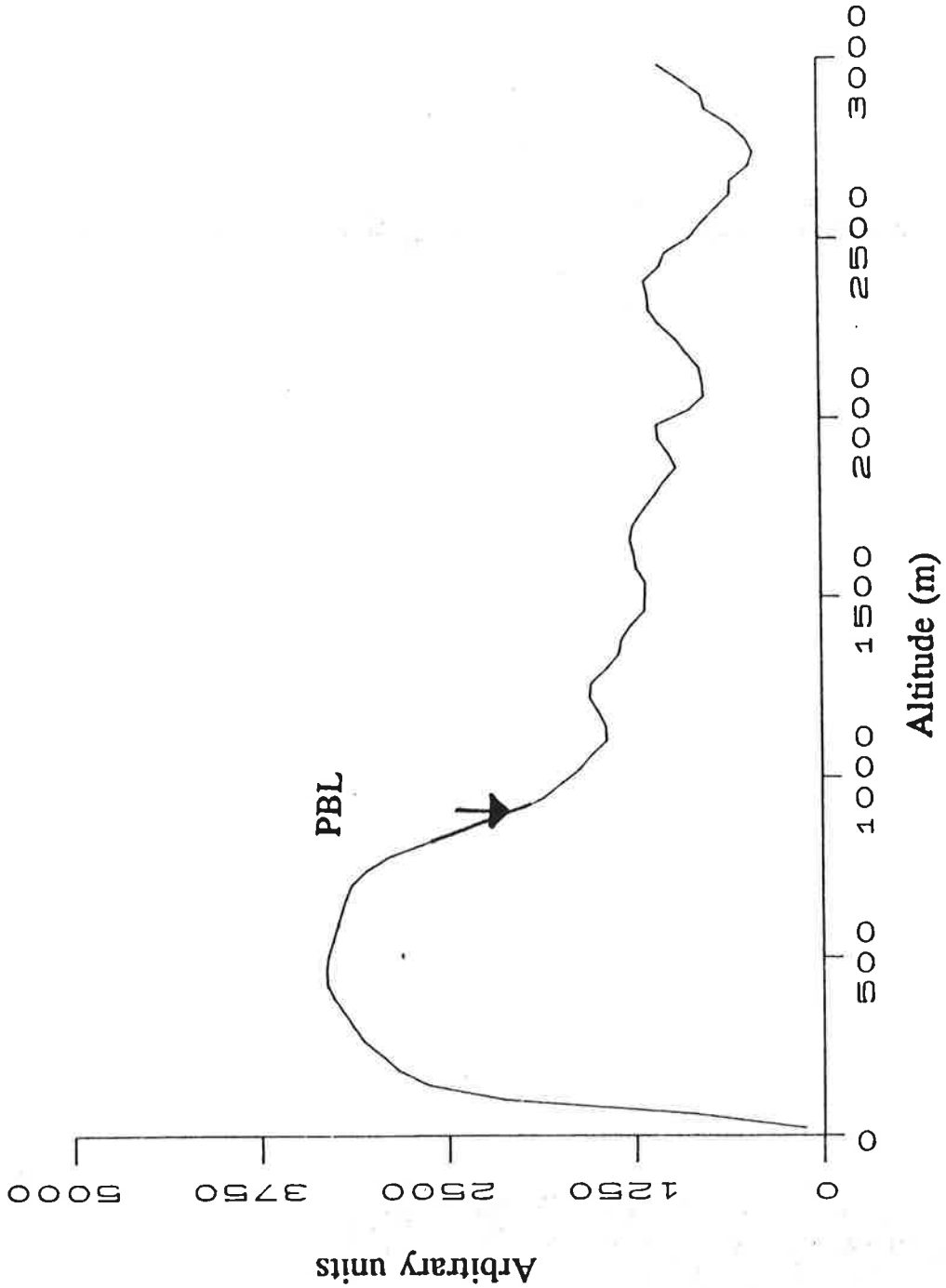

Figure 5.70: Example of a back-scatter signal. Filename: V16402 (period 2), Universal time: 17.45 - 18.00

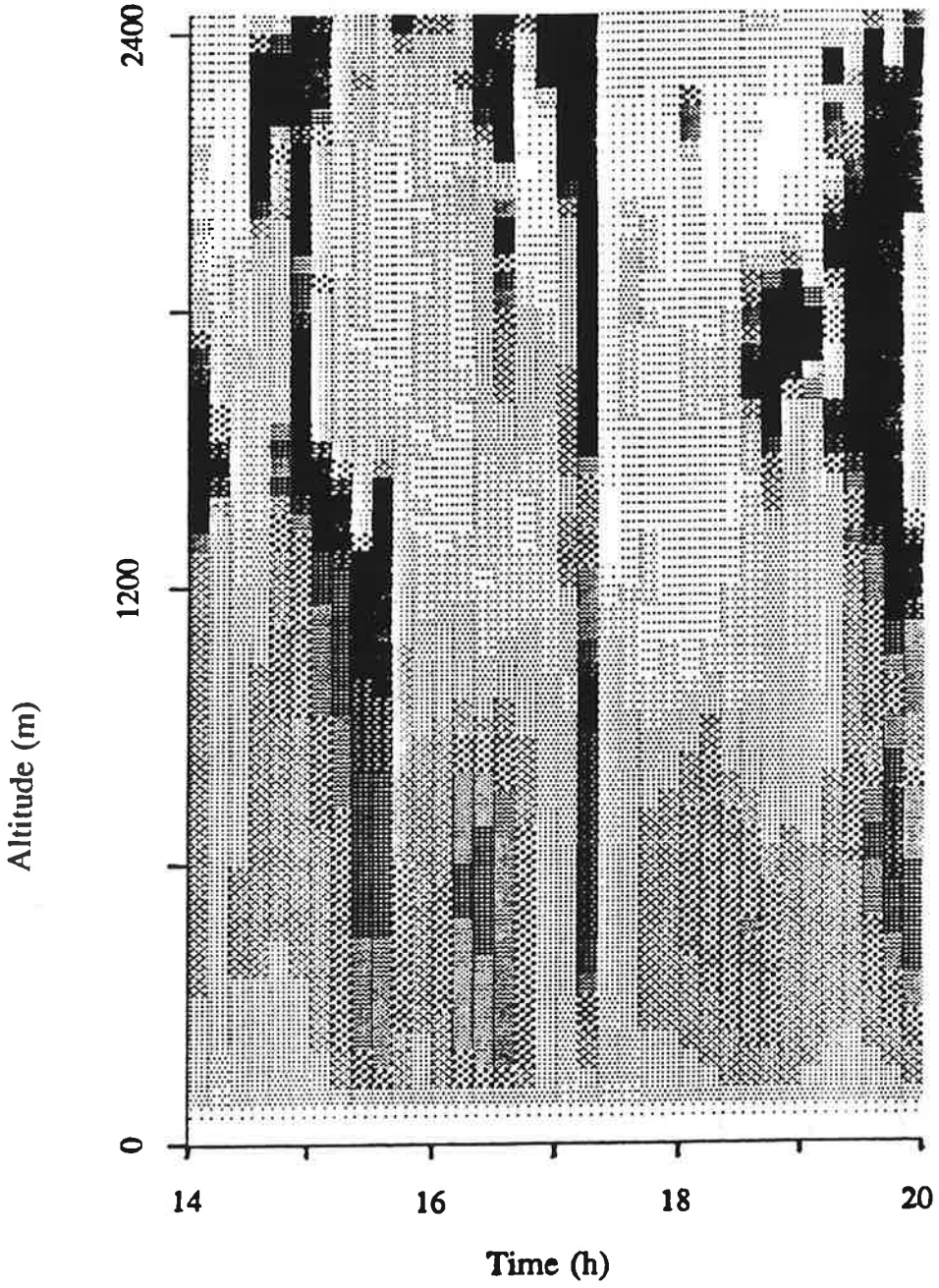

Figure 5.71: Example of a back-scatter signal over a 6-hour period (the black areas correspond with high back-scatter). Filename: V16402 (period 2), Universal time: 14.00 - 20.00

5.6 NO_2-lidar results

Overview

This chapter surveys all NO_2 DIAL measurements in the Trolix '91 campaign. In the next chapter special attention will be paid to measurements during prime interest periods, as defined at the end of the campaign at 91/06/28 (see figure 5.2).

Most tropospheric O_3 DIAL systems are vertically directed. Therefore NO_2 DIAL measurements have been taken at the highest possible elevation angle in order to cover a maximum altitude range. Table 5.14 shows the DIAL measurements taken, and the elevation angle of the measurements indicating altitude range. Each DIAL measurement represents an average of 1000 data pairs and 5 min. In some cases there are small time gaps where no measurements have been taken. All time values are expressed as Universal Time (UT).

In the first week of the campaign the transient recorder suddenly failed; repair was not possible. Since replacement of the transient recorder had already been planned, it took only a few days to adapt the software to operate with the new transient recorder. Unfortunately, there was no opportunity to test the new transient recorder.

Analysis of prime interest periods

NO_2 concentration profiles Not all DIAL measurements of prime interest periods are suitable for calculating NO_2 concentration profiles. For some measurements the DC level in the Lidar signals is too high (measurements at a high elevation angle). In this case the differential extinction of both signals is not calculated because the signal to noise ratio in the ln (I_{on}/I_{off}) curve (natural logarithm) is too high. However, these measurements may be suitable to calculate single wavelength extinction profiles. This will be reported in section [ ].

The NO_2 concentration over a range segment is computed using a linear fit of the curve ln (I_{on}/I_{off}) over that range segment. The result of the fit is normalized with the differential cross-section in order to obtain the NO_2 concentration in $\mu g \cdot m^{-3}$.

No measurements are available in periods 1, 3, 6, 7 and 8. The measurements in period 5 are not suitable for calculating NO_2 concentration profiles since the signal to noise ratio is too small.

Tables 5.13 and 5.15 show the results of NO_2 concentration profiles in periods 2 and 4 respectively. The calculated NO_2 concentration (with error) and the corresponding altitude range are shown. Figure 5.72 shows an example of a DIAL measurement in period 4.

Extinction profiles In an homogeneous part of th atmosphere, the extinction coefficient can be calculated from a single Lidar signal. The slope of the curve $ln(I \cdot r^2)$ is approximately equal to twice the extinction coefficient. The "off" wavelength (449.9 nm) is chosen to calculate extinction profiles.

In some stages of the prime interest periods, the particular part of the atmosphere concerned was homogenous enough to allow calculation of extinction profiles as described above. The calculated fit standard deviation is negligible compared with the uncertainty due to the homogeneous atmosphere assumption. The lower limit of the extinction accuracy is of an order of magnitude equal to the extinction difference between "on" and "off" wavelengths since valid NO_2 concentrations cannot be calculated for some measurements. Therefore the accuracy of the calculated extinction values amounts to about $0.02km^{-1}$.

Examples of a non-homogenous and a homogenous extinction profile are shown in Figures 5.73 and 5.74 respectively. Table 5.16 shows extinction results of periods 2 and 4; the boundary layer height (PBL) for each measurement is also presented [Jong 92].

Universal Time (UT)	Altitude	NO_2 $[\mu g \cdot m^{-3}]$
21:08:01 - 21:13:05	187 - 415	15 +/- 4
21:13:15 - 21:18:18	187 - 415	14 +/- 7
21:18:29 - 21:23:32	187 - 415	18 +/- 5

Table 5.13: Results of NO_2 concentration profiles for period 2 (91/06/13)

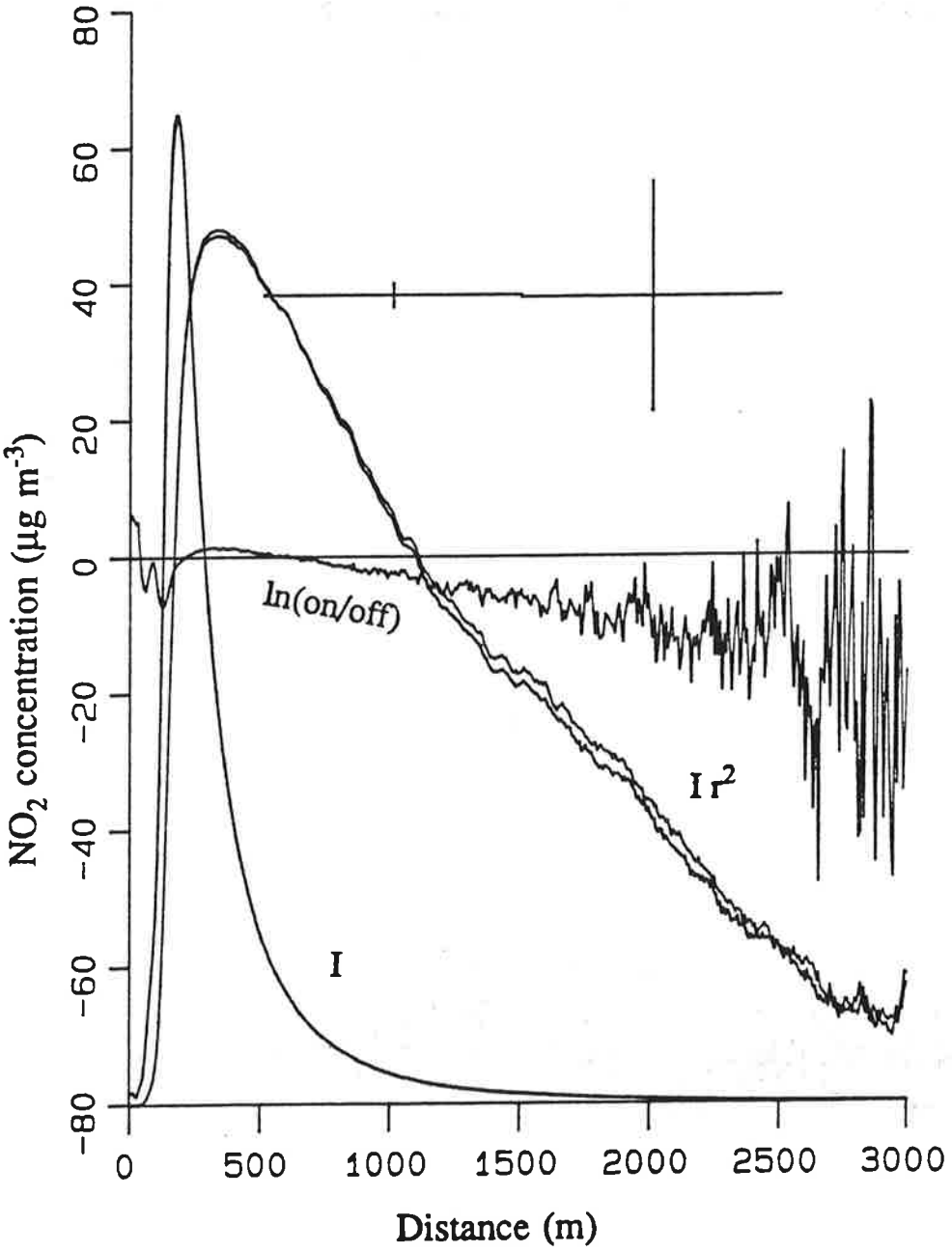

Figure 5.72: Example NO_2 Dial measurement. I_{on}, I_{off}; I_{on} r^2, I_{off} r^2; $\ln(I_{on}/I_{off})$; NO_2 concentration ($\mu g \cdot m^{-3}$). Filename: D17118 (period 4), Universal Time: 08.20 - 08.25, Elevation angle: 10°.

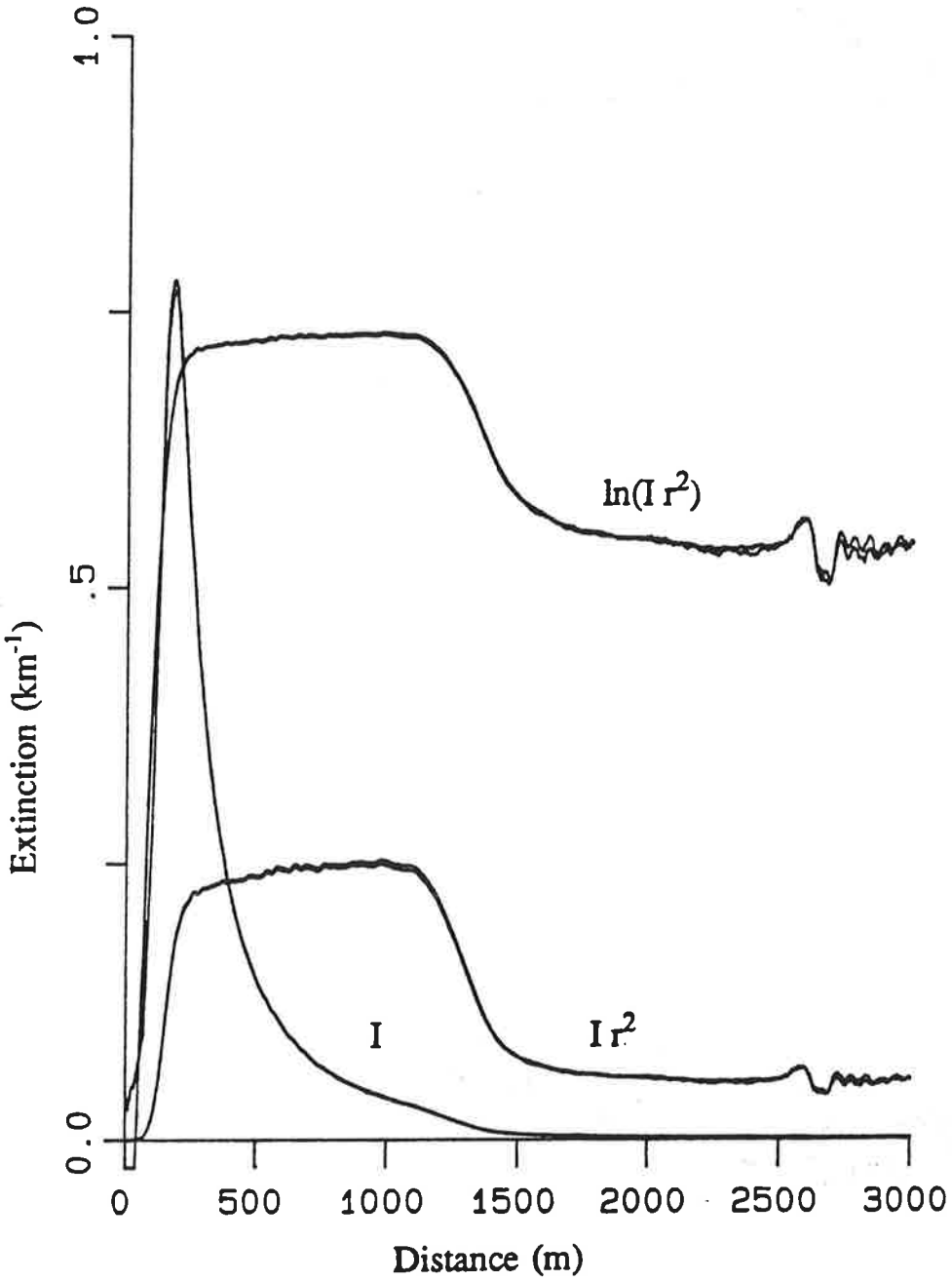

Figure 5.73: Example inhomogeneous extinction/backscatter profile. I_{on}, I_{off}; I_{on} r^2, I_{off} r^2; $\ln(I_{on}\ r^2)$; $\ln(I_{off}\ r^2)$. Filename: D16421 (period 2) Universal Time: 21:08 - 21:13 Elevation angle: 27°.

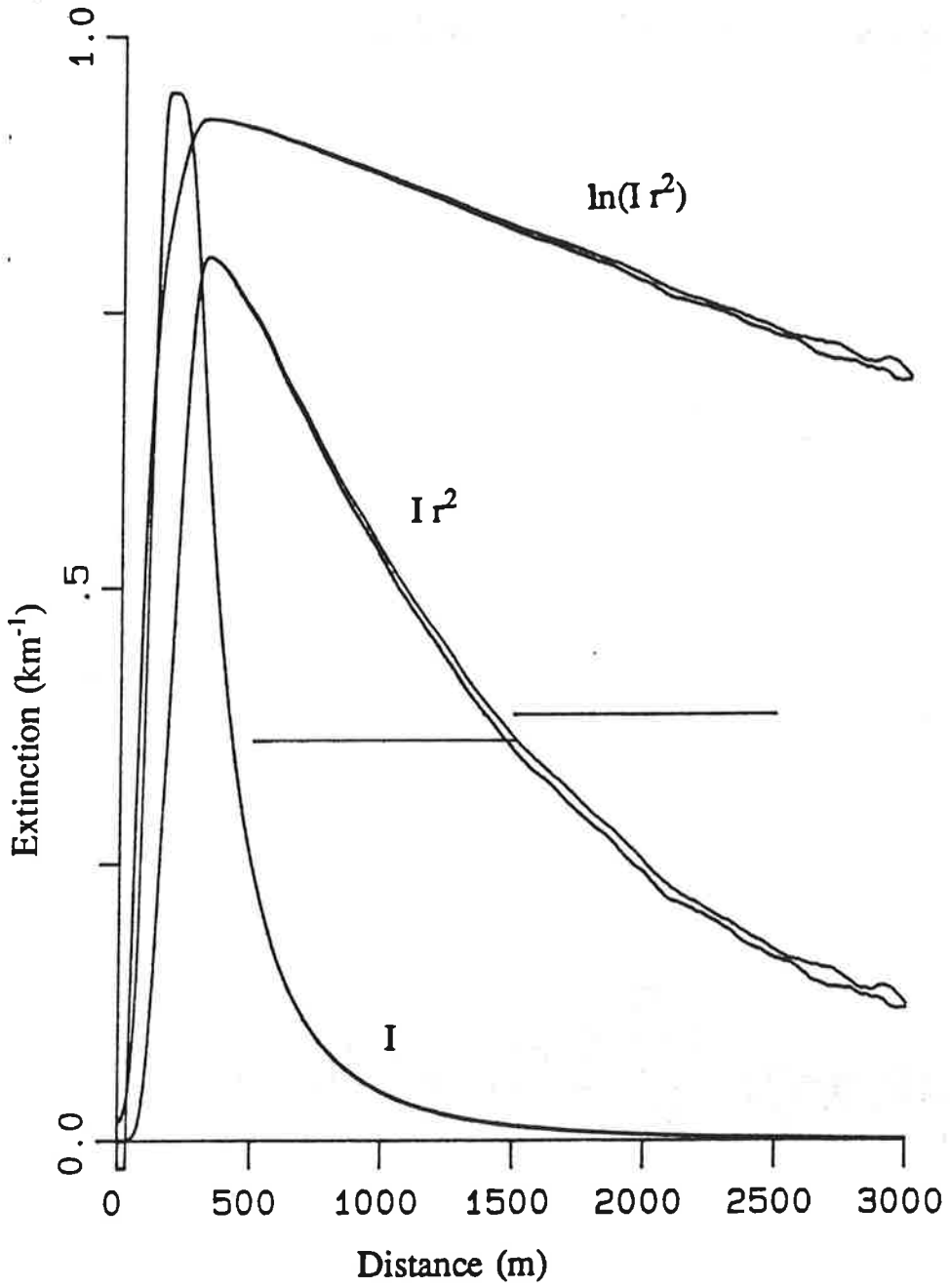

Figure 5.74: Example of homogeneous extinction/backscatter profile. I_{on}, I_{off}; $I_{on} \cdot r^2$, $I_{off} \cdot r^2$; $\ln(I_{on} \cdot r^2)$; $\ln(I_{off} \cdot r^2)$; extinction λ_{off} (km^{-1}).Filename: D17121 (period 4) Universal Time: 08:38 - 08:43, Elevation angle: 7°.

Date	Universal Time (UT)	Elevation angle [^{0}]	Data filename
91/06/13	15:15:31 - 15:20:32	3	D16401
	15:27:50 - 15:33:18		D16402
	18:52:29 - 19:12:58		D16403 ... D16405
	19:45:58 - 22:44:05	27	D16406 ... D16438
91/06/18	15:25:56 - 15:30:58	27	D16901
91/06/20	06:35:47 - 06:40:50	5	D17101
	06:47:52 - 06:52:36		D17102
	06:56:40 - 07:17:21	10	D17103 ... D17106
	07:24:34 - 07:34:49	15	D17107 ... D17108
	07:37:59 - 08:36:16	10	D17110 ... D17120
	08:38:56 - 09:11:26	7	D17121 ... D17126
	09:16:49 - 09:43:00	10	D17127 ... D17131
	09:46:32 - 10:15:34	15	D17132 ... D17136
	10:19:01 - 10:29:15	20	D17138 ... D17139
91/06/24	11:23:35 - 12:46:51	10	D17501 ... D17510 (a few 2000 averages)
	12:49:50 - 12:54:53	15	D17511
	12:48:11 - 13:25:31	10	D17512 ... D17516
	13:28:00 - 13:49:21	15	D17517 ... D17520
	13:51:32 - 14:01:45	10	D17521 ... D17522
	14:09:30 - 14:28:40	3	D17523 ... D17525
91/06/28	07:45:15 - 11:41:36	1	D17901 ... D17928
	11:49:31 - 11:54:32	2	D17929
	11:58:10 - 12:18:07	1	D17930 ... D17932

Table 5.14: Trolix '91 NO_2 DIAL measurements overview

Universal Time (UT)	Altitude	NO_2 $[\mu g \cdot m^{-3}]$	Altitude	NO_2 $[\mu g \cdot m^{-3}]$	Altitude	NO_2 $[\mu g \cdot m^{-3}]$
07:59:42 - 08:04:45	73 - 161	44 +/- 1	161 - 248	46 +/- 13	178 - 351	38 +/- 10
08:04:54 - 08:09:57	73 - 161	53 +/- 3	161 - 248	51 +/- 6	178 - 351	50 +/- 7
08:10:07 - 08:15:10	73 - 161	40 +/- 2	161 - 248	52 +/- 5	178 - 351	55 +/- 7
08:15:40 - 08:20:44	73 - 161	43 +/- 1	161 - 248	45 +/- 6	178 - 351	49 +/- 9
08:20:53 - 08:25:55	73 - 161	38 +/- 1	161 - 248	39 +/- 5	178 - 351	53 +/- 6
08:26:05 - 08:31:05	73 - 161	28 +/- 2	161 - 248	29 +/- 8	178 - 351	39 +/- 7
08:31:15 - 08:36:16	73 - 161	23 +/- 4	161 - 248	11 +/- 10	178 - 351	36 +/- 6
08:38:56 - 08:43:59	73 - 161	26 +/- 3	161 - 248	25 +/- 6	178 - 351	35 +/- 4
08:44:08 - 08:49:11	52 - 114	31 +/- 3	114 - 175	28 +/- 10	126 - 247	20 +/- 6
08:49:21 - 08:54:31	52 - 114	25 +/- 2	114 - 175	18 +/- 7	126 - 247	35 +/- 6
08:54:41 - 08:59:43	52 - 114	15 +/- 2	114 - 175	13 +/- 10	126 - 247	34 +/- 8

Table 5.15: Results of NO_2 concentration profiles for period 4.

Date (period)	Universal Time (UT)	Altitude [m]	Extinction (λ = 449.9) [km^{-1}]	Remarks
91/06/13 (2)	15:15:31 - 15:20:32	29 - 108	0.30	PBL: 700 +/- 40 m
	21:08:01 - 21:23:32			obviously inhomogeneous atmosphere, backscatter is increasing with height (figure 5.73)
91/06/20 (4)	07:59:42 - 08:04:45	90 - 178 176 - 350	0.51 0.60	PBL: 450 +/-80 m
	08:04:54 - 08:09:57	90 - 178 176 - 350	 0.62	PBL : 450 +/- 80 m
	08:10:07 - 08:15:10	90 - 350	0.43	PBL: 450 +/- 80 m
	08:15:40 - 08:20:44	90 - 350	0.40	PBL: 450 +/- 80 m
	08:20:53 - 08:25:55	90 - 264	0.33	PBL: 450 +/- 80 m
	08:26:05 - 08:31:05	90 - 438	0.38	PBL: 450 +/- 80 m
	08:31:15 - 08:36:16	64 - 308	0.36	PBL: 650 +/- 80 m
	08:38:56 - 08:43:59	64 - 308	0.36	PBL: 650 +/- 80 m (see figure 5.74)
	08:44:08 - 08:49:11	64 - 308	0.36	PBL: 500 +/- 80 m
	08:49:21 - 08:54:31	64 - 308	0.38	PBL: 500 +/- 80 m
	08:54:41 - 08:59:43	64 - 308	0.35	PBL: 500 +/- 80 m
91/06/24 (5)	12:11:51 - 12:21:59	176 - 524	0.19	PBL: 700 +/- 80 m
	12:22:08 - 12:32:16	176 - 524	0.22	PBL: 800 +/- 80 m
	12:36:35 - 12:41:39	176 - 524	0.21	PBL: 700 +/- 80 m
	12:41:48 - 12:46:51	261 - 780	0.21	PBL: 700 +/- 80 m
	12:49:50 - 12:54:53	176 - 524	0.19	PBL: 700 +/- 80 m
	12:58:11 - 13:03:14	176 - 524	0.23	PBL: 700 +/- 80 m
	13:03:23 - 13:08:25	176 - 524	0.27	PBL: 700 +/- 80 m
	13:08:52 - 13:13:56	176 - 524	0.23	PBL: 700 +/- 80 m
	13:14:05 - 13:19:07	176 - 524	0.24	PBL: 700 +/- 80 m

Table 5.16: Results extinction profiles (period 2, 4 and 5)

5.7 DOAS results

The double path DOAS was set up to make possible the intercomparison between DOAS, horizontal LIDAR and point monitors. The DOAS paths 2*884 m and 2*2000 m was located about 20 meters above the ground and topographically related to the other systems according to figure 5.75.

Simultaneous measurements with DOAS and horizontal LIDAR was conducted at two occasions. The first occasion was june 22, a clear day with fair visibility. In figure 5.76 is given a comparison between ozone concentrations measured with the different techniques.

A considerable spread out in the data can be seen. However, from the DOAS measurements over different paths a gradient of decreasing ozone concentration with increasing distance is evident. This gradient was also seen in the rangeresolved LIDAR recordings. As the LIDAR paths as well as the point monitor are located at "negative" DOAS distances (see figure 5.75), extrapolation of this gradient takes account for the major part of the differences in figure 5.76. The differential aerosol extinction between the two wavelenghts used by the LTH LIDAR system, 286.2 nm and 277.9 nm, (attuLTH), was measured to be 0.09. After correcting for the Rayleigh contribution (0.047) this corresponds to an error in the LIDAR measurements of 6.5 $\mu g \cdot m^{-3}$ unless aerosol correction is made. However due to the strong spatial variation in ozone concentration such a discrepancy could not be clearly seen in the data.

The second comparison period was June 26, weather was clear and visibility good. At this occasion the gradient was not as pronounced as it was June 22, and the agreement between concentrations measured with the different methods as shown in figure 5.77 are considerably better. The differential extinction parameter attuLTH was calculated to 0.06, indicating that particle extinction was negligible and that no error could be expected in LIDAR data not corrected for aerosol extinction.

In figure 5.78 is shown measurements of the differential extinction attuLTH during a night when fog was created.

From this figure is clearly seen the buildup of particle extinction as fog is created and light level goes down. Unfortunately no LIDAR data where taken during this period.

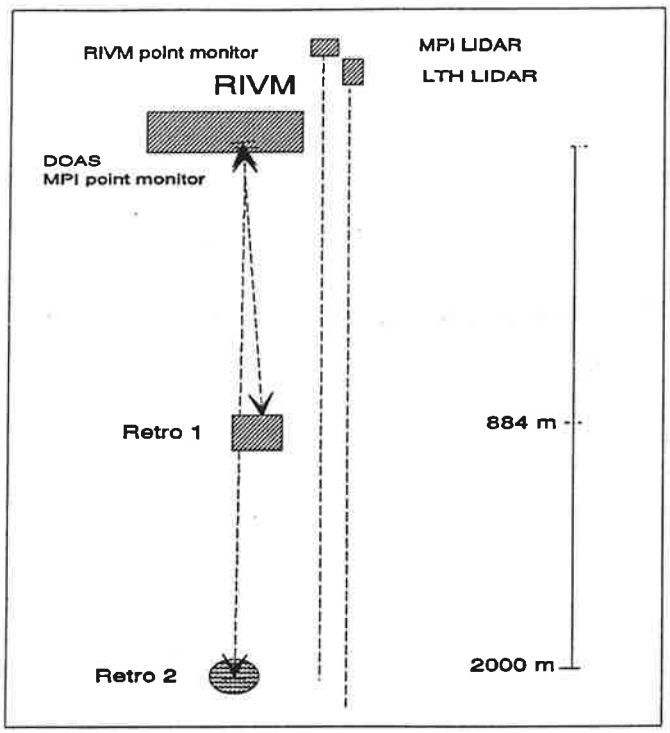

Figure 5.75: Map showing the topographic relations between the DOAS paths, the horisontal LIDAR systems and the point monitors.

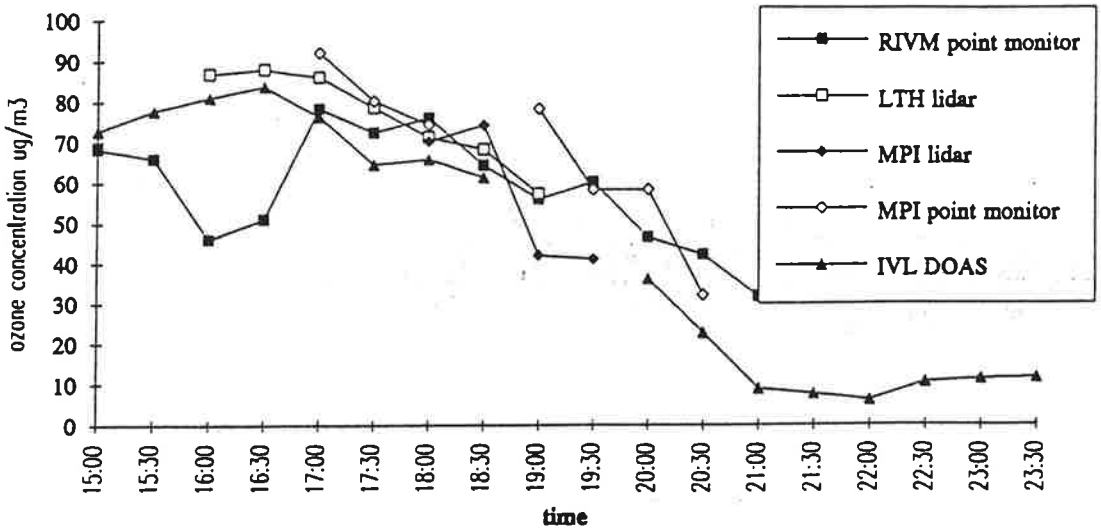

Figure 5.76: Comparison of ozone concentrations measured with different techniques June 22 1991.

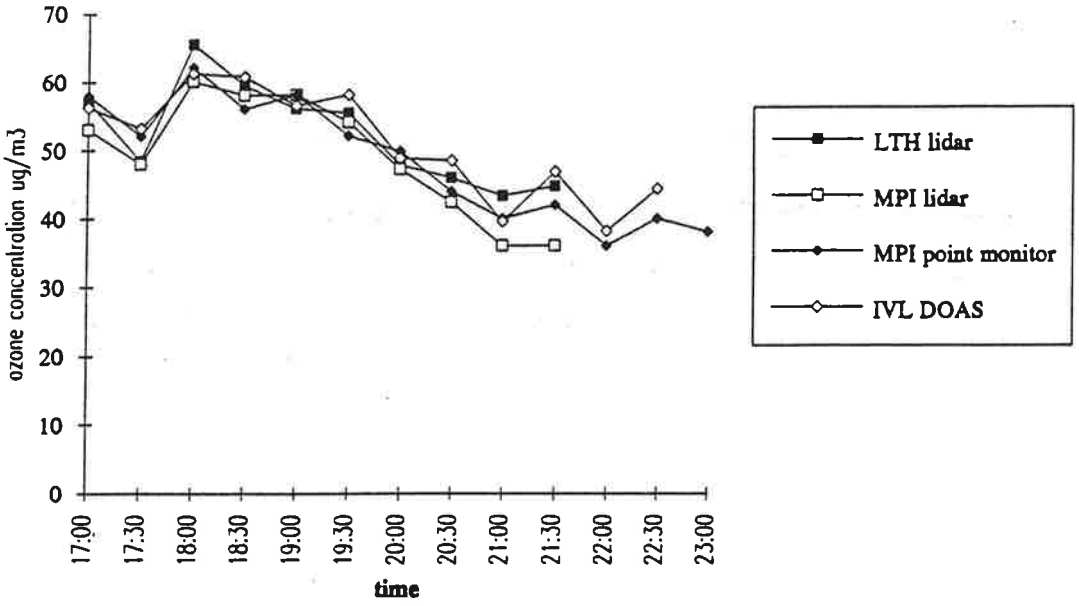

Figure 5.77: Comparison of ozone concentrations measured with different techniques June 26 1991.

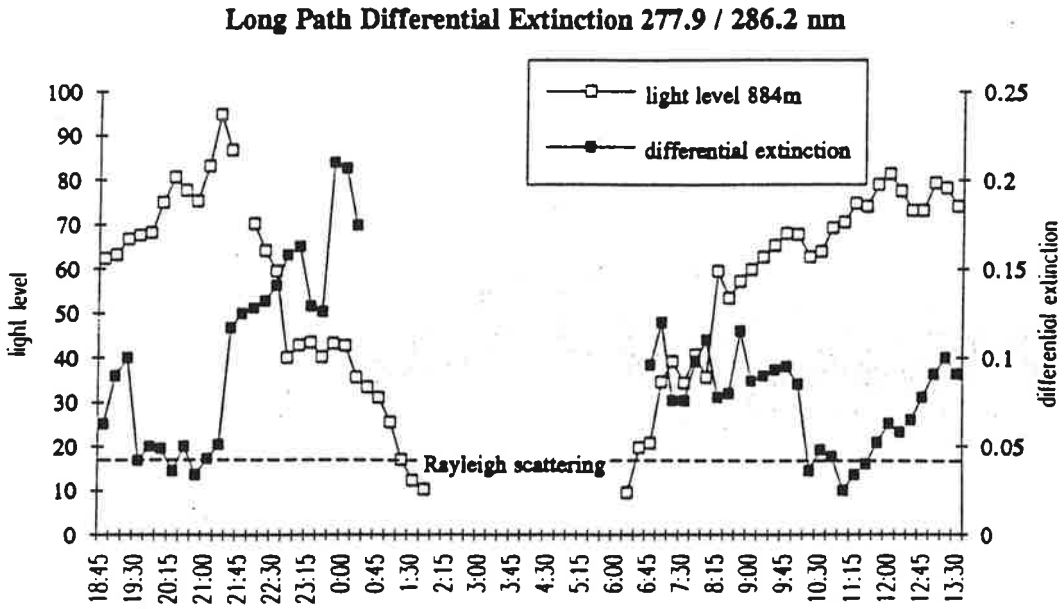

Figure 5.78: Differential extinction over 884-2000 m, and relative light intensity over 0-884 meters, during a period of fog.

5.8 Ground level chemistry

5.8.1 Monthly overviews

In the Trolix '91 campaign, minute concentration values of O_3, SO_2, NO, NO_2 and CO were measured and stored. Unfortunately, due to a technical failure, minute values of NO, NO_2, SO_2 and CO from 10-19 June are not available. In this period, only hourly averaged values are available for these components, while O_3 minute values are available from 10-28 June.

To accommodate the high total amount of data we chose a compact presentation as shown in tables 5.17 -5.21. Hourly averages of O_3, SO_2, NO, NO_2 and CO concentrations in June 1991, measured in Mid-European Time (MET=UT+1), are presented.

5.8.2 Periods of prime interest

Prime interest evaluation periods are listed in section [5.2]. For period 3-8, average minute concentration values are available for all compounds. For periods 1 and 2, only hourly averages are available, except for O_3. The most important compounds are O_3, SO_2 and NO_2. Concentration values for prime interest period 8 are shown as an example in Figures 5.79 - 5.81, for O_3, SO_2 and NO_2 respectively.

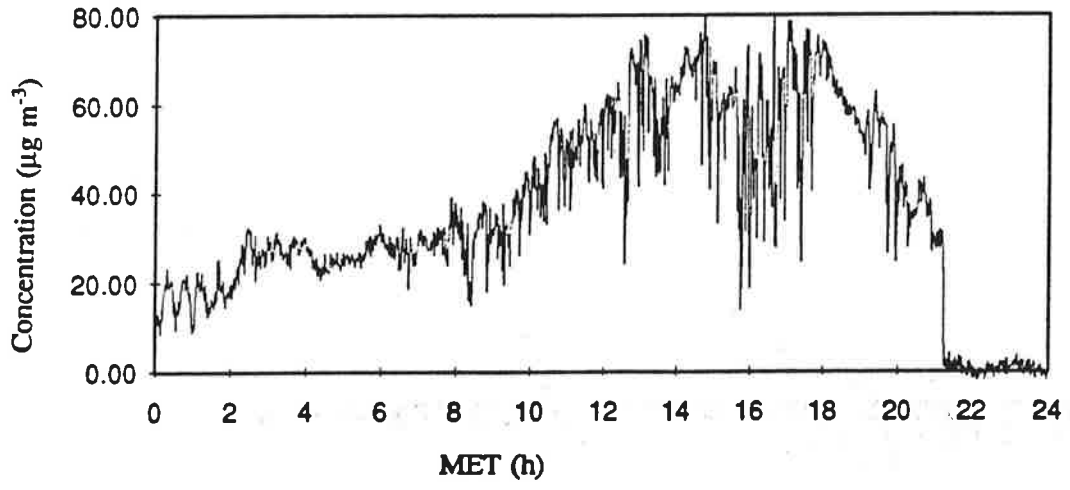

Figure 5.79: Average minute O_3 concentrations for period 8 (91/06/22).

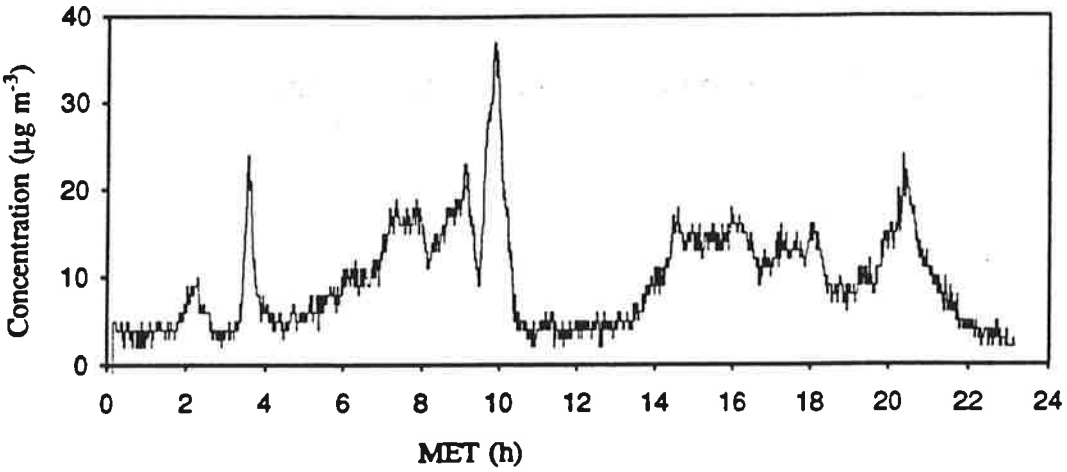

Figure 5.80: Average minute SO_2 concentrations for period 8 (91/06/22).

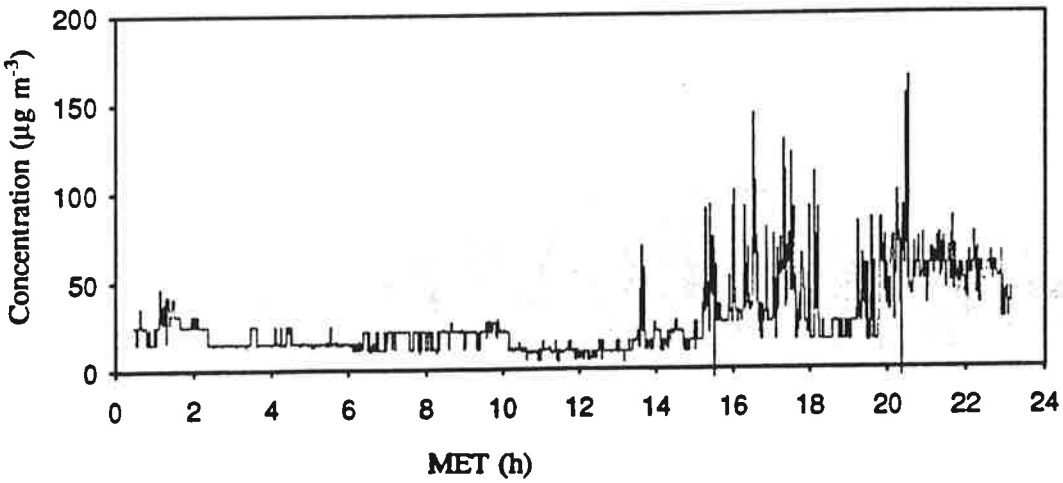

Figure 5.81: Average minute NO_2 concentrations for period 8 (91/06/22).

Day	10	11	12	13	14	15	16	17	18	19	20	21	22	23	24	25	26	27	28
Hour (MET)																			
1		32	19	51	59	42	61	1	2	37	1	0	16	0	28	13	19	22	56
2		28	36	49	54	44	72	1	3	54	1	1	18	4	33	15	19	31	59
3		45	40	49	49	46	76	1	1	37	1	2	25	15	31	13	11	30	64
4		48	25	48	46	28	46	1	0	24	1	1	18	13	18	14	2	17	41
5		44	42	46	40	39	68	1	1	34	2	1	26	27	16	23	18	17	58
6		34	28	38	33	40	64	2	0	20	3	1	25	23	7	13	18	6	60
7		24	27	24	24	50	65	4	8	13	8	2	29	35	20	4	15	4	44
8		29	21	16	22	32	63	13	16	11	14	3	28	41	10	3	8	4	36
9		37	22	30	29	28	88	26	13	20	37	13	40	60	31	5	11	3	62
10		47	26	36	27	37	66	37	34	18	39	27	34	46	34	5	30	9	52
11		60	30	34	28	40	64	36	38	24	50	54	46	47	42	4	32	19	50
12		59	32	31	29	33	55	44	27	26	50	75	51	51	49	6	36	22	58
13		73	31	44	31	21	58	45	32	26	54	78	58	46	51	5	32	38	64
14	55	56	20	50	43	14	61	58	34	16	47	90	59	48	53	7	38	23	57
15	67	47	19	67	52	17	56	72	30	23	50	92	67	47	48	8	49	17	59
16	63	44	12	66	57	28	66	57	76	25	51	76	54	50	47	9	46	42	60
17	51	44	9	69	69	28	58	63	73	15	56	51	53	44	28	15	61	36	65
18	56	37	11	67	74	39	66	61	72	22	48	25	65	44	28	15	51	52	66
19	37	36	13	65	57	43	67	68	70	32	29	19	62	22	28	11	40	66	
20	35	42	16	62	38	41	64	59	56	22	20	19	50	3	7	15	49	61	
21	26	45	11	59	35	44	48	35	35	39	28	16	37	3	1	16	46	53	
22	18	48	6	61	43	50	18	13	22	17	12	7	8	3	3	7	39	52	
23	18	37	3	60	46	55	4	2	39	3	4	5	0	11	8	7	36	58	
24	32	18	36	55	39	49	2	1	45	1	0	8	1	28	2	8	34	60	

Table 5.17: O_3 average hourly concentrations ($\mu g \cdot m^{-3}$) in June 1991

Hour	1	2	3	4	5	6	7	8	9	10	11	12	13	14	15	16	17	18	19	20	21	22	23	24
Day																								
10	3	3	3	5	6	8	19	15	9	9	7	6	5	8	16	20	24	13	8	9	11	13	11	6
11	5	5	6	9	12	12	12	16	16	14	10	8	8	10	9	11	7	13	22	6	5	6	6	8
12	13	16	19	23	18	9	8	10	13	10	11	14	15	9	6	6	7	10	12	17	14	11	10	11
13	5	5	5	5	4	5	5	5	7	7	3	4	3	3	4	3	15	11	3	3	4	3	4	8
14	6	5	5	6	7	8	10	13	14	14	13	19	18	11	14	12	13	9	16	16	37	19	6	11
15	8	9	8	7	8	5	2	4	5	3	2	2	2	4	4	3	5	6	4	3	2	1	1	3
16	2	2	2	2	1	1	1	1	1	1	1	1	1	1	1	1	1	1	1	1	2	3	2	2
17	1	1	1	1	1	2	4	23	38	23	20	18	22	23	28	19	11	14	12	10	8	5	3	2
18	1	1	1	4	4	3	5	6	9	10	16	14	7	13	25	24	29	8	12	12	23	21	8	5
19	6	6	6	8	7	10	12	9	8	6	5	5	6	5	8	15	12	10	5	5	4	3	3	5
20	7	9	6	7	7	8	9	13	14	15	13	13	6	3	3	2	2	2	2	3	4	4	2	2
21	1	1	1	1	1	1	2	2	3	16	40	29	14	12	9	7	9	6	6	6	4	5	6	5
22	4	4	6	9	5	7	10	16	15	22	9	4	4	6	13	14	13	13	10	10	16	7	3	2
23	2	2	4	4	8	13	12	12	20	19	14	5	3	3	4	3	3	4	3	3	2	2	2	2
24	3	3	4	7	5	5	4	4	4	4	3	3	4	5	3	6	32	38	29	18	13	8	4	4
25	4	3	3	2	2	2	3	3	5	5	6	5	3	3	4	3	2	3	3	3	3	3	2	3
26	8	14	10	9	7	9	8	8	6	10	20	10	11	15	8	17	17	5	6	4	4	3	4	4
27	2	3	5	5	6	10	6	3	2	2	2	2	1	2	5	2	2	3	10	19	16	11	6	5
28	3	2	2	2	2	2	4	3	2	1	2	6	3	4	3	2	2	2	1	4	2	1	1	1

Table 5.18: SO_2 average hourly concentrations ($\mu g \cdot m^{-3}$) in June 1991

Hour	1	2	3	4	5	6	7	8	9	10	11	12	13	14	15	16	17	18	19	20	21	22	23	24
Day																								
10	12	9	9	10	15	29	52	50	36	36	36	34	27	31	32	24	34	38	48	44	61	48	68	65
11	38	39	60	49	57	59	57	59	51	59	43	33	28	49	51	52	50	47	49	40	33	30	43	59
12	51	33	28	34	33	40	47	52	61	46	41	43	40	49	49	58	65	76	73	60	62	64	60	45
13	9	10	10	9	10	22	43	53	31	25	29	31	24	22	13	14	25	21	19	18	18	20	16	18
14	11	12	13	13	15	24	39	44	34	30	27	38	36	44	42	47	37	40	41	70	48	35	24	23
15	25	22	16	22	22	20	23	45	46	34	32	40	47	53	54	42	46	35	29	29	27	18	13	15
16	23	20	23	30	34	29	8	9	2	17	17	23	20	9	21	9	14	10	10	13	23	54	65	60
17	43	38	22	14	15	14	49	83	63	38	43	39	35	54	46	50	49	31	28	45	72	66	58	44
18	39	29	39	79	73	57	71	75	72	59	48	59	62	52	55	37	41	39	35	61	53	81	41	31
19	34	18	22	24	25	44	53	55	45	43	36	35	31	50	33	45	51	48	40	57	41	62	61	58
20	56	57	53	44	40	43	42	40	35	32	23	22	20	25	27	27	24	30	67	63	49	77	64	56
21	34	26	19	18	26	33	48	49	47	52	48	31	22	19	23	26	41	70	73	57	57	53	55	43
22	21	30	19	17	17	15	15	20	19	21	12	10	9	17	18	34	44	52	25	38	61	59	54	42
23	48	53	46	30	22	23	12	10	11	11	12	8	9	9	11	12	20	28	50	54	56	59	55	38
24	24	16	11	14	35	47	44	45	26	23	13	16	24	40	44	39	65	64	66	83	80	75	65	60
25	37	30	29	23	16	29	35	32	31	27	29	25	27	24	26	27	26	26	29	23	24	33	31	30
26	22	27	24	47	33	41	48	62	49	41	45	38	39	44	38	37	30	20	24	18	17	27	29	31
27	33	22	20	27	30	44	49	54	57	58	54	46	33	48	54	25	33	27	26	31	35	29	17	15
28	16	10	9	10	9	11	39	35	26	19	30	23	18	22	19	22	15	13	14	18	12	17	55	59

Table 5.19: NO_2 average hourly concentrations ($\mu g \cdot m^{-3}$) in June 1991

Hour	1	2	3	4	5	6	7	8	9	10	11	12	13	14	15	16	17	18	19	20	21	22	23	24
Day																								
10	0	0	0	0	0	0	5	11	5	6	5	6	5	7	7	3	5	6	8	5	6	2	11	18
11	2	8	19	15	20	24	24	25	28	27	23	12	9	18	17	18	14	6	4	1	0	0	1	1
12	0	0	0	0	0	1	3	8	13	11	9	6	8	7	11	15	16	17	12	7	5	9	8	5
13	0	0	0	0	0	1	9	11	7	5	4	7	5	5	3	3	5	3	2	0	0	0	0	0
14	0	0	0	0	0	2	7	10	10	6	7	16	16	26	24	26	10	10	6	7	0	0	0	0
15	0	0	0	0	0	0	0	3	3	3	3	4	6	11	11	3	4	2	1	0	0	0	0	0
16	4	5	5	8	11	8	2	2	1	5	7	9	4	0	5	1	0	0	0	0	0	15	37	40
17	12	20	19	18	31	60	##	##	32	11	11	11	8	13	11	14	20	4	1	2	14	21	32	26
18	28	38	55	41	14	54	46	31	23	13	12	9	14	10	10	10	13	12	9	18	7	12	0	0
19	0	0	0	0	0	2	4	13	8	6	9	7	10	9	11	7	14	7	2	10	2	16	19	10
20	7	5	4	3	4	11	16	20	12	8	4	3	3	3	4	3	4	3	12	4	2	30	44	37
21	27	29	43	61	##	##	##	90	46	21	8	3	4	3	3	2	2	13	9	3	1	1	4	1
22	0	2	0	0	0	0	1	2	2	3	2	1	1	2	2	7	7	13	3	8	14	20	33	41
23	66	17	2	0	0	1	0	0	2	2	2	1	1	1	2	0	1	2	11	21	20	6	2	0
24	0	0	0	0	5	12	11	18	3	4	3	3	7	20	18	9	17	8	9	32	53	18	9	6
25	0	0	0	0	0	2	8	11	16	15	17	18	11	13	12	11	10	6	5	2	1	4	1	1
26	0	0	1	4	0	3	4	9	15	18	20	16	18	19	11	8	5	2	2	0	0	0	0	0
27	0	0	0	0	1	7	15	33	31	27	14	12	6	10	13	2	2	0	0	0	0	0	0	0
28	0	0	0	0	0	0	2	3	1	1	3	3	3	2	2	2	1	0	0	0	0	0	9	15

Table 5.20: NO average hourly concentrations ($\mu g \cdot m^{-3}$) in June 1991 (**: not available)

Hour	1	2	3	4	5	6	7	8	9	10	11	12	13	14	15	16	17	18	19	20	21	22	23	24
Day																								
10	24	29	21	24	31	29	36	44	44	37	35	39	38	38	42	45	50	45	41	40	38	38	36	34
11	35	42	31	29	37	29	34	49	33	32	30	31	28	31	34	38	44	40	39	34	31	31	33	39
12	34	32	30	40	34	33	40	53	48	48	--	45	45	43	41	52	67	66	61	52	51	58	54	43
13	20	11	18	17	11	21	24	36	35	28	25	31	25	24	26	30	35	29	24	23	22	16	15	17
14	26	15	20	22	14	24	36	39	31	27	26	30	31	28	30	33	35	33	33	33	33	24	21	27
15	30	30	27	31	37	31	30	47	38	41	45	43	59	64	62	48	49	49	46	44	42	36	34	38
16	32	33	22	27	25	17	27	21	17	28	23	24	27	25	28	25	27	24	26	26	28	59	88	75
17	54	57	40	46	52	68	85	85	39	28	26	29	28	31	38	41	40	36	34	40	60	53	73	67
18	45	63	77	56	49	63	58	68	56	34	40	38	39	31	35	28	25	20	19	20	22	44	29	28
19	21	28	32	24	33	33	36	53	36	31	38	32	31	38	41	47	66	44	46	52	38	62	61	41
20	50	46	42	48	36	37	44	41	36	30	33	33	31	33	36	36	37	38	46	48	47	85	96	94
21	58	55	69	65	81	74	69	62	49	41	45	46	39	48	49	45	47	69	59	47	45	41	43	37
22	33	29	23	24	27	23	22	25	30	28	28	28	28	34	39	39	36	35	30	29	31	58	60	70
23	85	61	47	45	45	43	37	30	32	36	40	38	38	36	37	39	43	48	62	65	66	56	50	46
24	32	29	26	24	27	30	31	43	37	36	32	32	35	38	39	42	50	38	46	72	77	56	54	50
25	33	31	33	29	29	30	36	41	41	34	43	46	42	40	43	54	60	44	43	39	35	37	36	34
26	19	16	14	15	13	15	23	40	35	28	26	23	23	23	24	33	31	25	24	21	19	21	20	15
27	22	20	33	29	24	36	41	58	63	62	56	45	37	49	48	30	35	35	38	42	48	41	32	31
28	21	12	11	16	6	11	25	19	14	11	20	28	19	18	17	18	17	16	15	17	11	17	24	11

Table 5.21: CO average hourly concentrations ($\mu g m^{-3}$) in June 1991

Chapter 6

Intercomparison of results

6.1 Horizontal intercomparisons

In the horizontal intercomparisons the following systems were involved: LIT-lidar, MPI-lidar, IVL-DOAS, RIVM ground monitor, and MPI ground monitor. Both lidar systems were pointing in a direction very close to the DOAS horizontal path. The height of the lidars was about 5m above sea level, the DOAS instrument was mounted 20 m above ground in a laboratory. All three systems were pointing slightly upward, the DOAS to the two retroreflectors on top of two buildings, the lidars about 1° in order to get free of the obstacles in the beam path some hundred meters apart.

The MPI ground monitor was installed in the same laboratory as the DOAS, with the air sucked in 1.5 m in front of the building. The RIVM monitor was installed in a different part of the RIVM building complex. The LIT lidar measurements were evaluated in the range from 300 - 1050 m, the MPI lidar measurements were evaluated in the range 625 - 775 m, the DOAS range was 0 - 884 m. So the ranges covered by the instruments are quite different, and slight changes in the ozone concentration could occur due to the different land use in these regions. However, averaged over 15 min, the time resolution for the DOAS, these differences are unlikely to exceed some $\mu g \cdot m^{-3}$. Figures 6.1 and 6.2 show the intercomparison of the two ground monitors during the two horizontal intercomparison periods. Both instruments are based upon the same measurement principle of UV-photometry. They compare well most of the time with respect to the long term trends, but the RIVM instrument has a large number of spikes with lower ozone concentration. This is not only due to the higher time resolution of the recorded data of this instrument. The individual readings of the MPI monitor every 8 seconds did not show these spikes, but they are seen in many of the RIVM traces during the experiment. It turned out that these spikes are not due to instrument malfunction, but that in fact ozone depleted air was sucked in occasionally, due to the installation close to a laboratory building with considerable traffic around. Thus the upper enclosing curve for this monitor seems to be more appropriate for comparison with the remote sensing instruments, which are unlikely to be influenced by such local depletions.

Fig. 6.3 shows the results of all instruments for the period of 15:00 to 21:00 UT on June 22. For the MPI lidar, results for both wavelength pairs, 248/313 and 277/313 nm are shown. The agreement between LIT-lidar, DOAS, and ground monitors is quite good,

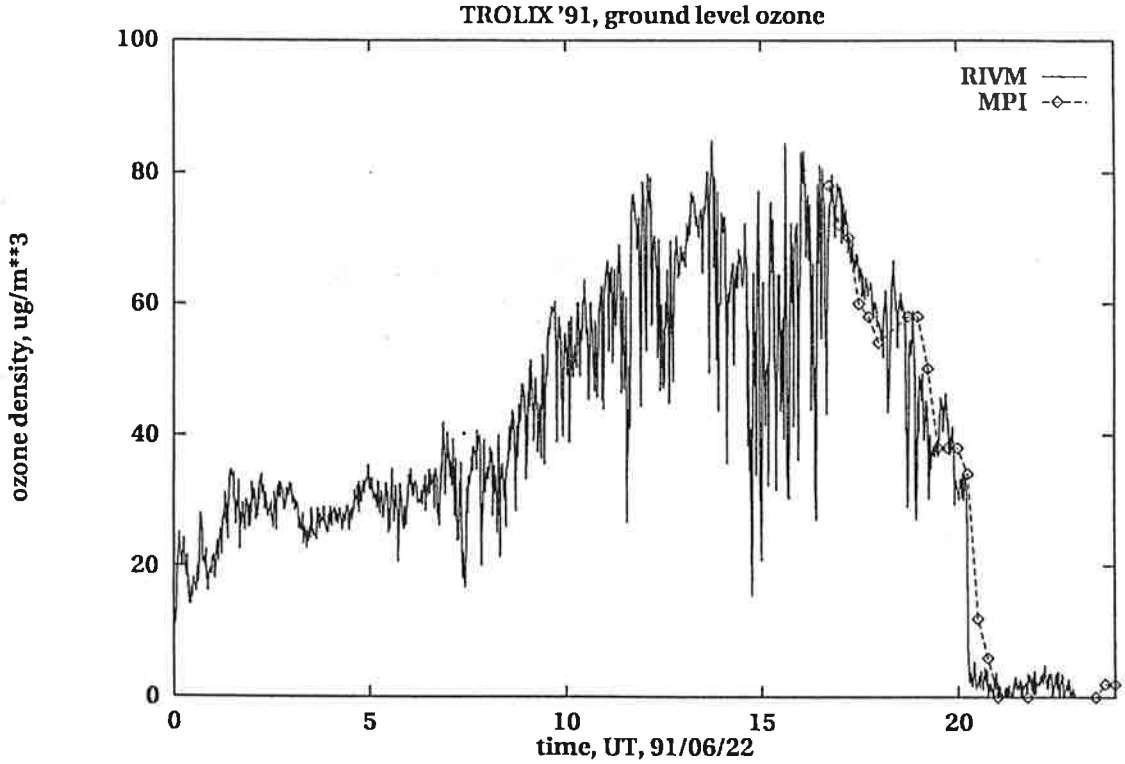

Figure 6.1: Intercomparison of RIVM and MPI ground level UV-photometric ozone monitors, June 22

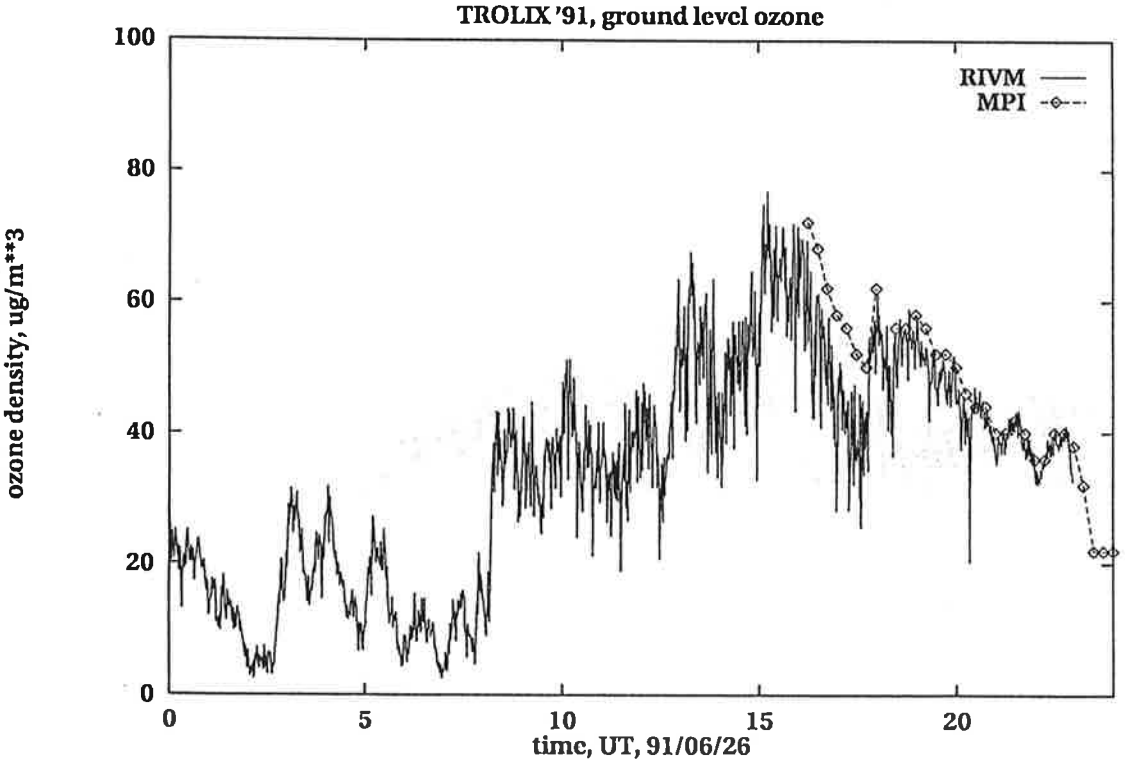

Figure 6.2: Intercomparison of RIVM and MPI ground level UV-photometric ozone monitors, June 26

on the order of a few $\mu g \cdot m^{-3}$. The lidar results are slightly larger than the monitor and DOAS data, about 10 $\mu g \cdot m^{-3}$. This is expected, since lidar results have not been corrected for differential aerosol extinction (which would lower the results by about 5 $\mu g \cdot m^{-3}$). For the MPI lidar the changes in time follow the patterns observed by the other instruments, but the absolute values are about 25 $\mu g \cdot m^{-3}$ higher for the 277/313 nm pair, and 17 $\mu g \cdot m^{-3}$ higher for 248/313 nm.

Fig.6.4 shows a similar intercomparison performed on June 26. The only difference in the instrumental part is the change of wavelengths for the MPI lidar, which used 268 and 292 nm (first and second Stokes SRS in deuterium). For this experiment, all instruments agree very close, e.g. the mean difference between MPI lidar and MPI monitor is 2.2 $\mu g \cdot m^{-3}$, for the other instruments this is about the same.

Aerosol interference problems are much reduced in horizontal measurements, in particular when averaged over several minutes. It is not likely that strong horizontal gradients in the aerosol backscatter coefficient persist at the same location for extended periods of time, so in this respect the atmosphere can be assumed almost homogeneous. Thus differential backscatter gradient errors are expected to be small. The aerosol extinction can be estimated by the slope method in this case, in particular from the 313 nm signal. An example has been given in fig. 5.36 of section 5.3.4. The correction for differential aerosol extinction is quite small, for the 277/313 nm wavelength pair, as a worst case, this is only 4 $\mu g \cdot m^{-3}$, assuming a λ^{-1} dependence as usual. The DOAS aerosol extinction measurements gave an aerosol correction corresponding to 6.5 and 2.7 $\mu g \cdot m^{-3}$ ozone for the two days respectively (at wavelength pair 277,9/286,2 nm).

SO_2 interference is estimated using the measurements of the RIVM/LLO-network. SO_2 concentrations were $\approx 13 \mu g \cdot m^{-3}$ for June 22, and 4 - 17 $\mu g \cdot m^{-3}$ for June 26. Of the measurements shown here, the results of the 277/313 nm pair are most sensitive to SO_2. The correction to be applied to the ozone values would be -2 $\mu g \cdot m^{-3}$ for June 22. For the 268/292 nm measurements this correction is even smaller. The LIT lidar wavelengths had been selected for minimum SO_2 interference. DOAS and ground monitors are supposed to be free from SO_2 interference problems. In conclusion, SO_2 interference has not been a problem in these measurements.

Water vapor has been claimed to cause a serious interference problem in this wavelenth range, too [Karm 90]. For the water vapor absorption coefficient of $0.8 \cdot 10^{-4} m^{-1} \cdot \mathrm{Torr}^{-1}$ given there, and the water vapor partial pressure of 9.8 Torr measured at the nearby KNMI meteo station, an absorption coefficient of $7.8 \cdot 10^{-4} m^{-1}$ would follow for wavelengths $< 280 nm$. This is obviously not consistent with the measurements shown here. In particular, the 277/313 nm and the 268/292 nm results had to be $130 \mu g \cdot m^{-3}$ and $60 \mu g \cdot m^{-3}$ larger than the other results, respectively, if the claimed cross sensitivity was correct. From the intercomparisons shown here it is obvious, that the water vapor absorption claimed in [Karm 90] cannot be correct.

So these horizontal intercomparisons show, that excellent agreement can be achieved between lidars, DOAS, and standard in situ measurements. For the 277/313 nm pair of the MPI system a slight overestimation of about 18 $\mu g \cdot m^{-3}$ occurs after correction for differential aerosol extinction and SO_2 differential absorption. The lidar systems, both the excimer laser based of MPI and the dye laser based of LIT, are stable over many hours of continuous operation.

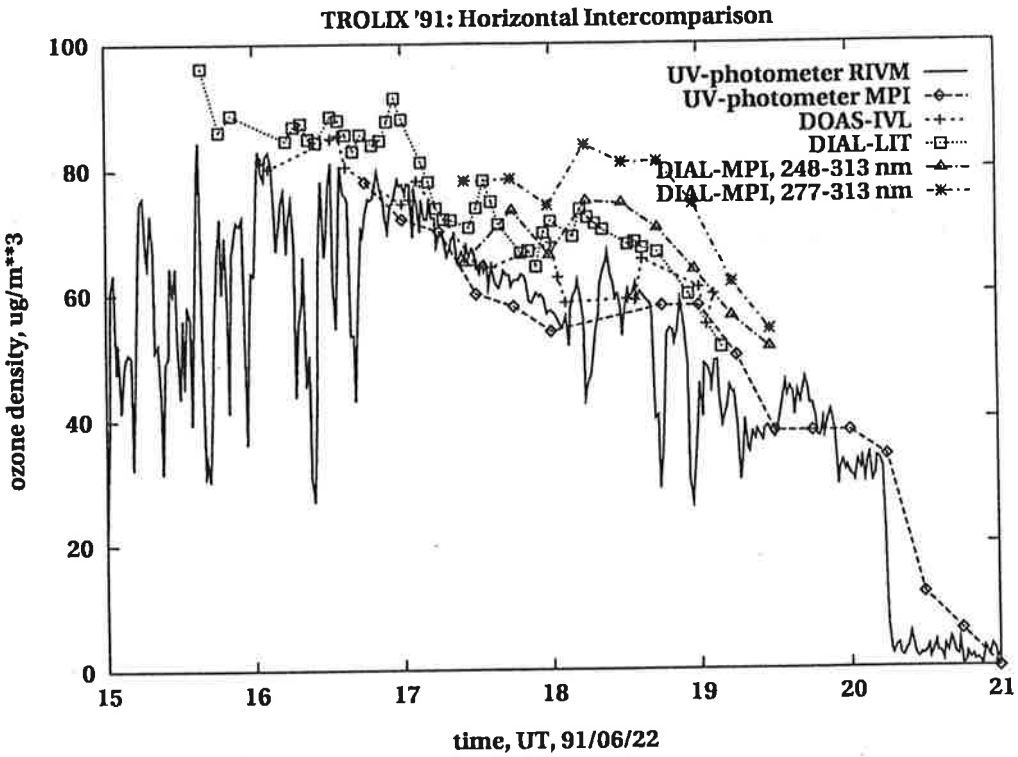

Figure 6.3: Intercomparison of DOAS, LIT- and MPI-DIAL, and ground level UV-photometric ozone monitors, June 22. Lidars pointing horizontally.

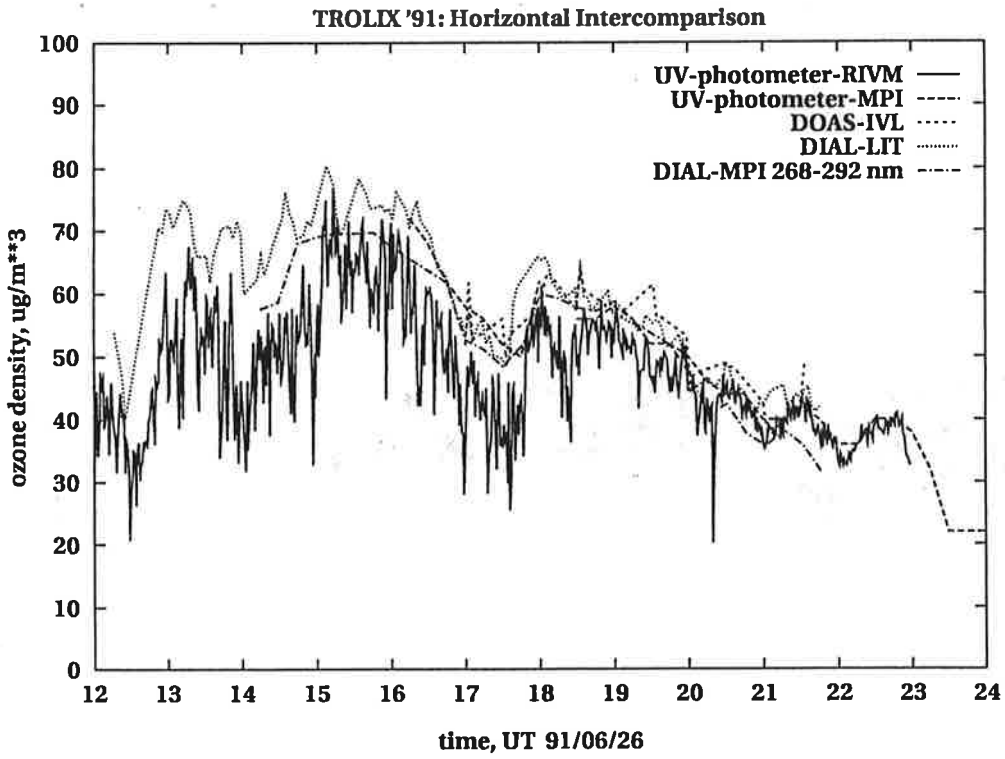

Figure 6.4: Intercomparison of DOAS, LIT- and MPI-DIAL, and ground level UV-photometric ozone monitors, June 26. Lidars pointing horizontally.

6.2 Flight intercomparisons

During the campaign three helicopter flights have been performed for intercomparison of lidars and in situ instrument at heights up to $\approx 1500m$. For the individual measurement systems the results have already been presented in chapter 5. In this paragraph the results of all successfully operated systems are shown simultaneously.

Fig. 6.5 shows the results for flight 1 on June 20, averaged approximately over the time period 08:25 - 08:40 UT (slightly different for different systems). This had been selected because it was free from low clouds, and the helicopter was close to its maximum height. The meteorological situation was not in favour of lidar measurements: a highly variable broken cloud deck at low altitudes made adjustments very difficult, and aerosol load both in the boundary layer and in the layer beyond was high and highly variabel. The results show rather large scatter, but the main feature, a steep increase of ozone concentration on top of the boundary layer, is seen in all traces. First it has to be noticed that there is a rather large difference of 12 - 22 $\mu g \cdot m^{-3}$ between the two heliborn in situ measurements. Both systems had been calibrated before and after the flight, showing no significant deviations. So the source of the discrepancy is not known yet.

The aerosol interference is rather large in this case for the whole range up to 2 km, this is demonstrated in fig.6.6 , where the differences between a choice of aerosol corrected retrievals and the uncorrected value is given for the 277/313 nm result of the MPI-system. This can certainly explain part of the differences between the results of different lidar systems, since the aerosol correction varies up to a factor of two for different wavelengths combinations, but some other problems can be detected as well. This will be further addressed in section 6.4, where a direct intercomparison of the lidar signals is presented.

For flight 2 on June 24 the situation was much more homogeneous, so less trouble was expected from the lidars. The results, except for the MPI system, which was misaligned on this day, are presented in fig. 6.7 . They show rather good agreement with less than $\approx 8\mu g \cdot m^{-3}$ differences over most of the range for all instruments. Only at both ends of the measurement range all lidars seem to have some problems.

For the third flight on the very last day of the campaign, June 28, data are available only for the LIT and MPI lidars, and the RIVM heliborn in situ ozone monitor. The values for ascent and descent of the helicopter show differences up to 40 $\mu g \cdot m^{-3}$. Again this was a bad situation for an intercomparison, since a highly variable low cloud deck was present, as demonstrated in fig. 5.52 of section 5.3.4. This may explain some variability, but it is hard to believe that changes can be that large, in particular when the LIT-lidar shows almost no changes over one hour of measurements in this period. LIT lidar results are about 30 $\mu g \cdot m^{-3}$ lower than MPI results, but there is almost no overlap in height range for these two instruments. The range of the LIT lidar is completely below the clouds, while the MPI lidar starts about at the cloud base. In this situation it is not useful to start an interpretation of the differences, since the atmosphere was too inhomogeneous for a good intercomparison of instruments with different sampling properties.

So lidar results show good agreement among eachother and with heliborne in situ measurements when the atmosphere is rather homogeneous. Inhomogeneous cases are not suitable for intercomparisons, the actual reasons for the observed differences of all instruments, including the in situ measurements, could not be determined.

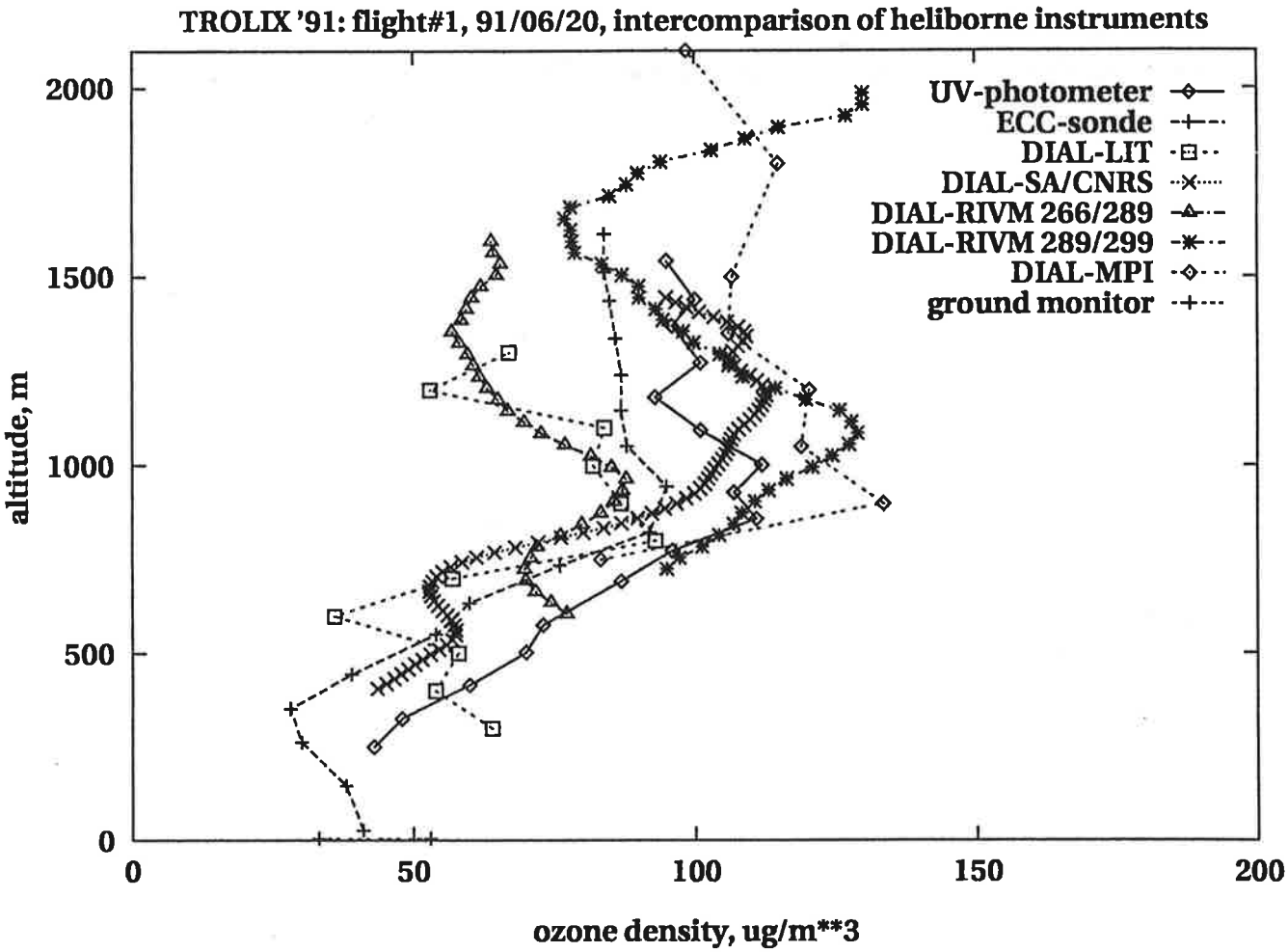

Figure 6.5: Intercomparison of Lidars and in situ instruments for helicopter flight 1 on June 20.

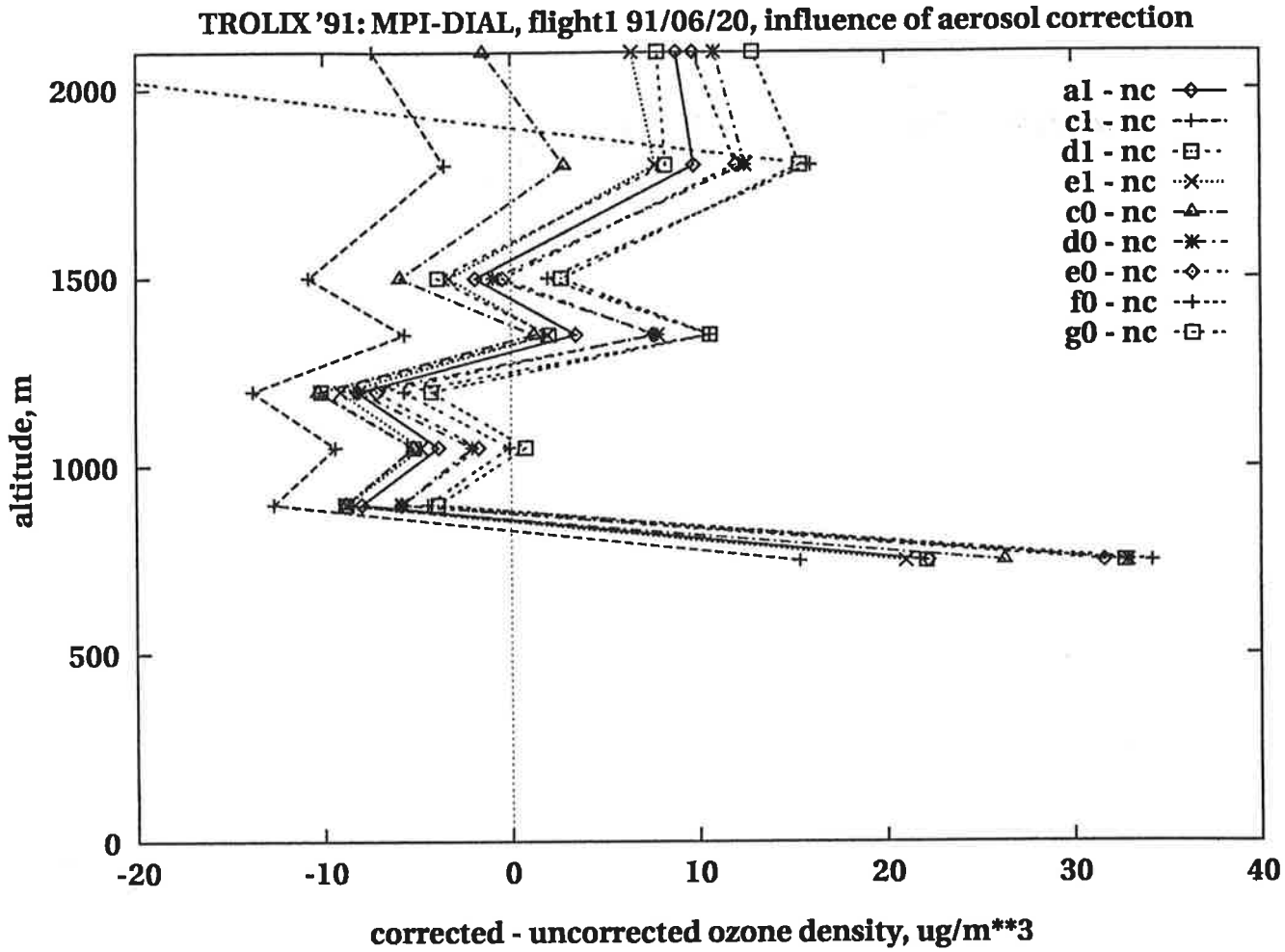

Figure 6.6: Aerosol corrections for the flight intercomparison, 91/06/20 08:25-08:40 UT. nc is the uncorrected curve, in the labeling the letters have the meaning a:$\beta_{cal} = 0.1$, $S = 25$, c:$\beta_{cal} = 1.0$, $S = 25$, d:$\beta_{cal} = 0.1$, $S = 35$, e:$\beta_{cal} = 0.2$, $S = 25$, f:$\beta_{cal} = 0.0$, $S = 25$, g:$\beta_{cal} = 0.1$, $S = 15$. The number (0 or 1) indicates the exponent of the λ-dependence of the aerosol backscatter and extinction, λ^0 and λ^{-1}, respectively.

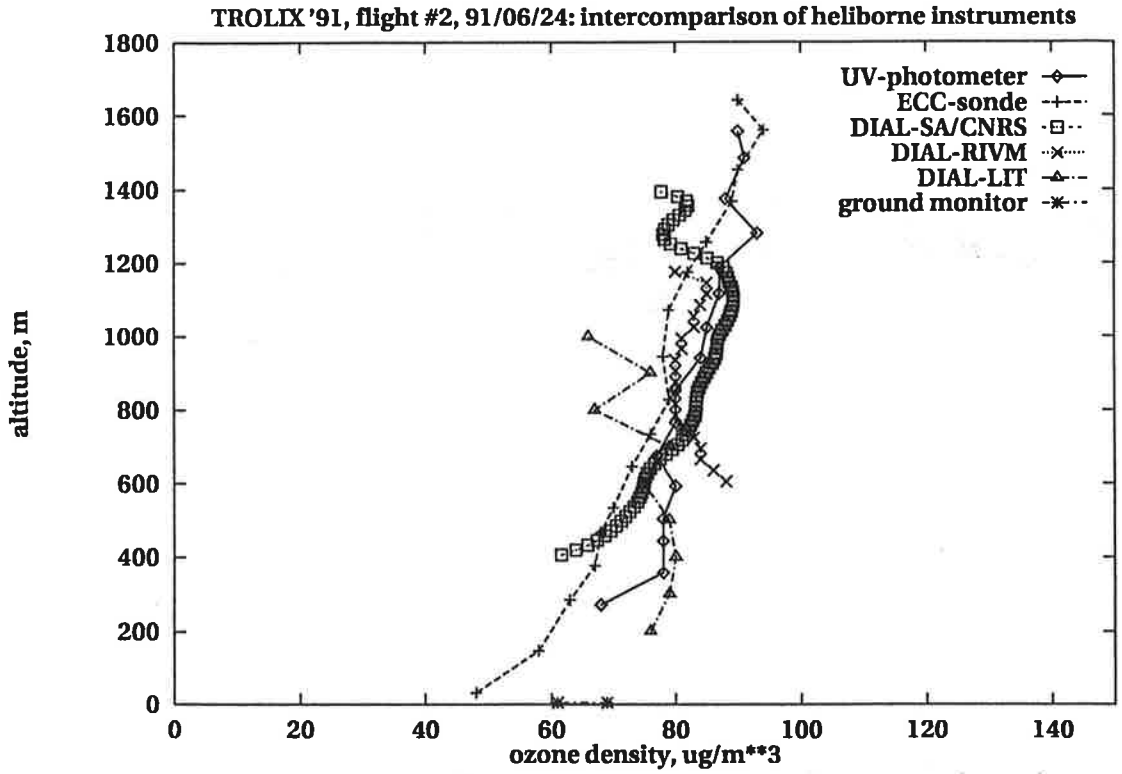

Figure 6.7: Intercomparison of Lidars and in situ instruments for helicopter flight 2 on June 24.

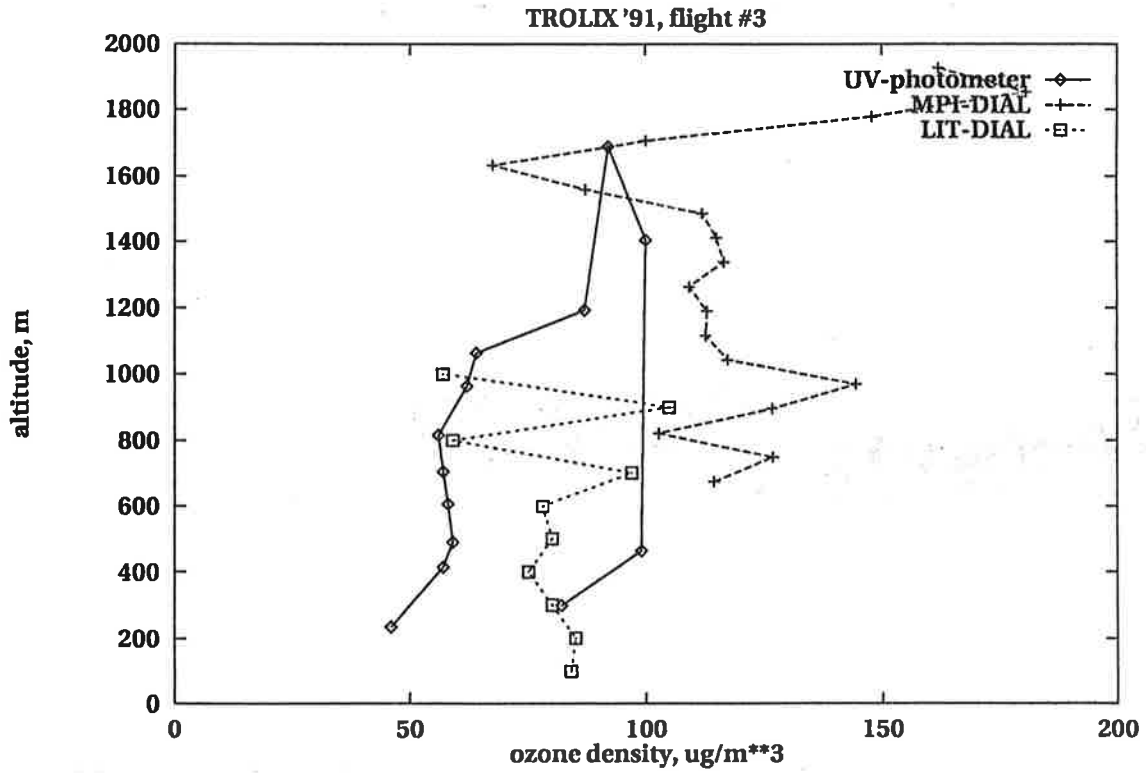

Figure 6.8: Intercomparison of Lidars and in situ instruments for helicopter flight 3 on June 28.

6.3 Lidar-Lidar-intercomparisons

Vertical lidar measurements with no other direct intercomparison have been evaluated for periods on three selected days, as given in table 5.2 in section 5.2. On June 11, only results from LIT and MPI are available and presented in fig. 6.9. No major change in the vertical distribution has been observed over the period from 10:05 to 12:39 UT in both systems, but a considerable difference of $20 - 25\mu g \cdot m^{-3}$ is observed in the overlapping range of both systems. This is quite similar to what had been observed for these wavelengths in the horizontal intercomparison, so at least this internally consistent.

Fig. 6.10 -6.13 show the available results for June 13, a day with scattered cumulus clouds at the top of the mixed layer around 1.5 km, and a second broken cloud deck in the beginning at about 2.5 km. The selected periods are almost cloudfree.

The ranges of the lidar systems are quite different, but with some overlap. For all four selected periods, the CNRS/SA and MPI results agree rather well in the region of overlap. LIT shows a decrease with height in the boundary layer as opposed to CNRS/SA, the concentrations on the average are roughly the same. RIVM shows an oszillation pattern already addressed in section 5.3.1, and generally lower values than CNRS/SA and MPI, again about $20-25\mu g \cdot m^{-3}$ (the exact number is hard to estimate because of the oszillation pattern superimposed on a bump).

Fig. 6.14 shows results from June 26 for CNRS/SA (266/299 nm) and MPI (268/292 nm). The results show rather large differences of up to $60\mu g \cdot m^{-3}$, in particular at the low end of the measurement range. This is somewhat surprising, since for MPI the deuterium wavelengths 268/292 nm are employed in this measurement, which gave excellent agreement in the horizontal intercomparison just before. Aerorosol interference is rather unlikely to explain this difference, since the aerosol distribution was quite uniform. So the reason for the apparent discrepancy presently remains open.

In these intercomparisons for several occasions rather large differences have been observed, while for others the agreement is good. The reasons for the observed differences are hard to assess. The high values of the MPI measurements using the 277/313 line pair are quite persistent through all measurements in this campaign analysed so far. It should be further investigated, wether or not they may be due to water vapor absorption. Aerosol interference certainly is another reason for rather large deviations, particularly in regions of inhomogeneous aerosol distribution. Some other reasons for the observed differences will be given in the next section, were signals are compared directly. On the other hand, for homogeneous cases, found e.g. in horizontal measurements, the agreement is remarkably good.

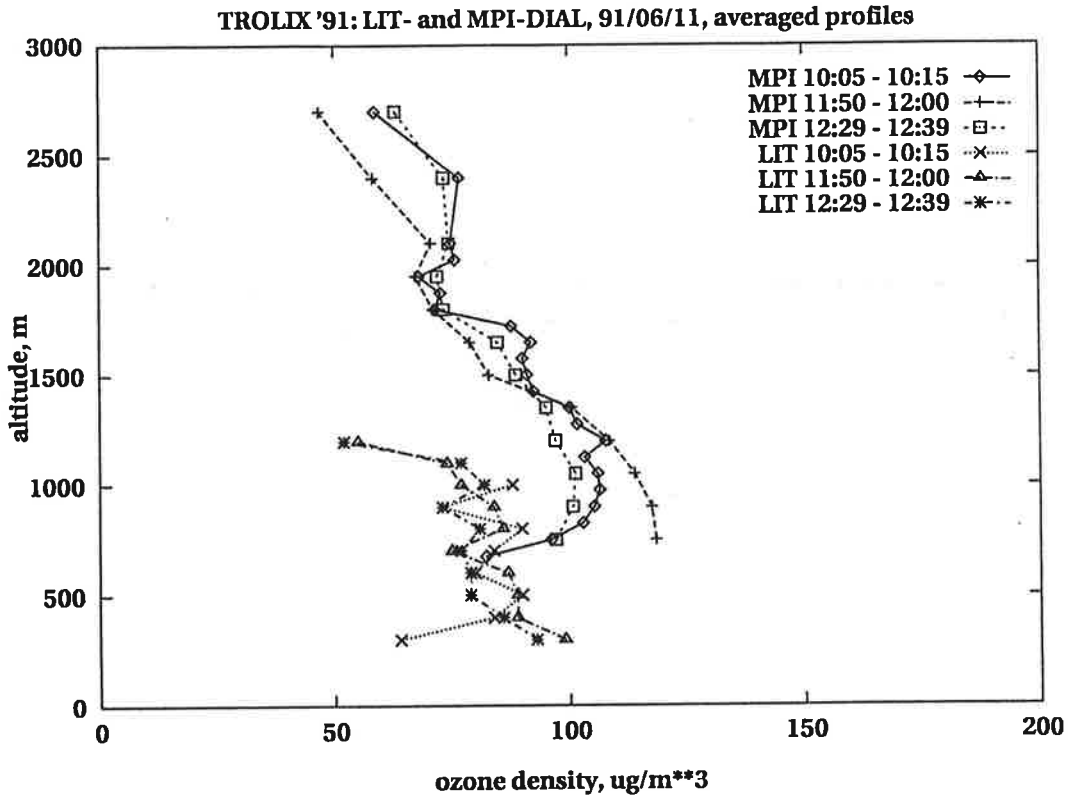

Figure 6.9: Intercomparison of Lidars on June 11.

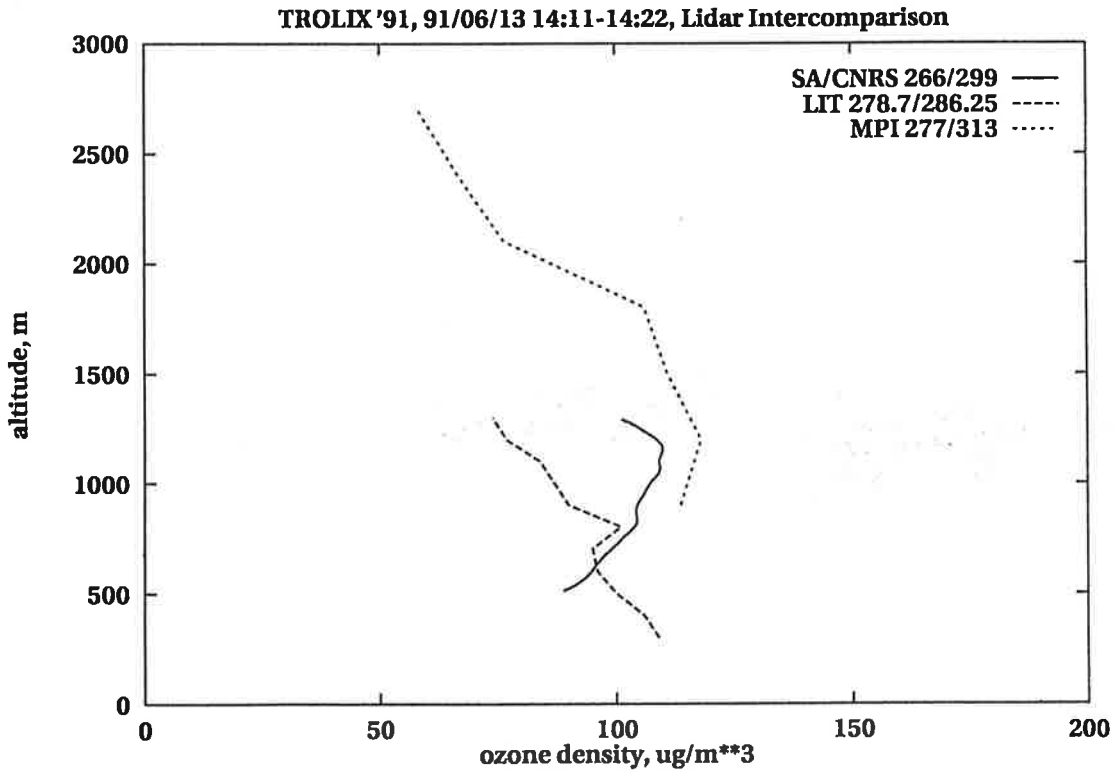

Figure 6.10: Intercomparison of Lidars on June 13.

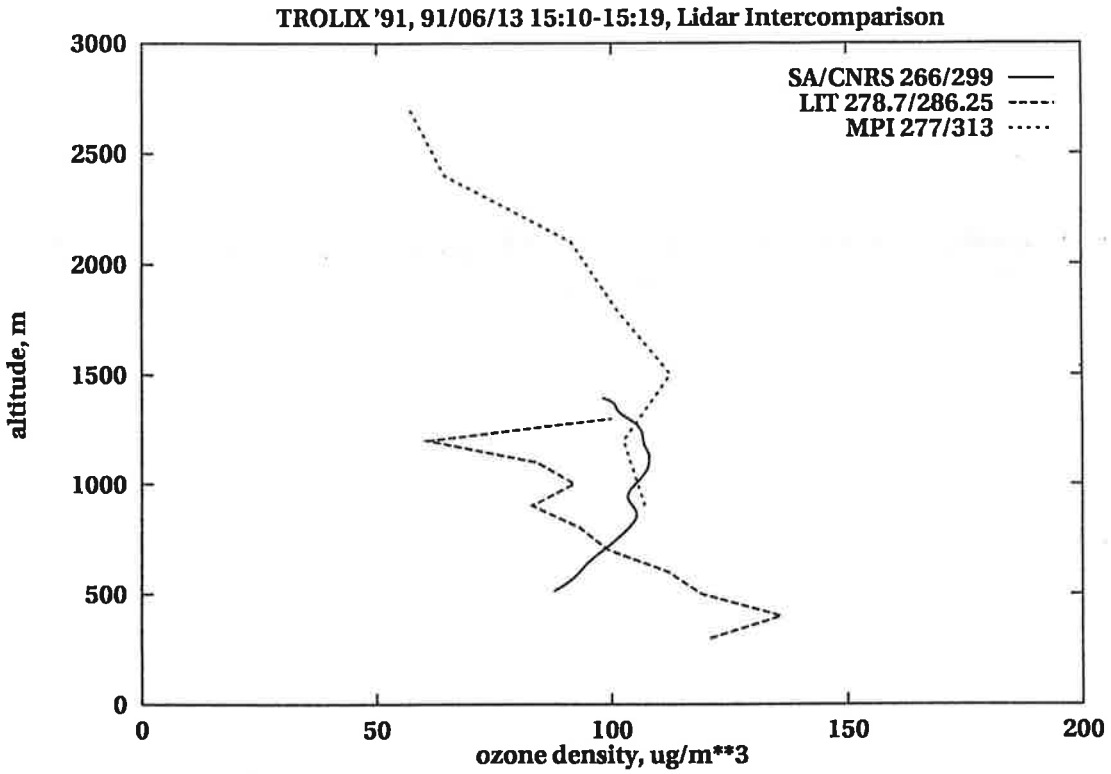

Figure 6.11: Intercomparison of Lidars on June 13.

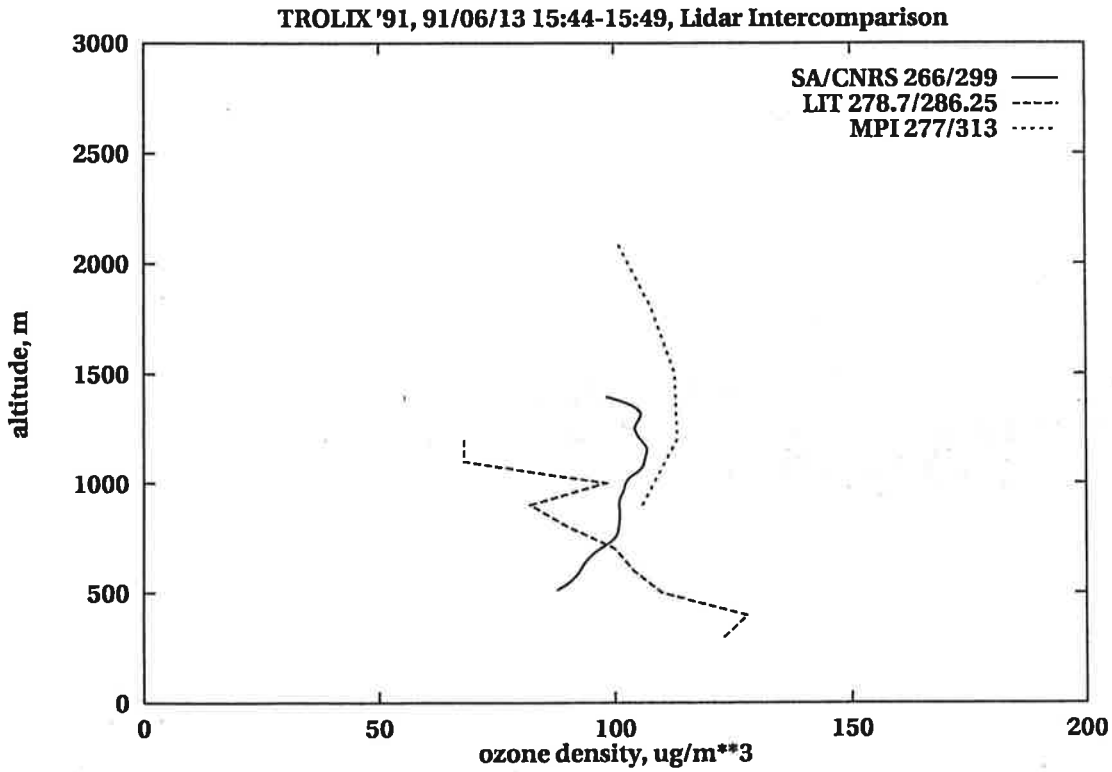

Figure 6.12: Intercomparison of Lidars on June 13.

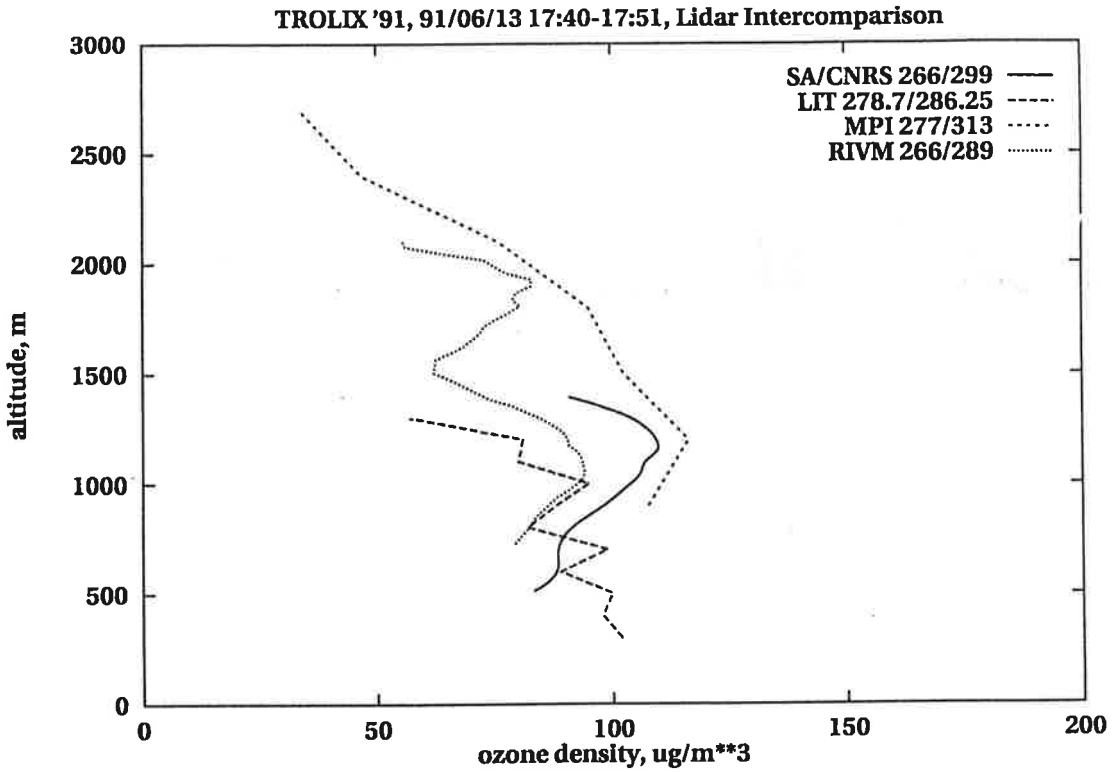

Figure 6.13: Intercomparison of Lidars on June 13.

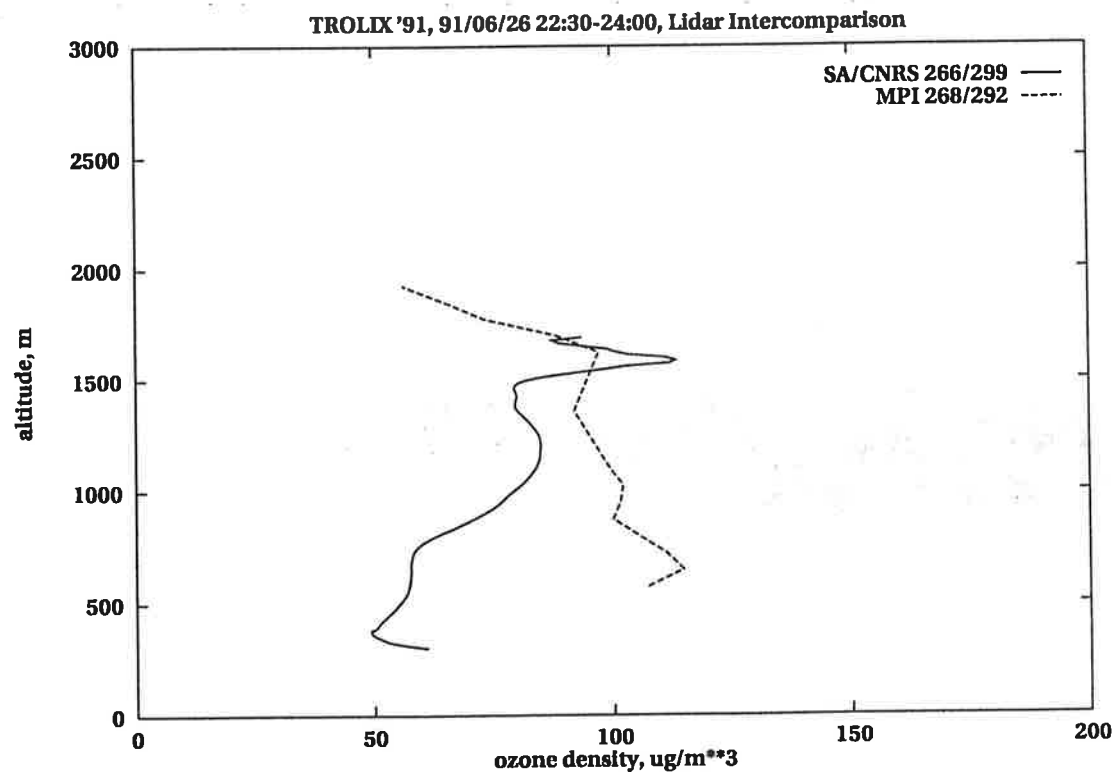

Figure 6.14: Intercomparison of Lidars on June 26.

6.4 Lidar signal intercomparison

As a period for a first intercomparison of range corrected lidar signals from different systems at different wavelengths a 5 min interval during the first flight intercomparison is chosen. RIVM, LIT, and MPI lidars were pointing vertically, CNRS/SA was pointing 30° off zenith. Since 11 signal traces at 8 wavelengths have to be presented, the display is split. Fig. 6.15 shows an intercomparison of RIVM at 266, 289, and 299 nm, and MPI at 248, 277, and 313 nm. From this figure it can be concluded that the overlap functions for the two systems are different, the MPI measurements start at considerably greater height. For both systems the shortest wavelength, 248 and 266 nm, is completely absorbed at the cloud height of 2.6 km. In spite of this, in both systems a considerable signal level is still indicated at this altitude, which is interpreted as a memory effect in the photomultiplier. This is also indicated in the 277 nm trace at heights $> 2.2km$. Further, there is a minor difference in the height scales of the two systems, which is clearly detected at the cloud level. The fine structure of the signals matches excellently between all signals in their useable range. This structure obviously is caused by the aerosol variability, and is measured in the same way by both systems.

Fig. 6.16 shows the intercomparison between the two NdYAG laser based systems of RIVM and CNRS/SA, for 266, 289, and 299 nm. For the CNRS/SA system, the signals get very noisy beyond $\approx 1300m$, the cloud at 2.6 km is not detected by this system. It has to be noted, that for the CNRS/SA system a correction for memory effects of the photomultiplier has already been applied, in contrast to the other systems. This may be the reason for the large difference for the 266 nm signals, and also for the differences at the far end for the other two signals as well. But even with this correction, at least for the range $> 2km$ the signals seem to be unreliable.

The structure of the top of the boundary layer at about 800 m is different for the two sets of measurements, which is probably due to the different pointing of the systems. For greater heights no comparison of the fine structure is possible because of the noise in the CNRS/SA measurements.

Fig. 6.17 shows an intercomparison between LIT at 278.7 nm and 286.3 nm, and again MPI at 248, 277, and 313 nm. The LIT system has a special electronic circuit varying the gain of the PMT in the first 1000 m, so this range is deliberately distorted, but in the same way for both wavelengths of this system. So below 1000 m no direct intercomparison is possible with signals of other systems. Beyond that height, again the fine structure of the signals agrees very well, but the slope of both LIT signals is smaller than that of the 277 nm of the MPI system, even if the ozone absorption is accounted for.

Both measurements are internally consistent, and consistent with the a priori knowledge. The ozone concentration is known with considerable uncertainty only, and the aerosol properties are unknown. Thus from these figures it cannot be concluded, wich measurement is the correct one.

From a first direct signal intercomparison it is obvious, that there are some problems for an evaluation using the combined data set. The CNRS/SA system probes a different part of the atmosphere, which excludes these measurements from a direct intercomparison

with the other systems, perhaps with the exception of cases of a homogeneous atmosphere, which hardly ever was present during this experiment. The LIT system has built in the special gain variation circuit, which allows intercomparison with other systems for ranges greater than 1000 m only (up to the maximum range of about 1500 m for this system). So best chances for a combined data set seem to be for the MPI and RIVM lidars. At the present stage of evaluation, both systems suffer from uncorrected memory effects of the detector, which show up clearly at the far end of the range, where the signal level is low. Other cases with less complicated areosol structure have to be analysed next to make sure that a sufficient range of reliable measurements exists for both systems.

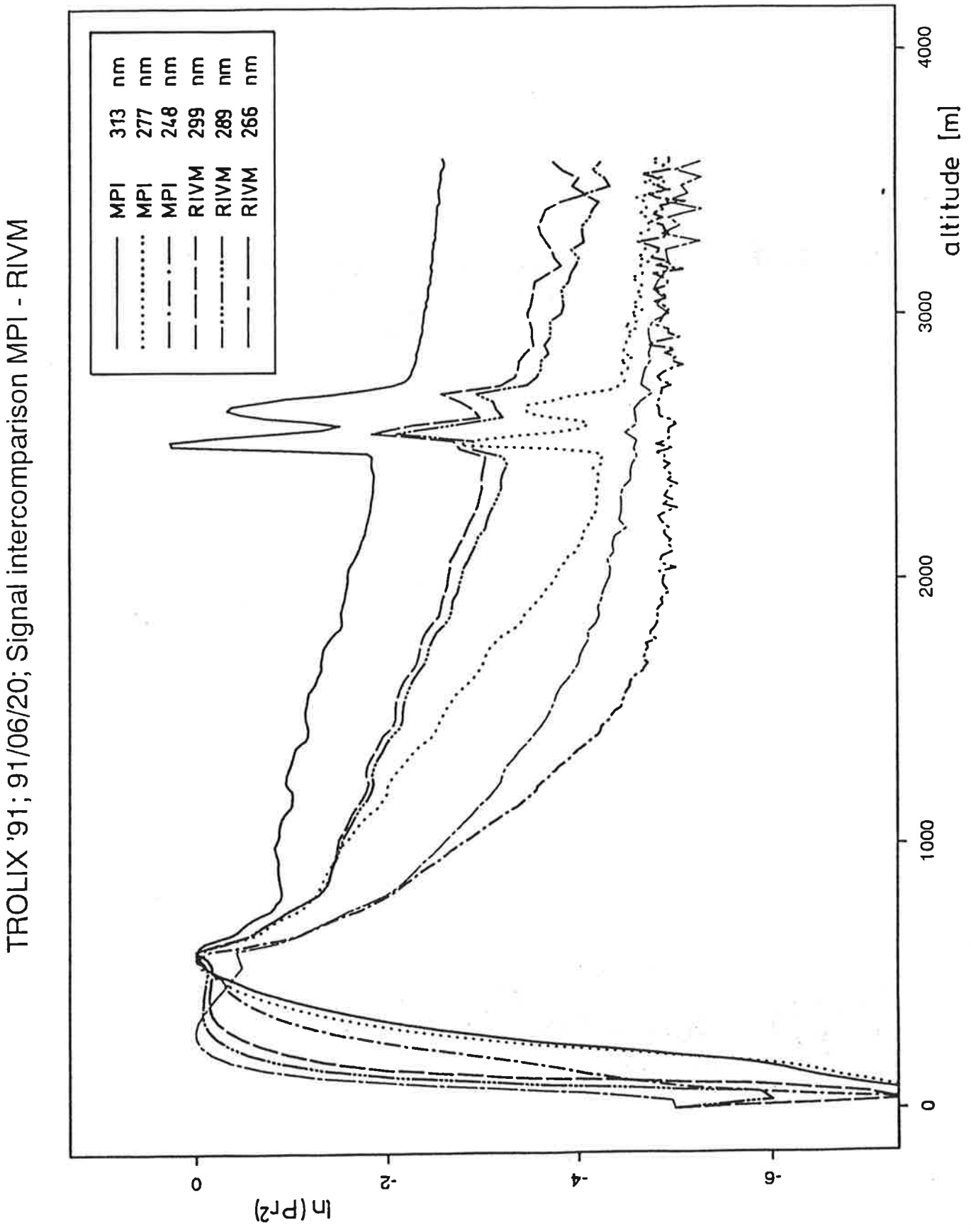

Figure 6.15: Intercomparison of range corrected signals, June 20, 1991, 08:30 UT.

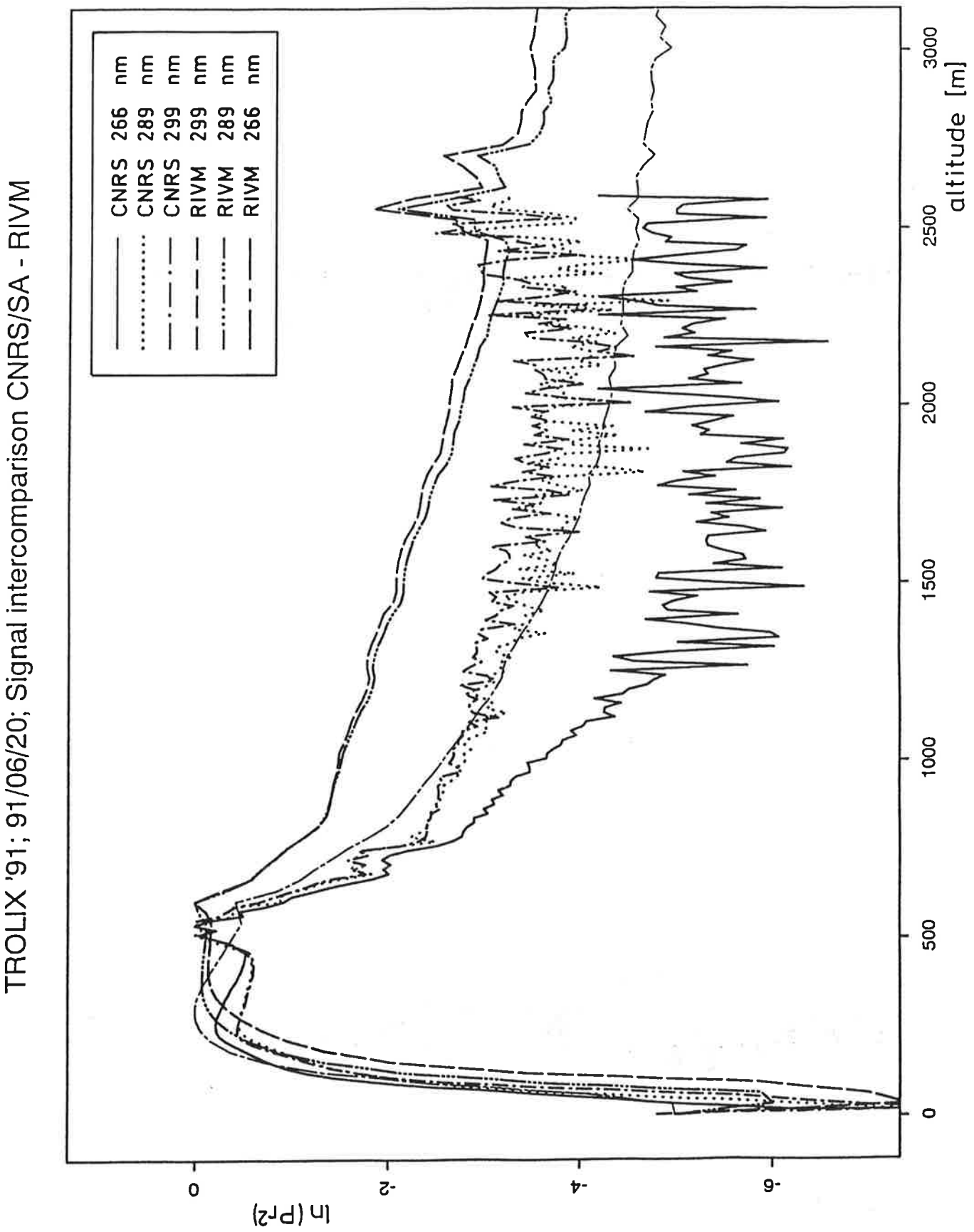

Figure 6.16: Intercomparison of range corrected signals, June 20, 1991, 08:30 UT.

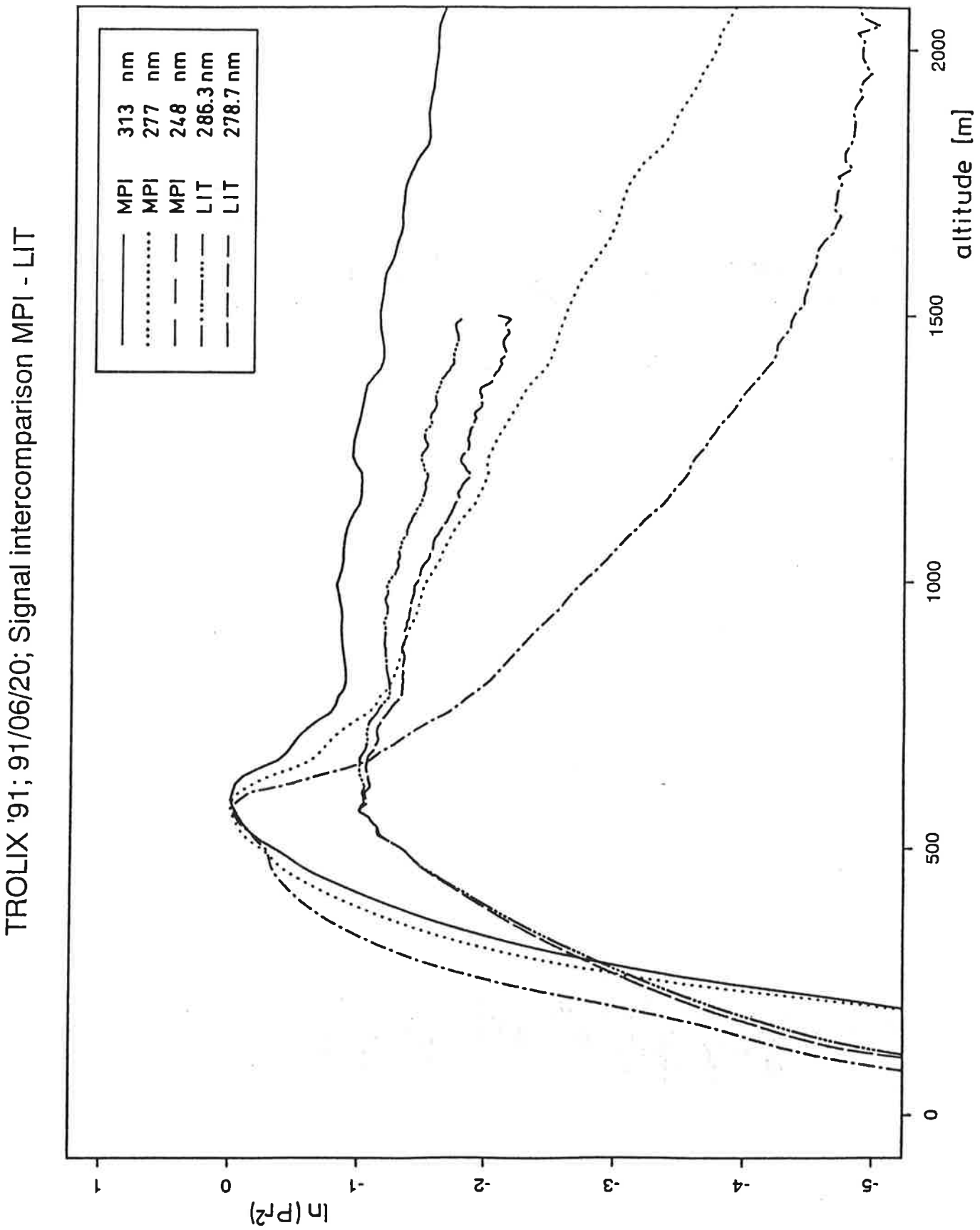

Figure 6.17: Intercomparison of range corrected signals, June 20, 1991, 08:30 UT.

Chapter 7

Conclusions

The bad weather conditions during this experiment were not in favor of lidar measurements, and quite untypical for situations to which tropospheric ozone research is focussed. In spite of this, a fairly large number of measurements have been performed. At the present stage of evaluation, it is not completely clear, which of the initial goals of this experiment will be reached. However, some important conclusions can already be drawn.

- All four lidar systems participating in this experiment, which were quite different in construction, were operating reliably, no major technical problems were encountered.
- From this experiment, all groups have detected some problems in the existing hardware, which restrict the range of operation. Corresponding studies of details have been initiated to come to further system improvements, mainly in the areas of
  - suppression of detector memory effects
  - improvement of data acquisition systems
  - provisions for easier adjustment of overlap between transmitter and receiver, in particular under bad weather conditions
- In situ measurement systems, in particular when operated from a helicopter, have their own problems.
- For a homogeneous aerosol distribution, excellent accuracy of lidar measurements has been demonstrated.
- High temporal and spatial resolution has been achieved for measurements of the vertical distribution of ozone. So far lidars are the only systems to provide this information.
- For inhomogeneous aerosol distribution considerable errors are introduced. The correction scheme has to be improved to yield accurate results under adverse conditions. More work has to go into a sufficient characterization of aerosol properties.

- With respect to systematic errors, water vapor interference has been shown to be not as severe as had been claimed. It may still be important, a reassessment of absorption data is required.

Further evaluation of the collected data set will address the aerosol interference and the interference with water vapor. Studies of individual system properties will be extended, and the data set will be used to study the relation between ground level ozone concentrations and vertical distribution for several meteorological conditions.

When the technical improvements have been incorporated, further intercomparison experiments seem to be appropriate. They should include better weather conditions, more flights, extension to greater altitudes, and better control over airborne in situ instruments. In situ measurements of aerosol properties would be highly desirable. These items should be considered in any future intercomparison experiment, whether it will be a standalone experiment or incorporated in a larger field campaign.

Acknowledgements All groups participating in this experiment are particularly grateful to the hosting institute, the RIVM, for the excellent support given in any respect in the course of this experiment.

We would also like to thank the Royal Dutch Airforce, Squadron 298, for technical assistance, and for performing the helicopter flights, which were a central part of this experiment.

The supply of extensive weather information by the KNMI both for planning purposes during the experiment, and for the evaluation phase are gratefully acknowledged.

We would like to thank Dr.H. Smit from the 2.Institut für Chemie, KFA Jülich, for providing the equipment and detailed advice for the preparation of the ECC-sondes.

This experiment was performed within the frame of the TESLAS subproject of the EUROTRAC cooperative environmental research project.

Bibliography

[Ance 89] Ancellet, G., A. Papayannis, J. Pelon, G. Megie: " DIAL Tropospheric Ozone Measurement Using a Nd:YAG Laser and the Raman Shifting Technique", J.Atm.Ocean.Tech., 6, 5, 832-839 (1989)

[Apit 91] Apituley, A.: "RIVM contribution to TESLAS field campaign TROLIX '91 for intercomparison of Tropospheric Ozone LIDAR systems", RIVM report 222201009

[Axel 90] Axelsson, H., H. Edner, B. Galle, P. Ragnarsson and M. Rudin: "Differential Optical Absorption Spectroscopy (DOAS) Measurements of Ozone in the 280-290 nm Wavelength Region", Appl. Spectr, 44, 1654-1658 (1990)

[Berg 91] Bergwerff, J.B.: "Airborne O_3 measurements during TROLIX '91", RIVM report 222201005

[Brow 85] Browell, E.V., S. Ismail, and S.T. Shipley: "Ultraviolet DIAL measurements of ozone profiles in regions of spatially inhomogeneous aerosols", Appl. Opt., 24(17), 2827-36.(1985)

[Ched 85] Chedin, A., N.A. Scott, C. Wahiche, P. Moulinier: "The Improved Initialization Inversion Method : a high resolution physical method for temperature retrievals from satellites of the TIROS-N serie", J.Clim.Appl.Meteor., 24, 2 (1985)

[Druc 91] Calibration certificate no. 91.162 model DPI 260, Druck Ltd.

[Edne 87] Edner, H., K. Fredriksson, A. Sunesson, S. Svanberg, L. Unéus, and W. Wendt: "Mobile remote sensing system for atmospheric monitoring", Appl. Optics 26, 4330-4338 (1987)

[Edne 89] Edner, H., G.W. Faris, A. Sunesson, and S. Svanberg:"Atmospheric atomic mercury monitoring using differential absorption lidar techniques", Appl. Optics 28, 921-930 (1989)

[Ferg 83] Ferguson, J.A. and D.H. Stephens: "Algorithm for inverting lidar returns", Appl. Optics 22, 3672-3675, (1983)

[Fern 84] Fernald, F.G.: "Analysis of atmospheric lidar observations: some comments", Appl. Optics 23, 652-653, (1984)

[Gall 91a] Galle, B., H. Axelsson, K. Gustavsson, P. Ragnarsson and M. Rudin: "A Transmitting/Receiving Telescope for DOAS Measurements using Retro-reflector Techniques", submitted to Applied Optics (1991)

[Gall 91b] Galle, B. et.al.: "A long path Absorption Method for Aerosol Absorption Measurements", Swedish Environmental Institute, Göteborg, Sweden (1991)

[Gall 92] Galle, B., and J. Mellqvist: "A Long Path Method for Measurement of Spectrally Resolved Particle Attenuation", Conference Proceedings, SPIE, Berlin (1992)

[Godi 89] Godin, S., J. Pelon, and G. Megie: "Systematic lidar measurements of the stratospheric ozone vertical distribution", Geophys. Res. Lett., 16(6), 547-50.(1989)

[Hink 76] Hinkley E.D.: "Laser monitoring of the atmosphere", Berlin/Heidelberg: Springer Verlag (1976)

[Jong 91a] Jonge, C.N. de, D. P. J. Swart, J. B. Bergwerff: "DIAL meettechniek voor detectie van NO_2: Bepaling van de systemkwaliteit d.m.v. experimenten en simulatie", National Institute of Public Health and Environmental Protection (RIVM), Bilthoven, no. 222701001, October (1991)

[Jong 91b] Jonge, C.N. de: "NO_2 DIAL measurements during TROLIX '91", RIVM report 222201003 (1991)

[Jong 91c] Jonge, C.N. de: "Ground based measurements duringTROLIX '91 at Bilthoven", RIVM report 222201008 (1991)

[Jong 92] Jonge, C.N. de: "Planetary boundary layer Lidar measurements during TROLIX '91", RIVM report 222201004 (1992)

[Karm 90] Karmazin, S.E., V.M. Klimkin, S.F. Luk'yanenko, M.M. Makogon, I.N. Potapkin, I.S. Tyryshkin, V.N. Fedorishchev, A.L. Tsvetkov: "A new absorption band of water vapor H_2O: A fresh extinction channel radiation in the near- ultraviolet", 15th International Conference on Laser Radar, Tomsk, USSR (1990)

[Klet 81] Klett, J.D.: "Stable analytical inversion solution for processing lidar returns", Appl. Optics 20, 211-220, (1981)

[Komh 67] Komhyr, W.D.: Rev. Sci. Instr. 38, 981 (1967)

[Komh 69] Komhyr, W.D.: Ann. Geophys. 25, 203 (1969)

[Komh 86] Komhyr, W.D.: (1986)

[Lab 89] "Laboratory for Air Research, National Air Quality Monitoring Network; Technical Description", National Institute of Public Health and Environmental Protection (RIVM), Bilthoven, The Netherlands, December (1989)

[McDe 90] McDermid, I.S., S.M. Godin, and T.D. Walsh: "Lidar measurements of stratospheric ozone and intercomparisons and validation", Appl. Optics 29, 4914-4923.(1990)

[McEl 85] McElroy, T.: "Map Handbook 15, 1", ed. by D.G. Murcray (1985)

[Meas 84] Measures, R.M.: "Laser Remote Sensing", Wiley, New York (1984)

[Megi 77] Megie, G., J.Y. Allain, M.L. Chanin, and J.E. Blamont: "Vertical profile of stratospheric ozone by lidar sounding from the ground", Nature (London), 270(5635), 329-31,(1977)

[Milt 90] Milton, M., A. Sunesson, J. Pelon, G. Ancellet, J. Bösenberg, W. Carnuth, H. Edner, L. Stefanutti: "Raman-Shifted Laser Sources for DIAL Measurements of Ozone in the Free Troposphere", 15th International Conference on Laser Radar, Tomsk, USSR (1990)

[Moli 86] Molina, L.T., and M. J. Molina: "Absolute Absorption Cross Sections of Ozone in the 185- to 350-nm Wavelength Range", J. of Geophys. Res., 91, 14501-14508 (1986)

[Neub 91] Neuber, R., B. Krueger, O. Schrems: "Remote measurements of ozone concentration and aerosols in the Arctic stratosphere", Fresenius. J. Anal. Chem., 340(10), 650-3.(1991)

[Papa 89] Papagiannis, A., G. Ancellet, J. Pelon, and G. Megie: "Multiwavelength lidar for ozone measurements in the troposphere and the lower stratosphere", Appl. Opt., 29(4), 467-76,(1990)

[Pelo 82] Pelon, J. and G. Megie: "Ozone monitoring in the troposphere and lower stratosphere: evaluation and operation of a ground-based lidar station", J. Geophys. Res. C 87(C7), 4947-4955,(1982)

[Pelo 86] Pelon, J., S. Godin, and G. Megie: "Upper Stratospheric (30-50 km) Lidar Observations of the Ozone Vertical Distribution", J. Geophys. Res. 91, 8667-8671.(1986)

[Penn 57] Penndorf, R.: "Tables of the Refractive Index for Standard Air and the Rayleigh Scattering Coefficient for the Spectral Region between 0.2 and 20.0u and Their Application to Atmospheric Optics", J. Opt. Soc. Am., 47, 176-182 (1957)

[Plat 79] Platt, U., D. Perner, and H.W. Platz: J. of Geophys. Res., 79, 1629-1632 (1979)

[Sale 85] Salemink, H.W.M., E.A. van Maanen: "Toepassingen van de LIDAR-meettechniek in atmosferisch onderzoek", National Institute of Public Health and Environmental Protection (RIVM), Bilthoven, May (1985)

[Sasa 85] Sasano, Y., E.V. Browell, and S. Ismail: "Error caused by using a constant extinction/backscattering ratio in the lidar solution", Appl. Optics 24, 3929-3932, (1985)

[Sasa 89] Sasano, Y., H. Nakane, S. Hayashida-Amano, N. Sugumoto, and I. Matsui: "Multiple-wavelength DIAL and a new analysis technique to deduce the ozone profile without systematic errors due to aerosol effects", in "Ozone in the Atmosphere", R.D. Bojkov and P. Fabian (Eds.), 743-746, Deepak Publishing, Hampton (1989)

[Scho 74] Schotland, R.M.: "Errors in the lidar measurement of atmospheric gases by differential absorption", J. Appl. Met. 13, 71-77.(1974)

[Shet 79] Shettle, E.P., and R.W. Fenn: "Models of the aerosols of the lower atmosphere and the effects of humidity variations on their optical properties", AFGL-TR 79-0214 (ADA 085951)(1979)

[Sonn 91] Sonnemann, G., G.v. Cossart, and J. Fiedler: "Evaluation of the flight data of the ECC-sonde and of the data of the radiosonde within the frame of TROLIX '91-intercomparison-experiment in Bilthoven/Netherlands", Observatory for Atmospheric Research Kühlungsborn, Germany

[Sune 90] Sunesson, J.A.: "RIVM Tropospheric Ozone LIDAR, Feasibility and definition", RIVM report 222201002, (1990)

[Sune 91] Sunesson, J.A., and A. Apituley: "RIVM Tropospheric Ozone LIDAR, System description and first results", RIVM report 222201006, (1991)

[Swar 85] Swart, D.P. J.: "De OMA - Lidar: een compact mobiel systeem voor gaslastbepaling van NO−2, SO_2 en O_3 en remote-sensing in de menglaag", National Institute of Public Health and Environmental Protection (RIVM), Bilthoven (1985)

[Ther 42] "Instruction manual: Chemiluminescence NO_x model 42", Thermo Environmental Instruments Inc.

[Ther 49] "Instruction manual: UV Photometric Ambient O_3 Analyzer model 49", Thermo Environmental Instruments Inc.

[Thom 90] Thomsen, O.: "Messungen des Absorptionsquerschnitts von Schwefeldioxid im Wellenlängenbereich von 265 bis 298 nm", Report GKSS 90/E/36, 117 pages, 1990

[Toel 79] Toeller, H.: "Messtechnik und Automatik", VDI-Verlag GmbH,56-59, Düsseldorf (1979)

[Uch 83] Uchino, O., M. Maeda, H. Yamamura, and M. Hirono: "Observation of Stratospheric Vertical Ozone Distribution by a XeCl Lidar", J. Geophys. Res. 88, 5273-5280.(1983)

[Wern 83] Werner, J., K.W. Rothe, and H. Walter: "Monitoring of the Stratosperic Ozone Layer by Laser Radar", Appl. Phys. B 32, 113-118.(1983)

[Wood 78] Woods, P.T., B.W. Jolliffe: "Experimental and theoretical studies to dye laser differential lidar system for the determination of atmospheric SO_2 and NO_2 concentrations", Opt. Laser Technol., February (1978)